

Harnessing the catalytic transfer of magnetism

Alexander James John Hooper

Ph.D

Chemistry

University of York

March 2015

Abstract

In this thesis the research concentrates on NMR and MRI applications of the recently established hyperpolarisation technique, SABRE. Hyperpolarisation is a technique for generating enhanced magnetic resonance signals to improve resolution, contrast and signal to noise within NMR and MRI. One of the aims of this work was to develop the SABRE technique for applications in biomedical systems.

The thesis focusses on optimising the SABRE technique by catalyst modification. The connection between signal enhancement and a range of dependencies such as temperature, field and substrate are investigated. Results demonstrate that the rates of hydride and substrate ligand exchange were significant when optimising conditions. A range of biological substrate molecules were studied.

Work has also been completed on the development of SABRE techniques for use in biologically compatible solvent systems, focusing on using water soluble SABRE pre-catalysts. Other work performed, focused on optimising the SABRE technique to characterise small organic molecules. Pyridine was involved as a model substrate, studies on a range of molecules were examined these including substituted pyridines, pyrimidines, heteroatom - containing molecules.

The results shown in Chapter 4 demonstrate the potential of SABRE for the detection of 5-methylpyrimidine as a contrast agent for *in-vivo* study. They also discuss the hydrogenation of quinazoline, a novel and unexpected reaction. Work in Chapter 5 highlights the efforts made towards biocompatibility. This will include an approach for the removal of catalyst, which will focus on heterogeneous catalysis. Secondly, an approach to obtaining a catalyst that works sufficiently well in a biocompatible medium such as ethanol and water solution is detailed.

Contents

Abstract.....	2
Contents.....	3
List of Figures	12
List of Tables	26
List of Schemes.....	29
List of Equations.....	31
Acknowledgments.....	32
Declaration.....	33
1. Chapter 1 Introduction.....	34
1.1. Nuclear Magnetic Resonance (NMR).....	34
1.1.1. History of NMR.....	34
1.1.2. Uses of NMR.....	34
1.1.3. Developments in NMR	35
1.1.3.1. Fourier Transform Spectroscopy	36
1.1.3.2. Two dimensional (2D) and Three Dimensional (3D) NMR.....	36
1.1.4. How NMR works	37
1.2. Magnetic Resonance Imaging (MRI)	41
1.2.1. History of MRI	41
1.2.2. How MRI works.....	42
1.3. Magnetic Resonance (MR) sensitivity.....	45
1.4. Current Enhancement methods.....	46
1.4.1. Non-Boltzmann distribution	46
1.4.2. Brute Force.....	47
1.4.3. Optical Pumping (Hyperpolarised Noble Gases).....	47
1.4.4. Dynamic Nuclear Polarisation (DNP).....	49
1.4.4.1. History of Dynamic Nuclear Polarisation (DNP).....	49

1.4.4.2.	How DNP works	49
1.4.5.	<i>Parahydrogen</i> Induced Polarisation (PHIP).....	50
1.4.5.1.	Research of ParaHydrogen Induced Polarisation (PHIP) and its uses....	53
1.4.5.2.	<i>Parahydrogen</i> And Synthesis Allow Dramatically Enhanced Nuclear Alignment (PASADENA) and Adiabatic Longitudinal Transport After Dissociation Engenders Net Alignment (ALTADENA)	53
1.4.5.3.	Summary of PHIP type techniques	55
1.5.	Signal Amplification By Reversible Exchange (SABRE)	56
1.6.	Project aims.....	58
2.	Chapter 2 SABRE Catalyst Design.....	59
2.1.	Introduction	59
2.1.1.	History of N-Heterocyclic Carbenes	60
2.1.2.	Preparation of NHCs	62
2.1.3.	Silver NHC Complexes	64
2.1.4.	Transition metal complexation of NHCs	65
2.2.	Catalyst Design for SABRE	67
2.2.1.	Synthesis of carbene $\text{ImMe}_2\text{NPr}^i_2$ (1-a)	67
2.2.2.	Synthesis of carbene BzIMes (1-b).....	68
2.2.3.	Synthesis of metal complexes: $[\text{Ir}(\text{NHC})(\text{COD})\text{Cl}]$ (2-a, 2-b and 2-c)	70
2.2.4.	Activation of Complexes with Carbon Monoxide	73
2.2.5.	Electronic and Steric Effects.....	75
2.2.6.	Reactions of 2-a with pyridine and hydrogen	78
2.2.7.	Exchange Rate and Activation Parameters	84
2.2.8.	Ligand Loss	85
2.2.9.	Hydride Loss.....	86
2.3.	Summary	87
3.	Chapter 3 Exemplifying the SABRE method with pyridine	88
3.1.	Introduction	88

3.2.	Enhancement of ^1H NMR signals of pyridine by 2-a, 2-b and 2-c under SABRE	88
3.3.	Polarisation field plot	90
3.3.1.	Magnetisation type	94
3.4.	Only <i>Parahydrogen</i> Spectroscopy (OPSY)	95
3.5.	Effect of temperature to the SABRE catalyst	98
3.6.	Probing ^{13}C NMR experiments	101
3.7.	Comparison of SABRE Catalysts Performance with Pyridine	108
3.8.	Enhancements of pyridine derivatives	109
3.8.1.	2-methylpyridine	110
3.8.2.	3-methylpyridine	112
3.8.2.1.	Method 1 applied to ^1H NMR	112
3.8.2.2.	Effect of changing magnetic field of polarisation	113
3.8.2.3.	Effect of changing temperature	114
3.8.2.4.	Effect of magnetic field applied to ^{13}C nuclei	115
3.8.3.	4-methylpyridine	118
3.8.3.1.	Effect of polarisation to ^{13}C nuclei	121
3.8.4.	Nicotinamide	122
3.8.4.1.	Observable ^1H NMR spectra using method 1	122
3.8.4.2.	Effect of changing magnetic field of polarisation	124
3.8.4.3.	Effect of changing temperature	125
3.9.	Summary	127
4.	Chapter 4 Optimisation of the SABRE Effect for 5-methyl pyrimidine and quinazoline	130
4.1.	Introduction	130
4.1.1.	Screening a large range of substrates to be used with SABRE	131
4.2.	SABRE with 5-methylpyrimidine	132
4.2.1.	Initial polarisation studies of 5-methylpyrimidine	132
4.2.2.	Optimising 5-methylpyrimidine for SABRE with catalyst 2-c	135

4.2.2.1.	Polarisation Transfer Field Plot.....	135
4.2.2.2.	Temperature	139
4.2.3.	Concentration	139
4.2.3.1.	The effect of concentration during polarisation when the ratio of 5-methylpyrimidine to catalyst stays the same	141
4.2.3.2.	The effect of concentration on polarisation transfer when the ratio of 5-methyl pyrimidine to catalyst changes.	145
4.3.	Imaging.....	148
4.3.1.	Imaging Results	150
4.4.	Effect of deuterium labelling.	157
4.4.1.	Synthesis of deuterated 5-methylpyrimidine isotopers	158
4.4.1.1.	4,6-d ₂ -5-methylpyrimidine.....	159
4.4.1.2.	2-d-5-methylpyrimidine	160
4.4.1.3.	2,4-d ₂ -5-methylpyrimidine.....	161
4.4.2.	Testing chlorinated and deuterated 5-methylpyrimidine analogues with SABRE	162
4.5.	Conversion of Quinazoline to 3,4-dihydroquinazoline followed by SABRE	165
4.6.	Summary	169
5.	Chapter 5 Heterogeneous and Water Soluble NHC Catalysts used for SABRE.....	171
5.1.	Introduction	171
5.2.	Heterogeneous Catalysis.....	172
5.2.1.	Introduction	172
5.2.2.	Immobilization on Polymer Supports	174
5.2.2.1.	Synthesis of an Iridium Supported Polymer	175
5.2.2.2.	Exemplifying the SABRE Method with an Iridium Supported Polymer P4	177
5.2.3.	Encapsulation of a SABRE catalyst.	178
5.2.3.1.	Exemplifying the SABRE method with an Encapsulated 2-c Catalyst ..	180
5.2.4.	Immobilization of NHC complexes on silica supports.....	183

5.2.4.1.	Introduction	183
5.2.4.2.	Synthesis of Iridium-NHC complexes supported to mesostructured silica material. 188	
5.2.4.3.	Exemplifying the SABRE method with an iridium complex supported on mesoporous silica.....	191
5.2.4.4.	Exemplifying PHIP heterogeneous hydrogenations reactions with an iridium supported mesoporous silica.	194
5.3.	Iridium NHC catalyst used for SABRE in a biocompatible solvent.	201
5.3.1.	Exploring SABRE efficiency with catalyst 2-e, 2-f and 2-g.....	205
5.4.	Summary	210
6.	Chapter 6 Conclusions and Future Work	212
6.1.	Conclusion.....	212
6.2.	Future Work.....	215
7.	Chapter 7 Experimental	217
7.1.	Instrumentation	217
7.2.	Standard Methods	217
7.2.1.	Preparation of <i>parahydrogen</i>	217
7.2.2.	Shake Method (method 1).....	217
7.2.3.	Flow Method (method 2).....	218
7.2.3.1.	Reproducibility of method 2	219
7.2.4.	Calculation of ^1H NMR enhancement factors	220
7.2.5.	Total Enhancement	221
7.2.6.	Calculation of ^1H MRI enhancement factors.....	221
7.2.7.	Chemicals and Solvents.....	222
7.3.	Reactions.....	222
7.3.1.	Synthesis of $\text{ImMe}_2\text{NPr}_2^j$ (1-a).....	222
7.3.2.	Synthesis of BzIMes (1-b).....	223
7.3.3.	Synthesis of $[\text{Ir}(\text{COD})\text{Cl}]_2$	225

7.3.4.	Synthesis of $[\text{Ir}(\mu\text{-OMe})(\text{COD})]_2$	225
7.3.5.	Synthesis of $[(\text{NHC})\text{AgCl}]$	226
7.3.6.	Synthesis of $[\text{Ir}(\text{NHC})(\text{COD})\text{Cl}]$ (2-a, 2-b)	227
7.3.7.	Synthesis of $[\text{Ir}(1\text{-a})(\text{CO})_2\text{Cl}]$ (3-a).....	228
7.3.8.	Synthesis of $[\text{Ir}(1\text{-b})(\text{CO})_2\text{Cl}]$ (3-b)	229
7.3.9.	Synthesis of $\text{LiOC}(\text{CF}_3)_3$	230
7.3.10.	Synthesis of $\text{AgOC}(\text{CF}_3)_3$	231
7.3.11.	Synthesis of 3-acetoxymethylpyridine	231
7.3.12.	Synthesis of $[\text{Ir}(\text{SIMesCh})(\text{COD})\text{Cl}]$ 2-f.....	232
7.3.13.	Synthesis of $[\text{Ir}(\text{SIMesTrimet})(\text{COD})\text{Cl}]$ (2-g)	233
7.3.14.	Synthesis of $[\text{Ir}(\text{IMesOH})(\text{COD})\text{Cl}]$ (2-e).....	234
7.3.15.	Synthesis of 2-d-5-methylpyrimidine.HCl	235
7.3.16.	Synthesis of 2,4-d-5-methylpyrimidine.....	235
7.3.17.	Synthesis of 4,6-d-5-methylpyrimidine.....	236
7.3.18.	Synthesis of silica material M-Bz-Im	237
7.3.19.	Synthesis of silica material M-Bz-Im-Ir ₍₁₎	238
7.3.20.	Synthesis of silica material M-Pr-Im-Ir ₍₂₎	239
7.3.21.	Synthesis of 3,4-dihydroquinazoline.....	240
7.4.	Characterisation of Catalyst Precursors and Their Active Analogues.....	241
7.4.1.	$[\text{Ir}(\text{IMes})(\text{COD})\text{Cl}]$ (2-c)	241
7.4.2.	$[\text{Ir}(\text{IMes})(\text{pyridine})_3(\text{H})_2]\text{Cl}$ (5-c).....	241
7.4.3.	$[\text{Ir}(\text{IMes})(\text{Benzimidazole})_3(\text{H})_2]\text{Cl}$ (5-c).....	241
7.4.4.	$[\text{Ir}(\text{IMes})(\text{Quinazoline})_3(\text{H})_2]\text{Cl}$ (5-c).....	242
7.4.5.	$[\text{Ir}(\text{IMes})(\text{Quinazoline})_2(\text{DCM})(\text{H})_2]\text{Cl}$ (5-c)	242
7.4.6.	$[\text{Ir}(\text{IMes})(3,4\text{-dihydroquinazoline})_3(\text{H})_2]\text{Cl}$ (5-c).....	243
7.4.7.	$[\text{Ir}(\text{IMes})(\text{oxazole})_3(\text{H})_2]\text{Cl}$ (5-c).....	243
7.4.8.	$[\text{Ir}(\text{IMes})(\text{isoxazole})_3(\text{H})_2]\text{Cl}$ (5-c)	244
7.4.9.	$[\text{Ir}(\text{ImMe}_2\text{NPr}'_2)(\text{COD})\text{Cl}]$ (2-a)	244

7.4.10.	[Ir(ImMe ₂ NPr ⁱ ₂)(pyridine)(COD)]Cl (4-a).....	244
7.4.11.	[Ir(ImMe ₂ NPr ⁱ ₂)(pyridine) ₃ (H) ₂]Cl (5-a).....	245
7.4.12.	[Ir(ImMe ₂ NPr ⁱ ₂)(pyridine) ₂ (MeOH)(H) ₂]Cl	245
7.4.13.	[Ir(BzIMes)(COD)]Cl (2-b)	246
7.4.14.	[Ir(BzIMes)(pyridine) ₃ (H) ₂]Cl (5-b).....	246
7.4.15.	[Ir(SIMesCh)(COD)]Cl (2-f).....	246
7.4.16.	[Ir(SIMesCh)(pyridine) ₃ (H) ₂]Cl (5-f)	247
7.4.17.	[Ir(SIMesTrimet)(COD)]Cl (2-g).....	247
7.4.18.	[Ir(SIMesTrimet)(pyridine) ₃ (H) ₂]Cl (5-g)	247
7.5.	Characterisation of Substrates and Associated Data.....	248
7.5.1.	Pyridine	248
7.5.1.1.	Hyperpolarised spectra.....	248
7.5.2.	3-methylpyridine.....	249
7.5.2.1.	Hyperpolarised spectra.....	249
7.5.3.	4-methylpyridine.....	250
7.5.3.1.	Hyperpolarised spectra.....	250
7.5.4.	Nicotinamide.....	251
7.5.4.1.	Hyperpolarised spectra.....	251
7.5.5.	3-acetoxymethylpyridine	252
7.5.5.1.	Hyperpolarised spectra.....	252
7.5.6.	5-methylpyrimidine	253
7.5.6.1.	Hyperpolarised spectra.....	253
7.5.7.	Benzimidazole	254
7.5.7.1.	Hyperpolarised spectra.....	254
7.5.8.	Imidazole.....	255
7.5.8.1.	Hyperpolarised spectra.....	255
7.5.9.	Oxazole.....	255
7.5.9.1.	Hyperpolarised spectra.....	256

7.5.10.	Isoxazole.....	256
7.5.10.1.	Hyperpolarised spectra.....	257
7.5.11.	Pyrazole.....	257
7.5.11.1.	Hyperpolarised spectra.....	258
7.5.12.	Thiazole	258
7.5.13.	1,2,4-Triazole.....	258
7.5.13.1.	Hyperpolarised spectrum	259
7.5.14.	Benzoxazole	259
7.5.14.1.	Hyperpolarised spectra.....	260
7.5.15.	2,1-Benzisoxazole.....	260
7.5.15.1.	Hyperpolarised spectra.....	260
7.5.16.	1,2-Benzisoxazole.....	261
7.5.16.1.	Hyperpolarised spectra.....	261
7.5.17.	Quinazoline	262
7.5.17.1.	Hyperpolarised spectra.....	262
7.5.18.	Pyrimidine	263
7.5.18.1.	Hyperpolarised spectra.....	263
8.	Appendices.....	264
8.1.	Collection of NMR data for the calculation of exchange rates.....	264
8.1.1.	Collection of NMR data for the calculation of exchange rates.....	264
8.1.2.	Calculation of thermodynamic activation parameters	264
8.1.3.	Collected rate constant and thermodynamic activation parameters of 2-a and with pyridine.	265
8.1.4.	Collected rate constant and thermodynamic activation parameters of 2-b and with pyridine.	266
8.1.5.	Collected rate constant and thermodynamic activation parameters of 2-c and with 5-methylpyrimidine.	267
8.1.6.	Collected rate constant and thermodynamic activation parameters of 2-c and with quinazoline in methanol-d ₄	269

8.1.7.	Collected rate constant and thermodynamic activation parameters of 2-c and with quinazoline in dichloromethane-d ₂ .	270
8.2.	Calibration graphs for concentration studies.	272
8.3.	Adapted pulse sequences used within this thesis	274
8.3.1.	Standard 90° pulse acquire sequence	274
8.3.2.	¹ H OPSYdq NMR pulse sequence – ph_OPsYdq	275
8.3.3.	1D refocused ¹³ C{ ¹ H} NMR pulse sequence (¹³ C{ ¹ H}_JR) – ph_zg_refocus..	277
8.3.4.	1D ¹³ C{ ¹ H} NMR pulse sequence refocused for both J coupling and chemical shift evolution (¹³ C{ ¹ H}_JCSR) – ph_zg_refocused_J+CS.	278
8.3.5.	1D ¹³ C INEPT NMR pulse sequence – ph_ineptnd	279
8.3.6.	1D ¹³ C{ ¹ H} INEPT NMR pulse sequence – ph_ineptrd	281
8.3.7.	2D ¹ H- ¹ H OPSYdq-COSY NMR pulse sequence – ph_OPsYdq_2D	283
9.	Abbreviations	285
10.	References	289

List of Figures

Figure 1.1 Schematic of a multiple pulse experiment of Ernst ²³	36
Figure 1.2 Chemical shifts in a rotating frame for spins A and X ¹¹	38
Figure 1.3 J-coupling in a rotating frame, where the vectors have an antiphase disposition after an evolution period of $\frac{1}{2} J$ and $\frac{1}{4} J$ s for doublets and triplets respectively ¹¹	39
Figure 1.4 ¹ H NMR spectrum showing the 3 distinct chemical environments of protons observed in ethanol. NMR spectrum recorded in CDCl ₃	40
Figure 1.5 ¹ H NMR Zeugmatography of thoracic cavity of a mouse ²⁶	41
Figure 1.6 Graph showing longitudinal relaxation (M_z/M_0) over time. T_1 is when 63 % of magnetisation has relaxed to equilibrium. 95 % is represented by $3 \times T_1$ ³⁴	43
Figure 1.7 Diagram showing T_1 relaxation returning to thermal equilibrium in the xy-plane, following at 90° r.f. pulse.....	44
Figure 1.8 Schematic diagram showing Boltzmann and non-Boltzmann distribution.	45
Figure 1.9 Schematic representation of distribution of spins in a magnetic field. A normal distribution shown on the left and a non-Boltzmann distribution shown on the right.	46
Figure 1.10 MRI images of excised lungs and heart of a mouse as hyperpolarised ¹²⁹ Xe enters the lungs ⁵¹	48
Figure 1.11 Schematic showing the four spin combinations of dihydrogen both <i>orthohydrogen</i> and <i>parahydrogen</i>	51
Figure 1.12 Schematic of <i>parahydrogen</i> generator used at York.....	52
Figure 1.13 Schematic of Boltzmann distribution <i>orthohydrogen</i> and non-Boltzmann distribution <i>parahydrogen</i> under PASADENA and ALTADENA conditions	54
Figure 1.14 Hydrogenation reaction of ¹³ C labelled compound acetylenedicarboxylic acid dimethyl ester for the detection of maleic acid dimethyl ester, in the presence of a rhodium as reported by Golman <i>et al.</i> ⁸⁷	55
Figure 1.15 Schematic of SABRE ⁹²	56
Figure 2.1 Representation of singlet and triplet forms of a carbene	59
Figure 2.2 Representation of Fischer and Schrock type carbene bonding	60
Figure 2.3 Five membered NHC and its precursor; where the base could be KO ^t Bu or NaOEt	60
Figure 2.4 Structures of the free carbene ligands 1-a (ImMe ₂ NPr ₂), 1-b (BzIMes) and 1-c (IMes) prior to complexation	67
Figure 2.5 Carbene complexes 2-a, 2-b and 2-c to be synthesised for use with SABRE	70
Figure 2.6 IR spectrum corresponding to the addition of CO to complex 3-a.....	74

Figure 2.7 <i>cis</i> and <i>trans</i> CO isomers of 3-a.....	75
Figure 2.8 Diagrams representation of the electronic effect (left) and the steric effect (right)	76
Figure 2.9 Schematic for the representation of a cone angle for a metal-phosphine, taken from a publication by Clavier and Nolan <i>et al.</i> in 2010 ¹⁴²	76
Figure 2.10 Estimation of the steric bulk of NHCs using a length parameter A_L and height parameter A_H , as proposed by Huang <i>et al.</i> in 1999 ¹⁴³	77
Figure 2.11 Schematic representing per cent buried volume taken from publication by Hillier <i>et al.</i> 2003 ¹⁴⁴	77
Figure 2.12 Graph showing the correlation between TEP and ν_{CO} for a series of phosphine and carbene ligands in $[\text{Ir}(\text{L})(\text{CO})_2\text{Cl}]$ as reported by R Kelly <i>et al.</i> , 2007, with the measured ν_{CO} data obtained for 3-a ($\text{ImMe}_2\text{NPr}^i_2$) and 3-b (BzIMes) from this study ¹⁴⁰	78
Figure 2.13 ^1H NMR spectrum of the aromatic region of a solution containing 4-a and pyridine showing both the bound and the free resonances of pyridine.....	80
Figure 2.14 ^1H NMR spectrum of complexes 4-a and 5-a showing the aromatic region only; bound and free pyridine resonances are attributed.....	80
Figure 2.15 ^1H COSY NMR spectrum showing selected coupled resonances attributed to bound pyridine protons in complexes 4-a (blue) and 5-a (red, <i>trans</i> ligand orientation and green <i>cis</i> ligand orientation).....	81
Figure 2.16 ^1H NOESY NMR spectrum of complexes 4-a and 5-a, with the exchange peaks between free pyridine and the <i>trans</i> pyridine ligand of 5-a circled in red.....	82
Figure 2.17 ^1H - ^{13}C HSQC NMR spectrum of complexes 4-a and 5-a, identifying the ^{13}C resonances in the associated complexes.....	82
Figure 2.18 The reaction co-ordinate for the dissociative reaction for the loss of ligand.....	84
Figure 3.1 Observed ^1H NMR spectra for pyridine resonances 2, 3 and 4. The thermal is represented on top and polarised on the bottom, shaken at approximately 65 G.....	89
Figure 3.2 Observed ^1H NMR signal intensity changes for pyridine resonances 2, 3 and 4 as a function of the PTF using catalyst 2-a and method 2.....	91
Figure 3.3 Graphical representation of the observed ^1H NMR signal enhancement profile using the activated catalyst 2-a and pyridine as a function of PTF over the range of 0 – 150 G.....	91
Figure 3.4 Graphical representation of the observed ^1H NMR signal enhancement profile as a function of PTF over the range of 0 – 150 G, produced for pyridine using catalyst a) 2-b b) 2-c.....	93

Figure 3.5 Observed ^1H signal enhancement field profile for position 3 of pyridine using the activated catalyst 2-b.....	94
Figure 3.6 Pulse sequence for a double quantum selected OPSY NMR experiment.....	95
Figure 3.7 A series of ^1H OPSYdq NMR signal intensity profiles for the pyridine resonances 2, 4 and 3 as a function of PTF (-140 G to 0.5) using a) 2-a b) 2-b and c) 2-c. Spectra for 2-c was taken from literature ¹⁴⁹	96
Figure 3.8 A series of ^1H OPSYsq NMR signal intensity profiles for the <i>meta</i> pyridine resonance as a function of PTF (0.5 to 140 G) resulting after SABRE using 2-c.....	97
Figure 3.9 Graphical representation of the ^1H NMR signal enhancements seen for pyridine using catalyst 2-a as a function of temperature at a PTF of a) 0.5 G and b) 65 G	98
Figure 3.10 Graphical representation of the ^1H NMR signal enhancements seen for pyridine using catalyst 2-b as a function of temperature at a PTF of a) 0.5 G and b) 65 G	99
Figure 3.11 Graphical representation of the ^1H NMR signal enhancements seen for pyridine using catalyst 2-c as a function of temperature at a PTF of a) 0.5 G and b) 65 G	99
Figure 3.12 $^{13}\text{C}\{^1\text{H}\}$ and ^{13}C NMR spectra of pyridine, using 2-a in a single scan. The thermal trace is presented on the top. The polarised traces are presented in the middle and on the bottom, which were obtained using method one at approximately 65 G with a signal-to-noise ratio for $^{13}\text{C}\{^1\text{H}\}$ of 47, 201 and 89 for position 2 to 4 respectively and for ^{13}C of 14, 61 and 39 for position 2 to 4 respectively	101
Figure 3.13 Observable states of I_x type that could be seen under SABRE	102
Figure 3.14 The effect of selected combinations of multiple quantum states which affect the peak shape in a SABRE experiment	103
Figure 3.15 Expansion of the selected resonances of Figure 3.12, for pyridine resonances 2, 3 and 4. The top spectra represents a ^{13}C experiment and the bottom traces a $^{13}\text{C}\{^1\text{H}\}$ experiment.....	103
Figure 3.16 Illustration of the resulting spectra which are obtained for $^{13}\text{C}\{^1\text{H}\}$ NMR experiment pair of perfect antiphase ^{13}C signals.....	104
Figure 3.17 Observed $^{13}\text{C}\{^1\text{H}\}$ NMR signal intensity profile for pyridine resonances 2, 3 and 4 as a function of PTF changes using 2-a and method 2.....	104
Figure 3.18 Pyridine $^{13}\text{C}\{^1\text{H}\}$ NMR signal-to-noise ratios, obtained on the flow system using 2-a and standard conditions	105
Figure 3.19 Observed ^{13}C NMR signal intensity for pyridine resonances 2, 3 and 4 as an effect of changing polarisation transfer field using 2-a and method 2	106

Figure 3.20 Pyridine ^{13}C NMR signal-to-noise ratios, obtained on the flow system using 2-a and standard conditions	106
Figure 3.21 ^{13}C NMR spectra of pyridine, using catalyst 2-b and obtained in a single scan. The thermal trace is presented on the top and the polarised trace is presented on the bottom. Expansion of the polarised trace is presented below to see resonances ^1H - ^{13}C coupling.....	107
Figure 3.22 Pyridine ^{13}C NMR signal-to-noise ratios, obtained on the flow system using 2-b and standard conditions	107
Figure 3.23 Structures of pyridine derivatives which have been investigated using catalysts 2-a and 2-b a) 2-methylpyridine b) 3-methylpyridine c) 4-methylpyridine d) nicotinamide	109
Figure 3.24 Observed ^1H NMR spectra for 2-methylpyridine, with the thermal trace represented on top and the polarised trace on the bottom; PTF of 65 G with a) catalyst 2-a and b) catalyst 2-b.....	110
Figure 3.25 Observed ^1H NMR hydride region of 2-methylpyridine which is only visible after 512 scans.....	111
Figure 3.26 Observed ^1H NMR spectra of 3-methylpyridine, thermal trace is represented on top, and the polarised trace on the bottom; PTF undertaken at 65 G with a) catalyst 2-a and b) catalyst 2-b.....	112
Figure 3.27 Observed ^1H NMR signal intensity profiles for 3-methylpyridine resonances as an effect of changing PTF using 2-a and method 2.....	113
Figure 3.28 Graphical representation of the observed ^1H NMR signal enhancement for 3-methylpyridine as a function of PTF with catalysts a) 2-a and b) 2-b, over the range 0 to -140 G.....	114
Figure 3.29 Graphical representation of the ^1H NMR signal enhancements seen for 3-methylpyridine using catalyst 2-a as a function of temperature at a PTF of a) 0.5 G and b) 65 G.....	114
Figure 3.30 Graphical representation of the ^1H NMR signal enhancements seen for 3-methylpyridine using catalyst 2-b as a function of temperature at a PTF of a) 0.5 G and b) 65 G.....	115
Figure 3.31 $^{13}\text{C}\{^1\text{H}\}$ NMR spectra of 3-methylpyridine obtained as a function PTF with catalyst 2-a and method 2 (result of a single scan). Circled in red are the strongest signals, followed by weak signals in blue and green	115

Figure 3.32 3-methylpyridine $^{13}\text{C}\{^1\text{H}\}$ NMR signal-to-noise ratios, obtained on the flow system using 2-a and standard conditions	116
Figure 3.33 ^{13}C NMR spectra of 3-methylpyridine obtained as function of PTF with catalyst 2-a and method 2 (result of a single scan). Coloured circles used to highlight the ^{13}C resonances	116
Figure 3.34 3-methylpyridine ^{13}C NMR signal-to-noise ratios, obtained on the flow system using 2-a and standard conditions.....	117
Figure 3.35 Observed ^1H NMR spectra of 3-methylpyridine, thermal trace is represented on top, and the polarised trace on the bottom; PTF undertaken at 65 G with a) catalyst 2-a and b) catalyst 2-b.....	118
Figure 3.36 Observed ^1H NMR signal intensity for 4-methylpyridine resonances as an effect of changing polarisation transfer field using 2-a and method 2.....	119
Figure 3.37 Graphical representation of the observed 4-methylpyridine ^1H NMR signal enhancement field profile using the activated catalyst a) 2-a and b) 2-b at 293 K.....	119
Figure 3.38 Graphical representation of ^1H NMR signal enhancements to 4-methylpyridine resonances obtained using activated catalyst 2-a as a function of temperature measured at a) 0.5 G and b) 65 G	120
Figure 3.39 Graphical representation of ^1H NMR signal enhancements to 4-methylpyridine resonances obtained using activated catalyst 2-b as a function of temperature measured at a) 0.5 G and b) 65 G	120
Figure 3.40 Observed $^{13}\text{C}\{^1\text{H}\}$ NMR signal intensity for 4-methylpyridine using catalyst 2-a and method 1 at a field of a) 0.5 G b) 65 G.....	121
Figure 3.41 Observed ^1H NMR spectra of 3-methylpyridine, thermal trace is represented on top, and the polarised trace on the bottom; PT undertaken at 65 G with a) catalyst 2-a and b) catalyst 2-b.....	122
Figure 3.42 Observed ^1H NMR signal intensity changes for nicotinamide resonances, as a function of the PTF using catalyst 2-c and method 2	124
Figure 3.43 Graphical representation of the observed nicotinamide ^1H NMR signal enhancement field profile using the activated catalyst a) 2-a and b) 2-b	124
Figure 3.44 Plots of polarisation transfer field for hyperpolarised ^1H NMR signal for nicotinamide reported by Mewis <i>et al.</i> 2014 ¹⁵⁶	125
Figure 3.45 Graphical representation of the ^1H NMR signal enhancements seen for nicotinamide using catalyst 2-a as a function of temperature at a PTF of a) 0.5 G and b) 65 G	126

Figure 3.46 Graphical representation of the ^1H NMR signal enhancements seen for nicotinamide using catalyst 2-b as a function of temperature at a PTF of a) 0.5 G and b) 65 G	126
Figure 4.1 Range of substrates screen using catalyst 2-c to test the activity in a SABRE measurement.....	131
Figure 4.2 Observed ^1H NMR spectra of 5-methylpyrimidine after SABRE, detailing positions 2, 4 and 7, in conjunction with catalyst 2-c. The corresponding thermal NMR spectra are presented on top and polarised NMR spectra on the bottom; a) at a PTF of 0.5 G and b) at a PTF of 65 G	132
Figure 4.3 Observed ^1H NMR signal intensity field profiles for 5-methylpyrimidine resonances as an function of changing PTF, over the range 0 to -140 G, using 2-c	135
Figure 4.4 a) Graphical representation of the observed ^1H NMR signal enhancement of 5-methylpyrimidine using catalyst 2-c as a function of PTF over the range of 0 – 140 G b) total ^1H NMR signal enhancement	135
Figure 4.5 ^1H OPSYdq NMR signal intensity profiles for the 5-methylpyrimidine resonances as a function of PTF.....	136
Figure 4.6 Schematic of equilibrium of complex 5-d, with addition of pyridine and H_2 to form the more efficient complex 6-d, reported by Fekete et al. 2014 ¹⁶¹	137
Figure 4.7 Observed ^1H NMR spectra for 5-methylpyrimidine resonances. The thermal is represented on top, polarised sample 2 containing acetonitrile in the middle and polarised sample 1 on the bottom shaken at approximately 50 G	138
Figure 4.8 ^1H NMR spectra of the hydride region for sample 2 containing 5-methylpyrimidine and acetonitrile	138
Figure 4.9 Graphical representation of the ^1H NMR signal enhancements seen for 5-methylpyrimidine using catalyst 2-c as a function of temperature at a PTF of a) 0.5 G and b) 65 G.....	139
Figure 4.10 ^1H NMR enhancements obtained for catalyst loading of 2-c as reported by Cowley <i>et al</i> 2011 ⁹³	140
Figure 4.11 Corresponding ^{13}C NMR INEPTrd spectrum for a quinoline sample at a concentration of 0.6 mM ¹⁶³	140
Figure 4.12 Thermal ^1H NMR spectrum of 5-methylpyrimidine (top) and a hyperpolarised spectrum of sample 8 (bottom) polarised with 2-c using shake and drop method (method 1) at 65G.....	142

Figure 4.13 Two single scan spectra of hyperpolarised 5-methylpyrimidine with 2-c using ^{13}C (top) and ^{13}C INEPTrd NMR pulse sequence	143
Figure 4.14 Signal-to-noise ratio graphs for sample 1-7 of Table 4.5 for the NMR measurement a) ^{13}C and b) INEPTrd when the effect of concentration is studied and substrate to catalyst, 2-c, ratio remain constant at 20 : 1.....	144
Figure 4.15 Observed ^1H NMR spectrum of 5-methylpyrimidine with thermal trace (top) and a hyperpolarised spectrum of sample 7 (bottom) with catalyst 2-c obtained at a PTF of 65G, with signal enhancements of -450, -582 and -149 respectively	145
Figure 4.16 Effect of substrate to 2-c excess on the level of polarisation transfer for a metal concentration of 5 mM	146
Figure 4.17 signal-to-noise ratio graphs for sample 1-7 of Table 4.5 for the NMR measurement a) ^{13}C and b) INEPTrd when the effect of concentration is studied, when catalyst 2-c concentration remains constant at 5 mM	147
Figure 4.18 ^1H RARE MRI images for an NMR tube containing 5-methylpyrimidine and 2-c, with the corresponding thermal images represented on the left and hyperpolarised images on the right at a PTF of 50 – 60 G with substrate ratio 20:1; the concentration of 2-c is: a) 15 mM, b) 10 mM and c) 5 mM	150
Figure 4.19 Influence of the amount of catalyst on the signal-to-noise ratio of 5-methylpyrimidine hyperpolarised/thermal images. In order to observe just the effect of 2-c, each Signal-to-noise ratio has been normalized to the concentration of substrate used ..	151
Figure 4.20 ^1H RARE MRI images for an NMR tube containing 5-methylpyrimidine and 2-c, thermal images shown on the left and hyperpolarised images on the right (collected for a PTF of 50 – 60 G, with substrate: catalyst ratio; a) 60:1 b) 40:1 and c) 20:1).....	152
Figure 4.21 Influence of the substrate: catalyst ratio on the signal-to-noise ratio of 5-methylpyrimidine hyperpolarised/thermal images.....	152
Figure 4.22 Arrangement of the phantoms and substrate (sub) in the bore of the magnet	153
Figure 4.23 ^1H MRI images of three samples, where the MRI pulse sequences are: a) RARE, b) FLASH and c) FISP. The left images reflect the thermal traces whilst the right images reflect the hyperpolarised traces. The signal-to-noise ratio of the hyperpolarised 5-methylpyrimidine signal versus that of water and oil is shown in graphs (d) and (e) respectively. Substrate = S, water = W and oil = O. Catalyst loading 1:20	154
Figure 4.24 ^1H MRI images of three samples, where the MRI pulse sequences are: a) RARE, b) FLASH and c) FISP. The left images reflect the thermal traces whilst the right images	

reflect the hyperpolarised traces. The signal-to-noise ratio of the hyperpolarised 5-methylpyrimidine signal versus that of water and oil is shown in graphs (d) and (e) respectively. Substrate = S, water = W and oil = O. Catalyst loading 1:60	155
Figure 4.25 ¹ H MRI images obtained for hyperpolarised 5-methylpyrimidine using FISP sequence in succession for a total acquisition of 9 s.....	156
Figure 4.26 Hyperpolarised ¹ H NMR for a) 2,6-d ₂ -pyridine and b) 3,4,5-d ₃ -pyridine with catalyst 2-a at a PTF of 65 G.....	157
Figure 4.27 ¹ H NMR spectrum of 4,6-d ₂ -5-methylpyrimidine in methanol-d ₄	160
Figure 4.28 ¹ H NMR spectrum of 2-d-5-methylpyrimidine in methanol-d ₄	161
Figure 4.29 ¹ H NMR spectrum for 2,4-d ₂ -5-methylpyrimidine in methanol-d ₄	162
Figure 4.30 Observed ¹ H NMR spectra for SABRE experiments with catalyst 2-c for a) 2,4-d ₂ -5-methylpyrimidine, b) 2-d-5-methylpyrimidine and c) 4,6-d ₂ -5-methylpyrimidine. The vertical expansion of b (x16) and c (x2) is based on spectra obtained for a.....	163
Figure 4.31 ¹ H NMR spectra showing the inequivalent hydride as a pair of doublets for [Ir(2-c)(H) ₂ (Quin) ₂ Cl] in dichloromethane-d ₂ at 226 K	166
Figure 4.32 Series of ¹ H NMR spectra following the conversion of quinazoline into 3,4-dihydroquinazoline by the addition of methanol-d ₄ to the sample [Ir(2-c)(H) ₂ (Quin) ₂ Cl] in dichloromethane-d ₂	167
Figure 4.33 Observed ¹ H NMR spectra of a) quinazoline when [Ir(2-c)(H) ₂ (Quin) ₂ Cl] in dichloromethane-d ₂ b) the product 3,4-dihydroquinazoline [Ir(2-c)(H) ₂ (Quin) ₃ Cl] after the addition of methanol to the dichloromethane-d ₂ in the presence of H ₂ . The thermal trace is represented on top, and the polarised trace on the bottom, under transfer a PTF of 65 G	168
Figure 4.34 Proposed stepwise outer-sphere mechanism for the hydrogenation of quinolines as reported by by Dobereiner et al 2011 ¹⁴⁸	169
Figure 5.1 Immobilisation of lipase on to glutaraldehyde-modified silica surface by the adsorption method ¹⁸⁸	173
Figure 5.2 Structure of vanadium complex encapsulated by zeolite frame work ¹⁹¹	173
Figure 5.3 Formation of palladium carbene complex tethered to a silica support ¹⁹²	174
Figure 5.4 ¹ H NMR spectra of a) P1 b) P2 c) P3, as using in the synthesis of P4.....	176
Figure 5.5 Observed ¹ H NMR spectra for pyridine resonances, a) the thermal is represented on top and polarised on the bottom shaken in PTF of 65 G, b) corresponding hydride region i) thermal ii) one minute after activating iii) 5 minutes after activating	177

Figure 5.6 Chemical structure of the transition metal catalyst a) iPr-Au-OTf, and the polymer matrices b) resorcin-4-arene, which in wet organic solvent self-assembles to form the encapsulated NHC catalyst, c) a hexameric host. Image taken from literature ²⁰⁶	178
Figure 5.7 Observed NMR signals a) ¹ H signals b) OPSYdq (including expansion) for the pyridine resonances under a PTF of 0.5 G	180
Figure 5.8 Observed ¹ H NMR signals observed for pyridine as a function of time a) aromatic region b) hydride region	181
Figure 5.9 Observed NMR signals of sample 1 a) ¹ H signals b) OPSYdq (including expansion) for the pyridine resonances under PTF of 0.5 G, using Sample 1	182
Figure 5.10 Silica-supported S1) second generation Grubbs-Hoveyda, developed by Kingsbury <i>et al.</i> , 2001 ²¹⁵ S2) Ruthenium complex, by Cetinkaya <i>et al.</i> , 2002 ²¹⁶ , S3-S4) second generation Grubbs, by Mayr <i>et al.</i> , 2002 and Krause <i>et al.</i> , 2003 ²²⁰ , S5) second generation Grubbs-Hoveyda by Fischer <i>et al.</i> , 2005 ²¹⁸ and S6) second generation Grubbs-Hoveyda by Li and Shi 2005 ²¹⁹	184
Figure 5.11 A simplified view of grafted oxide material after the grafting reaction (top), and a view of the inner surface of the channel pores of the mesostructured organic-inorganic material (bottom) ²²⁵	185
Figure 5.12 PASADENA ¹ H NMR spectrum acquired for hydrogenation of propyne by a) homogeneous Wilkinson's catalyst in benzene- _{d6} solution at T = 50°C b) immobilized Wilkinson's catalyst (1/PPh ₂ -SiO ₂) in benzene- _{d6} solution at T = 70°C. Taken from literature reported by Skovpin <i>et al.</i> ²²⁶	187
Figure 5.13 Heterogeneous mesoporous silica-supported iridium-NHC catalyst with different linker groups a) propyl: M-Pr-Im-Ir b) benzyl: M-Bz-Im-Ir	188
Figure 5.14 Observed ¹³ C CP-MAS NMR data for a) material M-Bz-Im b) M-Bz-Im-Ir and c) M-Bz-Im-IrCp, the final product from Scheme 5.4 which has been taken from literature reported by Maishal <i>et al.</i> , 2008 ²²⁵ , for comparison.	190
Figure 5.15 Structure of silica material, showing interaction with surface of siloxane bridges ²²⁸	191
Figure 5.16 Observed ¹ H NMR spectrum for pyridine using catalyst M-Bz-Im-Ir ₍₁₎ , at PTF of 0.5 G. Spectrum shows the antiphase hydrogen signal at δ 4.57 ppm	192
Figure 5.17 Observed ¹ H NMR Spectra of nicotinamide using catalyst M-Bz-Im-Ir ₍₂₎ , PTF undertaken at 65 G	193
Figure 5.18 Observed ¹ H NMR spectra for pyridine resonances when a control sample containing both catalyst 2-b and M-Bz-Im-Ir ₍₂₎ were shaken in a PTF of 65 G	193

Figure 5.19 Observed ^1H NMR spectra for the hydrogenation of phenylacetylene using catalyst 2-b in methanol- d_4	195
Figure 5.20 Observed ^1H NMR spectra for the hydrogenation of phenylacetylene using catalyst 2-b in dichloromethane- d_2	196
Figure 5.21 ^1H NMR polarisation spectrum of hydrogenation of styrene by a rhodium complex $[\text{Rh}(\text{COD})(\text{dppb})]\text{BF}_4$. Spectrum taken from literature reported by Harthun <i>et al.</i> 1996 ²³²	197
Figure 5.22 ^1H NMR polarisation spectrum of hydrogenation of phenylacetylene by a palladium complex a) experimental spectrum, b) simulation spectrum considering <i>cis</i> and geminal-hydrogenation in 3:1 ratio, c) simulation of spectrum of geminal <i>parahydrogen</i> into positions H^1 and H^3 , d) simulation spectrum of a <i>cis parahydrogen</i> transfer into positions H_1 and H_2 . Spectra taken from literature reported by Harthun <i>et al.</i> ²³² 1996	198
Figure 5.23 Observed ^1H NMR spectra for the hydrogenation of phenylacetylene using material catalyst M-Bz-Im-Ir ₍₁₎ in methanol solution	199
Figure 5.24 Observed ^1H NMR spectra for the hydrogenation of phenylacetylene using material catalyst M-Bz-Im-Ir ₍₂₎ in dichloromethane- d_2 solution	200
Figure 5.25 Examples catalyst designed to increase solubility by changing the of functionalised NHC substituent group to: - a) carboxylate, b) sulfonate, c) ammonium, d) carbohydrate and e) polymer	201
Figure 5.26 PHIP reaction for hydrogenation of (TFPA) in a 30 % ethanol solution, a) scheme of the <i>cis</i> addition of <i>parahydrogen</i> , b) ^{13}C NMR enhanced spectra with 17 % polarisation level obtained on a 4.7 T scanner, including a reference sample of natural abundance ^{13}C ethanol, c) <i>in-vivo</i> PHIP enhanced ^{13}C NMR image using rapid acquisition with relaxation enhancement (RARE) sequence. Images taken from literature reported by , Bhattacharya <i>et al.</i> 2011 ¹⁵⁷	202
Figure 5.27 ^1H NMR enhancement of ATZ in 90 % water, 10 % methanol at 54.4°C (top), compared to thermal polarisation (middle). The bottom spectrum is of the substrate without catalyst (16 scans). Image taken from literature reported by Zeng <i>et al.</i> 2014 ²⁴⁰ .	203
Figure 5.28 Water soluble iridium NHC complexes 2-e, 2-f and 2-g to be tested for SABRE activity in a biocompatible medium	205
Figure 5.29 Graphical representation of the observed ^1H NMR signal enhancement profile of pyridine (left) and total ^1H NMR signal enhancement (right) obtained in methanol solution using catalyst as a function of PTF using catalyst 2-e, 2-f and 2-g	206

Figure 5.30 Observed ^1H NMR signal intensity changes for pyridine resonances 2, 3 and 4 as a function of the PTF using catalyst 2-f and method 2 in a 67 % D_2O , 3 % DMSO and 30 % ethanol solution	207
Figure 5.31 a) Graphical representation of the observed ^1H NMR signal enhancement of pyridine using catalyst 2-f as a function of PTF over the range of 0 – 140 G b) total ^1H NMR signal enhancement, in a 67 % D_2O , 3 % DMSO and 30 % ethanol solution	207
Figure 5.32 a) Graphical representation of the observed ^1H NMR signal enhancement of pyridine using catalyst 2-e as a function of PTF over the range of 0 – 140 G b) total ^1H NMR signal enhancement, in a 67 % D_2O , 3 % DMSO and 30 % ethanol solution	208
Figure 5.33 SABRE with Oxazole, catalyst 2-f in a 30 % ethanol solution a) Observed ^1H NMR spectra obtained at the maximum PTF of 80 G, b) graphical representation of the observed ^1H NMR signal enhancement of oxazole as a function of PTF over the range of 0 – 140 G	209
Figure 5.34 SABRE with 3-hydroxypyridine, catalyst 2-f in a 30 % ethanol solution a) Observed ^1H NMR spectra obtained at the maximum PTF of 80 G, b) graphical representation of the observed ^1H NMR signal enhancement of oxazole as a function of PTF over the range of 0 – 140 G	209
Figure 5.35 Graphical representation of the enhancement levels achieved for oxazole, 3-hydroxypyridine and pyridine for SABRE with catalyst 2-f as a function of PTF over a range 0 – 140 G	210
Figure 7.1 Schematic representation of polariser and flow system	218
Figure 7.2 Comparing 6 ^1H NMR spectra measured consecutively using the polariser	220
Figure 7.3 when E = enhancement, S_{pol} = signal of polarised sample measured by integral, and S_{unpol} = signal of thermally polarised (reference) sample measured by integral.....	220
Figure 7.4 Labelled structure of pyridine with proton resonances labelled as <i>ortho</i> (σ), <i>para</i> (p) and <i>meta</i> (m)	221
Figure 7.5 Structure of 1-a ($\text{ImMe}_2\text{NPr}^i_2$)	222
Figure 7.6 Structure of 1-b (BzIMes).....	223
Figure 7.7 Structure of $[\text{Ir}(\text{COD})\text{Cl}]_2$	225
Figure 7.8 Structure of $[\text{Ir}(\mu\text{-OMe})(\text{COD})]_2$	225
Figure 7.9 Structure of NHC.AgCl.....	226
Figure 7.10 Structure of $[\text{Ir}(\text{NHC})(\text{COD})\text{Cl}]$ (2-a, 2-b)	227
Figure 7.11 Structure of $[\text{Ir}(1\text{-a})(\text{CO})_2\text{Cl}]$ (3-a).....	228
Figure 7.12 IR spectrum corresponding to the addition of CO to complex 3-a.....	229
Figure 7.13 IR spectrum corresponding to the addition of CO to complex 3-b.....	230

Figure 7.14 Structure of $\text{LiOC}(\text{CF}_3)_3$	230
Figure 7.15 Structure of $\text{AgOC}(\text{CF}_3)_3$	231
Figure 7.16 Structure of 3-acetoxymethylpyridine.....	231
Figure 7.17 Structure of $[\text{Ir}(\text{SIMesCh})(\text{COD})\text{Cl}]$ 2-f.....	232
Figure 7.18 Structure of $[\text{Ir}(\text{SIMesTrimet})(\text{COD})\text{Cl}]$ (2-g)	233
Figure 7.19 Structure of $[\text{Ir}(\text{SIMesTrimet})(\text{COD})\text{Cl}]$ (2-e)	234
Figure 7.20 Structure of 2-d-5-methylpyrimidine.....	235
Figure 7.21 Structure of 2,4-d-5-methylpyrimidine.....	235
Figure 7.22 Structure of 4,6-d-5-methylpyrimidine.....	236
Figure 7.23 Structure of M-Bz-Im	237
Figure 7.24 Structure of M-Bz-Im-Ir.....	238
Figure 7.25 Structure of M-Bz-Im-Ir.....	239
Figure 7.26 Structure of 3,4-dihydroquinazoline.....	240
Figure 7.27 Labelled structure of pyridine.....	248
Figure 7.28 ^1H NMR field dependence spectra for hyperpolarised pyridine sample.	248
Figure 7.29 Labelled structure of 3-methylpyridine	249
Figure 7.30 ^1H NMR field dependence spectra for hyperpolarised 3-methylpyridine sample.	249
Figure 7.31 Labelled structure of 4-methylpyridine	250
Figure 7.32 ^1H NMR field dependence spectra for hyperpolarised 4-methylpyridine sample.	250
Figure 7.33 Labelled structure of nicotinamide.....	251
Figure 7.34 ^1H NMR field dependence spectra for hyperpolarised nicotinamide sample. .	251
Figure 7.35 Labelled structure of 3-acetoxymethylpyridine.....	252
Figure 7.36 ^1H NMR field dependence spectra for hyperpolarised 3-acetoxymethylpyridine sample.....	252
Figure 7.37 Labelled structure of 5-methylpyrimidine.	253
Figure 7.38 ^1H NMR field dependence spectra for hyperpolarised 5-methylpyrimidine sample.....	253
Figure 7.39 Labelled structure of benzimidazole.....	254
Figure 7.40 ^1H NMR field dependence spectra for hyperpolarised benzimidazole.....	254
Figure 7.41 Labelled structure of imidazole.	255
Figure 7.42 Hyperpolarised spectrum of imidazole.....	255
Figure 7.43 Labelled structure of Oxazole.	255

Figure 7.44 ^1H NMR field dependence spectra for hyperpolarised oxazole sample.	256
Figure 7.45 Labelled structure of isoxazole.	256
Figure 7.46 ^1H NMR field dependence spectra for hyperpolarised isoxazole sample.....	257
Figure 7.47 Labelled structure of pyrazole	257
Figure 7.48 Hyperpolarised spectrum of pyrazole.....	258
Figure 7.49 Labelled structure of Thiazole.....	258
Figure 7.50 Labelled structure of 1,2,4-triazole.....	258
Figure 7.51 Hyperpolarised spectrum of 1,2,4-triazole.	259
Figure 7.52 Labelled structure of benzoxazole.	259
Figure 7.53 ^1H NMR field dependence spectra for hyperpolarised benzoxazole sample. ..	260
Figure 7.54 Labelled structure of 2,1-benzisoxazole	260
Figure 7.55 Labelled structure of 1,2-benzisoxazole.	261
Figure 7.56 Hyperpolarised spectra of 1,2-benzisoxazole.	261
Figure 7.57 Labelled structure of quinazoline.	262
Figure 7.58 Hyperpolarised spectra of quinazoline	262
Figure 7.59 Labelled structure of pyrimidine.....	263
Figure 7.60 ^1H NMR field dependence spectra for hyperpolarised pyrimidine sample.	263
Figure 8.1 A plot of the percentage of bound hydride and free hydrogen derived from ^1H NOESY NMR spectra against the mixing time implemented. This data was collected at 300 K and monitored the loss of hydride ligands from 2-b to free hydrogen, when 5-methylpyrimidine is studied.	264
Figure 8.2 The Eyring plots for hydride ligands and pyridine ligands loss from 2-a in the presence of pyridine with associated equations, produced from the data presented in Table 8.1.	265
Figure 8.3 The Eyring plots for hydride ligands and pyridine ligands loss from 2-b in the presence of pyridine with associated equations, produced from the data presented in Table 8.3.	267
Figure 8.4 The Eyring plots for hydride ligands and pyridine ligands loss from 2-c in the presence of 5-methylpyrimidine with associated equations, produced from the data presented in Table 8.5.	268
Figure 8.5 Eyring plots for hydride ligands and quinazoline ligands loss from 2-c in the presence of quinazoline with associated equations, produced from the data presented in Table 8.7.....	269

Figure 8.6 Eyring plots for hydride ligands and quinazoline ligands loss from 2-c in the presence of quinazoline with associated equations, produced from the data presented in Table 8.9.....	271
Figure 8.7 Graphical representation of the absolute integrals of the 5-methyl pyrimidine H A, H B and H C, obtained in a single scan ^1H NMR spectrum when 2-c catalyst concentration and substrate retain constant (mM),.....	272
Figure 8.8 Graphical representation of the absolute integrals of the 5-methyl pyrimidine H A, H B and H C, obtained in a single scan ^1H NMR spectrum when IMes catalyst concentration and substrate (mM) contained different ratio amounts.....	273

List of Tables

Table 1.1 Adapted table of temp versus <i>Orthohydrogen</i> / <i>Parahydrogen</i> population ³⁹	52
Table 2.2 Characteristic ¹ H NMR signals for the active complexes 5-a, 5-b and 5-c.	83
Table 2.3 Relevant thermodynamic and kinetic data relating to the loss of pyridine from 5-a, 5-b and 5-c*. The data for 5-c* taken from literature ⁹³ . Errors represented as 95% confidence limit, for the rate data, n = 7, for the Eyring data n = 5.	85
Table 2.4 Relevant thermodynamic and kinetic data relating to the loss of hydride ligands from 5-a, 5-b and 5-c. The data for 5-c*, taken from literature ⁹³	86
Table 3.1 Comparison of ¹ H NMR signal enhancement levels (fold) observed for pyridine using catalyst 2-a, 2-b and 2-c, shaken at 65G and 0.5G	90
Table 3.2 ¹ H NMR signal enhancements determined for the indicated pyridine resonances by catalyst 2-a under SABRE as a function of temperature	98
Table 3.3 ¹ H NMR signal enhancements of pyridine observed for a range of NHC catalyst, which were collected using the flow method, where results are given for highest level of polarisation at a specific field. * denotes values taken from literature presented by Lloyd <i>et al</i> , 2014 ¹⁵² which were measured at room temperature. # Lifetime not known	108
Table 3.4 A comparison of the ¹ H NMR polarisation enhancement for 2-methylpyridine using complex 2-a and 2-b	110
Table 3.5 Comparison of the ¹ H NMR polarisation enhancement data for 3-methylpyridine using catalysts 2-a and 2-b	112
Table 3.6 Comparison of the ¹ H NMR polarisation enhancement data for 4-methylpyridine using catalysts 2-a and 2-b	118
Table 3.7 A comparison of the ¹ H NMR polarisation enhancement for nicotinamide using catalysts 2-a and 2-b	123
Table 3.8 Total enhancements for pyridine, 3-methylpyridine, 4-methylpyridine and nicotinamide obtained at room temperature and at a PTF of 65 G.	127
Table 3.9 Total enhancements for pyridine, 3-methylpyridine, 4-methylpyridine and nicotinamide obtained at the optimal temperature and at a PTF of 65 G.	128
Table 4.1 Enhancement levels of substrates investigated with catalyst 2-c for SABRE, quoted as measured at the optimum PTF	131
Table 4.2 Comparison of the levels of ¹ H NMR signal enhancement observed for 5-methylpyrimidine using catalysts 2-a, 2-b and 2-c according to the shake method	133
Table 4.3 Activation parameters for the loss of 5-methylpyrimidine ligand and loss of hydride ligand when catalyst 2-c precursors are used	133

Table 4.4 T_1 values for 5-methylpyrimidine resonances obtained experimentally at 298 K	134
Table 4.5 The amounts of 2-c and substrate used in the corresponding concentration experiments with each made up with 0.6ml methanol- d_4	141
Table 4.6 1H NMR signal enhancement levels of free 5-methylpyrimidine proton resonances that were obtained using concentrations listed in Table 4.5.	142
Table 4.7 Summary of signal-to-noise observed in the stated NMR experiment for sample 4 for the spectra represented in Figure 4.13	143
Table 4.8 The amounts of 2-c and substrate used in the corresponding concentration experiments with each made up with 0.6ml methanol- d_4	145
Table 4.9 1H NMR signal enhancement levels for 5-methylpyrimidine	146
Table 4.10 Summary of maximum signal-to-noise ratio observed the resulting NMR experiment were ^{13}C was from sample 4 and ^{13}C INEPTrd *sample 2 and # sample 5 taken from Figure 4.17.....	147
Table 4.11 Comparison of 1H NMR signal enhancement levels (fold) observed for pyridine using catalyst 2-c.....	157
Table 4.12 Corresponding experimental conditions for the proposed Scheme 4.1 and conversion rates (* Isolation as the HCl salt)	158
Table 4.13 2H labelling of 4,6- d_2 -5-methylpyrimidine, and percentage label incorporation	160
Table 4.14 2H labelling of 2-d-5-methylpyrimidine, and percentage incorporation.....	161
Table 4.15 2H labelling of 2,4- d_2 -5-methylpyrimidine, and percentage incorporation	162
Table 4.16 Summarised 1H NMR enhancements levels observed for the 2H labelling of 5-methylpyrimidine, and percentage incorporation	164
Table 5.1 Comparison of 1H NMR signal enhancement levels (fold) observed for pyridine using IrEnCat as a function of time	181
Table 6.1 Recommended optimal conditions for the desired NMR or MRI measurement, including catalyst and substrate concentration and PTF. Listed in the table is the absolute signal-to-noise values achieved at these optimum conditions. ^absolute signal enhancement, signal-to-noise ratio of the hyperpolarised 5-methylpyrimidine signal versus that of #water and *oil	213
Table 7.1 Detailing the statistics estimating the reproducibility of method 2	219
Table 8.1 Rate constants for the loss of pyridine and hydride ligands from 2-a in the presence of pyridine at the indicated temperatures.....	265

Table 8.2 Thermodynamic parameters of activation for the loss of hydride and pyridine ligands with catalyst 2-a, errors are quoted as 95% confidence limit.....	266
Table 8.3 Rate constants for the loss of pyridine and hydride ligands from 2-b in the presence of pyridine at the indicated temperatures.....	266
Table 8.4 Thermodynamic parameters of activation for the loss of hydride and pyridine ligands with catalyst 2-b, errors are quoted as 95% confidence limit.....	267
Table 8.5 Rate constants for the loss of pyridine and hydride ligands from 2-c in the presence of 5-methylpyrimidine at the indicated temperatures.	267
Table 8.6 Thermodynamic parameters of activation for the loss of hydride and 5-methylpyrimidine ligands with catalyst 2-c, errors are quoted as 95% confidence limit....	268
Table 8.7 Rate constants for the loss of pyridine and hydride ligands from 2-c in the presence of quinazoline at the indicated temperatures in methanol-d ₄	269
Table 8.8 Thermodynamic parameters of activation for the loss of hydride and quinazoline ligands with catalyst 2-c in methanol-d ₄ , errors are quoted as 95% confidence limit.	270
Table 8.9 Rate constants for the loss of pyridine and hydride ligands from 2-c in the presence of quinazoline at the indicated temperatures in dichloromethane-d ₂	270
Table 8.10 Thermodynamic parameters of activation for the loss of hydride and quinazoline ligands with catalyst 2-c in dichloromethane-d ₂ , errors are quoted as 95% confidence limit. *calculated value.	271
Table 8.11 The amounts of 2-c and substrate used in the corresponding concentration experiments with each made up with 0.6ml d ₄ -methanol	272
Table 8.12 The amounts of 2-c and substrate used in the corresponding concentration experiments with each made up with 0.6ml d ₄ -methanol.	273

List of Schemes

Scheme 2.1 Dimerisation of 1,3-diphenylimidazolidin-2-ylidene (3)	61
Scheme 2.2 Synthesis of NHC complex (6) by deprotonation of 1,3-diphenylimidazolium perchlorate, and its subsequent reaction with mercury(II) chloride.....	61
Scheme 2.3 Schematic showing the steps involved in the isolation of the first reported free stable carbene, 1,3-di-1-adamantylimidazol-2-ylidene	62
Scheme 2.4 Synthetic routes to imidazolium salts; a) symmetrical one-pot synthesis from glyoxal; b) unsymmetrical two-step synthesis from glyoxal; c) aryl substitution from 1,2 diamines.....	63
Scheme 2.5 Synthesis of carbenes from a substituted imidazol-2-(3H)-thione, via a sulphur reduction.....	63
Scheme 2.6 Reduction of imidazol-2-(3H)-thione to imidazolium-2-ylidene and dimerized alkene.....	64
Scheme 2.7 Synthesis of 1,2,4-triazol-5-ylidene via vacuum thermolysis.....	64
Scheme 2.8 Synthesis of a silver NHC complex, via the deprotonation of the imidazolium salt, followed by the addition of silver triflate.....	65
Scheme 2.9 Synthesis of NHC transition metal complex reported by Wanzlick <i>et al.</i> ¹³⁰	66
Scheme 2.10 Synthesis of NHC transition metal complex reported by Öfele <i>et al.</i> ¹³¹	66
Scheme 2.11 Synthesis and reduction of imidazol-2-(3H)-thione to produce the carbene ImMe ₂ NPr ⁱ ₂ (1-a).....	68
Scheme 2.12 Synthesis of 1-mesitylimidazole from glyoxal and the drop-wise addition of 2,4,6-trimethylphenylamine	69
Scheme 2.13 Synthesis of BzIMes (1-b) via the reaction of benzylchloride and 1-mesitylimidazole	69
Scheme 2.14 Synthesis of [Ir(COD)Cl] ₂ from iridium trichloride trihydrate.....	70
Scheme 2.15 Synthesis of [Ir(NHC)(COD)Cl] (2). [2-b when R = BzIMes, 2-a when R = ImMe ₂ NPr ⁱ ₂ and 2-c when R = IMes] via [Ir(μ-OMe)(COD)] ₂ and [Ir(μ-Cl)(COD)] ₂	71
Scheme 2.16 Synthesis of a mono-NHC silver complex, followed by transmetalation, allows the formation of [Ir(NHC)(COD)Cl] (2) via [Ir(COD)Cl] ₂ . [2-b when R = BzIMes, 2-a when R = ImMe ₂ NPr ⁱ ₂ and 2-c when R = IMes].....	72
Scheme 2.17 Synthesis of [Ir(NHC)(COD)Cl] via the deprotonation of the parent imidazolium salt using either KHMDs (1) or KO ^t Bu (2). [2-b when R = BzIMes, 2-a when R = ImMe ₂ NPr ⁱ ₂ and 2-c when R = IMes].....	73

Scheme 2.18 Expected [Ir(NHC)(CO) ₂ Cl] complex formed after the addition CO. [3-b when R = BzIMes, 3-a when R = ImMe ₂ NPr ⁱ ₂ and 3-c when R = IMes]	74
Scheme 2.19 Route to 5-a via the initial formation of 4-a upon the addition of pyridine and H ₂ to 2-a	79
Scheme 4.1 Chlorinated precursors used in the synthesis of deuterium labelled 5-methylpyrimidine substrates. These were carried out as individual reactions to obtain the corresponding final product	158
Scheme 4.2 Proposed side reaction with protic solvent leads to ethers 2, 3 of Table 4.12	159
Scheme 4.3 Reaction leading to the formation of [Ir(2-c)(H) ₂ (Quin) ₂ Cl] in dichloromethane-d ₂ solution	165
Scheme 5.1 Polymerisation reaction to form an organometallic polymer, which can contain various transition metals within the backbone ¹⁹⁶	175
Scheme 5.2 Synthetic approach for the preparation of imidazolium salts containing a brush polymer and an NHC-based organometallic polymer ¹⁹⁵	175
Scheme 5.3 Sonogashira coupling reaction between iodobenzene and phenylacetylene in the presence of PdEnCat™30 ¹⁸⁵	179
Scheme 5.4 Preparation of silica-supported material M-Bz-Im-IrCp, a) TEOS, HCl, pluronic P123, room temperature; b) 2 M HCl/H ₂ O, 45°C; c) mesitylimidazole, toluene, reflux, 2 days, then TMSBr, Et ₃ N, toluene, room temperature, 48 hour; d) AgOC(CF ₃) ₃ , CH ₃ CN, 14 h, room temperature; e) [{Cp*IrCl ₂] ₂], 24 h, 60°C ²²⁵	186
Scheme 5.5 Synthesis of materials M-Bz-Cl and M-Bz-Im	189
Scheme 5.6 Synthetic approach for the preparation of imidazolium salts containing mesoporous silica and the NHC-based organometallic material M-Bz-Im-Ir ₍₁₎ via a) AgOC(CF ₃) ₃ and M-Bz-Im-Ir ₍₂₎ b) KHMDS	189
Scheme 5.7 Mechanism for the hydrogenation of phenylacetylene.....	194
Scheme 5.8 Synthesis of azolium salts a) IMesOH – (1-e) and b) where R = -N ⁺ (CH ₃) ₂ (CH ₂ CH ₂ OH)Cl ⁻ = SIMesCh – (1-f) and R = -N ⁺ (CH ₃) ₃ Cl ⁻ = SIMesTrimet (1-g).....	204

List of Equations

Equation 1.1 Normal Boltzmann distribution equation.....	45
Equation 1.2 The overall wavefunction consists of five components, the translational, electronic, nuclear, rotational and vibrational terms.....	51
Equation 8.1 Eyring equation.....	265

Acknowledgments

I would like to take this opportunity to thank my supervisors, Professor Simon Duckett and Professor Gary Green for their support and guidance throughout my research.

Secondly I would like to thank GlaxoSmithKline (GSK) for their financial support; in particular Andy Roberts who has been very supportive of my research, and has shown me great hospitality for which I am very grateful.

I would like to give a big high five to Ryan Mewis, for all his hard work and patience, especially when I had broken something and asking if it is fixable, in 10 minutes! I would also like to give a big thank you to fellow students Louise Highton, Lyrelle Lloyd and Jon Holmes who have been there since the start and most importantly formed good friendship.

I would like to thank the entire Duckett research group, in particular, Marianna Fekete for guidance with synthesis, Alexandra Olaru for help with MRI, the organic boys Mike Burns and Pete Rayner for labelling and Vicky Annis for endless supply of methanol. I would like to thank the following students and staff; Iman Khazal, Ralph Adams, David Williamson, Beatriz Eguillor, Fran Suarez, Chris Armstrong, Kevin Atkinson, Guan Dexin, Richard Green, Sarah-Louise Henshaw, Richard John, Amy Ruddlesden, Kate Appleby, Chris Lancaster, Barbara Procacci, Meghan Halse and Hayley Fenton. Thanks needs to also go to project student Josh Richards.

I would also like to thank staff at Lyon France especially Chloe Thieuleux and Reine Sayah for their collaborative work, and showing me the sights of the city.

I would like to thank all the technical and academic staff within the department for maintaining both equipment and the three buildings which have claimed residence of the Duckett research group since I started in York.

Finally I would like to thank my mum Kath and Gary and most importantly my partner Hannah for believing in me and their continuous support throughout my work.

Declaration

I can confirm, to the best of my knowledge that this work presented in this thesis is original and that if any diagrams, tables and text are used that are not original they have been identified throughout this thesis and referenced appropriately. This work has not previously been presented for an award at this, or any other, University.

1. Chapter 1 Introduction

1.1. Nuclear Magnetic Resonance (NMR)

Within the pharmaceutical industry, the ability to analyse samples of new drugs, to characterise them and any impurities that are present, is highly desirable¹. Furthermore, monitoring metabolites²⁻⁴ as their travel around the body, and additionally obtaining medically instructive images of soft tissue are also very important goals. Using Nuclear Magnetic Resonance (NMR) to understand the connectivity of atoms within a drug molecule for characterisation, and the drugs relationship with a target protein, or Magnetic Resonance Imaging (MRI), to gain images from inside the human body reflect further examples^{3, 5, 6}. One method that has the potential to achieve this is magnetic resonance (MR), a method whose basic physical principles can be readily understood. This is a truly diverse field which is currently limited by sensitivity⁶, and the work within this thesis aims to address this issue.

1.1.1. History of NMR

NMR is a useful quantitative technique for the analysis of complex mixtures as it has the ability to distinguish between nuclei in different chemical environments. The first concepts of NMR were established in 1930's by Rabi and his team at Columbia University in New York⁷. NMR was then developed by two independent groups of physicists in the United States of America in the 1940's. In late 1945, Purcell, Torrey and Pound discovered it was possible to observe signals from the protons of paraffin and therefore discovered solid state NMR⁸. In 1946, Bloch, Hansen and Packard detected signals from the protons of water and discovered liquid state NMR⁹. Both physicists, Purcell and Bloch, were awarded a Nobel Prize for their contributions to NMR. NMR has since grown and developed into an extremely useful technique that can be applied to many different research applications.

1.1.2. Uses of NMR

Within the pharmaceutical industry, NMR is widely used in both the liquid and the solid state^{3, 5, 6, 10}. Solid state NMR is used in formulation chemistry, investigating drugs and their interactions within a complex where identifying potential impurities and degradation products is very important²⁻⁴. However, it will be liquid state NMR which will be discussed throughout this thesis. Liquid state NMR is used widely in the identification of

metabolites¹⁰ and the characterisation of substrates and impurities during the development of new drugs¹. However, even with all the developments and improvements that have taken place within NMR over the last thirty years, the fundamental method of NMR remains broadly the same^{11, 12}.

1.1.3. Developments in NMR

The development of NMR stems from the discovery of chemical shift¹³ which is now used to provide diagnostic information in species as diverse as proteins and amino acids. Increases in magnetic field strength^{14, 15} and more sensitive probes, such as cryoprobes¹⁶ or cold probes now mean that multi-dimensional NMR is used widely for studying small molecules and the interrogation of other less sensitive nuclei such as ¹³C. The invention of the cryoprobes increased the sensitivity by at least 3-fold⁶. The invention of high resolution capillary tubes has also aided in the routine collection of NMR spectra. Although these probes do not increase sensitivity, they require smaller volumes of sample, which can be an advantage as they effectively allow increased concentrations to be used when only small amounts of sample are available¹⁷. The probe filling factor (ratio of sample volume to probe volume, that will affect acquisition time), is optimised, high signal-to-noise then results.

The most significant improvements in NMR detection methods were made by Richard R Ernst and he was awarded a Nobel prize for his contributions to NMR¹⁸ in 1992. The work he performed over 20 years transformed NMR into one of the most important instrumental measuring techniques in chemistry. Ernst's developments included dramatically increasing both sensitivity and resolution of the instrument, improved multi-dimensional NMR experiments and harnessing computing power which helped larger more complicated molecules to be studied¹⁸.

Sensitivity is the main disadvantage within NMR and much work has been performed to try and increase this. The minimum sample amounts for an analysis in NMR, the limit of detection is in the range of $10^{-9} - 10^{-11}$ mol of sample but more sensitive techniques have been invented which enable greater sensitivity to be reached, such as Fourier Transform methods which take the sensitivity level down to less than $10^{-12} - 10^{-15}$ mol⁶.

NMR is widely used in many different areas of science such as protein structure determination^{19, 20}, sample characterisation and studying cell metabolism²¹. It has also been useful for analysis of other biological macromolecules²².

1.1.3.1. Fourier Transform Spectroscopy

In 1966²³, Ernst developed the use of Fourier Transform spectroscopy in NMR from pulse excitation experiments that he performed, and this reflects one of the major improvements in NMR (Figure 1.1). The continuous wave (CW), technique usually involved the sample being interrogated with one fixed frequency source at one time and varying the magnetic field to observe all the resonances. NMR usually gives weak signals using CW, which means that the observed signal will be poor, which in turn gives poor signal-to-noise ratio. Ernst developments allowed significant changes from CW to Fourier analysis, such that the whole spectrum could be collected in seconds rather than minutes giving an increase in sensitivity²³, which was augmented by signal averaging.

In 1966, Ernst stated that Fourier analysis gave an increase in sensitivity by 100 fold in a given period of time²³. This increase in sensitivity enabled chemists to use NMR for the analysis of small amounts of material and isotopes with low abundances i.e. ¹³C.

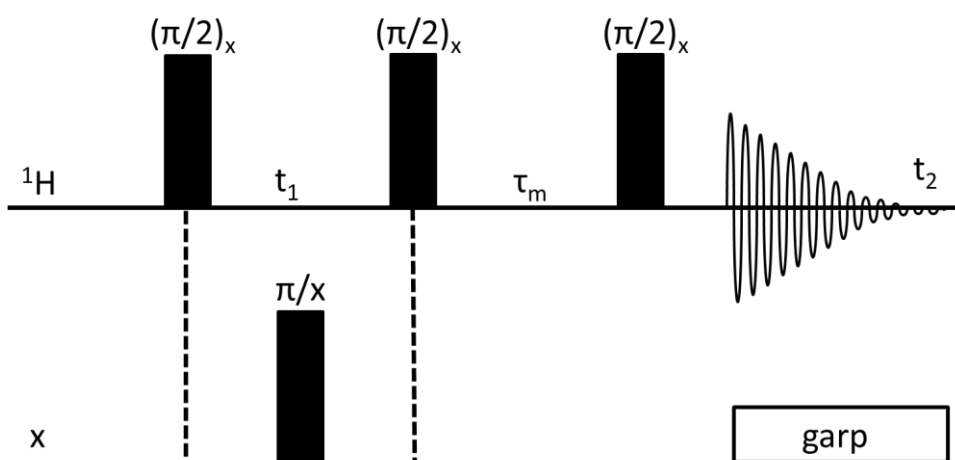


Figure 1.1 Schematic of a multiple pulse experiment of Ernst²³

1.1.3.2. Two dimensional (2D) and Three Dimensional (3D) NMR

In the 1970's, Ernst and Co. also made improvements to two dimensional (2D) NMR spectroscopy²⁴ which enabled the observation of the connectivity of nuclei according to chemical shift, which is useful for studying very large molecules. This connectivity can be used to determine covalently bound nuclei, or nuclei which are close in space, but are not covalently bound. In 1987 they also improved three dimensional (3D) NMR techniques²²,

which is most commonly used for the characterisation of large complexes such as in protein structure determination and in complex mixtures of substrates.

There are a couple of tricks that can be used to increase the sensitivity of NMR which correspond to increasing the energy difference between magnetic states of interest. This can be done by increasing the magnetic field strength of measurement and/or to decreasing the temperature of measurement.

1.1.4. How NMR works

NMR works by placing magnetic nuclei into a magnetic field. The interaction with the field causes the nuclei to align in the same direction with the field (low energy state) or opposite to the field (high energy state). The nuclei are then subjected to radio waves and they absorb different energies and can switch between these different energy states. One view is then to suggest that this energy is released as the nuclei return to equilibrium when the radio wave is switched off. This released energy is then detected and a spectrum is generated. The measure of the position of the signal in the spectrum is called the chemical shift and multiplicity, or splitting, of the signal is indicated by the number and type of adjacent nuclei where $I \neq 0$.

Chemical shift of a proton in a NMR spectrum is dependent on the electron cloud density of its bonds. The greater the density of the electronic cloud, the greater the electronic shielding that lowers the B_0 magnetic field which the nucleus would normally reside. This would move the chemical shift up-field in a ^1H NMR measurement. This can be further explained using a vector model with a sample containing two groups of chemically distinct but uncoupled spins A and X, following a 90°_x pulse. Both vectors start in the x-y plane along the y axis of the rotating frame. If the X spin has a greater electronic density, then the X vector will be moving faster than the rotating frame by a difference of ν Hz, as seen in Figure 1.2. This will mean that X will move ahead of A, and so the difference in chemical shift between the spins is simply represented here by vectors precessing at different rates¹¹.

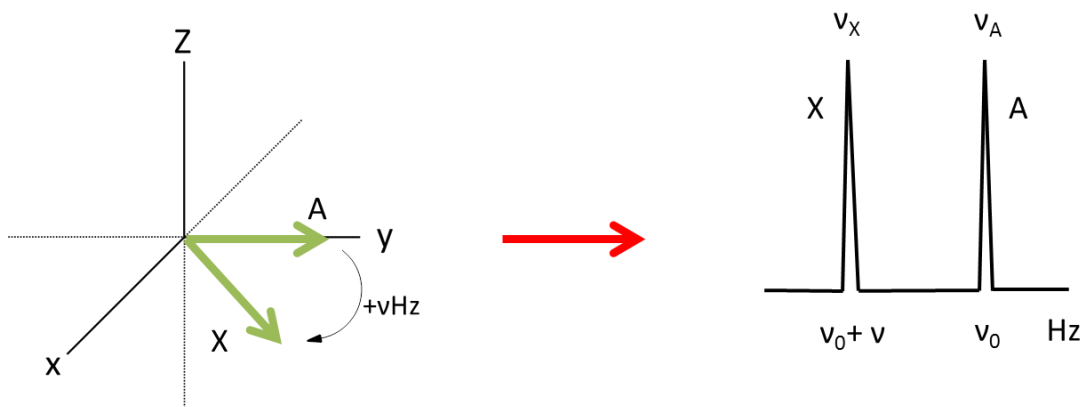


Figure 1.2 Chemical shifts in a rotating frame for spins A and X¹¹

Three pieces of valuable information are obtained from a ^1H NMR spectrum. These are; chemical shift, which helps determine the chemical environment, signal intensity which is proportional to the number of protons present in that environment and splitting of the signal into components which indicates the number of nearby protons ($n + 1$ rule)²⁵.

J-coupling is a result of through bond interactions, based on the s-orbital overlap coupling, in which the spin of one nucleus perturbs the spin of the opposite nucleus. The J coupling is field dependent and as the effect is transmitted through the bonding electrons, the J-coupling increases with increasing s-character of the chemical bond. This can be described using a rotating frame model as shown in Figure 1.3. The doublet, the two lines are represented by two vectors processing at $+J/2$ and $-J/2$ Hz, and the triplet, the central line remains static and the outer two move at $+J$ and $-J$ Hz. The ability to control the orientation of the multiple vectors is desirable. This can be achieved simply by choosing an appropriate delay period $\frac{1}{2} J$ or $\frac{1}{4} J$ for the vector evolve to obtain a doublet or triplet respectively¹¹.

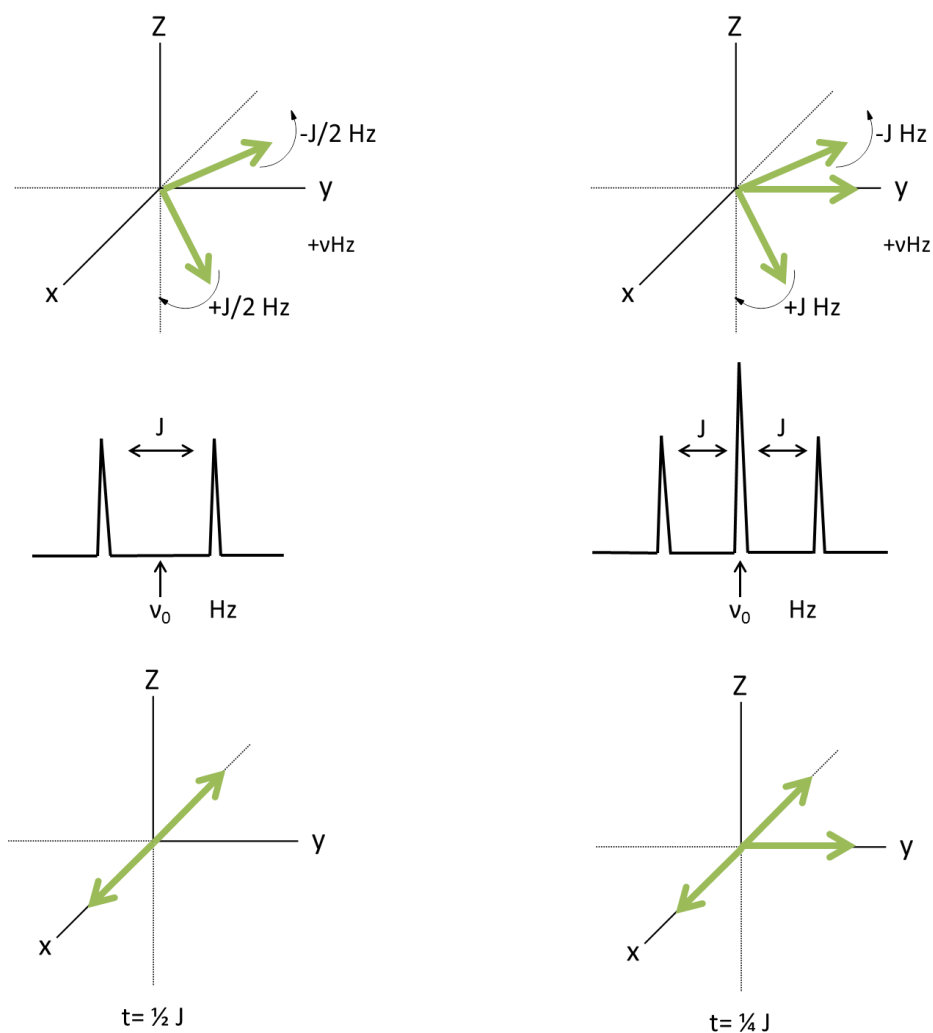


Figure 1.3 J-coupling in a rotating frame, where the vectors have an antiphase disposition after an evolution period of $\frac{1}{2} J$ and $\frac{1}{4} J$ s for doublets and triplets respectively¹¹

This information can be used to analyse and characterise molecules (Figure 1.4). However under FT conditions it would be more accurate to view the signal as the result of an induced voltage that is associated with a magnetic state alignment that is created by radio frequency excitation. The result is however the same, an NMR spectrum.

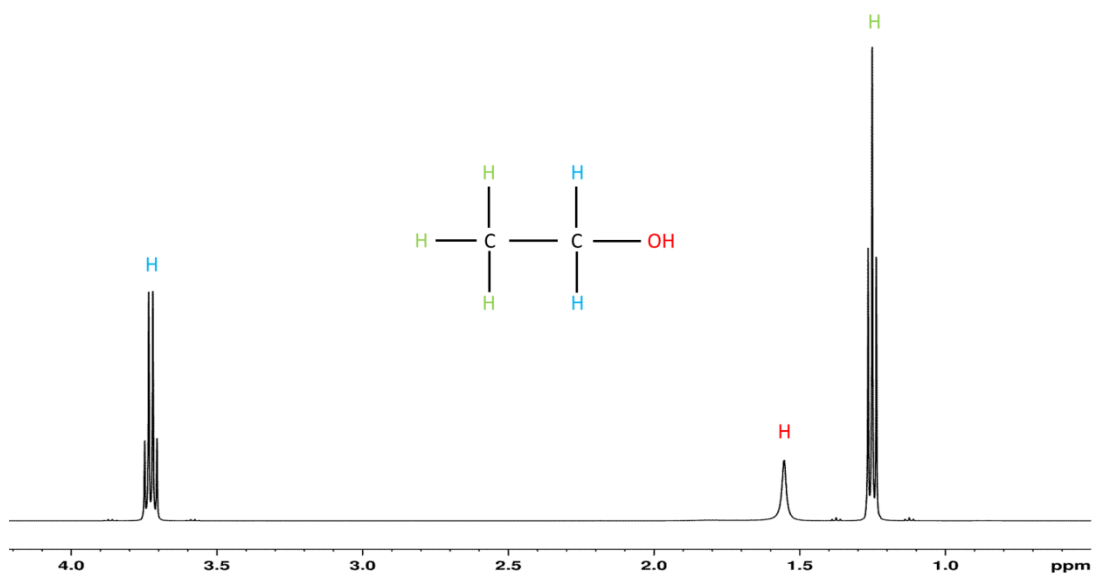


Figure 1.4 ^1H NMR spectrum showing the 3 distinct chemical environments of protons observed in ethanol. NMR spectrum recorded in CDCl_3

The nuclei of atoms are characterised by a nuclear spin quantum number, I , which does not always equal 0 and can be a multiple of a $\frac{1}{2}$. Nuclei's which possess no spin quantum number, i.e. $I = 0$ will not exhibit nuclear magnetic resonance and so these nuclei can be referred to as "NMR Silent"¹¹. The most common nuclei used in NMR have a nuclear spin quantum number of $\frac{1}{2}$, important examples include ^{13}C , ^1H and ^{15}N as these are the main atoms of interest in drug molecules and metabolites. ^1H is the most common isotope and has a natural abundance of 99.98% and as a consequence are easily detected using NMR and can be referred to as protons. Other common nuclei of interest are ^{13}C and ^{15}N , but both of these nuclei have much lower abundances (1.108% and 0.37% respectively) and different gyromagnetic ratios, which therefore require longer NMR experiment times. The nuclei studied in this thesis will all have $I = \frac{1}{2}$.

1.2. Magnetic Resonance Imaging (MRI)

This technique uses the same principles as NMR, however, the information is collected and interpreted in a different manner, which makes it possible to produce images which are able to distinguish different types of soft tissue within animals or humans.

1.2.1. History of MRI

In the 1970's, the groups of Lauterbur and Mansfield whilst working independently showed that spatially resolved NMR signals could be recorded which were later called MRI²⁶⁻²⁸. They shared a Nobel Prize for their work on MRI in 2003.

In 1973, Lauterbur performed experiments which showed the thoracic cavity of a mouse by using magnetic field gradients to produce a spatially resolved 3D map, a technique he called NMR Zeugmatography, which means imaging from joining together the main and gradient magnetic fields (Figure 1.5)²⁶. Mansfield also produced spatial information in NMR by using magnetic field gradients²⁹. Further research performed in 1975 by Ernst, used Fourier analysis and is the basis of modern MRI. Research performed in the late 1970's showed how MRI was used for both scientific and biological work such as non-invasive *in-vivo* imaging. A series of both animal and human images were then reported throughout the 1970's exemplifying this technique^{28, 30}.

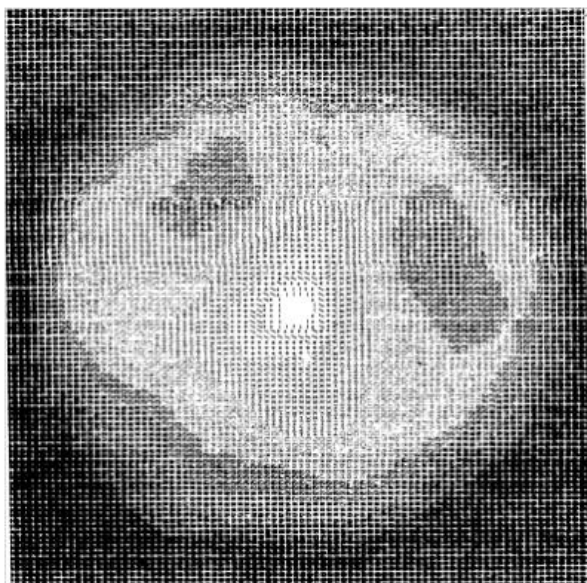


Figure 1.5 ^1H NMR Zeugmatography of thoracic cavity of a mouse²⁶

Lauterbur concluded from his research in the 1970's that different relaxation rates would be observed for different biological tissues and suggested a possibility to use this quality to study tumours. Further work was performed in 1971 and 1972 by Damadian and Weisam who used measurements of T_1 and T_2 relaxation times with the aim to distinguish between healthy tissues and tumours^{28, 30}. Damadian discovered that the hydrogen signal observed from cancerous cells is different to the hydrogen signals observed from healthy cells; cancerous cells contain more water and hence more hydrogen atoms²⁸.

1.2.2. How MRI works

MRI works by measuring the way hydrogen atoms absorb energy and then relax, re-emitting that energy. The body contains about 60% of hydrogen nuclei also referred to as protons, and protons are very sensitive to magnetic fields. Water is of high abundance in the body and so MRI is a successful technique to produce images of the body. MRI uses magnetic field gradients applied in 3D to encode the MR signal spatially and therefore produce a map or image. MRI suffers the same weaknesses as NMR with weak signal intensity due to the same physical basis of the method. ^1H MRI imaging is further limited by the presence of water in the body. MRI does, however, have an advantage over x-ray techniques as it is able to study soft tissues, ligaments and cartilage without the need for surgery.

Further research in 1986³¹, in MRI has meant that Blood Oxygen Level Differences (BOLD) can be examined in the brain, known as functional MRI (fMRI) which has provided very good information on the brain function. Also in the 1990's, MRI has been used to produce neuro-imaging and musculoskeletal-imaging. This is a very useful imaging technique and allows internal organs such as the brain, heart and eyes to be studied, and also allows for observation of blood movements through vessels and organs³².

The MRI instrument consists of a large magnet which generates the magnetic field, shim coils, radiofrequency (RF) coils, receiver coil, gradient coil and a computer to produce the final image. The signal intensity of MR images are determined by proton density, T_1 and T_2 relaxation times and flow of protons.

This follows from the fact that when a sample is placed in an applied magnetic field, B_0 , a net magnetisation is created in the direction of the field (the z-axis). When an NMR pulse is applied, this alignment is perturbed away from the equilibrium state. T_1 is defined as the

time required for the net magnetisation to relax back to equilibrium magnetisation. For the relaxation process to occur, energy is lost from the spins as heat to the surrounding nuclei, through collisions, rotations and electromagnetic interactions. This was described as 'nuclear induction' which can be described mathematically by the Bloch model, whereby T_1 is defined as the time required to change the z-component of the magnetisation by a factor of e^{-1} .

$$M_z = M_0(1 - e^{-\frac{t}{T_1}})$$

T_1 is therefore the time required for the z-component to reach 63 % ($1-1/e$) of the original level. After three T_1 periods, the bulk magnetisation is therefore 95 % of the original level and the measurement can be repeated. This situation is represented graphically in Figure 1.6

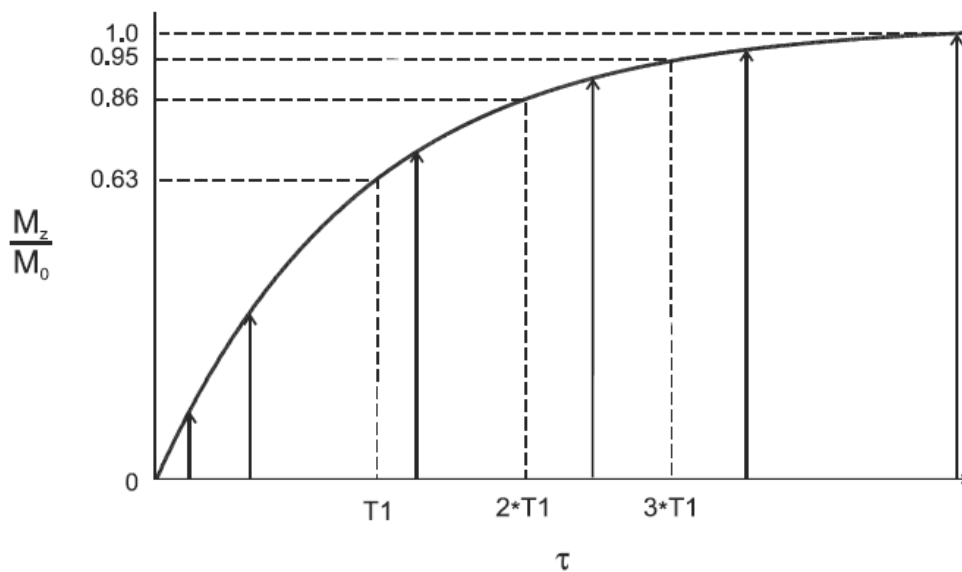


Figure 1.6 Graph showing longitudinal relaxation (M_z/M_0) over time. T_1 is when 63 % of magnetisation has relaxed to equilibrium. 95 % is represented by $3 \times T_1$ ³⁴

The T_1 relaxation process is shown diagrammatically in Figure 1.7.

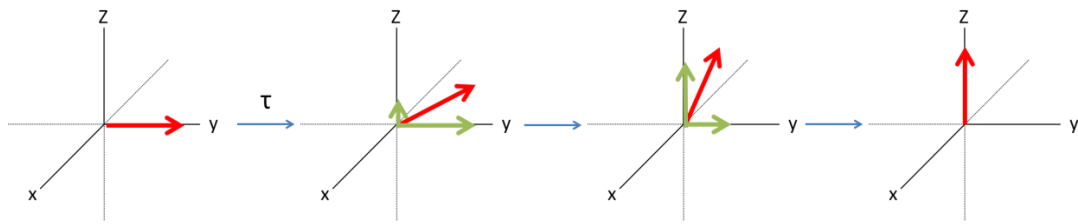


Figure 1.7 Diagram showing T_1 relaxation returning to thermal equilibrium in the xy -plane, following at 90° r.f. pulse

In MRI, the detected signal is generated by the whole of the sample that is placed in a homogenous field and no chemical shift information is routinely obtained. The route to turn this response into information retrieved from individual part of the sample requires the use of gradients. These gradients are applied across the sample, to create areas of different magnetic strength field and therefore different precessional frequencies. The gradients can be applied in three directions, x , y , z axis and are used for slice selection (z axis), phase coding (x axis) and frequency encoding (y axis) to produce a 3D image. The information is collected in what is known as K -Space, can then be transformed via Fourier transformation to generate an image³⁵.

1.3. Magnetic Resonance (MR) sensitivity

NMR and MRI are techniques which are very important in both analytical chemistry and non-invasive medical imaging. But they both have the one disadvantage of having low intrinsic sensitivity when compared to other techniques. The lack of sensitivity within NMR was also acknowledged by Ernst in 1992 during his Noble prize lecture¹⁸ and can be quantified as in Equation 1.1.

$$\frac{N^-}{N^+} = e^{-\Delta E/kT}$$

k = Boltzmann constant, N+ and N- = Number of spins in each energy levels

Equation 1.1 Normal Boltzmann distribution equation

The low sensitivity is a result of the fact that the NMR response is directly proportional to the difference between the number of spins in these two energy levels. Due to the low sensitivity, it would be an advantageous to enhance NMR and MRI signals. One method to achieve this is by improving hardware i.e. increasing the sensitivity by using a larger magnet. The larger magnet size creates a larger energy gap between lower and upper energy levels (see Figure 1.8), greater population difference and so therefore a greater number of transitions are observed leading to increased signal intensity³⁶. Additional equipment can also be used to improve sensitivity such as cryoprobes which work by reducing the background noise in the detector circuit¹⁶.

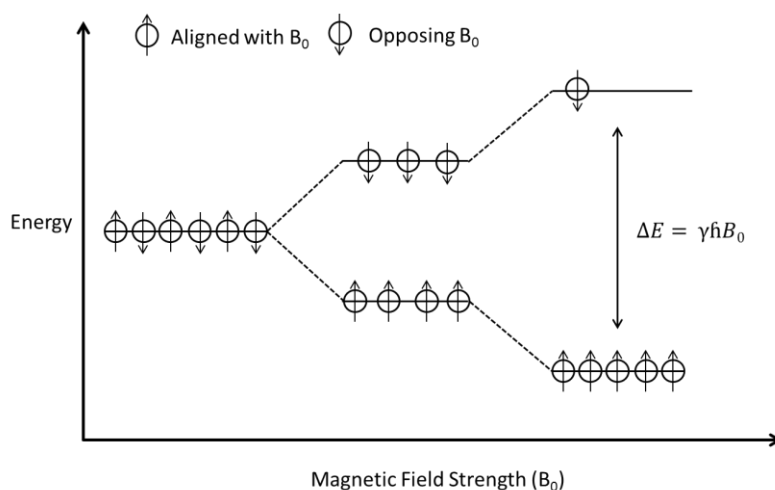


Figure 1.8 Schematic diagram showing Boltzmann and non-Boltzmann distribution.

The most powerful NMR spectrometer can be found in Lyon, France and its magnet can generate a magnetic field of 23.5 T (giving a resonance frequency of 1 GHz), this instrument

is used in molecules of interest in medicines, and biological and material science. The most powerful MRI uses a magnetic field of 9.4 T which can be found in Julich, Germany. Researchers are hoping that this powerful MRI will be able to see metabolic processes within the brain, giving images of great detail which have never been seen before. But even though these hardware advantages are available and have transformed experiments and improved sensitivity, they have proven very costly and taxing on resources. There is also a limit to the extent of further improvements via these methods.

1.4. Current Enhancement methods

With the extent of technological advancements reaching a plateau, new methods of signal enhancement must be developed. Without changing the external environment (magnets/cryoprobes) as discussed before, a change must be made to the sample. This can be achieved by producing a non-Boltzmann distribution which will increase signal intensity. Methods which achieve this include Dynamic Nuclear Polarisation (DNP)³⁷, Optical Pumping (OP) applicable for hyperpolarised noble gases³⁸ and *parahydrogen* based methods³⁹. *Parahydrogen* is the method which will be developed in this thesis.

1.4.1. Non-Boltzmann distribution

Signal enhancement can be achieved by producing a non-Boltzmann distribution of spins rather than Boltzmann distribution. A non-Boltzmann distribution creates an un-even distribution of spin states and therefore more transitions and hence greater signal intensity can be observed.

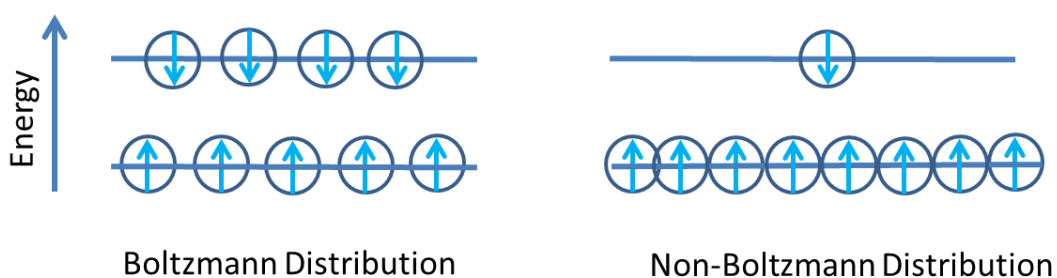


Figure 1.9 Schematic representation of distribution of spins in a magnetic field. A normal distribution shown on the left and a non-Boltzmann distribution shown on the right.

The various methods developed to achieve this non-Boltzmann distribution are discussed below.

1.4.2. Brute Force

Brute Force is a method of producing a hyperpolarised state that was first used between 1958 and 1961 by Abragam and Proctor⁴⁰. In brute force NMR, hyperpolarisation is produced by exposing the sample to a high magnetic field and a temperature close to zero Kelvin for a time long enough for the new Boltzmann equilibrium to be established. Upon thawing, to room temperature, a hyperpolarised state is created^{38, 41, 42}.

There are two disadvantages with working under these conditions. The time it takes to reach polarisation at very low temperature and maintaining the level of polarisation after returning to room temperature. Both of these link to the longitudinal relaxation time T_1 .

Current areas of research are trying to reduce the T_1 at very low temperatures, as equilibration can take a long time⁴³. This can be achieved by adding nano-particles⁴⁴, but even with this development, brute force is rarely used due to its extreme experimental conditions.

1.4.3. Optical Pumping (Hyperpolarised Noble Gases)

Optical Pumping is a hyperpolarisation technique by which a non-Boltzmann distribution of spins is created. Typical noble gases used in this technique are ^3He and ^{129}Xe . Of the two, ^{129}Xe takes a longer time to hyperpolarise and produces a lower signal-to-noise ratio but is much more soluble in blood and so ^{129}Xe is better for studying blood and tissues⁴⁵⁻⁴⁸. ^3He is quicker to hyperpolarise than ^{129}Xe and, due to a higher gyromagnetic ratio, would yield greater signal-to-noise ratios, therefore ^3He is better to be used for the study of void space imaging of lungs⁴⁹. Both these noble gases have been successfully used in research, but it is ^{129}Xe that has been most successful as it is more lipophilic and will dissolve in blood and other lipid rich tissues, therefore this is the chosen gas to carry out further research⁵⁰.

The lungs are an area of great interest for medical imagers as it is possible to understand a large number of conditions; however lungs are a water free gas space which makes it difficult to produce an image using normal proton MRI. Hyperpolarised noble gases such as ^{129}Xe , and ^3He , are being used to overcome this as the gas can be inhaled to reveal an image of the inside of the lungs.

In 1994, Albert *et al.* used this hyperpolarised noble gas technique in biomedical imaging to study the lungs of a mouse. The images showed that this was a good hyperpolarised

technique and an image was produced of the lungs, but these images were quite poor and were not able to provide any structural information (Figure 1.10)⁵¹.

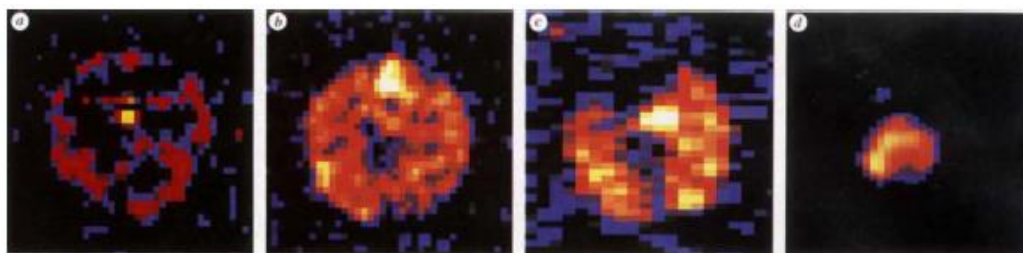


Figure 1.10 MRI images of excised lungs and heart of a mouse as hyperpolarised ^{129}Xe enters the lungs⁵¹

Significant improvements have been made to this technique, and it can now be used to distinguish between healthy and diseased lungs⁵².

Other research was also performed in 1996, which used hyperpolarised xenon to study blood. The research showed an increase in sensitivity when using hyperpolarised xenon and comparing the results to thermally polarised spectra⁴⁶.

Further research is on-going for the use of hyperpolarised noble gases to investigate airway geometry and volumes⁵³. Research is also being performed to produce other uses for hyperpolarised noble gases, such as tracking changes in perfusion or up-take of gas into tissue^{54, 55}. ^{129}Xe is a good gas to use for this task due to the large sensitivity of the chemical shift to molecular environment and good solubility into blood and tissues. This has meant that encapsulated Xenon biosensors have been developed and these are particularly good at targeting specific analytes^{56, 57}. Laser-polarized xenon NMR benefits from good signal-to-noise and spectral simplicity with the added advantage of substantial chemical-shift sensitivity. The biosensor is designed to bind both xenon and protein, in doing so it is expected that the binding of a ligand to the target protein, will reflect in a change of the xenon NMR spectrum⁶⁰. These have the advantage over proton MR as perfusion studies there is no ^{129}Xe present in the tissue, and therefore there is no background signal. Such methods could also be used to study brain function by perfusion tracking⁵⁰.

1.4.4. Dynamic Nuclear Polarisation (DNP)

This is a technique which primarily hyperpolarises ^{13}C and ^{15}N nuclei which exhibit significantly lower sensitivity compared to proton. DNP consists of polarisation transfer of electrons in nuclei in solids by irradiation with a radiofrequency near to the electron resonance frequency³⁸.

1.4.4.1. History of Dynamic Nuclear Polarisation (DNP)

The first DNP experiments were performed in the 1950's by Albert Overhauser at low magnetic field and until recently this technique was limited due to lack of availability of high frequency microwave sources. The first applications of DNP were performed in 1960's, to generate polarised targets for solid state physics experiments. In the 1970's extensive work was performed in solution state NMR experiments to study interactions in solutions and molecular motion. The limited resources meant that DNP could not develop that fast, but in the 1980's and 1990's the interest in solid state DNP grew to enhance the sensitivity of solid state NMR. The availability of the gyrotron, as a high frequency source in 1993, resulted in this approach being used in structural biology. For example, the groups of Griffin and Herzfeld used the DNP technique to study bacteriorhodopsin^{58, 59}, but since this point, its use has expanded to include investigations into self-assembled peptides⁶⁰, ribosome structural biology⁶¹ and bacterial cell interactions⁶². In the 2000's, further research was performed in material science⁶³. The method has also been modified to become dissolved-phase or dissolution DNP⁶⁴. Performed in this way, DNP can be used to detect and investigate tumours (2010 – 2012)⁶⁵.

1.4.4.2. How DNP works

DNP generates a non-Boltzmann distribution by transferring polarisation from unpaired electrons to nuclei in solids³⁸. This process occurs at very low temperature in a high magnetic field which requires high frequency microwave irradiation. DNP exploits the much larger polarisation of the electron spin reservoir rather than relying on the nuclear spin reservoir, which arises due to differences in their gyromagnetic ratios. The transfer of polarisation from the electrons to the nuclei is achieved by the irradiation step.

For liquid state NMR, the only DNP mechanism used is the Overhauser Effect (OE). For solid state NMR, the DNP mechanisms use the Solid Effect (SE), the Cross Effect (CE) and Thermal Mixing (TM)⁶⁶.

Dissolution DNP is widely used in research and two significant advances are the ability to hyperpolarise pyruvate and water. Hyperpolarisation of pyruvate is widely used but the hyperpolarisation of water is still in its early stages⁶⁷⁻⁶⁹.

Hyperpolarised water has been created using dissolution DNP and OE, but it is dissolution DNP which has given larger enhancements and longer T_1 values which allow *in-vivo* measurement^{64, 70}. There are still some disadvantages with this technique, most significantly the long polarisation time, of an hour. The T_1 relaxation time of water is short but can be lengthened by adding D_2O . A second disadvantage is the signal enhancement is relatively weak so post-processing is required to help enhance image quality⁷¹. Hyperpolarised pyruvate is also of interest and has been used because of the following advantages: ease of availability, high solubility in water, relatively long relaxation time (T_1), rapid biological transport and metabolism, and a different metabolic profile between healthy cells and tumour cells⁷². Pyruvate undergoes metabolism in the body to form lactate, alanine and bicarbonate, and these have specific and distinct ^{13}C chemical shifts. The formation of lactate decreases after successful chemotherapy treatments and therefore this can be monitored as a measure of the efficacy of a treatment course. This hyperpolarised pyruvate reflects a non-invasive imaging technique, of utility in cancer diagnosis. The imaging method used to achieve this is called Chemical Shift Imaging (CSI)⁷³.

DNP and CSI imaging with pyruvate were originally used in studies of a range of organs in a range of species. Based on these results, hyperpolarised pyruvate is going through phase 1 clinical trials^{65, 69, 72, 74, 75}.

1.4.5. Parahydrogen Induced Polarisation (PHIP)

Parahydrogen Induced Polarisation (PHIP) is a method which creates a non-Boltzmann distribution through the addition of *parahydrogen* and most commonly occurs hydrogenatively⁷⁶.

A dihydrogen molecule (H_2) consists of two hydrogen atoms which are covalently bonded⁷⁷. Each of these nuclei has a spin angular quantum number of $\frac{1}{2}$ and these can be $+\frac{1}{2}$ or $-\frac{1}{2}$ when placed into a magnetic field. These states can also be referred to as α or β , with α being parallel and β being anti-parallel to the external magnetic field. Consequently, a

dihydrogen molecule might be thought of having four possible spin configurations, $\alpha\alpha$, $\beta\beta$, $\alpha\beta$ or $\beta\alpha$, with $\alpha\beta$ and $\beta\alpha$. However as the latter two are not distinguishable, they are really described by the linear combination⁷⁶, $\alpha\beta + \beta\alpha$, and $\alpha\beta - \beta\alpha$. Three of these spin configurations are symmetric ($\alpha\alpha$, $\beta\beta$ and $\alpha\beta + \beta\alpha$) to particle interchange and called *ortho*hydrogen. They reflect the triplet spin isomer. The other spin configuration ($\alpha\beta - \beta\alpha$) is anti-symmetric; this is called *para*hydrogen and is a singlet. At room temperature, normal hydrogen contains essentially 75% *ortho*hydrogen and 25% *para*hydrogen (Figure 1.11)⁷⁶.

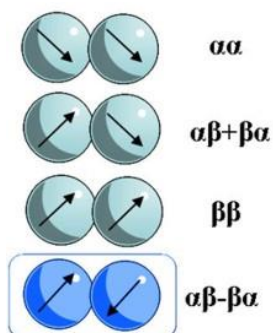


Figure 1.11 Schematic showing the four spin combinations of dihydrogen both *ortho*hydrogen and *para*hydrogen

As the wavefunction (Ψ_{overall}) of H_2 must be anti-symmetric and is a combination of translational, electronic, nuclear, rotational and vibrational terms (Equation 1.2)⁷⁸, the nuclear spin is linked to the rotational state.

$$\Psi_{\text{overall}} = \Psi_{\text{(translational)}} \Psi_{\text{(electron)}} \Psi_{\text{(nuclear)}} \Psi_{\text{(rotational)}} \Psi_{\text{(vibration)}}^{78}$$

Equation 1.2 The overall wavefunction consists of five components, the translational, electronic, nuclear, rotational and vibrational terms.

This is because the translational, electronic, vibrational wavefunctions are always symmetric, and so to produce an anti-symmetric wave function, the nuclear and rotational wavefunctions must differ in symmetry⁷⁸. *Ortho*hydrogen, with its symmetric nuclear spin configuration ($\alpha\alpha$, $\beta\beta$, $\alpha\beta + \beta\alpha$) must be rotationally anti-symmetric ($J= 1, 3, 5\dots$). *Para*hydrogen with an anti-symmetric nuclear spin configuration ($\alpha\beta - \beta\alpha$) must be rotationally symmetric ($J= 0, 2, 4\dots$). As $J = 0$ is the lowest rotational state, the most stable isomer is the para isomer and it exists preferentially at low temperature. At room temperature all four spin configurations are approximately equally populated resulting in 75% *ortho*hydrogen and 25% *para*hydrogen³⁹.

Temperature (K)	% <i>Parahydrogen</i>	% <i>Orthohydrogen</i>
0	100.00	0.00
20	99.82	0.18
75	51.86	48.18
150	28.54	71.76
273	25.13	74.87
> 273	25.00	75.00

Table 1.1 Adapted table of temp versus *Orthohydrogen* / *Parahydrogen* population³⁹

As the temperature decreases, the amount of *parahydrogen* increases, until at 20 K hydrogen exists as 99.8% *parahydrogen*. (Table 1.1)

The inter-conversion between *parahydrogen* and *ortho*hydrogen is normally prohibited due to the need to change both spin and rotational states⁷⁹. If a specific isomer is formed it is therefore stable for a period of time. In fact, a change from *ortho*hydrogen to *parahydrogen* requires a catalyst. The process of *parahydrogen* formation occurs by cooling ultra-pure hydrogen over a suitable catalyst, such as charcoal or iron dioxide, used because they are paramagnetic.

At the University of York there are two *parahydrogen* generators, one which cools to 30K, producing *parahydrogen* close to 99%, and the second, now commercially available which cools to 38K and produces 90% *parahydrogen* (Figure 1.12).

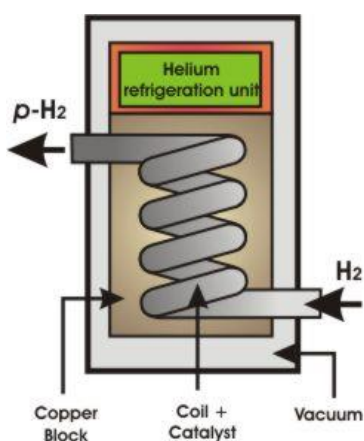


Figure 1.12 Schematic of *parahydrogen* generator used at York

Parahydrogen has no net spin angular momentum and so is NMR silent. However, reaction products derived from *parahydrogen* are often produced with non-Boltzmann nuclear spin

state populations and exhibit greatly enhanced NMR signals. The observation of *parahydrogen* enhanced signals occurs commonly in hydrogenation reactions. When a hydrogenation product is derived from natural abundant dihydrogen molecules, all four hydrogenation product spin states are equally populated, and so this results in low sensitivity in NMR. But if the hydrogenation product is derived from *parahydrogen* only the $\alpha\beta$ or $\beta\alpha$ states are populated. The fact that these states are populated, and the $\alpha\alpha$ and $\beta\beta$ states are not results in the large NMR signals.

1.4.5.1. Research of ParaHydrogen Induced Polarisation (PHIP) and its uses

The first research which was recorded on *parahydrogen* was in the 1980's by Bowers and Weitekamp. The experiments performed in 1986 and 1987 considered the hydrogenation of acrylonitrile to form propionitrile and were catalysed by Wilkinson's catalyst, tris-(triphenyl-phosphine) rhodium (I) chloride. The resulting NMR spectra showed enhanced signals in both the propionitrile transitions and in hydride region of the catalyst. This was the first publication of *ParaHydrogen Induced Polarisation* (PHIP)^{80, 81}.

Since then, there have been numerous papers which have showed the uses and effectiveness of PHIP under various conditions and in a variety of compounds. NMR and MRI have both been used as a technique to view enhanced signals in this way, and will be discussed in more detail later on. There are two areas in which PHIP has been used with magnetic resonance and these are mechanistic organometallic chemistry and hydrogenation reactions (used in NMR and MRI).

1.4.5.2. *Parahydrogen* And Synthesis Allow Dramatically Enhanced Nuclear Alignment (PASADENA) and Adiabatic Longitudinal Transport After Dissociation Engenders Net Alignment (ALTADENA)

The experiments performed by Bowers and Weitekamp in 1986 - 1987, showed the results of the incorporation of *parahydrogen* whilst the sample was in an NMR magnet of 200 MHz. This result was called *Parahydrogen* And Synthesis Allow Dramatically Enhanced Nuclear Alignment (PASADENA). In a typical PASADENA NMR experiment, two pairs of signals are observed of equal intensity, with each pair consisting of one component in absorption (pointing upwards) and one component in emission (pointing downwards). Signals of this type can also be called anti-phase doublets. In a typical ALTADENA NMR experiment, a total of two components are observed, one for each signal but they have different phases (Figure 1.13)^{80, 81}.

A year later, in 1988 Pravica and Weitekamp performed experiments showing what occurs when *parahydrogen* is added to the solution outside the NMR spectrometer and therefore the magnetic states are produced in low field. This is called Adiabatic Longitudinal Transport After Dissolution Engenders Net Alignment (ALTADENA). The key difference between the two methods stems from where the symmetry of the *parahydrogen* is broken. When the reaction happens in low field the *parahydrogen* remains in a singlet state, even though the symmetry of the molecule has been broken. This nuclear spin symmetry is then broken by transfer into high field. This results in a higher population of the $\beta\alpha$ spin state which then affects the signals observed in NMR as detailed in Figure 1.13⁸².

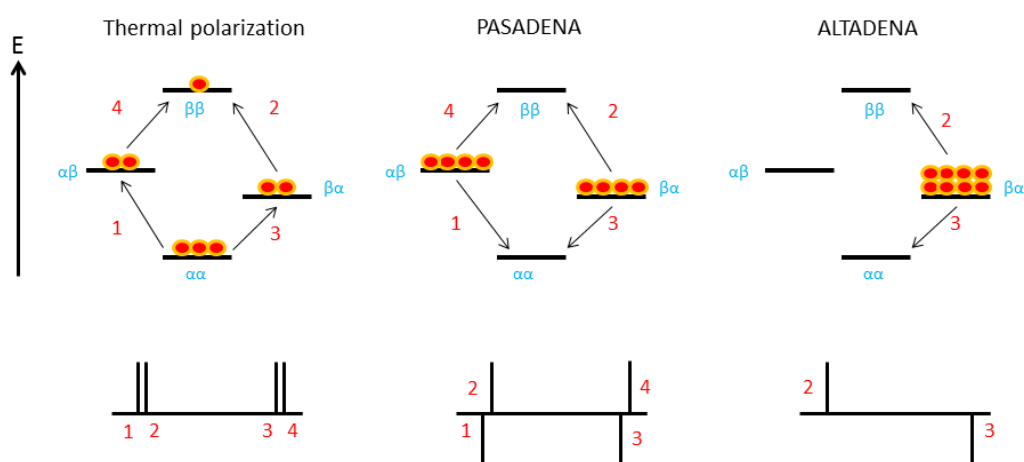


Figure 1.13 Schematic of Boltzmann distribution *orthohydrogen* and non-Boltzmann distribution *parahydrogen* under PASADENA and ALTADENA conditions

An important area of PHIP-enhanced spectra is the ability to detect reaction intermediates⁸³ with metal hydride complexes of particular interest. These are often found in low concentration and/or can be short lived due to continued reactions occurring^{84 85}.

PHIP is also a powerful tool which can be used to expand the understanding of reactivity and characterisation of complexes or unusual systems. An example was recorded in 2004 by Anwar *et al.* where addition of *parahydrogen* to a metal complex resulted in the observation of previously unobserved hydride signals as a result of hyperpolarisation⁸⁶.

Research into PHIP also extends into the observation of enhanced signals in MRI, which can be observed *in-vivo*. In this case, polarisation on ^{13}C was measured, due to its longer lifetime, typically in tens of seconds, compared to the very short lifetime of ^1H . Golman *et al.* followed the hydrogenation of a ^{13}C labelled compound acetylenedicarboxylic acid dimethyl ester for the detection of maleic acid dimethyl ester, in the presence of a rhodium

catalyst (Figure 1.14)⁸⁷. The longer lifetime of ^{13}C allows a longer period of time for the polarised substrate to move within the body to the area of interest, which is an advantage. Another advantage is that ^{13}C gives a very low background signal.

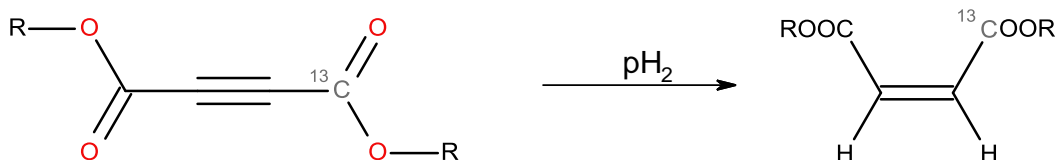


Figure 1.14 Hydrogenation reaction of ^{13}C labelled compound acetylenedicarboxylic acid dimethyl ester for the detection of maleic acid dimethyl ester, in the presence of a rhodium as reported by Golman *et al.*⁸⁷

This technique was used on rats and showed that it can be used to provide structural blood vessel information. Due to the ^{13}C giving very little background signals it means that the enhancement doesn't have to be that high. Two further research studies for PHIP in *in-vivo* studies were performed in 2005 and 2006 by Goldman *et al.*, using species like guinea pigs and rats. Both of these species showed greater detail than observed in the research performed on rats. This is because guinea pigs have larger blood vessels but also greater polarisation was achieved by the *parahydrogenation* reaction. Within a few years, these examples have shown that the polarisation achievable has increased by 10 fold and that improvements are likely to continue^{88,89}.

A recent research study in 2012 by Zacharias *et al.*, has shown that a significant advantage has been achieved by using hyperpolarised diethyl succinate- $1-^{13}\text{C},2,3\text{-d}_2$ in aqueous solution. This molecule undergoes metabolism to form four products; succinate, aspartate, malate and fumarate, which these were observed in the MRI scan, therefore this system was able to track the molecule and its metabolism. This advantage of PHIP means that it can be used to study biological applications and also only takes minutes to produce the hyperpolarised state⁹⁰.

1.4.5.3. Summary of PHIP type techniques

To summarise, ^{13}C hyperpolarised molecules generated by PHIP can be used in various areas of MRI these are diffusion imaging, perfusion and high resolution angiography. A significant advantage of using ^{13}C over ^1H is the little background signal observed. ^{13}C also has a longer lifetime which is an advantage and allows the acquisition of hyperpolarised metabolites. The only potential disadvantage with ^{13}C imaging is that standard clinical MRI scanners are equipped for ^1H imaging only. One issue with the standard PHIP technique is the requirement that a hydrogenable precursor must be available. Another technique,

known as Signal Amplification By Reversible Exchange (SABRE), has been developed to overcome this limitation.

1.5. Signal Amplification By Reversible Exchange (SABRE)

SABRE is a technique which was first reported in 2009. SABRE uses *parahydrogen* as the source of hyperpolarisation, and is a non-hydrogenative process^{79, 91, 92}. This is an advantage over PHIP as no chemical change occurs to the compound of interest. The first research reported using SABRE in 2009, examined polarisation transfer to pyridine, nicotinamide, nicotine, pyrazine, quinolone and quinazoline⁹². These substrates were studied at a concentration of 100mM (0.062 mm) in 0.6 ml of methanol-d₄.

SABRE consists of three components, *parahydrogen* (polarised H₂ gas), a catalyst (a metal based agent) and the substrate of interest (Figure 1.15).

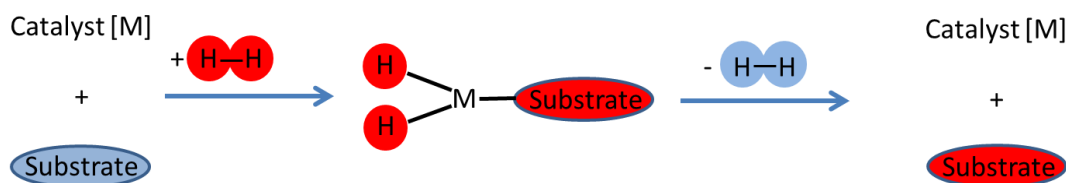


Figure 1.15 Schematic of SABRE⁹²

The catalyst allows polarisation to flow from *parahydrogen* into the substrate when both are bound to the metal complex. The bound ligands must form a spin coupled system for this to happen⁹³. This has been rationalised theoretically on the basis of a density functional theoretical study for a defined spin system⁹⁴.

Within the SABRE process two significant terms are created. These are longitudinal magnetisation I_z and longitudinal two spin order magnetisation $I_z S_z$. The size of the flip angle will therefore control the appearance of any NMR spectra. I.e. if a 90° angle is used, then only the I_z magnetisation signals will be seen. But if a smaller flip angle is used, then the detection of the $I_z S_z$ term is possible. Research performed by 2011 by Cowley *et al.* proved that the population of the I_z and $I_z S_z$ states varied with the magnetic field experienced by the sample at the point of polarisation transfer⁹³. Control of this parameter therefore reflects a novel way to select a magnetic state. These two types of magnetisation can also be differentiated by the application of Only *Parahydrogen* Spectroscopy (OPSY) protocol⁹⁵.

Other research performed in 2010 by Gong *et al.* tested the sensitivity of the SABRE technique and showed that 4.9 μl of pyridine could be detected. The signals observed were recorded on a low field NMR spectrometer at 250 kHz. This result illustrates that SABRE can be used to detect trace amounts of substrate⁹⁶ using an inductive coil like that used at high field.

SABRE has now been exemplified in literature for a number of applications which include the detection of trace amounts of substrate^{92, 96}, to make invisible NMR signals visible⁹⁶ and to increase the scope of potential substrates that can be examined. Research performed in 2011 by Glogglér *et al.* looked into different types of substrates, successfully polarising amino acids at low field⁹⁷. Further research was also performed in 2012 by Dücker *et al.* which further increased the scope of substrates that can be hyperpolarised using SABRE, in this case they investigated eight substrates, that all contained 5-membered nitrogen containing aromatic rings⁹⁸.

There have been two types of polarisation-transfer catalyst (PTC) used in SABRE, both of them are of the form $[\text{Ir}(\text{L})(\text{COD})\text{Cl}]$, where L can be either a phosphine ligand, or more commonly a carbene ligand. Initial research was performed using Crabtree's catalyst, which contained tricyclohexylphosphine (PCy_3)⁹⁹. Analogues were then investigated where the phosphine was replaced with other phosphine ligands (PPh_3 for example), but in doing this, the levels of polarisation measured for pyridine changed and the observed trends suggested a more electron rich metal centre was needed. This can be achieved by replacing the phosphine ligands with carbenes⁹⁹. Further research was performed in 2011 and 2012 which used a range of carbene ligands and *N*-heterocyclic carbene ligand which resulted in increased levels of signal ligand enhancement¹⁰⁰.

It is therefore possible to conclude that SABRE reflects an exciting opportunity to create hyperpolarised molecules. These molecules might be expected to contribute to clinical diagnosis in due course. Prior to this point a number of developments are needed which are set out in my thesis aims.

1.6. Project aims

The aims of this project are to conduct research to further improve the levels of signal enhancement that it is possible to create via the application of SABRE. I set out a route to explore this optimisation through a range of homogeneous catalysts. These involve a synthetic strategy that is based on modifying the steric effects of a carbene ligand. I then develop methods to produce a heterogeneous catalyst. This work reflects the need to remove the catalyst from the substrate. These systems are examined initially for SABRE using the probe pyridine.

I then expand on these studies by moving to a range of methylpyridines and nicotinamide to test catalyst tolerance to the substrate. Studies on temperature, concentration and the magnetic field experienced by the sample the point of SABRE are used to inform future experiments. As part of this programme 5-methylpyrimidine was discovered to reflect a good target because of its long T_1 . A novel hydrogenation reaction involving quinazoline was also observed which led to an unexpected reaction mechanism. The results of my thesis will therefore illustrate progress towards the goal of *in-vivo* MRI use with SABRE whilst demonstrating that it can be used as a mechanistic probe of catalysis.

2. Chapter 2 SABRE Catalyst Design

2.1. Introduction

A free carbene, CR_2 , can exist in three distinct forms which reflect singlet and triplet spin isomers. In one of the singlets, the electrons are paired together in the sp^2 lone pair, in the other singlet, one electron is located in each of the sp^2 and p orbitals with opposite spin, but in the triplet the spin states are the same (Figure 2.1).

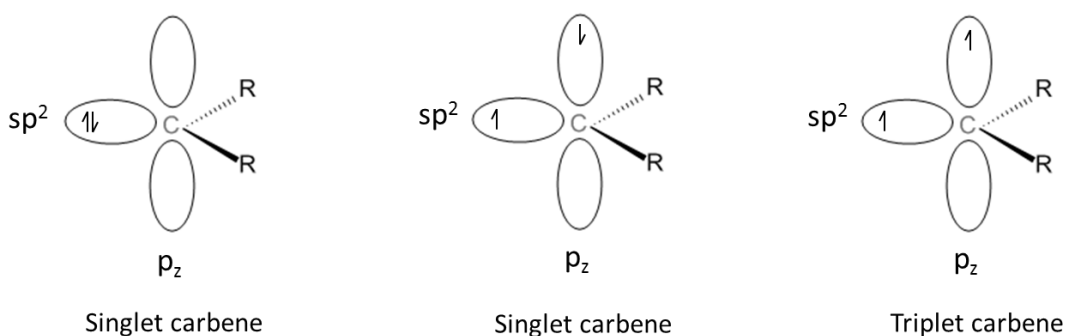


Figure 2.1 Representation of singlet and triplet forms of a carbene

In 1964, Fischer¹⁰¹ introduced the concept of a double bond between a transition metal and carbon through the synthesis of $(\text{CO})_5\text{W}=\text{C}(\text{Ph})(\text{OMe})$ which reflects the successful binding of a carbene to the metal centre. Such complexes contain electrophilic heteroatoms and are stabilized by metals in a low oxidation state. Their chemical bonding is based on a sigma type electron donation of the lone pair of the carbon sp^2 orbital into an empty metal d-orbital and π -type back bonding of another d-orbital into the empty p-orbital of the carbene carbon; the heteroatom can also donate into this orbital to increase stability.

Schrock, in 1975¹⁰², prepared a number of tantalum complexes which included $(\text{Np})_3\text{Ta}=\text{CH}(\text{CMe}_3)$ and $(\eta^5\text{-Cp})_2\text{MeTa}=\text{CH}_2$ that also featured a metal carbon double bond. These types of complex were subsequently referred to as nucleophilic alkylidene complexes and are commonly formed when the metal centre also coordinates strong donor ligands that have no π acceptor capability to the metal, which is in a high oxidation state. The bonding between Fisher and Schrock carbene complexes therefore differs dramatically because in the former the carbene carbon is electron poor while in the latter it is electron rich.

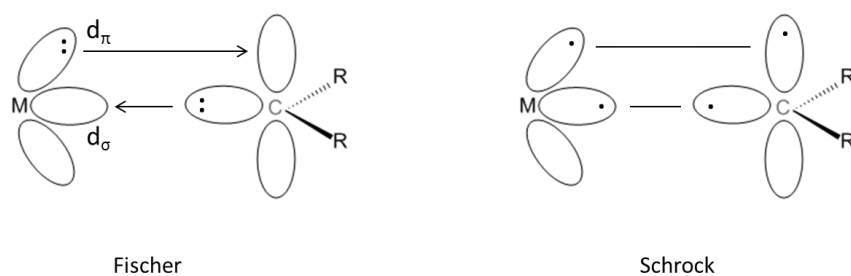


Figure 2.2 Representation of Fischer and Schrock type carbene bonding

One more recent example is reflected in the class of ligands provided by *N*-heterocyclic carbenes (NHCs). These are neutral compounds, which possess a divalent carbon atom with six valence electrons that can be stable in their own right. There are many examples of NHCs that have been reported which contain four¹⁰³, five, six¹⁰⁴⁻¹⁰⁶ and even seven^{107, 108} membered heterocycles, but most NHCs are based on five membered rings. An example of a generic NHC and its precursor can be seen in Figure 2.3. The behaviour of this type of NHC will be discussed further in the following section.

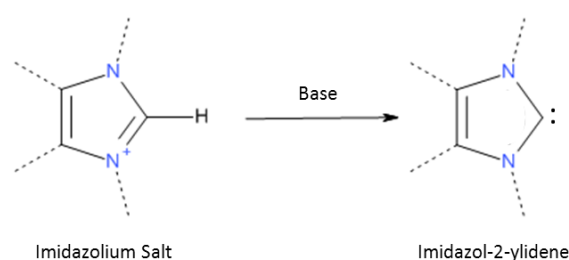
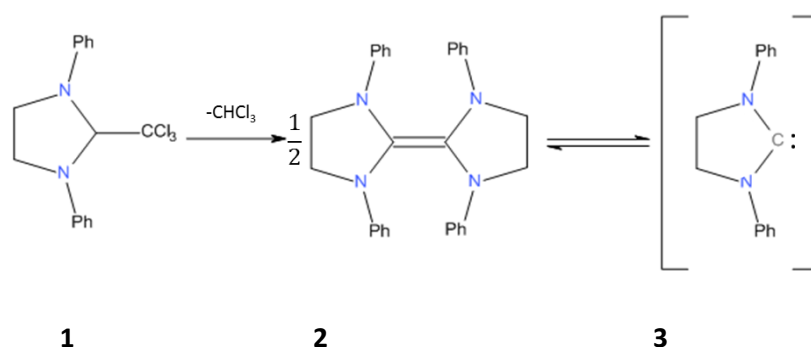


Figure 2.3 Five membered NHC and its precursor; where the base could be KO^tBu or NaOEt

2.1.1. History of *N*-Heterocyclic Carbenes

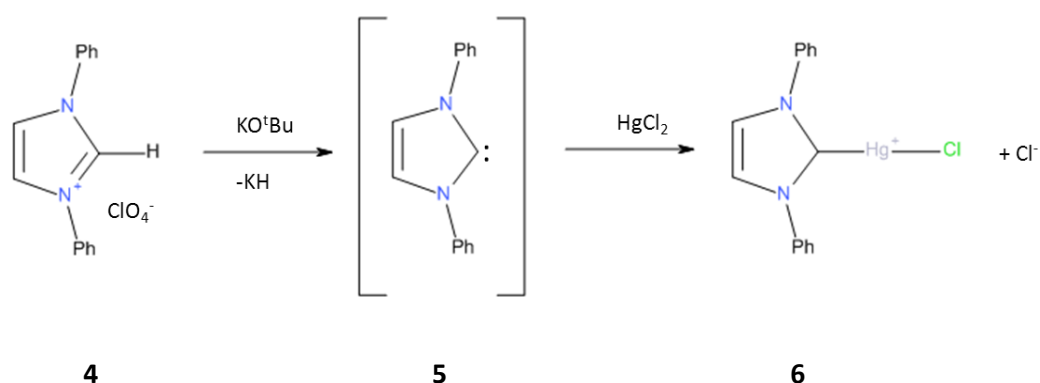
The first attempt to isolate a free NHC was reported in 1960 by Wanzlick *via* the synthesis of 1,3-diphenylimidazolidin-2-ylidene (**3**) by the thermal elimination of chloroform from compound **1**, as shown in Scheme 2.1. However, this resulted in the formation of the electron rich olefin, **2**, not the proposed free carbene. Wanzlick assumed that there was an equilibrium between the free carbene and the isolated dimer¹⁰⁹, but initial reports by other groups studying related cross coupling reactions between olefins did not support this idea. For example, Lemal *et al.* carried out experiments with various dimers using conditions more extreme than those used by Wanzlick, and in these experiments the dimers showed no dissociation^{110, 111}. However, this worked was revisited in the 1990s by Denk *et al.* who reported on a series of related crossover reactions employing a wide range of dimers under

similar - or milder - conditions to those used by Lemal, and now their results supported Wanzlick's original equilibrium idea¹¹²⁻¹¹⁴.



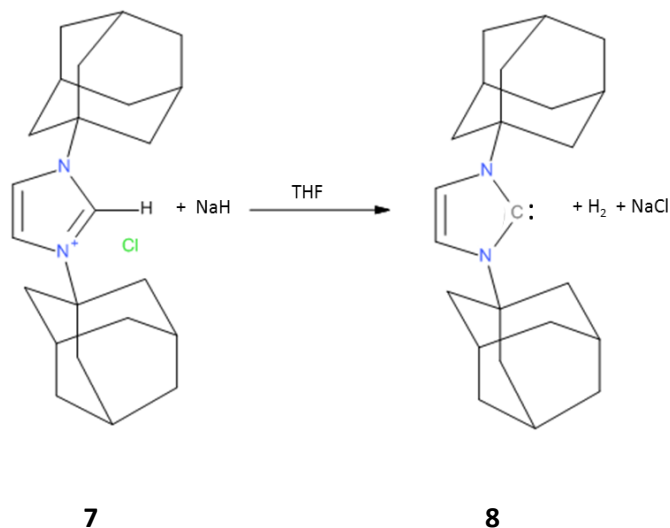
Scheme 2.1 Dimerisation of 1,3-diphenylimidazolidin-2-ylidene (**3**)

In 1970, Wanzlick and Schönherr, carried out further work in this area and showed that it was actually possible to deprotonate the imidazolium salt, 1,3-diphenylimidazolium perchlorate (**4**), using potassium *tert*-butoxide. While the free carbene (**5**) was not isolated, it could be trapped by reaction with mercury(II) chloride as its mercury adduct (**6**). This reaction is shown in Scheme 2.2¹¹⁵.



Scheme 2.2 Synthesis of NHC complex (**6**) by deprotonation of 1,3-diphenylimidazolium perchlorate, and its subsequent reaction with mercury(II) chloride

Thirty years after Wanzlick's original work, Arduengo *et al.* reported the isolation of the first stable crystalline NHC. This was achieved by deprotonation of 1,3-adamatylimidazolium chloride (**7**) with sodium hydride, in the presence of catalytic amounts of either potassium *tert*-butoxide or dimethylsulfoxide, to give the free carbene (**8**) as shown in Scheme 2.3. This discovery resulted in a new found interest in NHCs, their chemistry and their applications¹¹⁶.

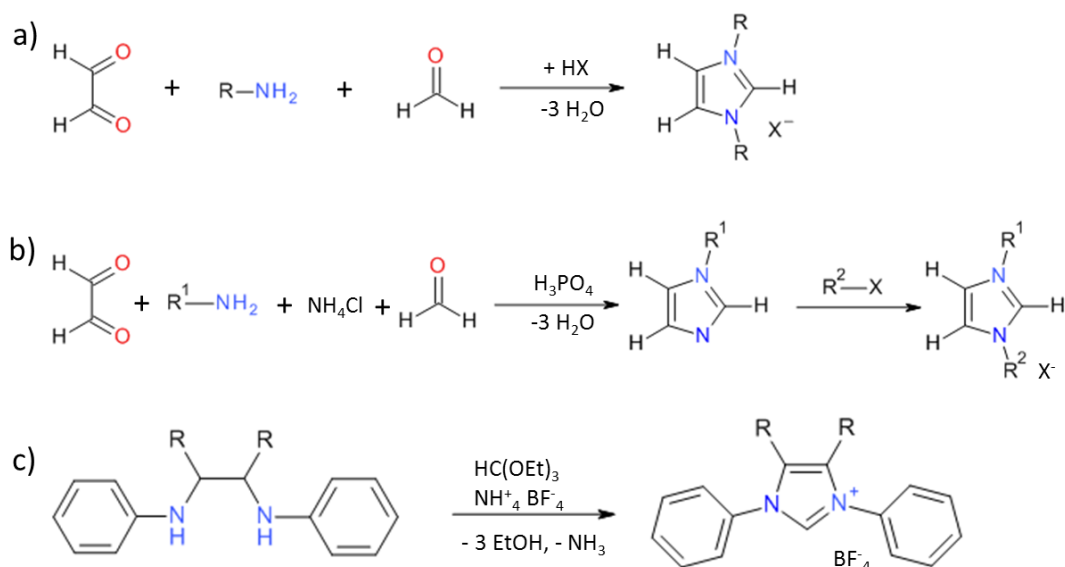


Scheme 2.3 Schematic showing the steps involved in the isolation of the first reported free stable carbene, 1,3-di-1-adamantylimidazol-2-ylidene

2.1.2. Preparation of NHCs

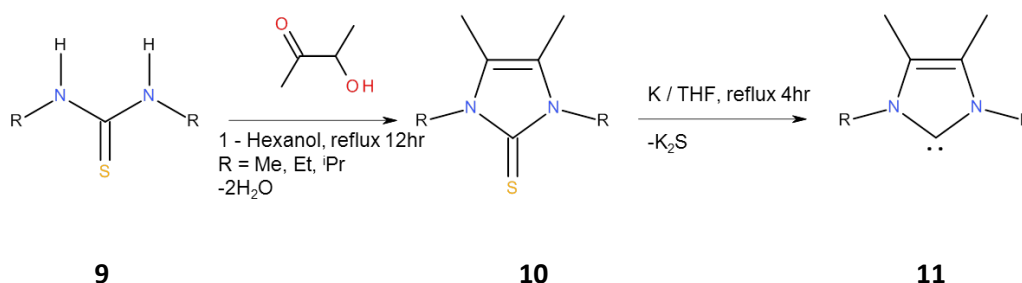
Since the isolation of 1,3-di-1-adamantylimidazol-2-ylidene by Arduengo, the first free stable NHC, many possible ways to synthesise imidazolium and imidazolinium salts have been found. These salts act as precursors to NHCs which have now been isolated through a variety of methods. In fact, there are many synthetic routes to producing symmetrical, unsymmetrical and aryl substituted imidazolium and imidazolinium salts, some of which are illustrated in Scheme 2.4¹¹⁷⁻¹¹⁹.

Symmetrical N-substitution strategies for the synthesis of imidazolium salts were first reported by Wallach *et al.*¹²⁰ in 1925 (Scheme 2.4 (a)) based on a one-pot synthesis starting from glyoxal, primary amine and formaldehyde. A variation of this synthesis (Scheme 2.4 (b)) has been reported by Gridnev *et al.*¹²¹; it is a two-step synthesis that is suitable for symmetrical N-substitution. Scheme 2.4 (c) shows the one-step synthesis of an aryl substituted imidazolium salt that can be produced by reaction with a 1,2 diamine (produced from a Pd-catalysed Buchwald Coupling).



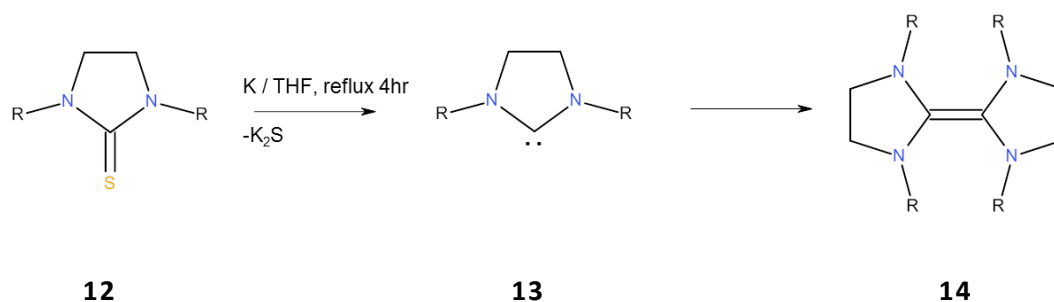
Scheme 2.4 Synthetic routes to imidazolium salts; a) symmetrical one-pot synthesis from glyoxal; b) unsymmetrical two-step synthesis from glyoxal; c) aryl substitution from 1,2 diamines

Kuhn *et al.* reported a two-step method for the production of a thermally stable, alkyl-substituted NHC. This was achieved by the reduction of imidazol-2-(3H)-thione with potassium in refluxing THF¹²². However, this route was dependent on the R substituent attached to the nitrogen which could not be labile. A similar challenge was faced by Arduengo during their related attempts to isolate free carbenes¹²³.



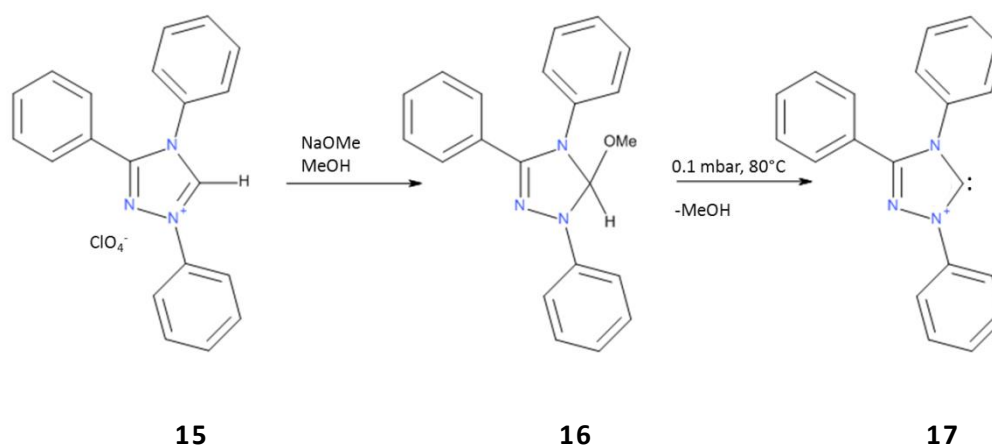
Scheme 2.5 Synthesis of carbenes from a substituted imidazol-2-(3H)-thione, via a sulphur reduction

A similar synthetic method has been described by Denk *et al.* for the synthesis of imidazolidin-2-ylidenes (**13**) and their corresponding electron-rich alkene dimers (**14**) that was based on thione precursors¹¹² (**12**).



Scheme 2.6 Reduction of imidazol-2-(3H)-thione to imidazolium-2-ylidene and dimerized alkene

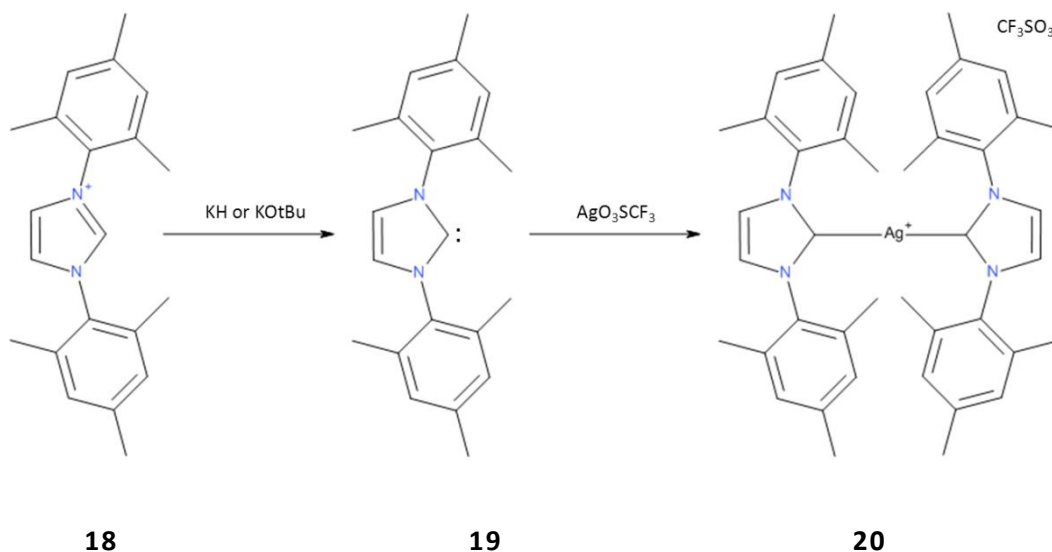
The first crystalline triazole-derived carbene, 1,2,4-triazol-5-ylidene, was reported by Enders *et al.* in 1995 (Scheme 2.7). They produced a methoxy-derivative by reacting 1,3,4-triphenyl-1,2,4-triazolipume perchlorate (**15**) with sodium methoxide (NaOMe). The endothermic elimination of methanol, under vacuum thermolysis, led to the first commercially available NHC carbene (**17**)¹²⁴.



Scheme 2.7 Synthesis of 1,2,4-triazol-5-ylidene via vacuum thermolysis

2.1.3. Silver NHC Complexes

The first silver NHC complex (**20**), shown in Scheme 2.8, was reported by Arduengo in 1993¹²⁵, Scheme 2.8. It was synthesised through the deprotonation of imidazolium salt (**18**) to make the free carbene and then reacting the resultant product with silver triflate (AgO_3SCF_3). Whilst this method has been widely used, the harsh conditions used to generate the free carbene (**19**) which employ strong bases such as KO^tBu or KH that can deprotonate other sites and lead to decomposition. This decomposition pathway is especially relevant when a methylene group is adjacent to the nitrogen centre of an imidazolium ring.



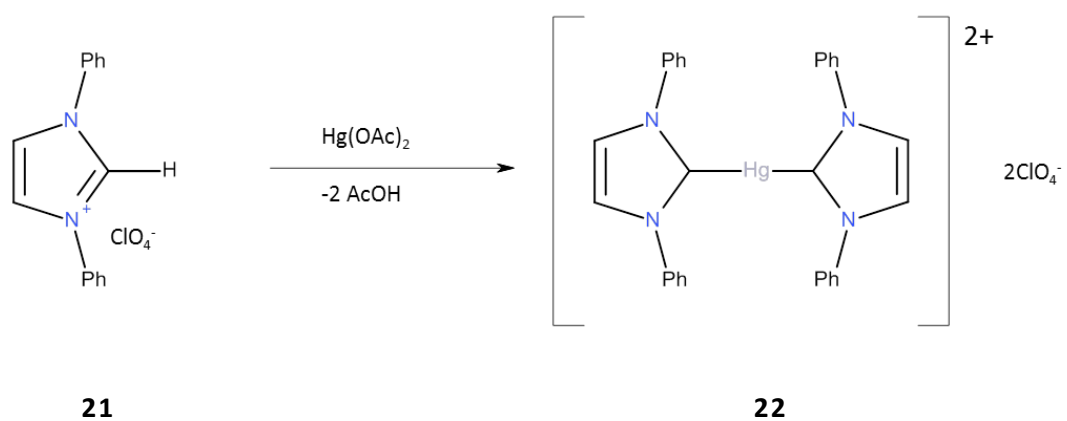
Scheme 2.8 Synthesis of a silver NHC complex, via the deprotonation of the imidazolium salt, followed by the addition of silver triflate

The use of silver oxide (Ag_2O) in such a carbene preparation was first reported by Wang and Lin in 1998¹²⁶. Since this point, other silver base have been used with Guerret *et al.* creating a silver NHC polymer by using silver acetate (AgOAc)¹²⁷. Furthermore, Tulloch *et al.*¹²⁸ used Ag_2CO_3 as the metalation agent, but found that the reaction times exceeded those for Ag_2O . Despite these alternatives, Ag_2O still remains the most widely used reagent as the ensuing reaction can be easily monitored through the uptake of the insoluble silver salt, and the reaction can be carried out in an array of solvents which include DCM, DMSO, acetone, acetonitrile, methanol, DMF and water, without the need for heating.

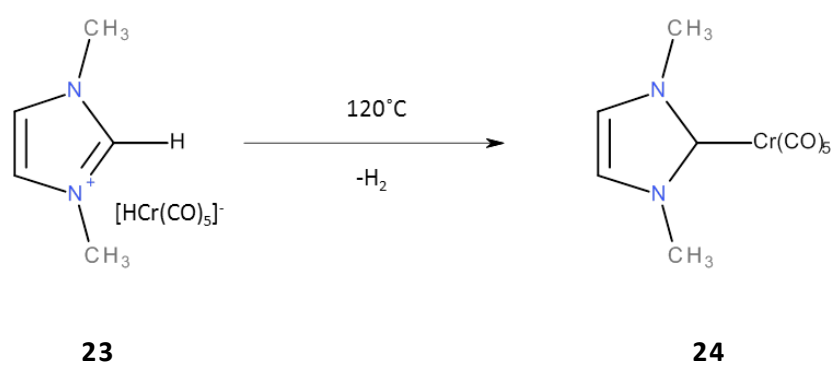
Work conducted by Garrison *et al.*¹²⁹ showed that NHC reactions could be carried out in water, which suggests that the deprotonation and subsequent metalation is a concerted reaction. Tulloch *et al.*¹²⁸ also showed how the NHC's steric bulk affects the uptake of silver oxide, with the result that NHCs with larger side chains often required refluxing.

2.1.4. Transition metal complexation of NHCs

The first transition metal NHC complexes were reported by Wanzlick *et al.*¹³⁰ and Öfele *et al.*¹³¹ in 1968. Although Wanzlick was unable to isolate the free carbene, he was able to prepare mercury NHC (**22**) by reaction of an imidazolium salt (**21**) of Scheme 2.9) with mercury acetate, which is basic enough to deprotonate the imidazolium salt. This resulted in the formation of a bi-cationic mercury complex. Shortly afterwards, Öfele reported the synthesis of the chromium NHC (**24**) from a $[\text{HCr}(\text{CO})_5]^-$ imidazolium salt (**23**) through the thermally driven loss of H_2 according to Scheme 2.10¹³¹.



Scheme 2.9 Synthesis of NHC transition metal complex reported by Wanzlick *et al.*¹³⁰



Scheme 2.10 Synthesis of NHC transition metal complex reported by Öfele *et al.*¹³¹

2.2. Catalyst Design for SABRE

As noted in Chapter 1, SABRE employs a carbene ligand because it conveys the necessary electron donating character required for optimal reactivity and, therefore, SABRE efficiency. Based on the methods of Kuhn and Arduengo, it is possible to conceive that different carbene based catalysts could be used in the SABRE process. Figure 2.4 exemplifies three such NHC options, that could subsequently be used to form three derivatives of $[\text{Ir}(\text{NHC})(\text{COD})\text{Cl}]$ which might be expected to be air stable. The three different carbenes used in this part of the thesis are therefore $\text{ImMe}_2\text{NPr}^i_2$ (**1-a**), BzIMes (**1-b**) and IMes (**1-c**). The free carbenes, **1-a** and **1-b** are not commercially available and were therefore prepared as part of this work. Carbene **1-c** has been used extensively in the research group and was sourced internally.

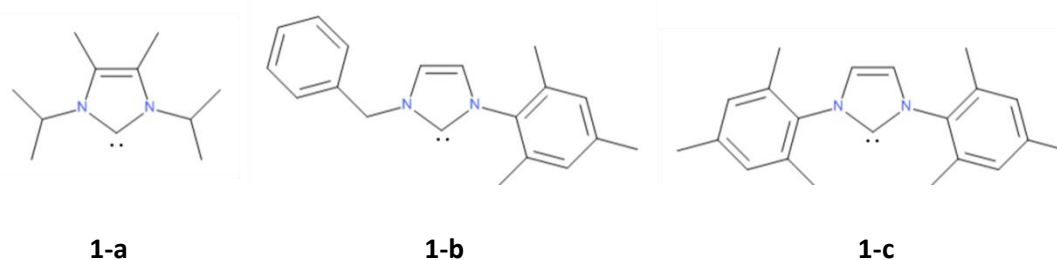
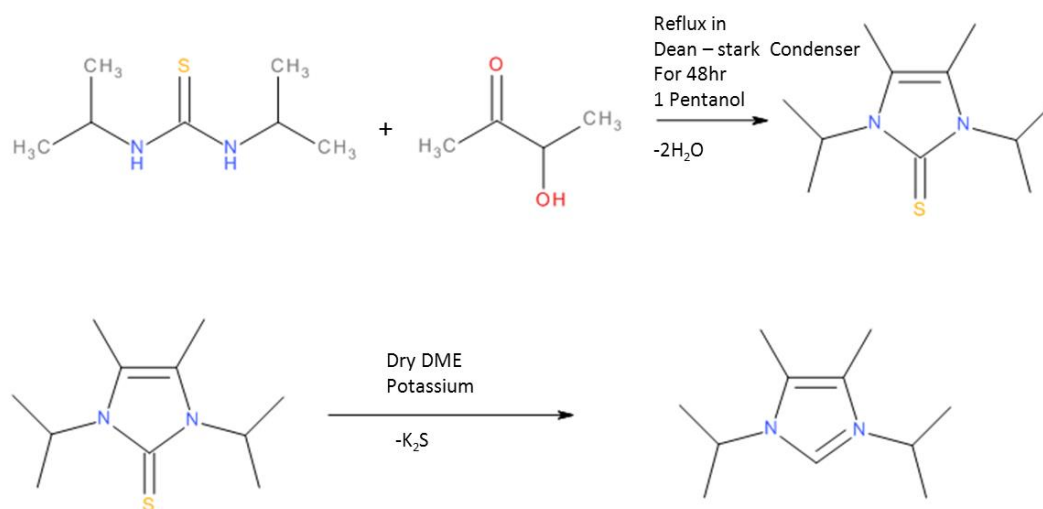


Figure 2.4 Structures of the free carbene ligands **1-a** ($\text{ImMe}_2\text{NPr}^i_2$), **1-b** (BzIMes) and **1-c** (IMes) prior to complexation

2.2.1. Synthesis of carbene $\text{ImMe}_2\text{NPr}^i_2$ (**1-a**)

The synthesis of **1-a** followed the two-step process reported by Kuhn *et al.* 1993¹²³. The first step is cyclisation of the NHC ring, and the second is reduction of the corresponding imidazol-2-(3H)-thione (Scheme 2.11). This NHC proved difficult to synthesise according to this literature approach because of the Na/K amalgam employed. The first step makes use of a Dean-Stark condenser to collect the by-product water from the reaction. This reaction was monitored over a period of 48 hours, which was the point at which no more water was formed, and is indicative of the reaction reaching completion. The second step in the literature uses a potassium and sodium amalgam as a reducing agent. It was decided to try this final step using only potassium to reduce the sulphur group to form the free NHC. The final product, the free carbene, is air sensitive, producing a yellow oil from a yellow solid when left standing. This final product was therefore stored in a glove box under a nitrogen

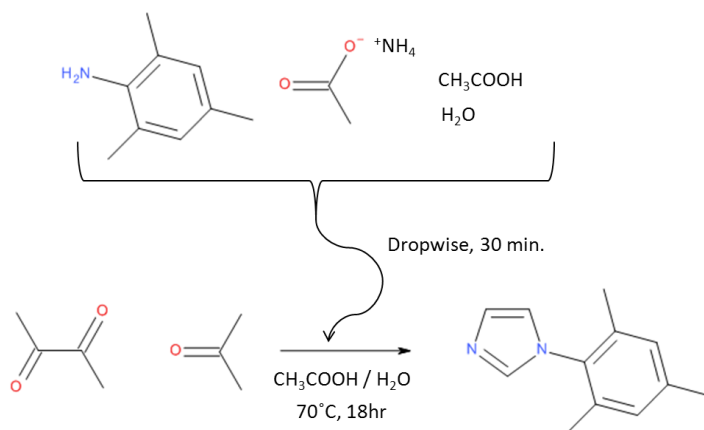
atmosphere. Typically yields of between 80% and 90% were achieved. The product was characterised by NMR and MS, these data are presented in Experimental Section 7.3.1.



Scheme 2.11 Synthesis and reduction of imidazol-2-(3H)-thione to produce the carbene $\text{ImMe}_2\text{NPr}_2$ (**1-a**)

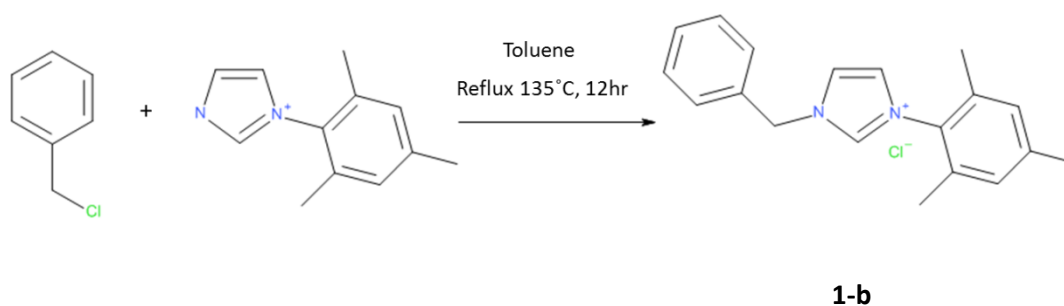
2.2.2. Synthesis of carbene BzIMes (**1-b**)

The synthesis of 1-(2,4,6-trimethylphenyl)-1H-imidazole (1-mesitylimidazole, **1-b**) was reported by Arduengo and co-workers¹³², but a slight modification of the method has subsequently been developed by Occhipinti *et al.*¹³³ (Scheme 2.12). Occhipinti's method uses glacial acetic acid, aqueous formaldehyde and glyoxal, which were mixed at 70°C. An aqueous solution of 2,4,6-trimethylphenylamine, glacial acetic acid and ammonium acetate was then added in a drop-wise manner over a period of 18 hours at 70°C to the glyoxal acetone mixture. After recrystallization in ethyl acetate, 1-mesitylimidazole was obtained as a beige crystalline solid in a yield of 65%. Characterisation data for 2,4,6-trimethylphenylamine are presented in the Experimental Section 7.3.2.



Scheme 2.12 Synthesis of 1-mesitylimidazole from glyoxal and the drop-wise addition of 2,4,6-trimethylphenylamine

The second step is straight forward. It involves taking 1-mesitylimidazole, dissolving it in dry degassed toluene and adding benzylchloride dropwise over 30 minutes, followed by heating at reflux for 12 hours (Scheme 2.13). The final product of this reaction, **1-b**, was washed with hot pentane to obtain a colourless powder in good yield (97%). Characterisation data for **1-b** are presented in the Experimental Section 7.3.2.



Scheme 2.13 Synthesis of BzIMes (**1-b**) via the reaction of benzylchloride and 1-mesitylimidazole

2.2.3. Synthesis of metal complexes: [Ir(NHC)(COD)Cl] (2-a, 2-b and 2-c)

This section will discuss the routes through which carbenes **1-a**, **1-b** and **1-c** can be complexed to a metal centre to give complexes **2-a**, **2-b** and **2-c** (Figure 2.5). These studies were completed in order to determine the best synthetic route to an immobilised NHC (Chapter 5).

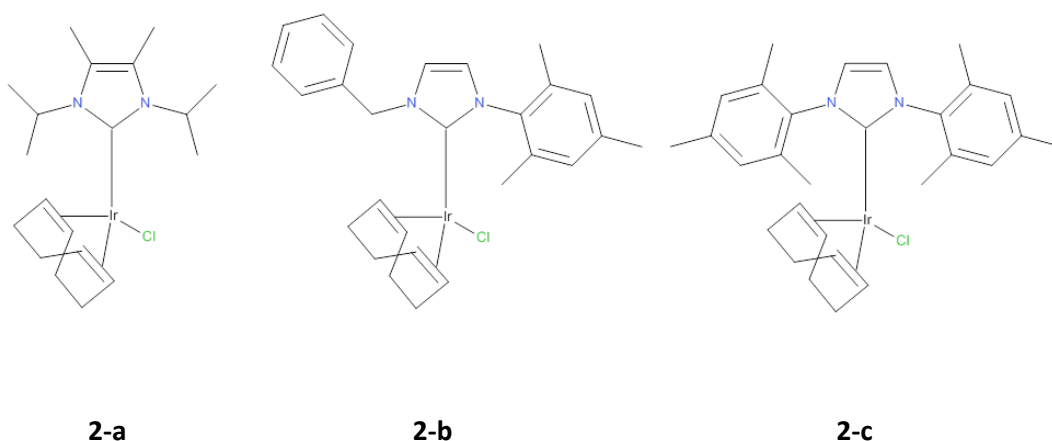
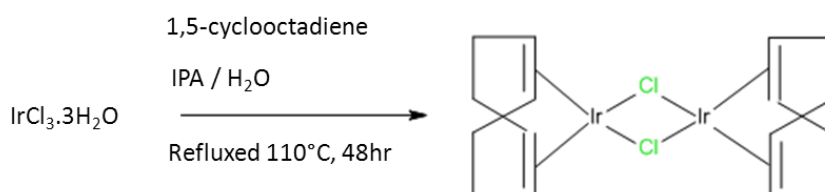


Figure 2.5 Carbene complexes **2-a**, **2-b** and **2-c** to be synthesised for use with SABRE

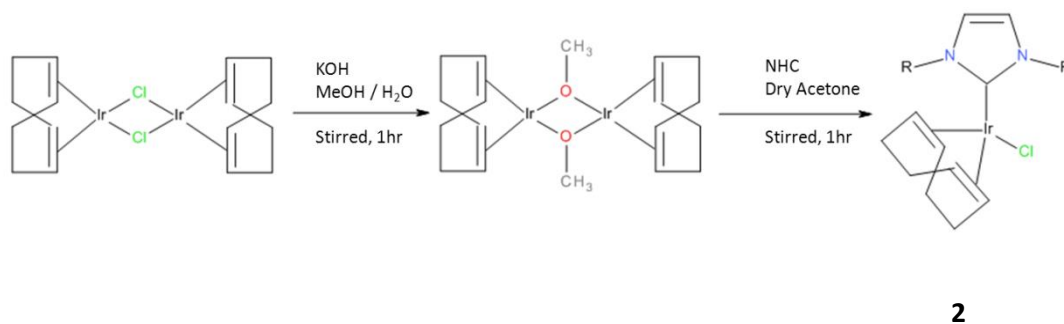
The first stage of this synthesis was the preparation of *bis*(1,5-cyclooctadiene)diiridium(I)dichloride ($[\text{Ir}(\text{COD})\text{Cl}]_2$) (Scheme 2.14), which is used in all of these reactions. This material was synthesised from iridium trichloride trihydrate which was suspended in a 1:2 deoxygenated mixture of water and isopropyl alcohol. 1,5-cyclooctadiene (COD) was added to this mixture and the resulting solution heated to 98°C for between 24 and 48 hours. After cooling, a red precipitate formed, which was collected by filtration and dried; a typical yield was 55 %, and the corresponding characterisation data, can be found in Experimental Section 7.3.3.



Scheme 2.14 Synthesis of $[\text{Ir}(\text{COD})\text{Cl}]_2$ from iridium trichloride trihydrate

Using the $[\text{Ir}(\text{COD})\text{Cl}]_2$, it is possible to prepare *bis*(1,5-cyclooctadiene)di- μ -methoxydiiridium ($[\text{Ir}(\mu\text{-OMe})(\text{COD})]_2$). This complex was synthesised by dissolving

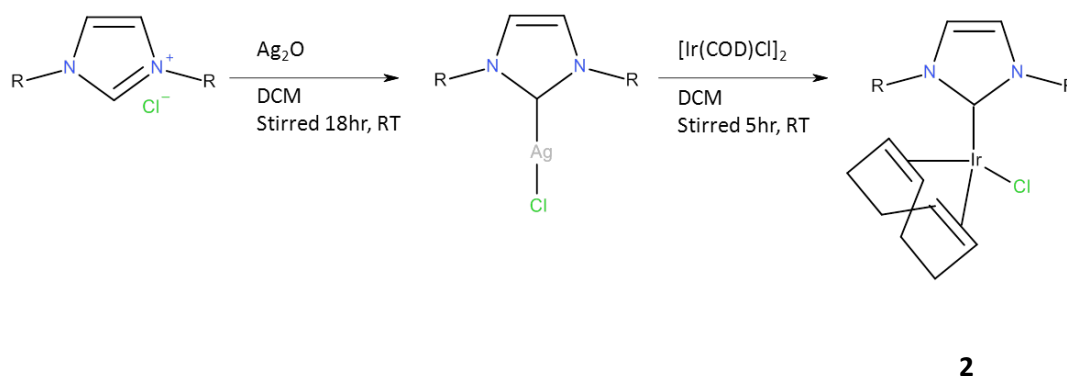
$[\text{Ir}(\text{COD})\text{Cl}]_2$ in methanol in the presence of KOH. After 1 hour, a yellow solution formed. Water was then added with the result that yellow solid precipitated. It was important to remove the supernatant liquor relatively quickly after the water was added, as the solid can degrade in solution. The $[\text{Ir}(\mu\text{-OMe})(\text{COD})]_2$ formed in this way was then taken up into acetone and the NHC added to form the corresponding NHC complex. The yields for this final step were typically between 70% and 80%. More details on these synthetic procedures, and the corresponding characterisation data, can be found in Experimental Section 7.3.4.



Scheme 2.15 Synthesis of $[\text{Ir}(\text{NHC})(\text{COD})\text{Cl}]$ (**2**). [**2-b** when $\text{R} = \text{BzIMes}$, **2-a** when $\text{R} = \text{ImMe}_2\text{NPr}^i_2$ and **2-c** when $\text{R} = \text{IMes}$] via $[\text{Ir}(\mu\text{-OMe})(\text{COD})]_2$ and $[\text{Ir}(\mu\text{-Cl})(\text{COD})]_2$

Another route to **2** involved making the corresponding mono-NHC silver based intermediate (Scheme 2.16), and then undertaking a transmetalation reaction to form the final product. The process was achieved by reaction of the NHC with silver oxide, which acts to deprotonate the NHC to form a neutral silver complex. The silver product was isolated as white solid in good yield (92%). Although this is a light sensitive reaction, the positive aspects of the reaction are; air did not have to be excluded and neither solvent pre-treatments nor strong bases were required.

The next step was to coordinate a transition metal centre to the carbene via a transmetalation reaction. The most widely used metal used in such reaction is palladium, but this process has been adapted for a variety of transition metals including iridium. This aspect of the synthesis was carried out as per the literature¹³⁴, by adding the $[\text{Ir}(\text{COD})\text{Cl}]_2$ into a solution of the NHC-silver intermediate. The resulting solution was stirred for 5 hours at room temperature. This procedure readily gave a yellow solid after purification.

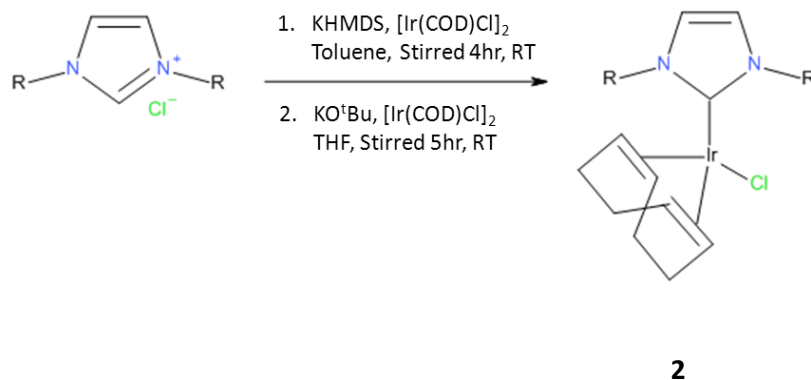


Scheme 2.16 Synthesis of a mono-NHC silver complex, followed by transmetalation, allows the formation of $[\text{Ir}(\text{NHC})(\text{COD})\text{Cl}]$ (**2**) via $[\text{Ir}(\text{COD})\text{Cl}]_2$. [**2-b** when $\text{R} = \text{BzIMes}$, **2-a** when $\text{R} = \text{ImMe}_2\text{NPr}^t$ and **2-c** when $\text{R} = \text{IMes}$]

Another method to synthesise the imidazolium complex which has been explored is to use the silver alkoxide, $\text{AgOC}(\text{CF}_3)_3$, in place of Ag_2O . This route was examined because Ag_2O is a relatively poor silver source for heterogeneous catalysis, as it has been found not to be compatible with silica or BuLi , KO^tBu , NaH , K_2CO_3 and Cs_2CO_3 ¹³⁵. It was therefore important to optimise the conditions for synthesis under homogeneous conditions. Although there are many examples of copper alkoxides, it was Reisinger *et al.*¹³⁶ who initially reported the novel synthesis of the first donor-free silver alkoxide. Maishal *et al.*¹³⁷ used the silver alkoxide route for both homogeneous and heterogeneous catalysis with iridium, gold palladium and ruthenium in the transmetalation step. Full details for the synthesis of $\text{AgOC}(\text{CF}_3)_3$ can be found in Experimental Section 7.3.9.

The final method to be discussed is the use of a base in the form of an *in situ* reaction. These reactions require a free stable NHC, and can become challenging if other acidic protons are present in the ligand precursor. They involve the conversion of an NHC halide precursor into the corresponding alkoxide, which must be sufficiently basic to deprotonate the NHC; this is then complexed to iridium.

This reaction was carried out in two different ways using two different alkoxides (Scheme 2.17). Reaction 1 uses potassium *bis*(trimethylsilyl)amide (KHMDS) while reaction 2 uses potassium *tert*-butoxide (KO^tBu). The base was added with the NHC at the start of the reaction, and the resulting solution stirred for 30-40 minutes before $[\text{Ir}(\text{COD})\text{Cl}]_2$ was added. After stirring for another 4-5 hours at room temperature, a yellow solid resulted in yields of 78% and 85% respectively.

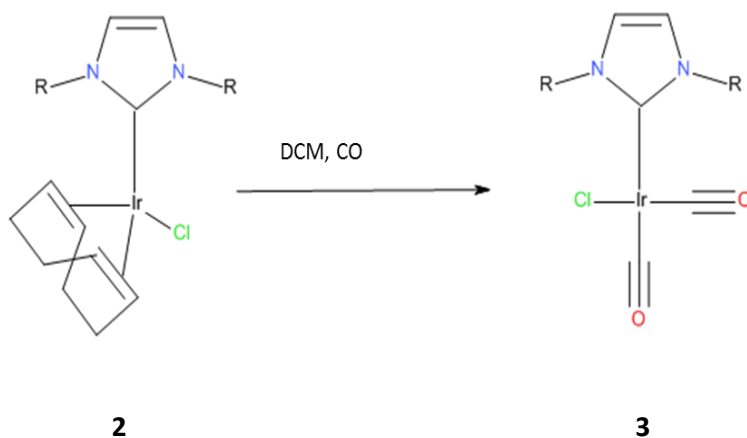


Scheme 2.17 Synthesis of $[\text{Ir}(\text{NHC})(\text{COD})\text{Cl}]$ via the deprotonation of the parent imidazolium salt using either KHMDS (1) or KO^tBu (2). [2-b when R = BzIMes, 2-a when R = $\text{ImMe}_2\text{NPr}_2$ and 2-c when R = IMes]

Based on these results, if the aim is to synthesise a homogeneous catalyst for SABRE (Chapter 2), the synthetic route to be chosen would involve deprotonation via KO^tBu , because it requires fewer steps and produces product in good yield. If a heterogeneous catalyst was being prepared, I would select a KHMDS or $\text{AgOC}(\text{CF}_3)_3$ route; the latter reagent has been shown to facilitate higher iridium loadings on a supported material¹³⁸.

2.2.4. Activation of Complexes with Carbon Monoxide

To date, there is no literature available that details the steric and electronic parameters of **2-a** and **2-b**. Following the work carried out by Chianese *et al.*¹³⁹, it should be possible to convert $[\text{Ir}(\text{NHC})(\text{COD})\text{Cl}]$ into $[\text{Ir}(\text{NHC})(\text{CO})_2\text{Cl}]$ (**3-a** and **3-b**) by reaction with CO. Upon the addition of CO, to **2**, the COD group is readily displaced and a noticeable colour change from bright yellow to pale yellow can be observed as **3-a** and **3-b** form. The *cis* isomer of these complexes (Scheme 2.18) is expected to give rise to just two CO bands in the IR spectrum. However, R. Kelly *et al.* observed three bands for the IAd derivative which suggests that a *trans* isomer can be present in solution¹⁴⁰. The *trans* IAd form was suggested to yield a single IR stretch at 2063 cm^{-1} while the *cis* form yields two stretches at 1979 and 1965 cm^{-1} .



Scheme 2.18 Expected $[\text{Ir}(\text{NHC})(\text{CO})_2\text{Cl}]$ complex formed after the addition CO. [**3-b** when R = BzIMes, **3-a** when R = $\text{ImMe}_2\text{NPr}'_2$ and **3-c** when R = IMes]

The IR spectrum for the reaction yielding **3-a** produces three IR stretches at 2054, 1982 and 1965 cm^{-1} for carbonyl ligands in the product as shown in Figure 2.6. This matches with the suggestion that both *cis* and *trans* isomers are present (Figure 2.7).

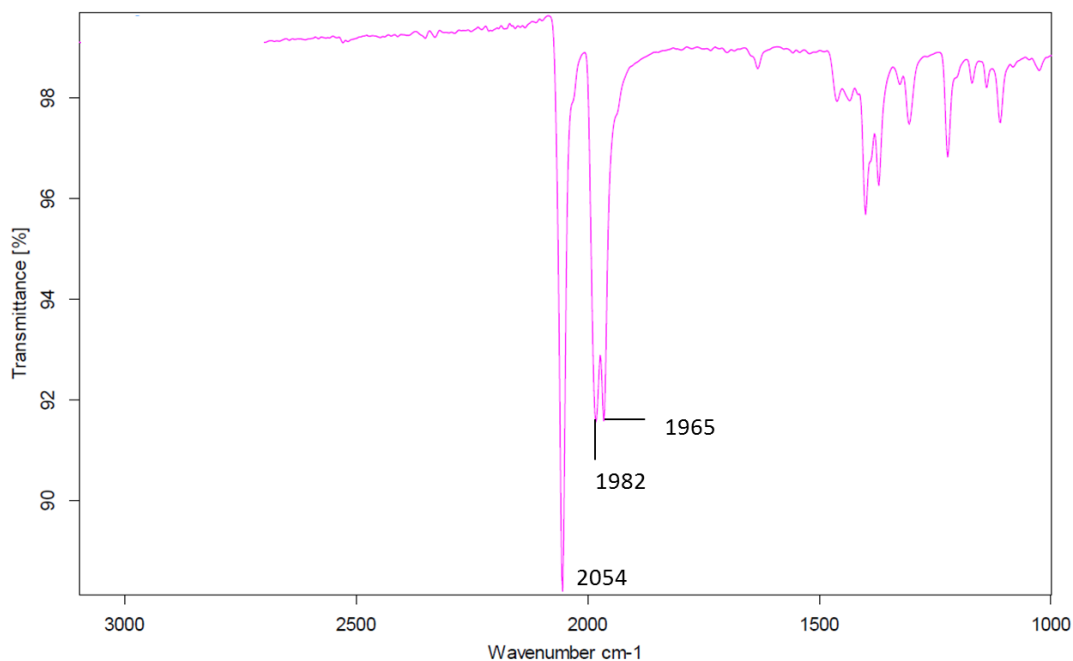


Figure 2.6 IR spectrum corresponding to the addition of CO to complex **3-a**

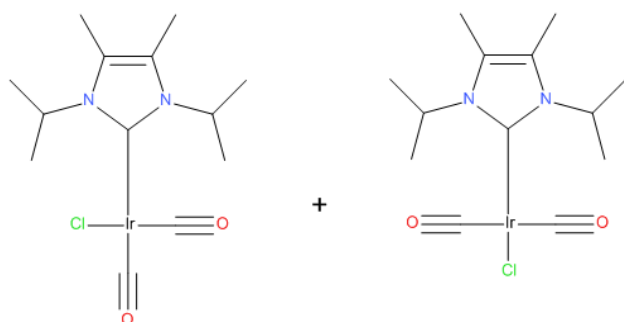


Figure 2.7 *cis* and *trans* CO isomers of **3-a**

We can therefore be confident that **3-a** was prepared by this route because of the MS and NMR data. The MS analysis was carried out in negative ion mode, which gave a molecular ion at 464 m/z with two consecutive losses of 28 m/z , indicating the loss of two CO molecules. Furthermore, the NMR data was conclusive with both ^1H and ^{13}C spectra showing no signs of COD and the two CO resonances appearing at 181.74 and 168.32 ppm.

In contrast, complex **2-b**, forms a single isomer of **3-b** upon reaction with CO. This isomer yields two IR CO stretches at 2057 and 1978 cm^{-1} which indicates that the *cis* geometry is more stable.

2.2.5. Electronic and Steric Effects

Electronic and steric ligand effects have been used to explain the resulting catalytic efficiency of metal complexes using NHCs and phosphine ligands. The electronic effect is due to changes in the NHC ligand which can give rise to different electron distributions within the molecule. Steric effects normally occur when the bulk around the metal centre changes. Because these properties are linked, changing the steric effects can influence the electronic parameter and vice versa. For example, a greater ligand angle, due to increased bulk, would influence the amount of *s*-character retained by the NHC or phosphine lone pair, thus altering the electronic parameter. Changing the atom bonding to the metal can also alter the electronic properties because of the resulting bond distance or bond angle changes.

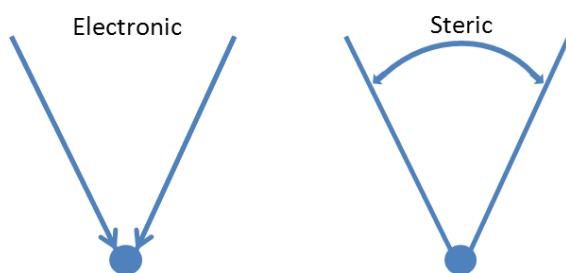


Figure 2.8 Diagrams representation of the electronic effect (left) and the steric effect (right)

Tolman in 1977¹⁴¹ experimentally estimated the electronic effect by measuring the CO stretching frequency (ν_{CO}) of $[\text{Ni}(\text{CO})_3(\text{L})]$ in an IR spectrum; this has become commonly known as Tolman's Electronic Parameter (TEP). This type of experiment was used to look at a range of different ligands. It was discovered that by increasing the electron density of the ligand, the CO bond length increased, resulting in greater π -back bonding between the metal and carbonyl groups and thus a smaller wave number was determined for the ν_{CO} stretch, which is indicative of a longer M-CO bond length.

A different parameter to estimate the steric effect was also proposed by Tolman; that of measuring the cone angle θ , for a static phosphine-metal bond¹⁴¹ (Figure 2.9). The apex angle of the cone was defined as being centred 2.28 Å from the centre of the phosphorus atom to the outmost substituents of the phosphine. This method could, in theory, be applied to an array of ligands, but is commonly used for tertiary phosphine ligands. The recent developments of biarylphosphines, bidentate ligands and NHCs, have required a new method to estimate steric effects, as it has proven difficult using Tolman's model to come up with a reliable indicator.

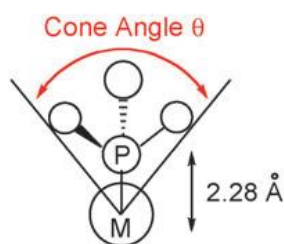


Figure 2.9 Schematic for the representation of a cone angle for a metal-phosphine, taken from a publication by Clavier and Nolan *et al.* in 2010¹⁴²

In 1999, Huang *et al.*¹⁴³ proposed that a measure of the steric bulk of NHCs could be achieved through the analysis of crystallographic data. In this published work, the metal-carbene bond length was measured to be 2.105 Å, but he decided that 2.00 Å could be considered as the average NHC to metal bond length. Huang and colleagues then presented two views, shown in Figure 2.10, which depict a length parameter A_L and a

height parameter A_H . Their method therefore utilised some of the properties of Tolman's approach and proved to work well as a simple model for symmetrical NHCs, but an improved method of calculation for steric bulk was still needed for more complex systems.

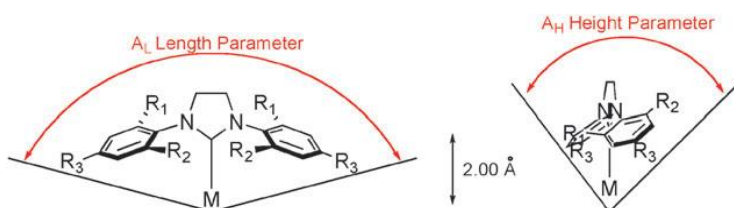


Figure 2.10 Estimation of the steric bulk of NHCs using a length parameter A_L and height parameter A_H , as proposed by Huang *et al.* in 1999¹⁴³

In 2003, Hillier *et al.*¹⁴⁴ published a new concept of “percent buried volume” ($\%V_{bur}$), which is defined as the percentage of the total volume of the sphere occupied by a ligand. The sphere is defined as a radius, with a metal centre at the core, which is calculated using crystallographic data. The larger the steric bulk of a ligand that occupies the space around the metal centre, the larger the $\%V_{bur}$. This model allows for the comparison of other types of NHCs (symmetrical and unsymmetrical) and the results can be compared with those provided by analogous data for tertiary phosphine containing systems.

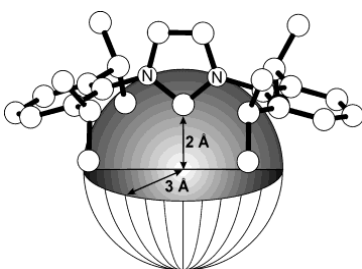


Figure 2.11 Schematic representing per cent buried volume taken from publication by Hillier *et al.* 2003¹⁴⁴

Gusev *et al.*, 2009¹⁴⁵ originally noted that by correlating the average CO IR stretching frequency of the $[\text{Ir}(\text{L})(\text{CO})_2(\text{Cl})]$ and the A_1 stretch from $[\text{Ni}(\text{L})(\text{CO})_3]$, that a linear correlation was observed for both NHC and phosphines. Others, such as Droge and Glorius *et al.* 2010, and Jokic *et al.* 2010, reported the donating ability of a bisoxazoline derived NHC used in the Suzuki-Miyaura reaction and the isolation of two $[\text{Ir}(\text{NHC})(\text{CO})_2\text{Cl}]$ complexes respectively^{146, 147}.

The work by R. Kelly *et al.*¹⁴⁰, investigated the correlation between TEP and the CO frequency of $[\text{Ir}(\text{NHC})(\text{CO})_2\text{Cl}]$ complexes such that the data collected in section 2.2.4 for **3-a**, can be compared to their results. It can be seen that **3-a** follows the general trend for TEP vs V_{CO} . Complex **3-b** could not be added to this graph as there are currently no TEP

values for this NHC complex. The ν_{CO} for complex **3-b** is 2017 cm^{-1} and therefore lies in between that of **3-a** and **3-c**, which is represented in Figure 2.12 by a red circle.

Given the close fit to the trend line for all those systems that do not possess a stable iridium *trans* dicarbonyl derivative it might seem sensible to suggest that **3-b** will also lie close to this line. However, the systems that lie close to that line are also all aromatic and given that **3-a** is aliphatic in nature, while **3-b** a mixture of the two, no firm conclusions can be drawn.

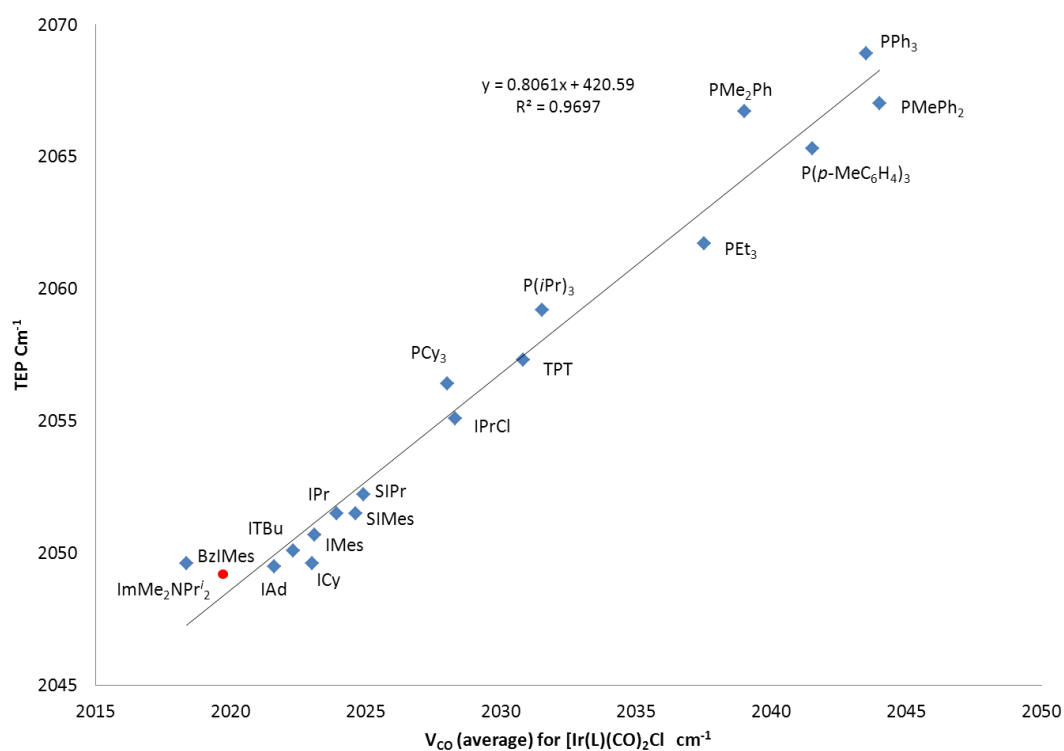
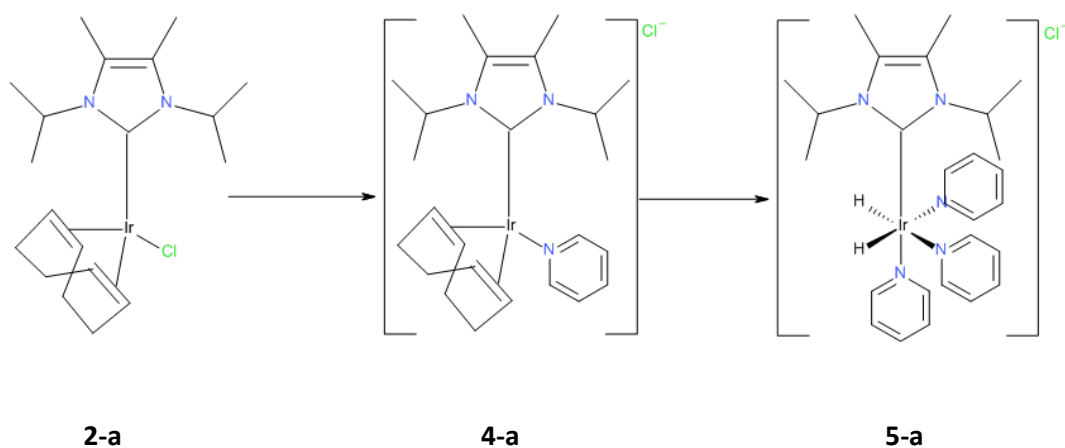


Figure 2.12 Graph showing the correlation between TEP and ν_{CO} for a series of phosphine and carbene ligands in $[\text{Ir}(\text{L})(\text{CO})_2\text{Cl}]$ as reported by R Kelly *et al*, 2007, with the measured ν_{CO} data obtained for **3-a** ($\text{ImMe}_2\text{NPr}^{\text{i}}$) and **3-b** (BzIMes) from this study¹⁴⁰

2.2.6. Reactions of **2-a** with pyridine and hydrogen

The formation of the active SABRE catalyst requires H_2 and a substrate, in this case pyridine, to simultaneously bind to the metal centre as shown in Scheme 2.19. In order for this to happen, complex **2** must first undergo ligand substitution where pyridine displaces the chloride to form $[\text{Ir}(\text{NHC})(\text{COD})(\text{py})]\text{Cl}$ **4-a**. This reaction has been followed by MS for **2-a**. Secondly, the addition of hydrogen to **4** then allows for the hydrogenation of COD and the formation of the desired product $[\text{Ir}(\text{H})_2(\text{NHC})(\text{py})_3]\text{Cl}$ **5-a**.



Scheme 2.19 Route to **5-a** via the initial formation of **4-a** upon the addition of pyridine and H_2 to **2-a**

The displacement of the chloride ion by pyridine using **2-a** can be followed NMR spectroscopy, as shown in Figure 2.13; the bound pyridine ligand signals are clearly visible. This intermediate can also be detected by MS, where the molecular ion $[Ir(ImMe_2NPr'_2)(COD)(py)Cl]^+$ for **3-a** results at 560.7 m/z. A further peak at 481.5 m/z corresponding to loss of 79.2 mass units (pyridine) is also observed. Similar observations were made for $[Ir(BzIMes)(COD)(py)Cl]$ with the new molecular ion being seen at 685.3 m/z and its 79.1 loss fragment providing a signal at 606.2 m/z. Furthermore, the characteristic isotope pattern for $^{35}Cl:^{37}Cl$ is no longer present in these ions.

The reaction with **2-a** does not reach completion, with 70% of the product forming with a 5-fold pyridine excess. The displaced chloride therefore competes for pyridine in this reaction. However, we note that H_2 does not add to **2-a** at a significant rate, it is only when **4-a** is formed that **5-a** results.

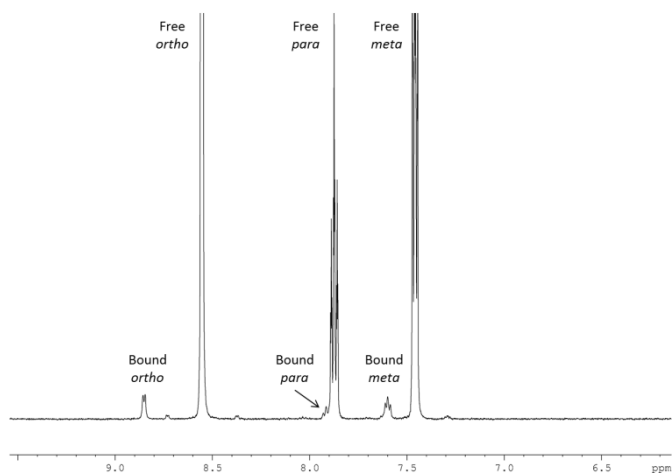


Figure 2.13 ^1H NMR spectrum of the aromatic region of a solution containing **4-a** and pyridine showing both the bound and the free resonances of pyridine

The time taken to form **5** in these reactions is highly dependent on the NHC. For **2-c**, the reaction takes in the region of 3 minutes, whereas for **2-a** and **2-b** it can take anywhere between 24 and 120 hours. This is due to the slow displacement of chloride and the slow addition of H_2 to **4-a** and **4-b**. The ^1H NMR spectrum shown in Figure 2.14 demonstrates that both **4-a** and **5-a** can be seen at the same time in these solutions. The remaining proton resonances are masked by those of free pyridine which is present in excess.

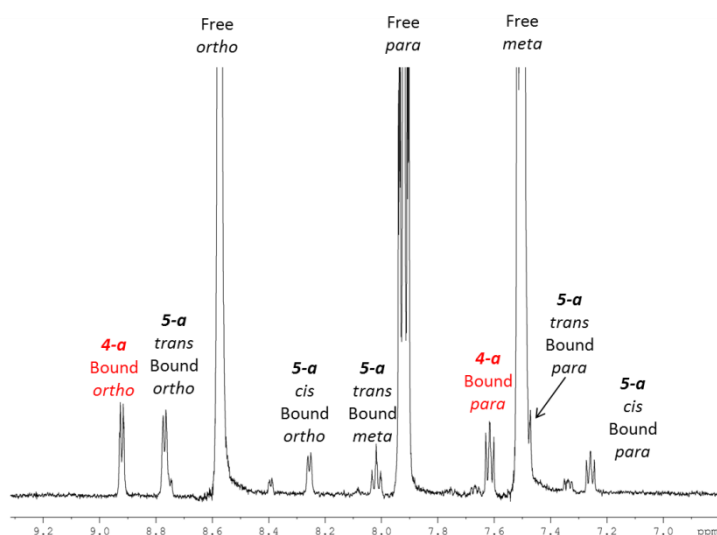


Figure 2.14 ^1H NMR spectrum of complexes **4-a** and **5-a** showing the aromatic region only; bound and free pyridine resonances are attributed

In order to locate the masked signals, a series of additional 1D and 2D NMR measurements were needed. The first of these experiments corresponded to a 2D COSY spectrum and is

shown in Figure 2.15. The blue lines connect the bound resonances for the $[\text{Ir}(\text{ImMe}_2\text{NPr}'_2)(\text{COD})(\text{py})\text{Cl}]$ complex, while the red lines indicate the *trans* pyridine ligands and the green lines show the *cis* pyridine ligand of $[\text{Ir}(\text{H}_2)(\text{ImMe}_2\text{NPr}'_2)(\text{py})_3\text{Cl}]$. Full characterisation data is presented in the Experimental Section 7.4.11, whilst key data is shown in Table 2.2.

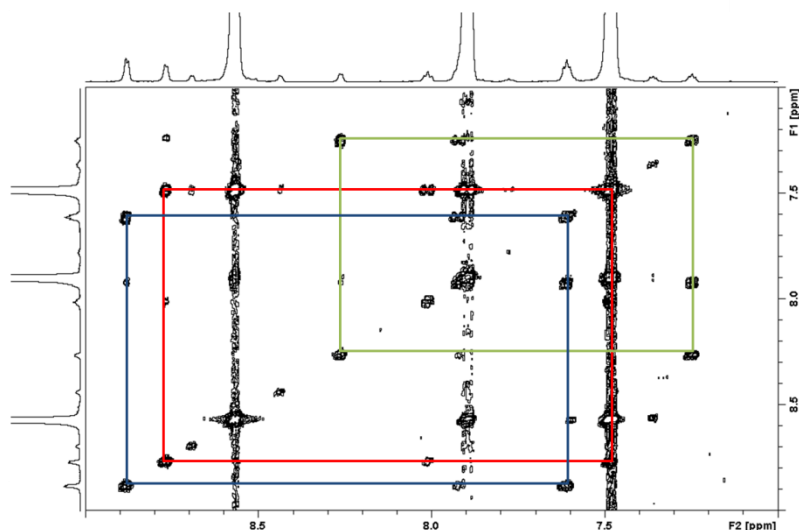


Figure 2.15 ^1H COSY NMR spectrum showing selected coupled resonances attributed to bound pyridine protons in complexes 4-a (blue) and 5-a (red, *trans* ligand orientation and green *cis* ligand orientation)

It has been reported by Cowley *et al.* 2011, that complexes of the same nature as **5-a** undergo loss of both hydrogen and pyridine on the NMR timescale⁹³. This process can be monitored by using either a selective NOE or 2D NOESY NMR experiment; these would for example show that the *trans* pyridine ligand signals of **5-a** exchange with those of free pyridine. This effect is illustrated in Figure 2.16 with the two signals circled in red denoting signals which exchange with free pyridine; the corresponding *meta* protons are hidden by the free pyridine signal at 7.50 ppm. Upon characterising this complex by HMQC methods the missing signals are readily located in Figure 2.17 .

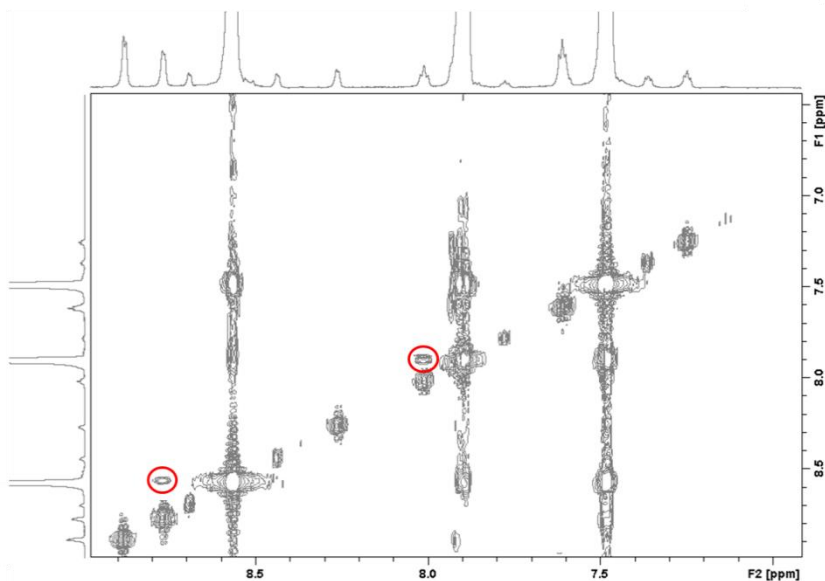


Figure 2.16 ^1H NOESY NMR spectrum of complexes 4-a and 5-a, with the exchange peaks between free pyridine and the *trans* pyridine ligand of 5-a circled in red

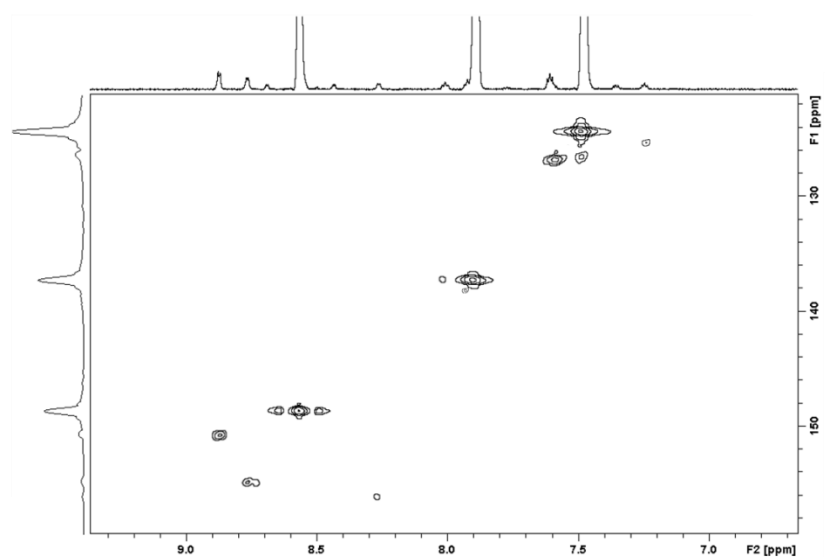


Figure 2.17 ^1H - ^{13}C HSQC NMR spectrum of complexes 4-a and 5-a, identifying the ^{13}C resonances in the associated complexes

Table 2.2 details the specific ^1H NMR signals of **5-a**, **5-b** and **5-c**. It can be seen that the chemical shifts of the hydride ligand resonances are different for each of the complexes. This difference will arise due to the difference in carbene electron donating ability.

Catalyst	Bound Pyridine (ppm)				Hydride (ppm)
	Resonance	<i>ortho</i>	<i>para</i>	<i>meta</i>	
ImMe ₂ NPr ⁱ ₂ (5-a)	<i>Trans</i>	8.78	8.01	7.50	-22.77
	<i>Cis</i>	8.26	7.93	7.25	
BzIMes (5-b)	<i>Trans</i>	8.36	7.80	7.24	-22.21
	<i>Cis</i>	8.22	7.76	7.11	
IMes (5-c)	<i>Trans</i>	8.93	7.99	7.49	-23.52
	<i>Cis</i>	8.61	7.89	7.28	

Table 2.2 Characteristic ¹H NMR signals for the active complexes 5-a, 5-b and 5-c.

2.2.7. Exchange Rate and Activation Parameters

Dissociative ligand exchange is possible in coordinatively saturated $18e^-$ species such as $[\text{Ir}(\text{H}_2)(\text{ImMe}_2\text{NPr}'_2)(\text{py})_3]\text{Cl}$ (**5-a**), which is octahedral in shape. This mechanism relies on the iridium bond, to either pyridine or hydrogen, being fully broken before the new bond forms; this avoids an unfavourable $20e^-$ intermediate species. The initial experiments reported by Cowley *et al.*⁹³ show that temperature altered the level of polarisation observed for the free pyridine sample under SABRE. This suggested that there was an optimal ligand exchange rate for the polarisation step. In this case, the complex underwent pyridine ligand dissociation, followed by hydrogen dissociation.

The observation process used a ^1H EXSY NMR measurement. It was found that when selectively exciting the bound *ortho* pyridine (8.77 ppm) or the hydride resonance (-22.70 ppm), exchange into free *ortho* pyridine (8.57 ppm) or hydrogen (4.57 ppm) was observed respectively. These experiments were carried out at a range of temperatures and, by altering the mixing time in the ^1H EXSY NMR, measurement data was collected from which a rate could be calculated using a kinetic model and the solver analysis package in Excel. A scheme for dissociative ligand or hydride loss is illustrated in Figure 2.18, which highlights the role of the transition state. Upon reaching this state, it is possible to fully dissociate into the product or re-associated back to reactants. From the rate measurements of ligand and hydride loss, the thermodynamic rate constants ΔH^\ddagger , ΔS^\ddagger and ΔG^\ddagger can be determined from an Eyring plot of $\ln(2k_{\text{obs}}/T)$ vs $1/T$.

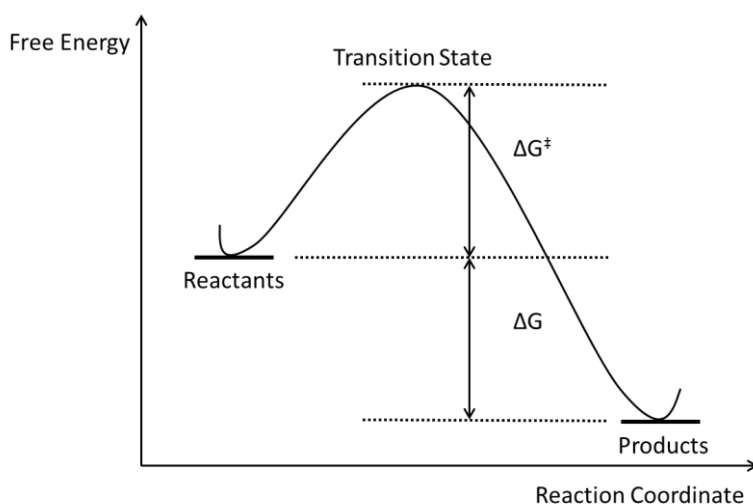


Figure 2.18 The reaction co-ordinate for the dissociative reaction for the loss of ligand

2.2.8. Ligand Loss

The rate constant for pyridine ligand loss reported by Cowley *et al.* (2011)⁹³ for **5-c** has been doubled, as the rate constant is quoted per mole of pyridine, and the data here are quoted as per mole of catalyst. The rate constant for **5-b** is the slowest, with the catalyst only starting to exchange in the 1D EXSY data at 290 K, in comparison to **5-a** and **5-c** which exchange at temperatures as low as 273 K. The errors associated with the values are upper and lower limits at 95% confidence, which were determined using jack-knife and bootstrapping methods (fully described in appendix). The observed values for ΔH^\ddagger and ΔS^\ddagger in **5-b** are larger in magnitude than those of the other two catalysts. The result of this is a slightly higher Gibbs free energy change and smaller rate constant.

	ImMe ₂ NPr' ₂ (5-a)	BzIMes (5-b)	IMes* (5-c)
Rate Constant / s ⁻¹ (300 K)	14.4 ± 0.1	7.3 ± 0.1	23.4 ± 0.1
ΔH^\ddagger / kJ mol ⁻¹	89.9 ± 3.6	130.5 ± 2.3	93.4 ± 3.1
ΔS^\ddagger / JK ⁻¹ mol ⁻¹	82.6 ± 12.9	213.2 ± 7.9	97.0 ± 13.0
ΔG_{300}^\ddagger / kJ mol ⁻¹	65.2 ± 0.03	66.5 ± 0.05	64.0 ± 2.2

Table 2.3 Relevant thermodynamic and kinetic data relating to the loss of pyridine from **5-a**, **5-b** and **5-c***. The data for **5-c*** taken from literature⁹³. Errors represented as 95% confidence limit, for the rate data, n = 7, for the Eyring data n = 5.

The loss of pyridine **5-b** has a higher enthalpic barrier (ΔH^\ddagger) than that of the identical process in the other two complexes. This suggests that the associated Ir-N bond is significantly stronger. The significantly larger ΔS^\ddagger value for ligand loss agrees with this hypothesis as the system becomes significantly more disordered upon loss of pyridine.

One possible explanation for this effect is that CH₂ linker and phenyl group allow the pyridine ligands of **5-b** to approach closer to the metal centre thereby producing a more stronger Ir-N bond and more ordered ground state. The loss pyridine via a dissociative route requires the breaking of this bond with little solvent stabilisation of the transition state. This substituent change also seems to increase the release in entropy of the system due to greater freer movement of the CH₂-Ph arm.

While **5-a** is predicated to involve binding of the more electron releasing carbene, which should again increase ΔH^\ddagger , this is not observed in practice. This suggests that steric interactions act to push off the pyridine in the ground state with the result that more facile

ligand loss takes place. The smaller gain in ΔS^\ddagger for **5-a** is therefore likely to reflect the simpler ligand structure.

2.2.9. Hydride Loss

The methods used to calculate the activation parameters for pyridine loss were also employed to probe those for H₂ formation.

	ImMe ₂ NPr ₂ ⁱ (5-a)	BzIMes (5-b)	IMes (5-c)
Rate Constant / s ⁻¹ (300 K)	5.0	0.56	9.0
ΔH^\ddagger / kJ mol ⁻¹	79.4 ± 3.2	96.4 ± 1.01	79.2 ± 0.2
ΔS^\ddagger / JK ⁻¹ mol ⁻¹	34.0 ± 10.9	77.5 ± 3.40	41.0 ± 3.0
ΔG_{300}^\ddagger / kJ mol ⁻¹	69.2 ± 0.003	73.1 ± 0.01	66.4 ± 0.3

Table 2.4 Relevant thermodynamic and kinetic data relating to the loss of hydride ligands from **5-a**, **5-b** and **5-c**. The data for **5-c***, taken from literature⁹³

H₂ loss from **5** has been proposed previously to proceed via the formation of a dihydrogen-dihydride intermediate¹⁴⁸. The Gibbs free energy change exhibited for this common process reflects all the changes that are required to reach the transition state for the slow step, which in this case includes pyridine loss. The barrier to hydride loss in **5** therefore reflects the underlying changes required for loss of pyridine in addition to those for H₂. It can be seen as a consequence of this complex reaction pathway that the rates of H₂ loss are lower than those of pyridine loss; furthermore as might be expected, the process is inhibited by added pyridine. The H₂ loss rate data for these NHC complexes; is presented in section 8.1.

One consequence of the H₂ loss process occurring after pyridine loss is that the observed rates are always slower than those of pyridine loss. Loss from **5-b** is, however, again slower than that from the other two complexes. While the resulting ΔH^\ddagger and ΔS^\ddagger changes are all positive, those for **5-a** and **5-c** and in fact quite similar despite their dramatic steric and electronic differences. ΔG^\ddagger which shows a trend that suggests a fine balance must exist between steric and electron effects.

2.3. Summary

In this chapter two new complexes have been prepared, for testing as SABRE catalysts. Their ligand exchange processes have been monitored by NMR methods. The underlying activation parameters have been shown to include key electronic and steric effects which act together in promoting ligand exchange. It has been established that the rates of pyridine and H₂ loss are quicker than those commonly associated with NMR relaxation (5 – 30 seconds). SABRE requires the build-up of a pool of material that has been in contact with what were two protons in *parahydrogen* molecule on a timescale that is faster than relaxation. I therefore predict that **5-a** and **5-b** will be SABRE active but perform less well than **5-c**. This hypothesis is tested in Chapter 3.

3. Chapter 3 Exemplifying the SABRE method with pyridine

3.1. Introduction

This chapter will investigate the use of the complexes **2-a**, **2-b** and **2-c** as catalysts for the SABRE polarisation of pyridine and pyridine type substrates. SABRE can be achieved in two ways, either by the shake method (method 1) or by using a flow polariser designed by Bruker (method 2) as described in the Experimental Section 7.2. Using these methods, the plan is to look at how the magnetic field and temperature affects the polarisation process. This section will also investigate how SABRE can be used to enable the recording of ^1H OPSYdq, ^{13}C and $^{13}\text{C}\{^1\text{H}\}$ NMR spectra in addition to simple ^1H NMR spectra. This is achieved by using a flow system which is automated, thereby giving greater reproducibility in the resulting spectra.

3.2. Enhancement of ^1H NMR signals of pyridine by **2-a**, **2-b** and **2-c** under SABRE

As described in the experimental, samples containing the substrate pyridine can be prepared in an NMR tube and used for shake and drop studies. This method is used extensively to investigate new substrates, as it is quick and easy to prepare the sample and doesn't consume large amounts of catalyst, substrate or expensive deuterated solvent. Pyridine was the first substrate to be chosen to compare the catalytic activity of **2-a** and **2-b** with that previously reported for **2-c**¹⁴⁹.

A typical ^1H NMR spectrum obtained for a hyperpolarised pyridine sample shaken at 65 Gauss (G) can be seen in Figure 3.1, with the observed resonances labelled as shown. The corresponding thermal trace is shown along the top. The polarized peaks of free pyridine appear in the emission (or negative amplitude) with the resulting signal enhancements measured as -113.7, -63.2 and -99.6 respectively. This process can be repeated under transfer in the Earth's magnetic field (0.5 G) and the new enhancement's values are -30.36, -20.14 and 31.23-fold respectively.

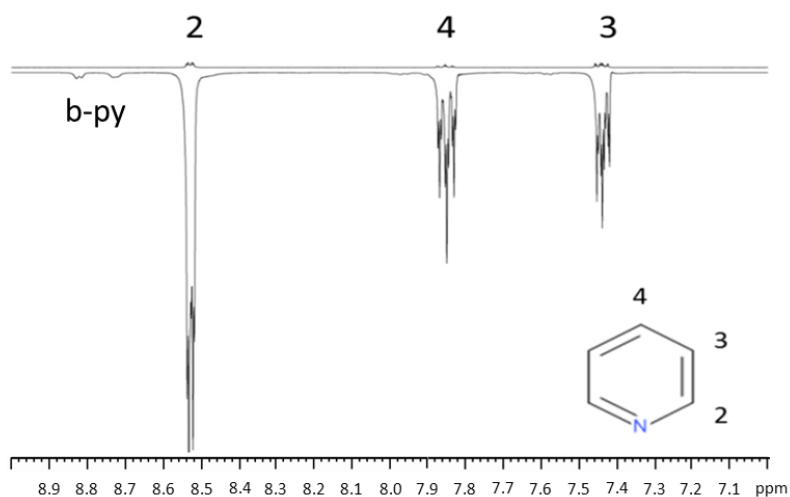


Figure 3.1 Observed ¹H NMR spectra for pyridine resonances 2, 3 and 4. The thermal is represented on top and polarised on the bottom, shaken at approximately 65 G

The polarized state is consumed during this measurement as a 90° observation pulse is applied. By shaking the sample in these two different fields, the level of enhancement is greatly affected; this will be discussed later in section 3.3. It is also evident on close examination of the NMR spectra in Figure 3.1 that weaker signals for the bound pyridine ligands (**b-py**) within the host complex [Ir(H)₂(ImMe₂ⁱPr)(Py)₃]Cl (**5-a**), are also visible and they too show emission character. This indicates that spontaneous polarization transfer occurs between *parahydrogen* and pyridine when both are in temporary contact with the metal complex.

When comparing the results obtained using active catalyst **2-a**, **2-b** and **2-c** it can be seen that:

- The same type of magnetisation is created for each of the ¹H pyridine proton signals.
- Positions 2 and 4 of pyridine always exhibit emission signals regardless of the magnetic field experience by the sample during SABRE.
- Position 3 of pyridine produces an absorption signal under polarisation transfer at 0.5 G but is emissive at 65 G.

The enhancement levels are summarised in Table 3.1.^a

Catalyst	Position	¹ H Signal Enhancements 0.5 G			¹ H Signal Enhancements 65 G		
		2 (<i>ortho</i>)	4 (<i>para</i>)	3 (<i>meta</i>)	2 (<i>ortho</i>)	4 (<i>para</i>)	3 (<i>meta</i>)
ImMe ₂ NPri ₂ (2-a)		-30.36	-20.14	31.23	-113.7	-63.2	-99.6
BzIMes (2-b)		-44.7	-50.67	28.48	-56.8	-113.6	-59.7
IMes (2-c)		-71.2	-61.7	40.3	-160.3	-123.4	-119.2

Table 3.1 Comparison of ¹H NMR signal enhancement levels (fold) observed for pyridine using catalyst 2-a, 2-b and 2-c, shaken at 65G and 0.5G

Catalysts; **2-a**, **2-b**, and **2-c** were present at a concentration of 5 mM (0.031 mm) and a 20-fold pyridine ligand excess was employed (100 mM, 0.062 mm) in 0.6 ml of methanol-d₄.

3.3. Polarisation field plot

As mentioned in the previous section, shaking the sample at 65 G or 0.5 G dramatically changes the level of signal gain. The use of the flow method allows us to observe the effect of the PTF with greater accuracy and in greater detail. A more detailed description of the flow method is presented in the Experimental Section.

In order to complete the study of complexes **2-a** and **2-b** they need to be activated in an ampoule under an atmosphere of H₂ for 48 hours prior to starting the measurements. This ensures that it is possible to compare the results of different catalysts with the active species being present at the same concentration in every sample. The samples were prepared according to standard conditions and a selection of the resulting spectra can be seen in Figure 3.2 and a graphical representation is shown in Figure 3.3. It is evident that the maximum enhancement occurs when the PTF lies between 60 and 80 G for all three pyridine resonances. There is a phase change for position 3, as between -150 to -40 G its ¹H NMR signal show emission type character, before producing an antiphase signal at -30 G, and absorption type magnetisation between -20 and 10. If the fields were inverted, identical behaviour would be seen (0 – 150 G).

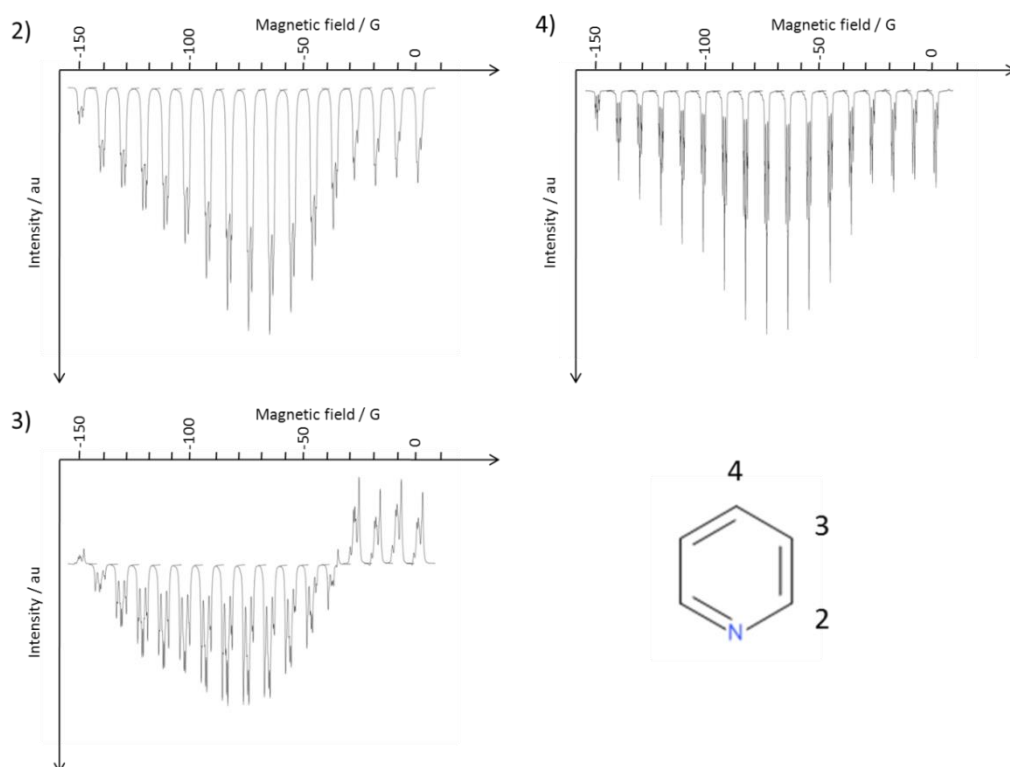


Figure 3.2 Observed ^1H NMR signal intensity changes for pyridine resonances 2, 3 and 4 as a function of the PTF using catalyst 2-a and method 2

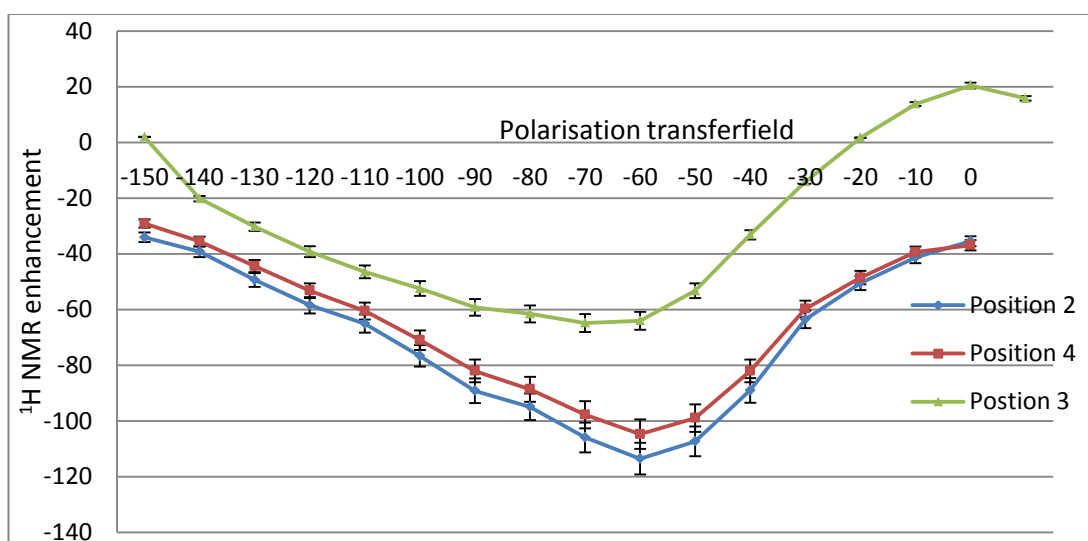


Figure 3.3 Graphical representation of the observed ^1H NMR signal enhancement profile using the activated catalyst 2-a and pyridine as a function of PTF over the range of 0 – 150 G

The proton signal enhancement values of Figure 3.3 are presented as a raw enhancement value.

Figure 3.2 reports on the appearance of the individual proton signals of pyridine as a function of SABRE after transfer in the specified field. It can be seen from the plot that each peak still contains the expected multiplicity and the signals for protons 2 and 4 track each other in intensity, appearing with a maximum intensity at 60 G. These measurements were made after the application of a 90 degree pulse and therefore contain normal Zeeman magnetisation of enhanced amplitude which can be on negative (emission) or positive (absorption) type.

For the *meta* proton (3) this situation is more complex. It starts out in emission but at 30 G changes to absorption. The underlying transfer into position 3 is, however, inefficient by comparison to that into the other two sites.

The reproducibility of the flow system is demonstrated in the Experimental Section, but for transfer at 60 G, the 95 % confidence limits are -110.63 ± 1.36 , -92.16 ± 0.70 and -55.33 ± 0.66 for positions 2, 4 and 3 respectively. Hence the errors in these data are $\approx 1\%$.

Similar data was collected using catalysts **2-b** and **2-c**. The corresponding graphical representations can be seen in Figure 3.4. The field profile for activated catalyst **2-c** has previously been reported by Cowley *et al.* 2011¹⁴⁹, but no enhancement values were presented.

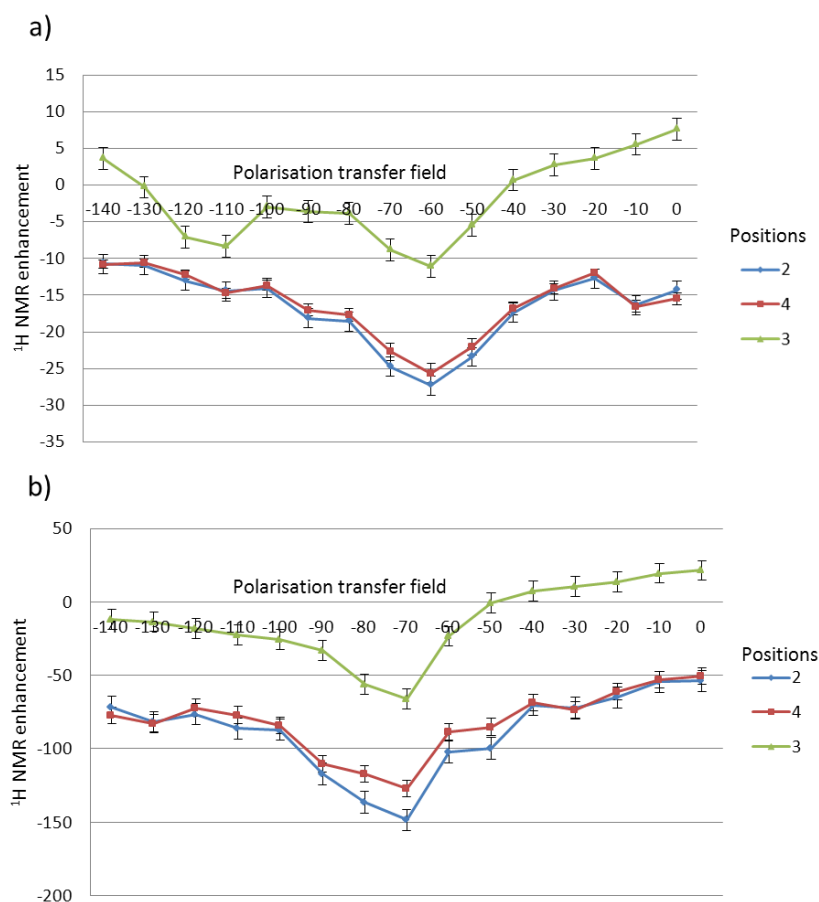


Figure 3.4 Graphical representation of the observed ^1H NMR signal enhancement profile as a function of PTF over the range of 0 – 150 G, produced for pyridine using catalyst a) 2-b b) 2-c

These data revealed:

- Both catalysts **2-a** and **2-b** deliver optimal SABRE at a PTF of 60 G.
- For **2-c**, a PTF of 70 G is required for optimum transfer.
- The order of SABRE efficiency for the investigated catalysts is **2-c > 2-a > 2-b**.
- Position 3 (*meta*) proton changes from emission to absorption at -30 G, or -50 G depending on the catalyst.
- The behaviour of the position 3 (*meta*) proton resonance is complex for all catalysts and better examined with either **2-c** or **2-a**.

3.3.1. Magnetisation type

It has been demonstrated that SABRE generates both single spin longitudinal (I_z) order and multiple spin longitudinal order ($I_z S_z$)^{76, 150-152}. It is assumed a pure 90° pulse is applied to the sample to simplify the magnetisation that is detected. Under these conditions I_z leads to I_x or I_y magnetisation depending upon the pulse phase. However, if the pulse angle was set incorrectly, $I_z S_z$ can lead to observable states; these are now antiphase such as $I_z S_x$. Given that the amplitude of these states is not equal, the detected signals can therefore be complex. This situation is revealed in Figure 3.5.

Care therefore needs to be taken when examining position 3 (*meta*) proton signals which clearly share higher spin order terms. These can, however, be robustly differentiated through the OPSYdq NMR experiment of section 3.4.

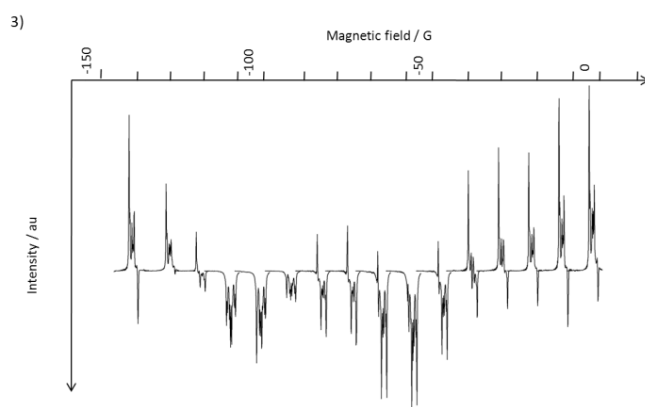


Figure 3.5 Observed ^1H signal enhancement field profile for position 3 of pyridine using the activated catalyst **2-b**

3.4. Only Parahydrogen Spectroscopy (OPSY)

The spin states produced from *parahydrogen* in a SABRE experiment can be either longitudinal (I_z) or longitudinal to spin order ($I_z S_z$) in type. The first 90° pulse of this method affects both of these types of magnetisation; the resulting $I_x S_x$ term is a mixture of zero and double quantum coherence. Both of the resulting in-plane magnetisation terms are then dephased by a gradient pulse. A second 90° pulse is then applied to the sample which further encodes the magnetisation. If this pulse is followed by a gradient of twice the original amplitude it will act to refocus the effects of the first gradient provided we are dealing with a two-spin order term. Hence this process will suppress any single spin order (thermal) signals whilst retaining signals relayed through a double quantum coherence associated with initial $I_z S_z$ magnetisation (Figure 3.6).

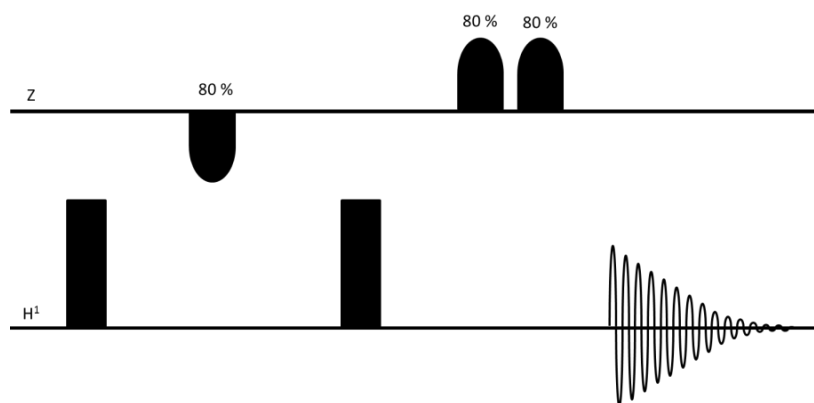


Figure 3.6 Pulse sequence for a double quantum selected OPSY NMR experiment

The resulting NMR spectra that are obtained using the ^1H OPSYdq NMR sequence and catalysts **2-a**, **2-b** and **2-c**¹⁴⁹ are presented in Figure 3.7. Maximum $I_z S_z$ magnetisation is observed experimentally at a PTF close to zero in accordance with the theoretical predication of Adams¹⁵³ and Green¹⁵⁰; this would be maximised for a true zero value.

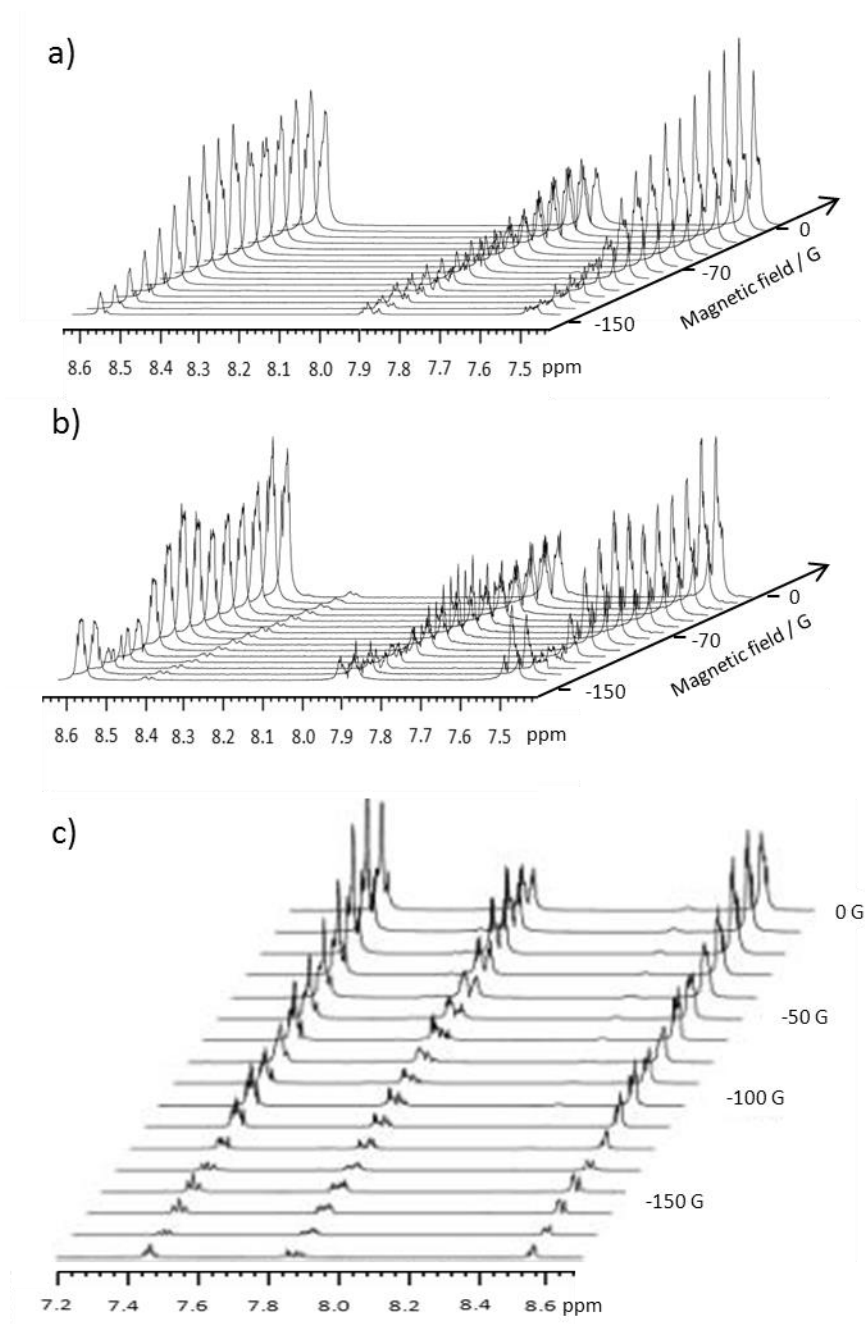


Figure 3.7 A series of ^1H OPSYdq NMR signal intensity profiles for the pyridine resonances 2, 4 and 3 as a function of PTF (-140 G to 0.5) using a) 2-a b) 2-b and c) 2-c. Spectra for 2-c was taken from literature¹⁴⁹

The OPSY measurements revealed:

- Maximum $I_z S_z$ character is created at low PTF value.
- The points of the phase change indicated in Figure 3.2 do not correspond to an $I_z S_z$ maximum and therefore must correspond to an I_z minimum.

The hypothesis that an I_z minimum exists was tested by deploying an OPSYsq (single quantum) measurement. This method selectively detects the I_z term rather than the $I_z S_z$

term. The series of NMR spectra shown in Figure 3.8 confirm that the point where the antiphase character is maximised corresponds to the point where the I_z level is a minimum.

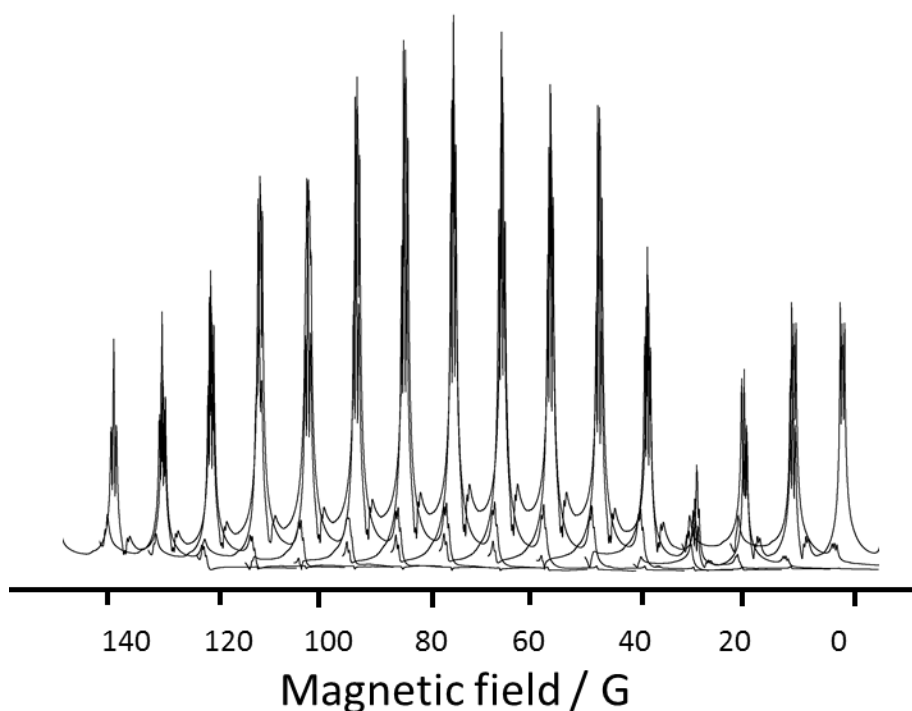


Figure 3.8 A series of ^1H OPSYsq NMR signal intensity profiles for the *meta* pyridine resonance as a function of PTF (0.5 to 140 G) resulting after SABRE using 2-c

In Summary:

- The order of activity in SABRE is **2-c > 2-a > 2-b**.
- PTF effects are exemplified.
- If a screening process looking for magnetisation transfer into an array of substrates were to be undertaken, a PTF value of 65 G would be suggested.
- SABRE is an exchange process phenomenon and should therefore depend upon temperature.

3.5. Effect of temperature to the SABRE catalyst

The effect of temperature can be most readily investigated through the shake method. Samples were activated and refreshed with *para*hydrogen without agitation. The NMR tube was then submerged in a water bath at the desired temperature for three minutes, quickly wiped dry, shaken for 10 seconds in a vertical motion and interrogated by NMR. These data are represented numerically in Table 3.2 and graphically in Figure 3.9.

Temperature (K)	¹ H Signal Enhancements 0.5 G			¹ H Signal Enhancements 65 G		
	2	4	3	2	4	3
333	-32.1	22.6	-29.8	-35.5	-35.4	-21.0
323	-33.4	21.2	-28.2	-56.3	-49.2	-32.4
313	-35.9	16.0	-34.0	-79.9	-74.4	-45.7
303	-22.6	10.2	-30.4	-78.2	-79.3	-48.3
294	-20.3	9.1	-16.8	-83.0	-82.9	-52.7
273	-13.6	5.7	-12.6	-64.1	-57.5	-23.9

Table 3.2 ¹H NMR signal enhancements determined for the indicated pyridine resonances by catalyst 2-a under SABRE as a function of temperature

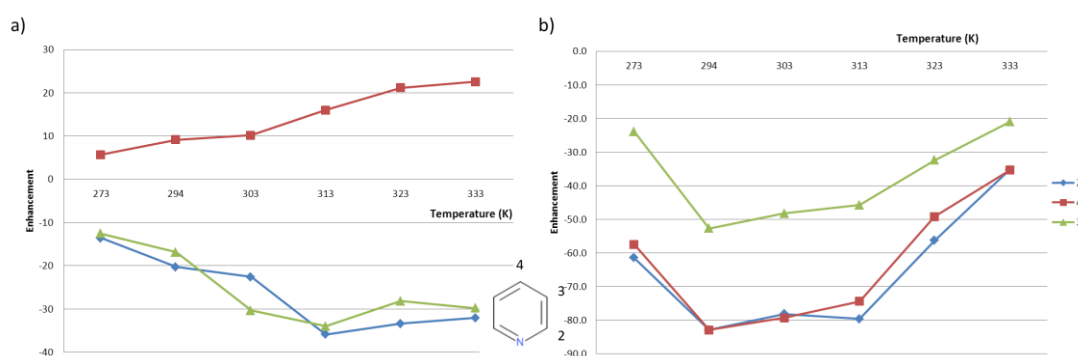


Figure 3.9 Graphical representation of the ¹H NMR signal enhancements seen for pyridine using catalyst 2-a as a function of temperature at a PTF of a) 0.5 G and b) 65 G

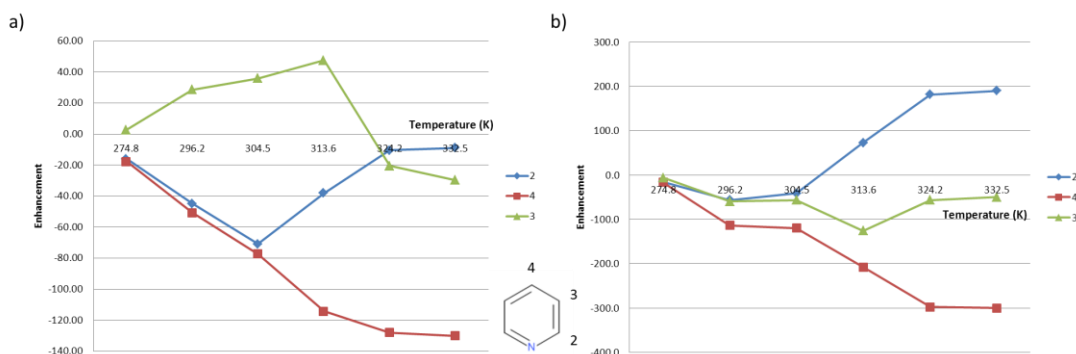


Figure 3.10 Graphical representation of the ¹H NMR signal enhancements seen for pyridine using catalyst 2-b as a function of temperature at a PTF of a) 0.5 G and b) 65 G

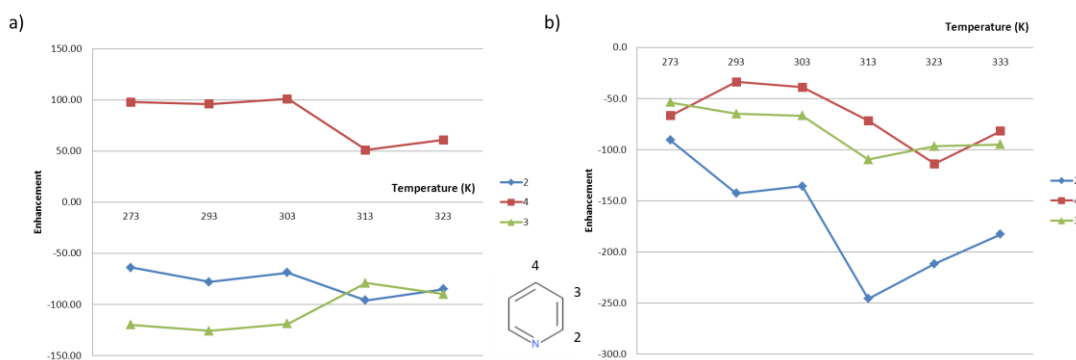


Figure 3.11 Graphical representation of the ¹H NMR signal enhancements seen for pyridine using catalyst 2-c as a function of temperature at a PTF of a) 0.5 G and b) 65 G

Figure 3.9 shows:

- Proton signals of free pyridine for position 2 (*ortho*) and 4 (*para*) increase in size between 273 K and 313 K, before falling slightly as the temperature increases to 333 K when PT takes place at a field of 0.5 G.
- Position 3 (*meta*) proton constantly increases in amplitude with temperature.
- Under a PTF of 65 G, resonances intensities for positions 2 (*ortho*), 3 (*meta*) and 4 (*para*) all show similar behaviour. They increase up to 294 K before plateauing and until 313 K and then falling at higher temperatures.

Upon comparing the values in Figure 3.9 with those in Figure 3.10 and Figure 3.11, it can be seen that all of the traces portray unique behaviour. Furthermore, the activity of catalyst 2-b surpasses that of 2-c at higher temperatures. This means that choosing an optimal catalyst is impossible.

Based on the lower temperature values, catalyst **2-b** would be discounted and yet, at high temperatures, it portrays the best performance. The problem therefore needs to be carefully defined before setting out to investigate and optimise such SABRE systems. For work to be completed at room temperature, catalyst **2-b** is unsuitable and hence **2-c** should be chosen as it provides for better enhancement.

The change in temperature reflected in these studies speeds up ligand exchange in all systems. This, in turn, acts to reduce the contact time of the hydrides and substrates on the metal centre of the PTC. It is therefore clear that:

- There is an optimal contact time for ligand and *parahydrogen* for PTC.
- The optimum lifetime is affected by the PTF.

Due to the fact that each pyridine resonance exhibits different behaviour, different optimum temperatures are required depending on which resonance we wish to enhance.

If we consider position 3, the *meta* proton, at a PTF of 65 G, it is possible to calculate the lifetimes at the optimum temperatures as follows:

- **2-a** at 294.0 K has a rate of 3.9 s^{-1} and hence lifetime of 0.256 s.
- **2-b** at 332.5 K has a rate of 986.1 s^{-1} and hence lifetime of 0.001 s.
- **2-c** at 313.0 K has a rate of 105.4 s^{-1} and hence lifetime of 0.009 s.

These data indicate that the optimum lifetimes are very different. We can therefore deduce that the hydride-hydride and hydride pyridine couplings must also differ dramatically in these catalysts. The classical route to polarisation transfer in an INEPT experiment requires the setting of a variable to $1/4J_{(HX)}$, the spin-spin coupling between the proton magnetisation donor and the x-nucleus receptor. It is not therefore surprising that such behaviour has been found, although the scale of difference is surprising.

3.6. Probing ^{13}C NMR experiments

It is also possible to investigate the effects of SABRE on ^{13}C nuclei, which include ^1H -coupled and ^1H -decoupled NMR experiments. Figure 3.12 shows the polarisation of the carbon resonances for the pyridine substrate in a ^{13}C NMR experiment using standard conditions and method 2. All of the pyridine carbon resonances can be clearly established in the $^{13}\text{C}\{^1\text{H}\}$ measurement with a signal-to-noise ratio for positions 2, 3 and 4 of 47, 201 and 89 respectively compared to the solvent signal of 13. The same method can be applied to the ^{13}C spectrum with positions 2, 3 and 4 now delivering signal-to-noise values of 14, 61 and 39 respectively with a solvent signal of 12.

In the normal carbon NMR experiment you would expect the signal-to-noise ratio of the $^{13}\text{C}\{^1\text{H}\}$ signals to be greater than those of a ^{13}C measurement because of each of the resonances are now split by the ^1H - ^{13}C coupling; these peaks collapse in the decoupled measurement, thus maximising the signal-to-noise ratio. This behaviour was also reflected in the corresponding ^{13}C SABRE experiments.

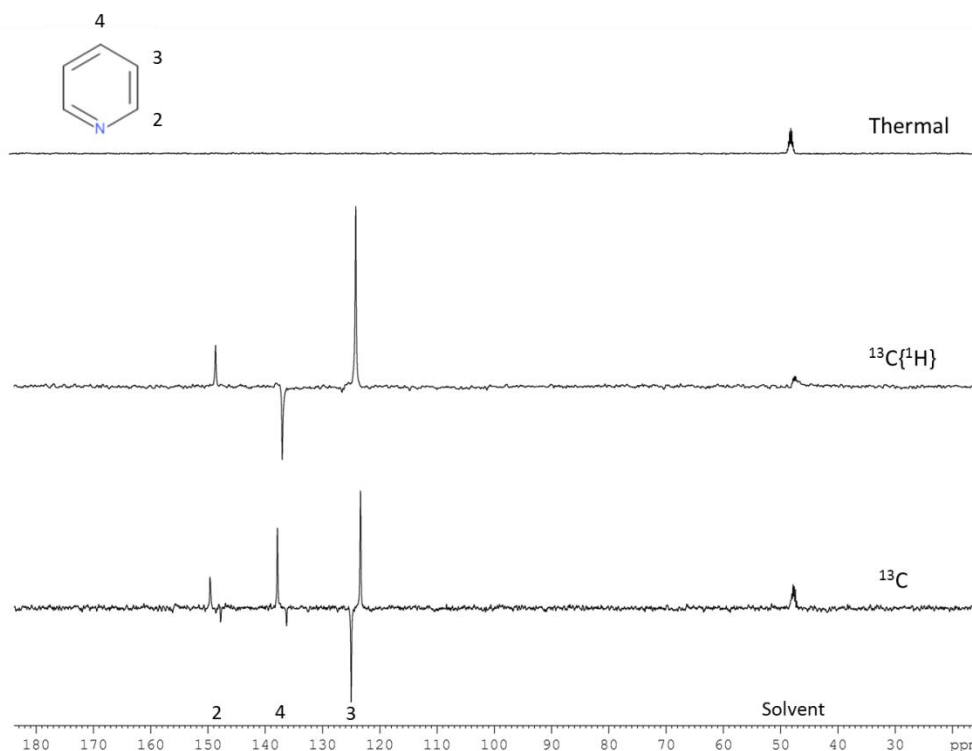


Figure 3.12 $^{13}\text{C}\{^1\text{H}\}$ and ^{13}C NMR spectra of pyridine, using 2-a in a single scan. The thermal trace is presented on the top. The polarised traces are presented in the middle and on the bottom, which were obtained using method one at approximately 65 G with a signal-to-noise ratio for $^{13}\text{C}\{^1\text{H}\}$ of 47, 201 and 89 for position 2 to 4 respectively and for ^{13}C of 14, 61 and 39 for position 2 to 4 respectively

Figure 3.13 shows the predicted observable states which are derived from *parahydrogen* in a SABRE experiment. The diagrams deal with nucleus **I**, which is split by two other nuclei, **S** and **T** by large and small coupling respectively. When ^{13}C is considered in Figure 3.12, **I** is represented as the ^{13}C centre, while **S** represents a ^1H nucleus one bond away with large coupling and **T** represents a ^1H two bond separated nucleus with a small coupling.

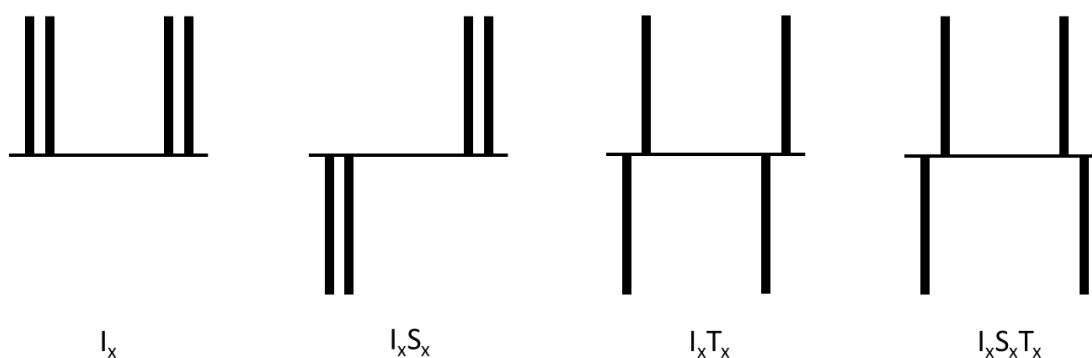


Figure 3.13 Observable states of I_x type that could be seen under SABRE

The magnetic state I_x results in in-phase magnetisation, with the signal split with respect to both **S** and **T**. As defined, the magnetic state $I_x S_x$ produces an antiphase signal with respect to the large coupling of **S** after excitation, whilst the magnetic state $I_x T_x$ produces an antiphase signal with respect to the small coupling of **T**. The state $I_x S_x T_x$ reflects a doubly antiphase signal, with respect to both large and small couplings of **S** and **T** respectively, after excitation.

The shape of the resonances in the ^{13}C spectra observed at positions 2, 3 and 4 in Figure 3.12 can be explained by combining different amplitudes of these states (Figure 3.14); Figure 3.15 shows three expanded features of Figure 3.11 for reference.

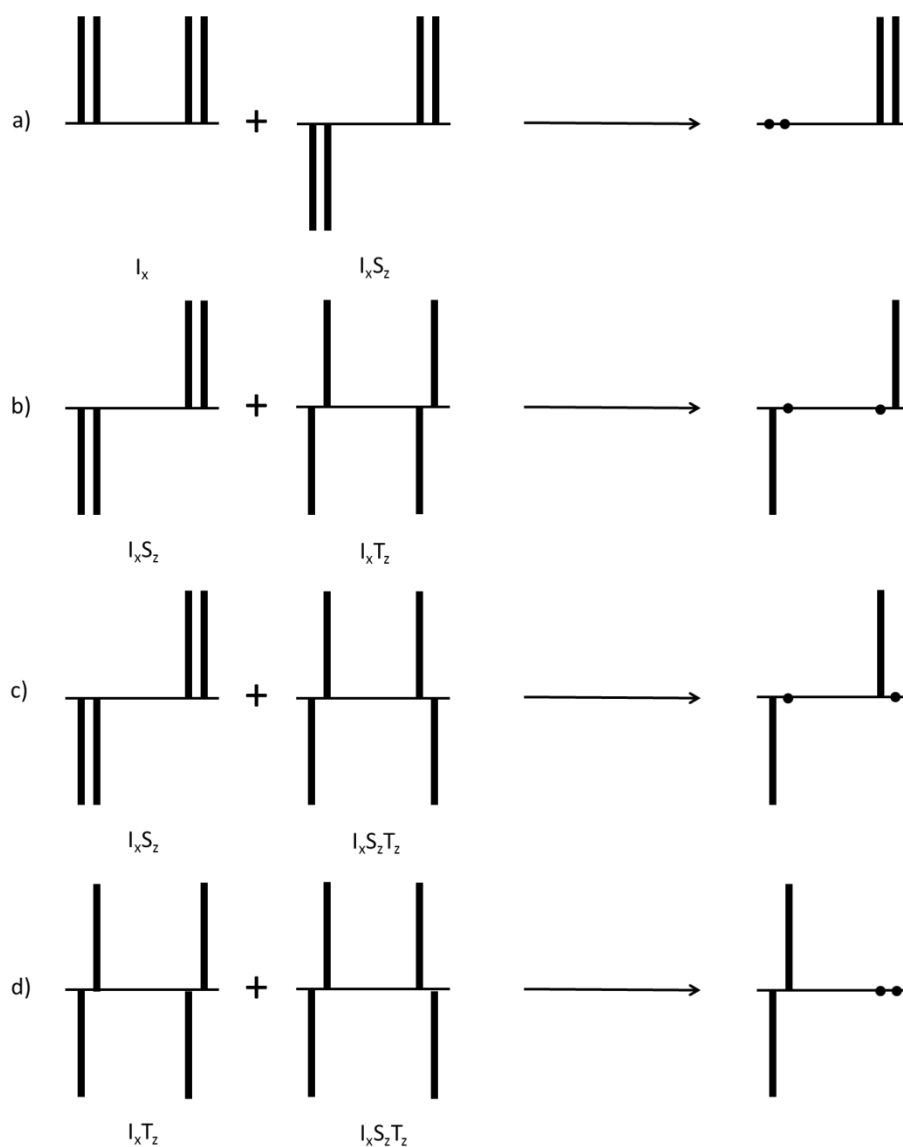


Figure 3.14 The effect of selected combinations of multiple quantum states which affect the peak shape in a SABRE experiment

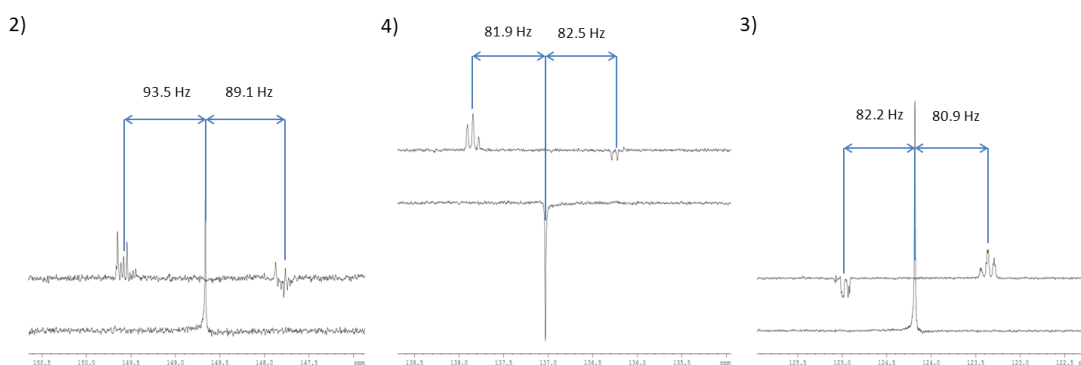


Figure 3.15 Expansion of the selected resonances of Figure 3.12, for pyridine resonances 2, 3 and 4. The top spectra represents a ^{13}C experiment and the bottom traces a $^{13}\text{C}\{^1\text{H}\}$ experiment

As shown previously in Figure 3.12, it is possible to obtain a $^{13}\text{C}\{^1\text{H}\}$ NMR spectrum for a pyridine sample. Based on a ^{13}C experiment which gives rise to antiphase signals, upon decoupling the expectation would be that no signal would be observed as the signal would cancel out (Figure 3.16). This is clearly not always the case and the single spin order magnetisation that is created can be readily probed as a function of PTF under decoupling

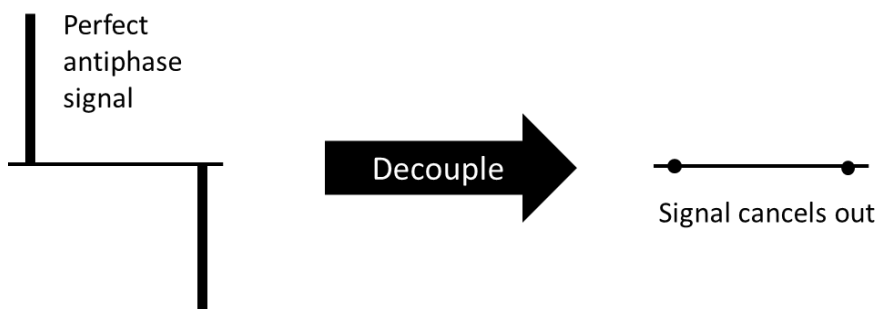


Figure 3.16 Illustration of the resulting spectra which are obtained for $^{13}\text{C}\{^1\text{H}\}$ NMR experiment pair of perfect antiphase ^{13}C signals

The corresponding spectral information is illustrated in Figure 3.17 and Figure 3.18. The maximum signal-to-noise, observed for all three ^{13}C resonances, was observed at 80 G. It is interesting to note that there is still high sensitivity to transfer fields and, that at 70 G, there is a minimum. This matches the ^1H optimum for catalyst **2-a**. It is therefore clear that decoupled spectra can be collected under SABRE.

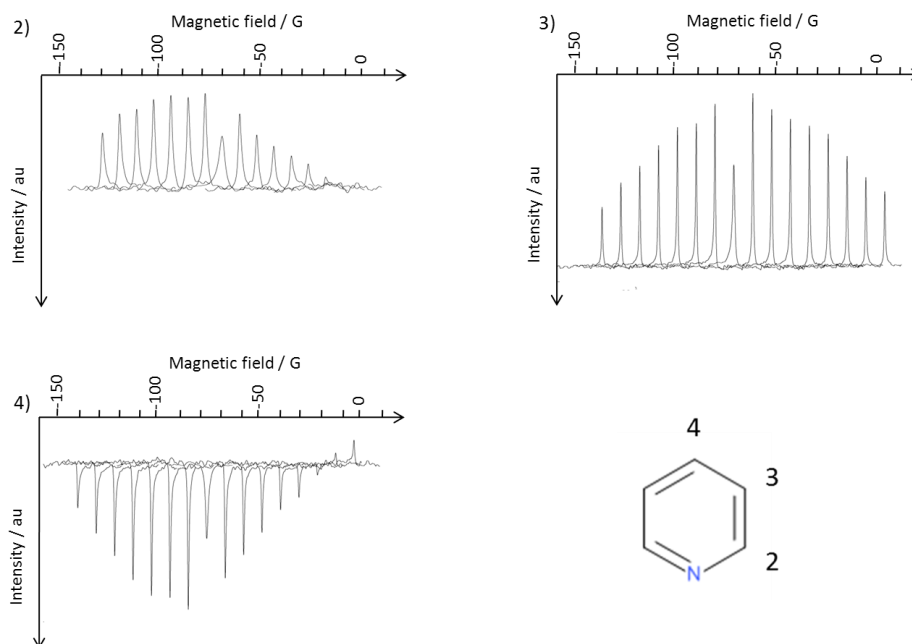


Figure 3.17 Observed $^{13}\text{C}\{^1\text{H}\}$ NMR signal intensity profile for pyridine resonances 2, 3 and 4 as a function of PTF changes using **2-a** and method 2

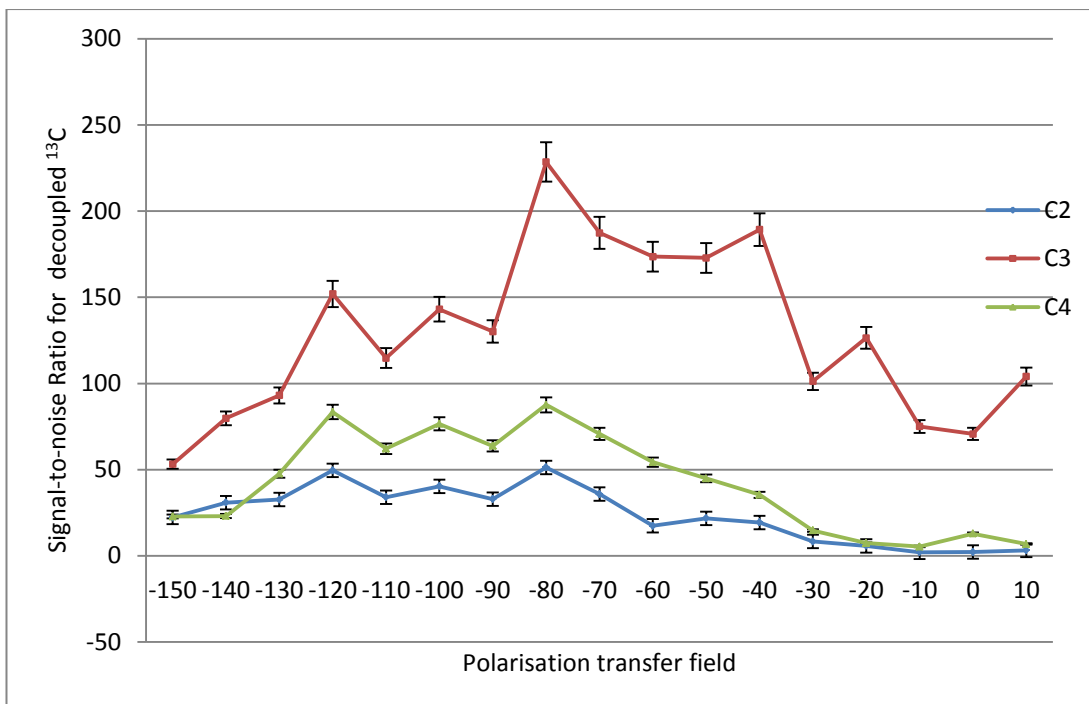


Figure 3.18 Pyridine $^{13}\text{C}\{^1\text{H}\}$ NMR signal-to-noise ratios, obtained on the flow system using 2-a and standard conditions

The corresponding ^{13}C NMR spectra are shown in Figure 3.19 which illustrates how for a PTF value of 60 G, the sum of 90 % $-I_zS_z$ and 10 % I_z and result in a close match with experiment; similar analysis confirms the following deductions.

These reveal:

- There is a complex variation in ^{13}C magnetic state population with PTF.
- Position 2 (*ortho*) – at PTFs between -150 to -60 G exhibits primarily I_zS_z type magnetisation.

At PTF < -60 G - I_zT_z terms including the small coupling are obtained.

- Position 3 (*meta*) – the same magnetic state $-I_zS_z$ is created at all fields, with optimum amplitude being found when the PTF is -40 G.
- Position 4 (*para*) – there are two evident, from -50 to 0 G both $I_zS_z + I_z$ are formed but between -60 to -140 both I_z and $-I_zS_z$ are seen.

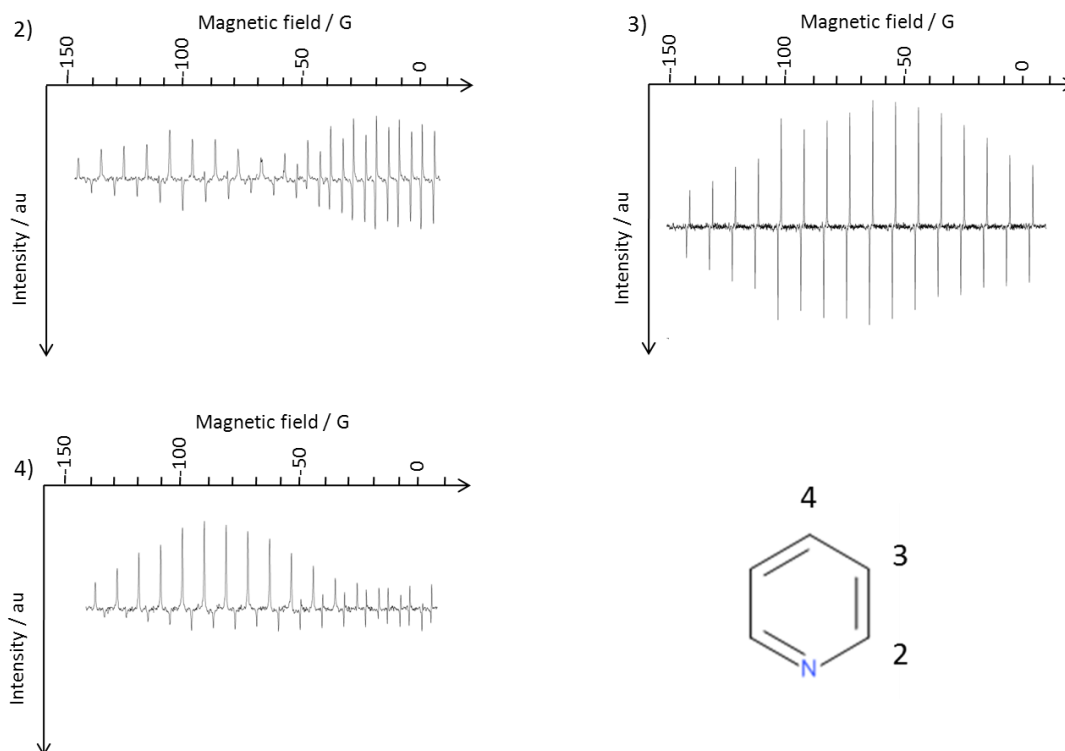


Figure 3.19 Observed ^{13}C NMR signal intensity for pyridine resonances 2, 3 and 4 as an effect of changing polarisation transfer field using 2-a and method 2

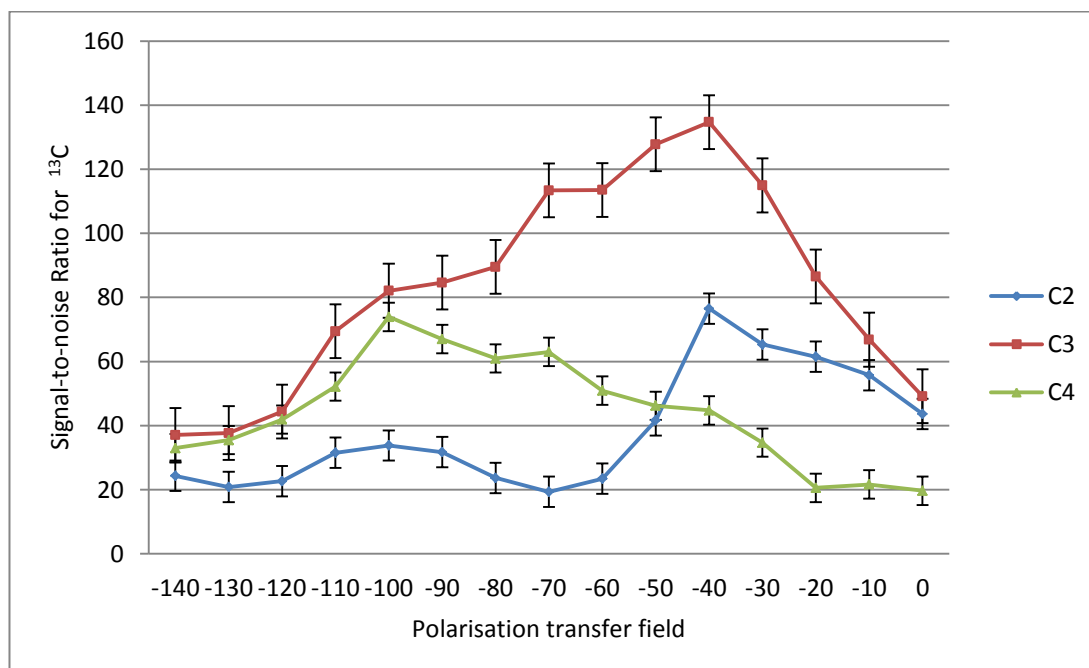


Figure 3.20 Pyridine ^{13}C NMR signal-to-noise ratios, obtained on the flow system using 2-a and standard conditions

When an analogous series of measurements were completed for catalyst **2-b**, no $^{13}\text{C}\{^1\text{H}\}$ signals were detected using the flow method or shake method. Given the poor performance of **2-b** at 294 K, $^{13}\text{C}\{^1\text{H}\}$ NMR measurements using this catalyst were not taken any further. Weak signals could be obtained in a ^{13}C NMR measurement. These are shown in Figure 3.21 and were obtained using method 1.

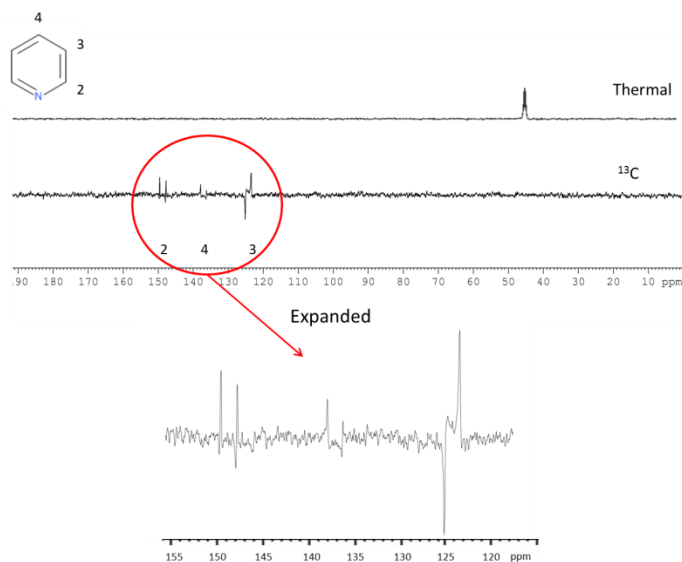


Figure 3.21 ^{13}C NMR spectra of pyridine, using catalyst **2-b** and obtained in a single scan. The thermal trace is presented on the top and the polarised trace is presented on the bottom. Expansion of the polarised trace is presented below to see resonances $^1\text{H}\text{-}^{13}\text{C}$ coupling

Figure 3.22 shows the resulting signal-to-noise ratios for the indicated pyridine resonances with catalyst **2-b** using the flow method. It is clear that a ^{13}C spectrum should employ a PTF of -40 G when using catalyst **2-b**.

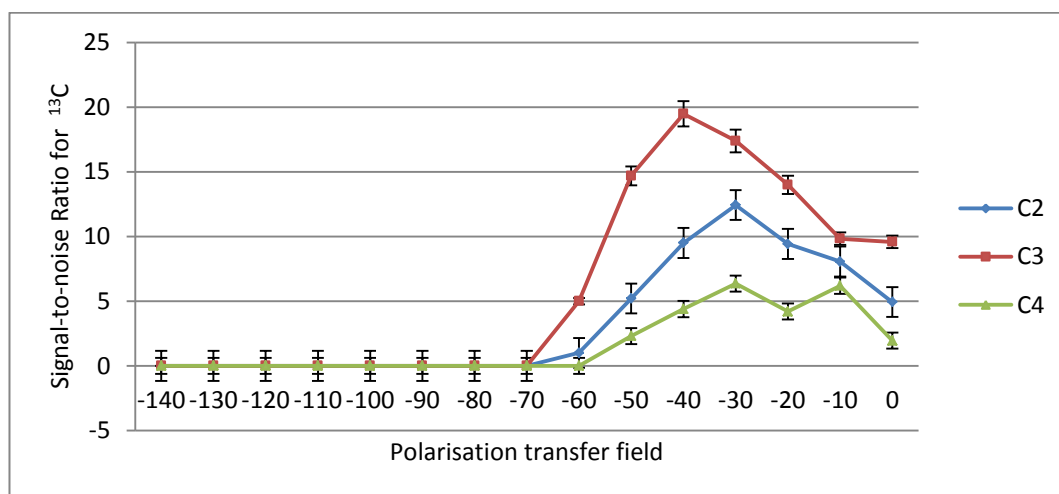


Figure 3.22 Pyridine ^{13}C NMR signal-to-noise ratios, obtained on the flow system using **2-b** and standard conditions

3.7. Comparison of SABRE Catalysts Performance with Pyridine

There has been extensive work carried out on optimising SABRE, and some of this was reported by Lloyd *et al*, 2014¹⁵². A summary of the reported polarisation enhancement data can be seen in Table 3.3.

Catalyst in the form: [Ir(NHC)(COD)Cl]	Rate (s ⁻¹)	NHC Buried Volume	Maximum for PTF	Observed ¹ H NMR signals enhancement			
				<i>Ortho</i> (2)	<i>Meta</i> (4)	<i>Para</i> (3)	Total
IMe*	0.6	26.3	-60	-1.7	-2.0	4.1	4.1
ImMe ₂ N ⁱ Pr ₂ (2-a)	14	38.4	-60	-113.6	-104.8	-64.0	500.6
ICy*	1.1	27.4	-60	-8.4	-9.2	-4.8	40.1
SIMes*	45	36.9	-90	-82.7	-102.7	-63.3	434.2
SiPr*	261	47.0	-150	-15.4	-11.9	-16	70.6
IPr*	78	44.5	-60	-17.1	-12.7	-19.6	79.2
IMes (2-c)	23	36.5	-60	-165.4	51	70.2	503.0
BzIMes [#] (2-b)	7	n/a	-60	-67.5	-61.2	-11.9	-134.5

Table 3.3 ¹H NMR signal enhancements of pyridine observed for a range of NHC catalyst, which were collected using the flow method, where results are given for highest level of polarisation at a specific field. * denotes values taken from literature presented by Lloyd *et al*, 2014¹⁵² which were measured at room temperature. # Lifetime not known

All of the above NHC catalysts undergo ligand exchange on an NMR time scale. Their rates of ligand loss follow the order of SiPr > IPr > SIMes > IMes (**2-c**) > ImMe₂NⁱPr₂ (**2-a**) > BzIMes (**2-b**) > ICy > IMe. The larger the NHC buried volume, the faster the pyridine loss rate. Catalyst **2-a** (ImMe₂NⁱPr₂) does not fit the steric trend and is sufficiently electron rich as to promote ligand exchange.

The results of changing the PTF confirm that, in the majority of cases, 60 G is the optimum field for transfer. It can be concluded from the results that **2-a** is a good catalyst and worthy of extended study. Catalyst **2-b** showed good performance at higher temperatures and was therefore studied further.

3.8. Enhancements of pyridine derivatives

It is also possible to polarise substrates that contain a pyridine-type moiety more generally using SABRE. Catalysts **2-a** and **2-b** were employed in association with the materials of Figure 3.23 to do this. These materials were selected in order to provide an indication of how polarisation transfers around the pyridine ring and to investigate the levels of polarisation in their methyl groups. This work will therefore widen the range of polarised materials and help optimise sensitivity. It follows a similar approach to that used for pyridine with both the shake method and the flow method being used.

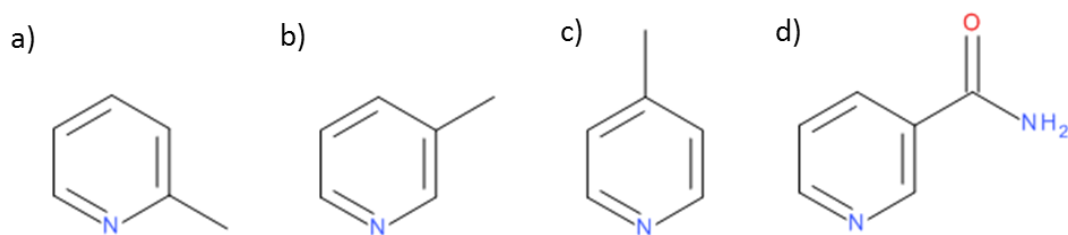


Figure 3.23 Structures of pyridine derivatives which have been investigated using catalysts 2-a and 2-b a) 2-methylpyridine b) 3-methylpyridine c) 4-methylpyridine d) nicotinamide

3.8.1. 2-methylpyridine

The first substrate to be examined was 2-methylpyridine. A typical ^1H NMR spectrum obtained using method 1 can be seen in Figure 3.24, and the signal enhancement levels are listed in Table 3.4. The level of polarisation passed into the substrate is very poor with both catalysts **2-a** and **2-b**. It can be said that there is little to no signal enhancement for 2-methylpyridine as the actual integral is smaller than that of the corresponding thermal trace.

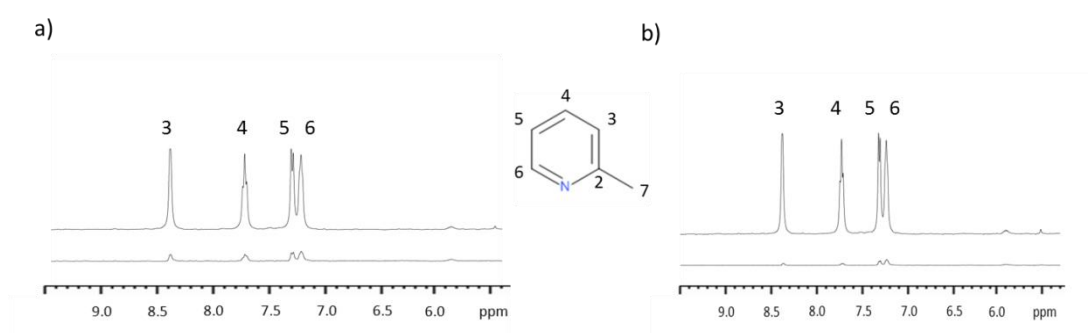


Figure 3.24 Observed ^1H NMR spectra for 2-methylpyridine, with the thermal trace represented on top and the polarised trace on the bottom; PTF of 65 G with a) catalyst 2-a and b) catalyst 2-b

Substrate	Catalyst	Field	^1H NMR enhancements for substrate positions:					
			2	3	4	5	6	7
2-methylpyridine	2-a	0.5 G	-	0.01	0.02	0.04	0.05	0.07
		65 G	-	0.07	0.09	0.11	0.15	0.26
	2-b	0.5 G	-	0.00	0.01	0.02	0.01	0.02
		65 G	-	0.01	0.02	0.05	0.02	0.01

Table 3.4 A comparison of the ^1H NMR polarisation enhancement for 2-methylpyridine using complex **2-a** and **2-b**

The reason why 2-methylpyridine is thought to give low levels of polarisation is that it is unable to bind to the catalyst. The NMR tube containing 2-methylpyridine and **2-a** was left for a further 24 hours under an atmosphere of hydrogen to see if the issue was due to incomplete activation of the catalyst. The results obtained from the addition of fresh

parahydrogen to the sample after this period gave a similar result to the one obtained initially, which was seen in Figure 3.24. Upon carrying out a longer ^1H NMR experiment (512 scans) it was possible to see a weak hydride present at -24.92 ppm, which can be seen in Figure 3.25. The presence of this hydride indicates that if the sample was given a longer time period to activate, it might be possible to see proton enhancement into substrate. This was left under hydrogen for a period of a week checking at regular intervals by carrying out method 1 but no enhancement was observed and the hydride no longer appears in the spectra. Over the period of seven days, the sample solution turns from a bright yellow to a yellow/brown in colour and small traces of coloured precipitate start to appear, indicating that the iridium is precipitating into solution. Catalyst **2-b** was left for the same amount of time but no hydride signal was observable after the same amount of scans and the sample began to precipitate after 48 hours.

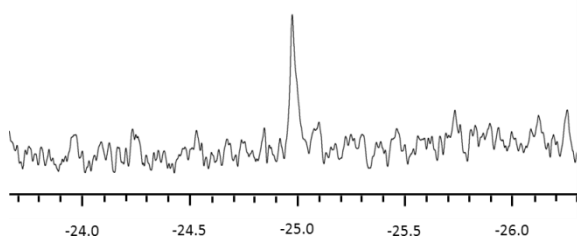


Figure 3.25 Observed ^1H NMR hydride region of 2-methylpyridine which is only visible after 512 scans

Further ^1H and ^{13}C NMR experiments were examined using the flow method and temperature using catalyst **2-a**, **2-b** and **2-c**, but no observable polarisation transfer was noted for 2-methylpyridine.

3.8.2. 3-methylpyridine

3.8.2.1. Method 1 applied to ^1H NMR

3-methylpyridine is one of many precursors to niacin, which is part of the vitamin B group. Niacin is also known as nicotinic acid, and another member of these precursors is nicotinamide.

Firstly the shake method was investigated for 3-methylpyridine with **2-a** and a ^1H NMR spectrum recorded after transfer at 65 G. Proton resonances 2, 4, 5, 6 and 7 all have emission type characters when shaken at 65 G, with enhancement levels of -46.5, -44.50, -40.09, -16.86 and -8.9-fold respectively. Exceptions to this emission behaviour were found in the ^1H NMR signals for position 5 and 7 with **2-a** after PTF at 0.5 G and position 4 with **2-b** after PTF at 0.5 G. **2-b** performs better than **2-a** in these studies.

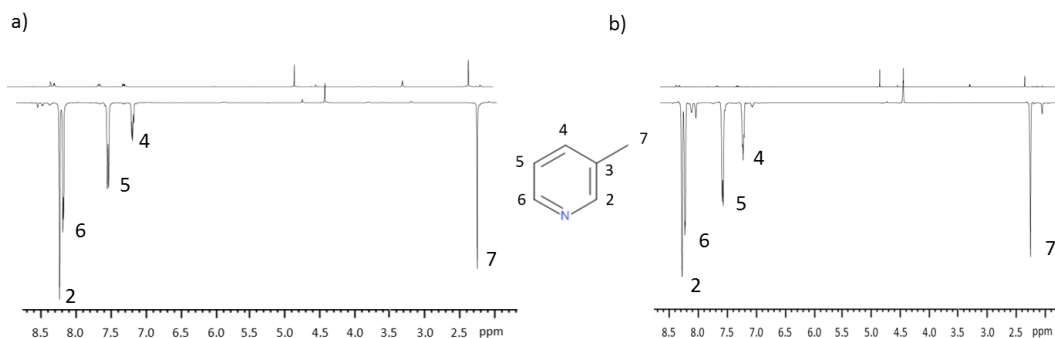


Figure 3.26 Observed ^1H NMR spectra of 3-methylpyridine, thermal trace is represented on top, and the polarised trace on the bottom; PTF undertaken at 65 G with a) catalyst **2-a** and b) catalyst **2-b**

Table 3.5 presents a series of results at 0.5 and 65 G for both catalysts **2-a** and **2-b**.

Substrate	Catalyst	Field	^1H NMR enhancements for substrate positions:					
			2	3	4	5	6	7
3-methylpyridine	2-a	0.5 G	-22.6	-	-15.4	14.3	-27.5	2.03
		65 G	-46.5	-	-40.1	-16.9	-44.5	-8.86
	2-b	0.5 G	-71.3	-	-26.9	-30.7	-75.3	-2.5
		65 G	-120.4	-	-40.3	-111.3	-113.5	-23.2

Table 3.5 Comparison of the ^1H NMR polarisation enhancement data for 3-methylpyridine using catalysts **2-a** and **2-b**

3.8.2.2. Effect of changing magnetic field of polarisation

3-methylpyridine was also examined using method 2. The resulting NMR spectra obtained using **2-a** can be seen in Figure 3.27 and a graphical representation of the ^1H NMR signal enhancement for both catalysts can be seen in Figure 3.28.

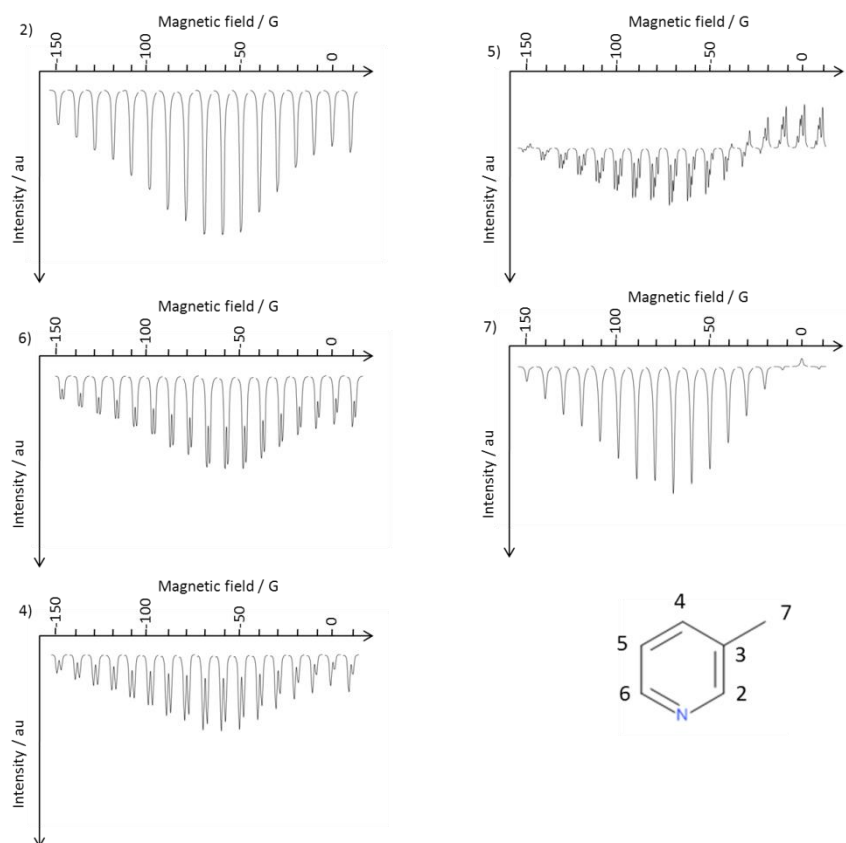


Figure 3.27 Observed ^1H NMR signal intensity profiles for 3-methylpyridine resonances as an effect of changing PTF using **2-a** and method 2

The maximum level of polarisation transfer to 3-methylpyridine using **2-a** is observed at a PTF of 60 G for resonances 2, 5 and 6 and at 70 G for resonances 4 and 7. For catalyst **2-b**, the maximum is observed at 60 G for resonances 2, 5, 6 and 7 and 10 G for position 4.

The two catalysts behave in a similar manner, with positions 2, 5 and 6 all presenting negative amplitude magnetisation across the field profile. The behaviour of **2-b** is again complex. For the first time, two maxima are clearly evident and both systems provide similar activity. Despite this behaviour, 60 G is still optimum for the detection of aromatic resonances. If the *para* proton is to be viewed, 0 G is optimal. For the methyl group, 65 G is a good compromise.

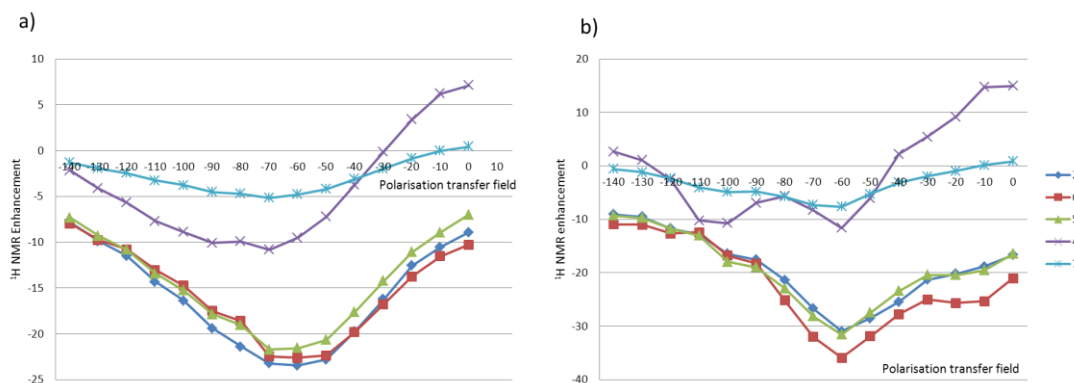


Figure 3.28 Graphical representation of the observed ^1H NMR signal enhancement for 3-methylpyridine as a function of PTF with catalysts a) 2-a and b) 2-b, over the range 0 to -140 G

3.8.2.3. Effect of changing temperature

When the effect of temperature was investigated with 3-methylpyridine with catalysts **2-a** and **2-b**, different behaviour was seen. These data are presented in Figure 3.29 and Figure 3.30:

- The activity of **2-a** at a PTF of 0.5 G falls with increase in temperature.
- The activity of **2-a** at a PTF of 65 G reaches a maximum at 296 K.
- The activity of **2-b** increases with increase in temperature at 0.5 G.
- The activity of **2-b** at 65 G is complex but generally optimised at 303 K.

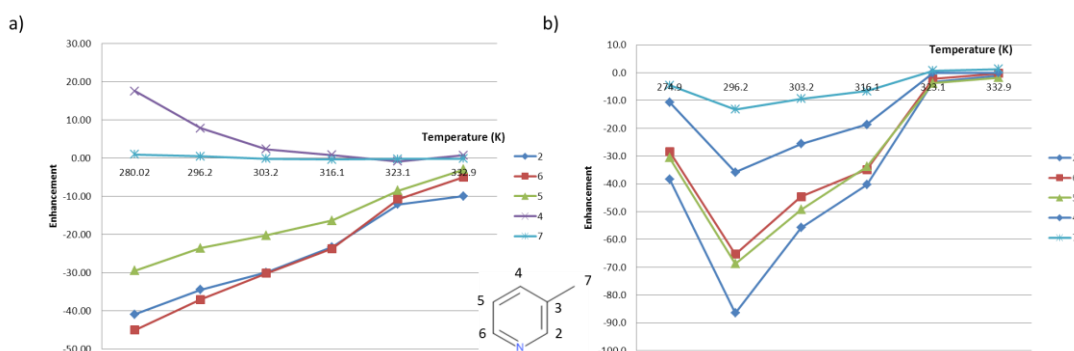


Figure 3.29 Graphical representation of the ^1H NMR signal enhancements seen for 3-methylpyridine using catalyst 2-a as a function of temperature at a PTF of a) 0.5 G and b) 65 G

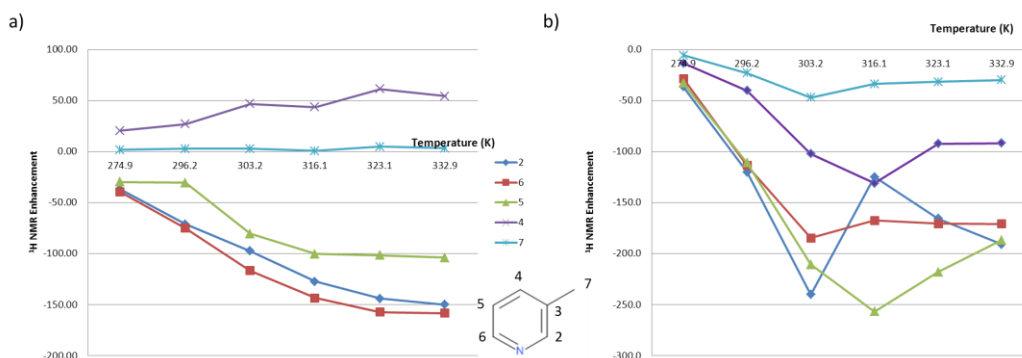


Figure 3.30 Graphical representation of the ^1H NMR signal enhancements seen for 3-methylpyridine using catalyst 2-b as a function of temperature at a PTF of a) 0.5 G and b) 65 G

3.8.2.4. Effect of magnetic field applied to ^{13}C nuclei.

Figure 3.31 - Figure 3.34 illustrate the corresponding ^{13}C and $^{13}\text{C}\{^1\text{H}\}$ NMR results that were obtained for 2-a and 2-b using method 2. The overall levels of signal enhancement were poor, but proved optimal with a PTF value of ≈ 50 -60 G for both types of measurement. The quality of these data is however much worse than that achieved for pyridine which suggests that the methyl group acts to prevent good SABRE.

Figure 3.31 shows three most prominent $^{13}\text{C}\{^1\text{H}\}$ NMR signals; positions 5, 4 and 3 which are circled in red at 60 G which have a signal-noise-ratio of 16.3, 5.4 and 8.7 respectively. The remaining signals were difficult to observe above the signal-to-noise of the NMR experiment. Position 6 can be seen circled in blue which is represented with an antiphase signal at 80 G. The methyl signal (position 7) can be seen very faintly at a field of 110 G which is circled in green with a poor signal-noise-ratio of 1.10. Although resonances 6 and 7 are observable, they cannot be described as being resolved from the baseline.

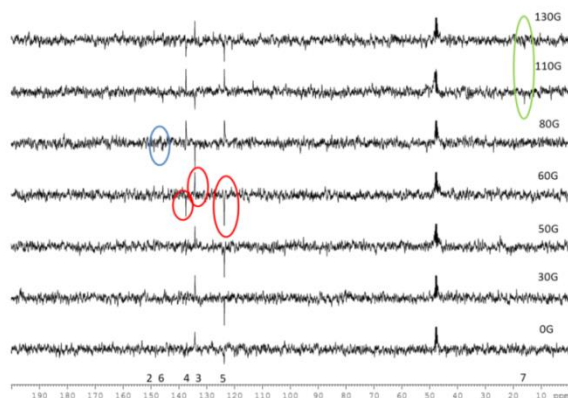


Figure 3.31 $^{13}\text{C}\{^1\text{H}\}$ NMR spectra of 3-methylpyridine obtained as a function PTF with catalyst 2-a and method 2 (result of a single scan). Circled in red are the strongest signals, followed by weak signals in blue and green

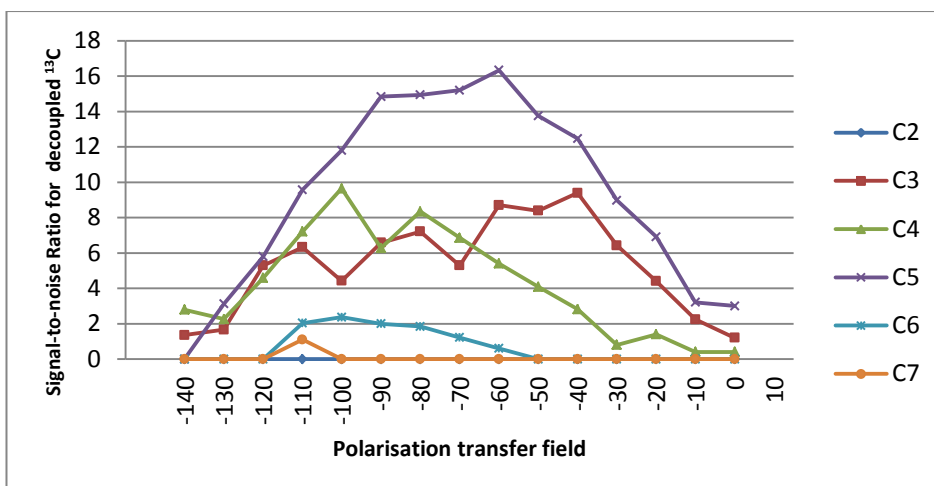


Figure 3.32 3-methylpyridine $^{13}\text{C}\{^1\text{H}\}$ NMR signal-to-noise ratios, obtained on the flow system using 2-a and standard conditions

These ^{13}C data reveal (Figure 3.33) that the quaternary carbon, 3 position (circled red), gives the largest enhancement with a signal-to-noise ratio of 11.2 at a PTF of 50 G. Position 5 and 4 maximum signal-to-noise ratio of 6.7 and 4.68 was achieved at a PTF of 60 G and 80 G respectively. The remaining signals prove had to resolve from the base line although it is possible to identify two pairs of antiphase signals (circled blue) which are generated from positions 2 and 6. Position 3 and 4 appear either antiphase or a single peak (red and yellow circle) which is dependent on the PTF. As these are single antiphase signals it can be concluded that these arise a combination of I_zT_z and $I_zS_zT_z$ which has been previously described in Figure 3.14. Due to the fact that a poor signal to noise is observed for the pairs of antiphase signals, it is very difficult to determine magnetisation that is contributed the combinations of quantum states I_z , S_z and T_z .

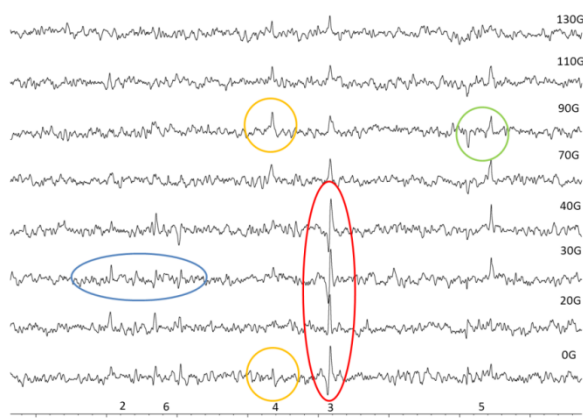


Figure 3.33 ^{13}C NMR spectra of 3-methylpyridine obtained as function of PTF with catalyst 2-a and method 2 (result of a single scan). Coloured circles used to highlight the ^{13}C resonances

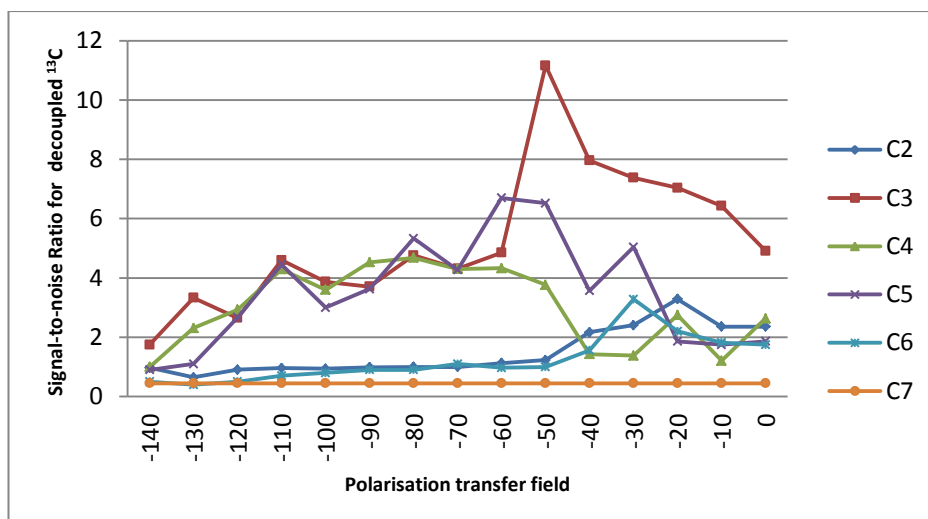


Figure 3.34 3-methylpyridine ¹³C NMR signal-to-noise ratios, obtained on the flow system using 2-a and standard conditions

3.8.3. 4-methylpyridine

4-methylpyridine was also studied. This substrate is symmetrical and should yield just three enhanced signals. It is also a precursor to synthesising 4-cyanopyridine, which in turn is a precursor to a variety of antituberculosis drug compounds such as isoniazid.

Figure 3.35 shows corresponding ^1H NMR data, whilst Figure 3.36 and Figure 3.37 illustrate the PTF effect, and Figure 3.38 and Figure 3.39 explore temperature.

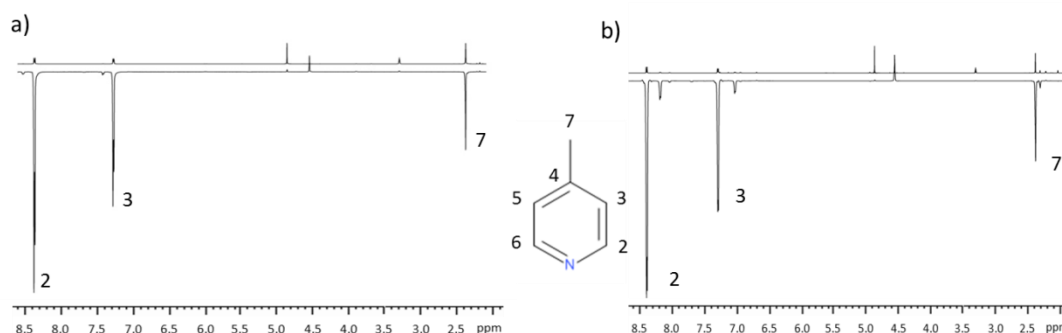


Figure 3.35 Observed ^1H NMR spectra of 4-methylpyridine, thermal trace is represented on top, and the polarised trace on the bottom; PTF undertaken at 65 G with a) catalyst 2-a and b) catalyst 2-b

The enhancement levels are summarised in Table 3.6. Under a PTF of 65 G each catalyst produces emission type magnetisation for all resonances, and produces the greatest enhancement level, although the position 3 (*meta*) proton, when used with catalyst 2-a, produces a greater level of enhancement at a PTF of 0.5 G than that produced at 65 G.

Substrate	Catalyst	Field	^1H NMR enhancements for substrate positions:					
			2	3	4	5	6	7
4-methylpyridine	2-a	0.5 G	-47.1	4.83	-	-	-	5.35
		65 G	-42.8	-26.2	-	-	-	-4.69
	2-b	0.5 G	-40.3	-1.79	-	-	-	2.83
		65 G	-192.3	-98.2	-	-	-	-30.9

Table 3.6 Comparison of the ^1H NMR polarisation enhancement data for 4-methylpyridine using catalysts 2-a and 2-b

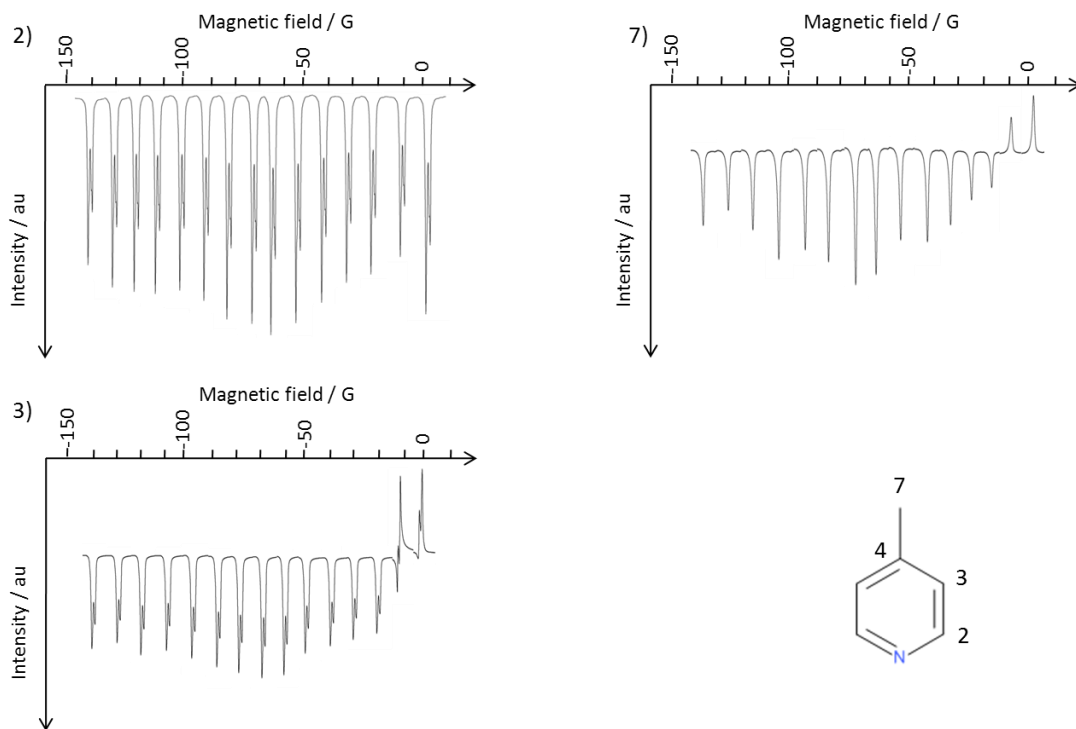


Figure 3.36 Observed ^1H NMR signal intensity for 4-methylpyridine resonances as an effect of changing polarisation transfer field using 2-a and method 2

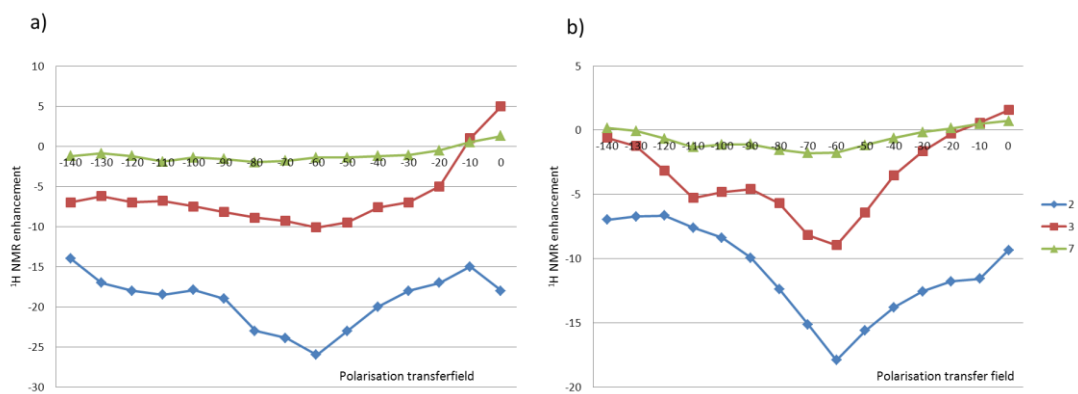


Figure 3.37 Graphical representation of the observed 4-methylpyridine ^1H NMR signal enhancement field profile using the activated catalyst a) 2-a and b) 2-b at 293 K

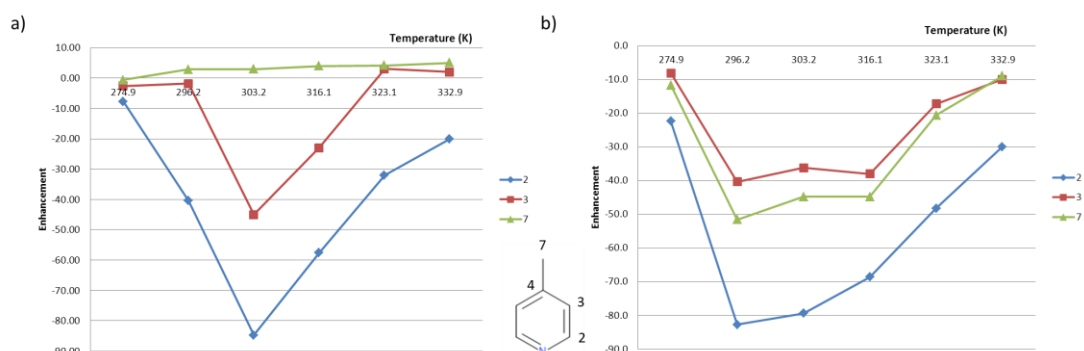


Figure 3.38 Graphical representation of ^1H NMR signal enhancements to 4-methylpyridine resonances obtained using activated catalyst **2-a** as a function of temperature measured at a) 0.5 G and b) 65 G

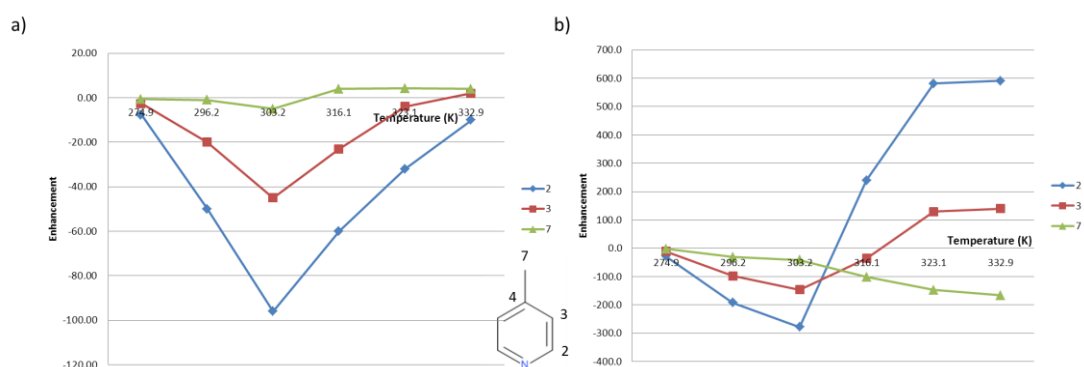


Figure 3.39 Graphical representation of ^1H NMR signal enhancements to 4-methylpyridine resonances obtained using activated catalyst **2-b** as a function of temperature measured at a) 0.5 G and b) 65 G

Comparison with 3-methylpyridine reveals:

- PTF variation is much reduced with good polarisation between -140 to -30 G.
- Complex antiphase character seen between 0.5 to -20 G.
- PTF of 0.5 G optimal at 303 K with catalyst **2-a** or **2-b**.
- PTF of 65 G optimal at 296 K with catalyst **2-a** and 332 K for **2-b**.
- Catalyst **2-b** at a PTF of 65 G and at a temperature of 332 K produced the optimal methyl enhancement level of -167-fold.

Interestingly, the total enhancement level for 3-methylpyridine was -738-fold, while for 4-methylpyridine it is -1643. These were both achieved using catalyst **2-b** when studying the temperature as a function of polarisation transfer and at room temperatures of 303 K and 332 K respectively. The total enhancement (absolute) for each substrate can be calculated by simply adding the enhancement level for each proton resonance (4-methylpyridine = $(2 \times 591) + (2 \times 147) + (167) = 1643$).

When operating at room temperature for the polarisation of 3-methylpyridine and 4-methylpyridine, **2-b** produces total enhancement levels of -385-fold and -613-fold respectively.

3.8.3.1. Effect of polarisation to ^{13}C nuclei

For 4-methylpyridine, it proved difficult to obtain any ^{13}C NMR spectra using the flow system and was only achievable for catalyst **2-a** via method 1, these data can be seen in Figure 3.40

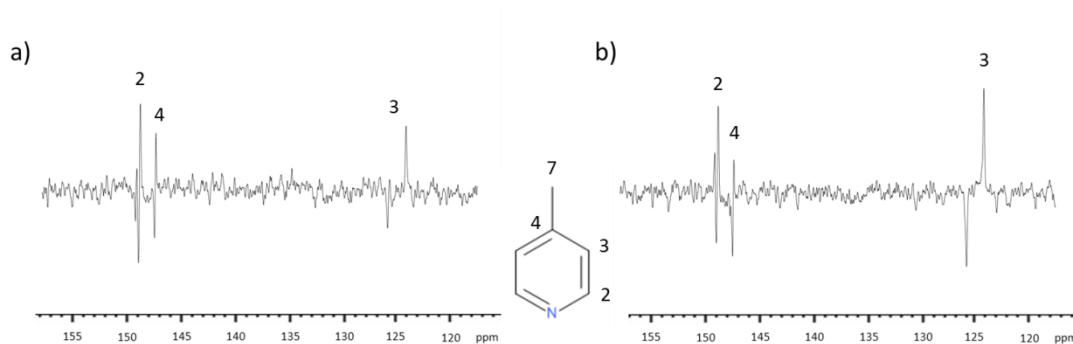


Figure 3.40 Observed $^{13}\text{C}\{^1\text{H}\}$ NMR signal intensity for 4-methylpyridine using catalyst **2-a** and method **1** at a field of a) 0.5 G b) 65 G

Analysis of these data shown in these NMR spectra revealed there to be very similar levels of polarisation transfer to the carbon positions of 3-methylpyridine. Position 2 achieved a slightly better signal-to-noise ratio of 7.81 after transfer at a field of 65 G when compared to 7.79 at 0.5 G. The same situation also held true for position 3 with the corresponding signal-to-noise ratios being 9.40 and 5.76 respectively. However, position 4 performed more efficiently at a field of 0.5 G with a signal-to-noise ratio of 5.12 rather than 3.02.

3.8.4. Nicotinamide

Nicotinamide has been used regularly within the Duckett group as it is a biologically relevant substrate, with importance in a clinical setting as it is used as chemo-and-radio sensitizer for cancer therapy¹⁵⁴, and there is evidence of it restoring cognitive deficits in Alzheimer's patients¹⁵⁵. It was first reported by Adams *et al.* 2009⁹² for its use in a SABRE experiment. In this paper, the catalyst used was $[\text{Ir}(\text{COD})(\text{PCy}_3)\text{BF}_4]$ (where PCy_3 = tricyclohexylphosphine), more recently Mewis *et al.* 2014¹⁵⁶ has exemplified nicotinamide using catalyst **2-c**, optimising conditions for use with the flow system (method 2). This section will determine whether catalysts **2-a** and **2-b** are more efficient at transferring polarisation to this substrate.

3.8.4.1. Observable ^1H NMR spectra using method 1

Typical ^1H NMR spectra for hyperpolarised nicotinamide samples produced by **2-a** and **2-b** can be seen Figure 3.41. A summary of the resulting polarisation enhancement results are presented in

Table 3.7.

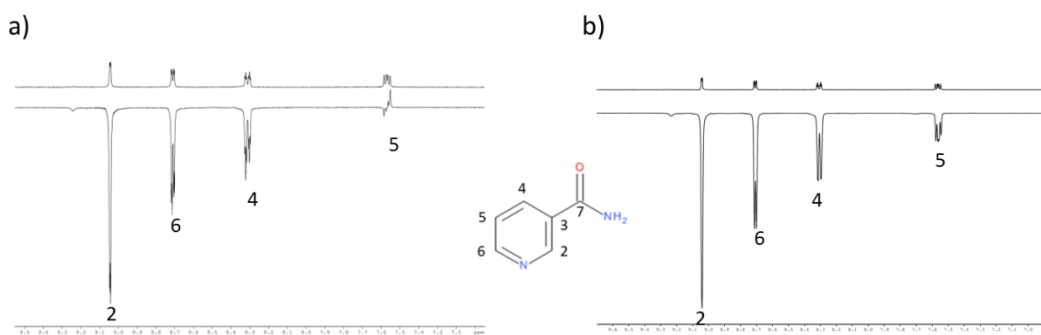


Figure 3.41 Observed ^1H NMR spectra of 3-methylpyridine, thermal trace is represented on top, and the polarised trace on the bottom; PT undertaken at 65 G with a) catalyst **2-a** and b) catalyst **2-b**

When comparing the results obtained using active catalyst **2-a**, **2-b** and **2-c** it can be seen:

- The same type of magnetisation is created for each of the ^1H proton signals.
- Positions 2 and 4 produce emission signals but position 5 produces an absorption signal under PTF at 0.5 G.
- Under a PTF of 65 G, each catalyst produces emission type magnetisation for all three resonances.

The results presented here show that catalyst **2-b**, at a transfer field of 65 G, is more efficient at polarisation transfer into the ^1H NMR resonances of nicotinamide when compared to **2-a**. The maximum polarisation transfer level was achieved for position 2 at -139.6-fold, which is better than that of any other position studied to date. Adams *et al.*⁹² quoted a total enhancement level of -345 which, if done in the same way for **2-b**, would reflect a -352-fold ^1H signal enhancement.

Substrate	Catalyst	Field	^1H NMR enhancements for substrate positions:					
			2	3	4	5	6	Total
Nicotinamide	2-a	0.5 G	-3.01	-	-1.01	3.10	-1.41	8.53
		65 G	-8.29	-	-4.12	-0.15	-6.12	18.58
	2-b	0.5 G	-48.4	-	-25.5	-16.8	-28.4	119.1
		65 G	-139.6	-	-82.4	-29.9	-100.5	352.4
	2-c	0.5 G	-44.1	-	-20.1	-16.1	-26.1	106.4
		65 G	-150.1	-	-107.1	-19.1	-110.3	386.6

Table 3.7 A comparison of the ^1H NMR polarisation enhancement for nicotinamide using catalysts **2-a** and **2-b**. Mewis *et al.*¹⁵⁶ did not present any results using method 1, so a series of appropriate experiments were completed and these data added to Table 3.7. It can be seen that catalyst **2-b** performs better at a polarisation field of 0.5 G, but **2-c** performs better at 65 G. Catalyst **2-c** gives a total ^1H NMR enhancement of 386, which is better than that of any other catalyst previously studied. The catalyst activity order is therefore: **2-c** > **2-b** > **PCy₃** > **2-a**; the total enhancements are 386, 352, 345 and 18.58 respectively.

3.8.4.2. Effect of changing magnetic field of polarisation

The polarisation field plot obtained for the nicotinamide sample using catalyst **2-a** can be seen in Figure 3.42, and a graphical representation can be seen in Figure 3.43. The experiment revealed the maximum polarisation transfer field to be 60 G for positions 2, 6 and 4 with enhancement factor of 8.2, 6.1 and 4.7 respectively. The maximum for position 5 was found to be at a field of 0.5 G (Earth's field) with enhancement factor of 3.1. The same finding was found for catalyst **2-b** and this is also consistent with the work carried out by Mewis *et al.*¹⁵⁶ with **2-c**. The order of catalyst activity based on method 2 would therefore be **2-c** > **2-b** > **2-a**, the same order as observed when using method 1.

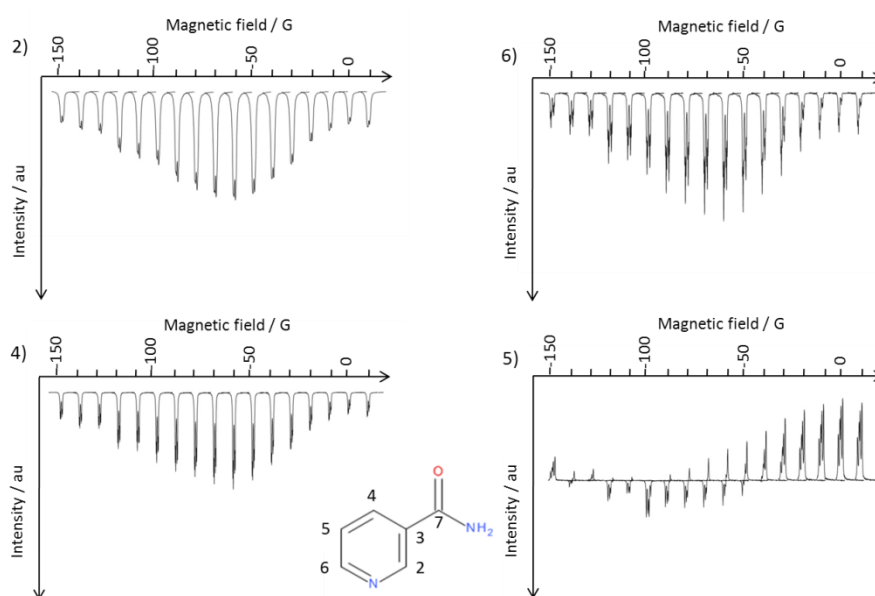


Figure 3.42 Observed ¹H NMR signal intensity changes for nicotinamide resonances, as a function of the PTF using catalyst 2-c and method 2

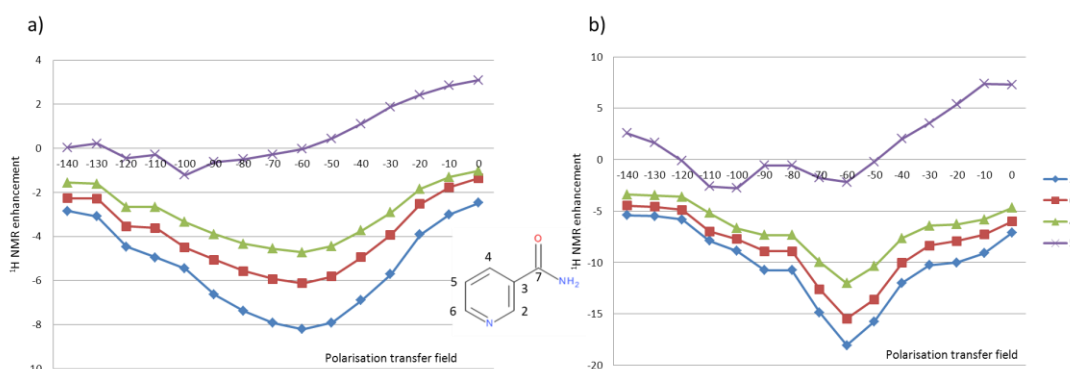


Figure 3.43 Graphical representation of the observed nicotinamide ¹H NMR signal enhancement field profile using the activated catalyst a) 2-a and b) 2-b

In comparison to the work presented for **2-c** in the literature¹⁵⁶ (Figure 3.44), the polarisation field profile for positions 2, 6 and 4 (Figure 3.44 A, B and C) are very similar. They all start in negative amplitude and gradually reach maximum polarisation transfer at 60 G before slowly declining at higher field. Position 5 exhibits the same type of behaviour for all three catalysts, yielding a positive signal amplitude at 0 G. It was noticeable when undertaking the present work for **2-c** that an antiphase signal is seen at 50 G. When **2-c** is compared to **2-a** and **2-b**, the antiphase signal remains for the next 5 and 4 gauss increments respectively before a perfect in-phase negative amplitude signal is again seen. All three catalysts then return back to positive amplitude at a field of 130 G.

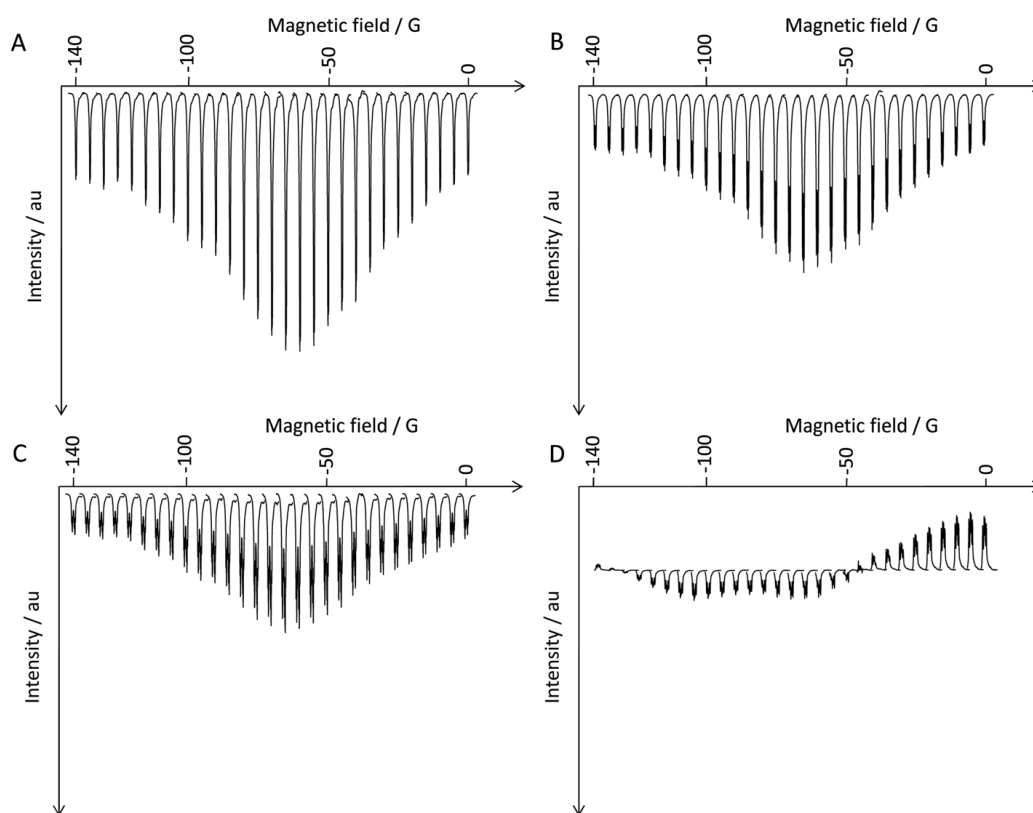


Figure 3.44 Plots of polarisation transfer field for hyperpolarised ^1H NMR signal for nicotinamide reported by Mewis *et al.* 2014¹⁵⁶

3.8.4.3. Effect of changing temperature

The effect of changing the temperature on nicotinamide SABRE is illustrated in Figure 3.45 and Figure 3.46. The activity of **2-a** at PTF of 0.5 G and 65 G, reaches a maximum for all resonances at 296 K. Also for **2-a**, the observed resonances intensities for each position show similar behaviour as temperature changes. For example at PTF of 0.5 G, they all increase up to 296 K, they all fall at 303 K before plateauing at 316 K, and then declining at higher temperatures. A similar behaviour is noted at a PTF of 65 G.

At a PTF of 0.5 G, the activity of **2-b** for nicotinamide resonances 2, 4 and 6, increases with increase in temperature up to 316 K, where it reaches its maximum, before declining at higher temperatures. The 5 position reaches a maximum signal enhancement at 333 K. At a PTF of 65 G, the activity **2-b** increases with increase in temperature reaching a maximum absolute level of 985-fold at 333 K. Furthermore, the activity of catalyst **2-b** surpasses that of **2-a** and **2-c** at higher temperatures.

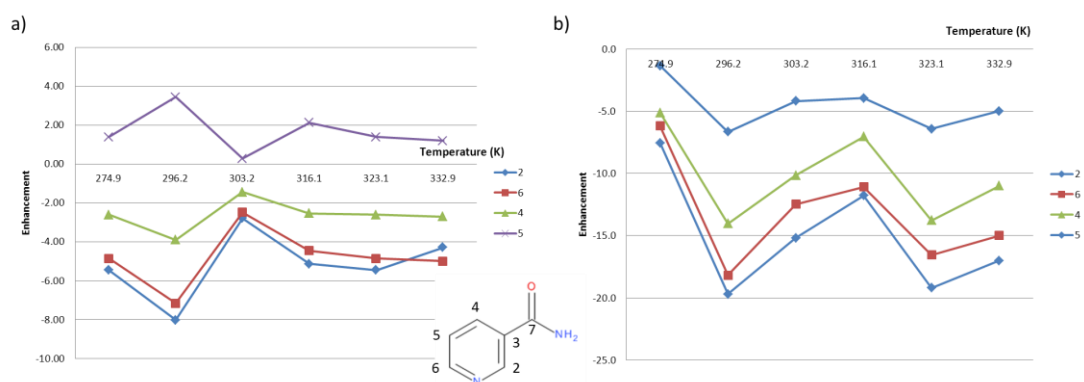


Figure 3.45 Graphical representation of the ^1H NMR signal enhancements seen for nicotinamide using catalyst **2-a** as a function of temperature at a PTF of a) 0.5 G and b) 65 G

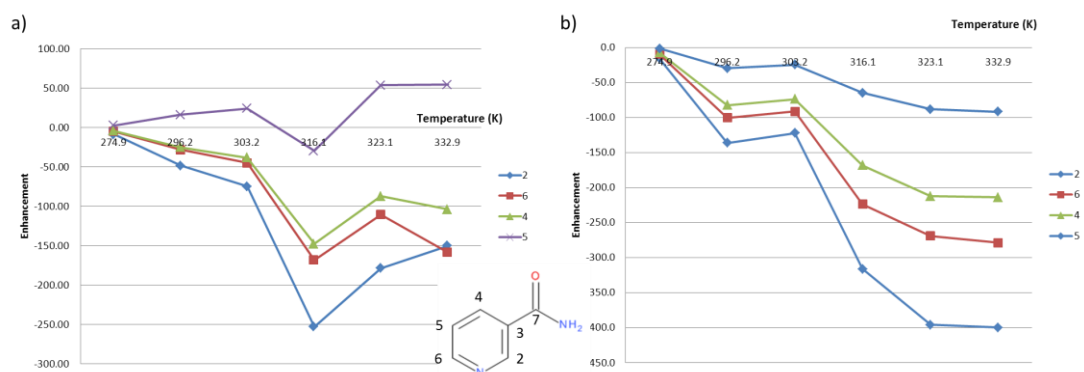


Figure 3.46 Graphical representation of the ^1H NMR signal enhancements seen for nicotinamide using catalyst **2-b** as a function of temperature at a PTF of a) 0.5 G and b) 65 G

3.9. Summary

The aim of this chapter was to use NMR as a tool, to identify and characterise a range of substrates using SABRE. The key points within this research was to be able to demonstrate that it was possible to see all of the substrates ^1H , ^{13}C NMR resonances, with a resolution that enables peak multiplicity to be attributed. The corresponding ^1H measurements showed very good levels of SABRE, while ^{13}C measurements have revealed that both I_z and higher order terms were created. Given that in normal practice such spectra are decoupled, it is desirable that the I_z character yielded by SABRE is maximised. This proved to be achieved using a PTF of ≈ 80 G in these materials. Catalyst **2-a**, has also proven to show good activity and might therefore reflect a sensible alternative to **2-c**.

This chapter reports an investigation into the effect of temperature and PTF on the level of SABRE delivered through catalysts **2-a** and **2-b** with a range of substrates. It has been shown that **2-a** and **2-b** react with *para*hydrogen in the presence of an array of pyridine type ligands to produce a series of SABRE-active catalysts. The performance of both complexes was affected by the PTF and the reactions temperature. The five ligands employed here were all optimally examined in the ^1H domain after polarisation transfer at between 60 and 70 G with **2-a**, **2-b** and **2-c**. The total signal enhancements produced in the detailed experiments are summarised in Table 3.8. It is clear from this information that of pyridine were to be examined, **2-c** should be chosen as the catalyst. However, upon extending the range of substrates, **2-b** proved to exhibit better performance, especially for the listed the methyl derivatives. Care must therefore be taken if only small amounts of material are available for examination since under these conditions an optimised catalyst should be employed.

Substrate	Total Enhancement / Catalyst		
	2-a	2-b	2-c
Pyridine	459	401	480
3-methylpyridine (methyl group)	156 -9	409 -23	102 -7
4-methylpyridine (methyl group)	142 -5	612 -31	185 -9
nicotinamide	19	352	387

Table 3.8 Total enhancements for pyridine, 3-methylpyridine, 4-methylpyridine and nicotinamide obtained at room temperature and at a PTF of 65 G.

For 2-a, the ligand exchange dynamics for pyridine, 3-methylpyridine, 4-methylpyridine and nicotinamide are commensurate with good activity at room temperature. For 2-b, warming is required to achieve most effective results. The enhancement levels are summarised in Table 3.9 with **2-b** surpassing the other two catalyst, with the optimum conditions being performed at higher temperature. Catalyst, **2-b** should be used at 332 K in any screen if good signal to noise is required. However, as the catalyst activation timescale is now 24-48 hours a more robust activation protocol needs to be developed.

Substrate	Total Enhancement / Catalyst / Temperature		
	2-a / Temp (K)	2-b / Temp (K)	2-c / Temp (K)
Pyridine	459 @ 294	780 @ 332	504 @ 296
3-methylpyridine (methyl group)	269 @ 269 -13	739 @ 303 -47	110* @ 300 -13
4-methylpyridine (methyl group)	295 @ 296 -52	1643 @ 332 -167	190* @ 300 -16
nicotinamide	59 @ 296	985 @ 332	390* @ 300

Table 3.9 Total enhancements for pyridine, 3-methylpyridine, 4-methylpyridine and nicotinamide obtained at the optimal temperature and at a PTF of 65 G.

The change in temperature reflected in these studies speeds up ligand exchange in all systems, so acting to reduce the contact time of the hydrides and substrate on the metal centre of the PTC. It is clear that all of these complexes are too stable from optimal activity at room temperature.

If we consider the effect of the methyl group, the substrate 4-methylpyridine provides the greatest level of signal enhancement was achieved by all three catalysts. The optimum was achieved using **2-b** giving a 167-fold signal enhancement obtained at a PTF 65 G and at 332 K. The order of catalyst activity for investigating the methyl group is **2-b** > **2-a** > **2-c**. This is surprising given the fact that the complex should be more stable and hence undergo slower ligand exchange. It has recently been reported that the T_1 of the bound substrate may reflect another critical factor in controlling the efficiency of SABRE. I would suggest that a further study using 4-methylpyridine might be undertaken to probe this effect in the future.

While the temperature can improve the enhancement factor to 1643-fold for 4-methylpyridine it is easier to undertaken investigations at room temperature. The

significance of just a 100-fold enhancement, with the signal-to-noise being proportional to the square root of number of scans, under standard conditions is high. It would now require 10,000 scans to obtain a similar spectrum to this 1 second acquisition. If the sample has to fully relax for a period of $5 \times T_1$ (12 seconds) then each scan would take 60 s. This means a comparable acquisition would be $60 \times 10,000 = 600,000$ seconds, which is 7 days. SABRE has therefore proven to be an excellent tool, yielding obtaining good quality data which in essence would take weeks to normally achieve.

4. Chapter 4 Optimisation of the SABRE Effect for 5-methyl pyrimidine and quinazoline.

4.1. Introduction

In the future, one of the potential applications of the SABRE technique lies in the field of MRI, where it should aid in the detection of biological substrates that play a clinical role. However, there are some major obstacles that remain before this can be achieved. These will require the development of methods to produce signal contrast, high resolution and readout with good signal-to-noise⁴⁵. For *in-vivo* measurement, a further challenge is associated with the lifetime of the ¹H hyperpolarised signal that is to be detected. This is affected by the relaxation of the proton spin states, referred to as T₁ relaxation. It is also important to consider the other possible factors as outlined in Chapter 3, such as catalyst, field, temperature and more recently, concentration. There have been many reports in the literature which detect ¹³C and ¹⁵N nuclei in a hyperpolarised image as the T₁ relaxation of these nuclei is much less efficient, but their natural abundance is much less than that of ¹H^{92, 157, 158}.

The previous chapters of this thesis have described studies on a series of mono-substituted pyridine probes. In this chapter, the molecule 5-methylpyrimidine which contains two nitrogen atoms within the aromatic ring is examined, amongst 13 other substrates. One chemical change that will be considered alongside these SABRE studies is that of deuteration. Literature reports have described how pyridine can become deuterated with these types of catalyst. If this process is rapid, it will affect the polarisation enhancement levels than can be produced¹⁵⁹.

This chapter will aim to optimise SABRE for 5-methylpyrimidine by examining the influence of catalyst, PTF, temperature and concentration, and will be investigated in high field NMR and by low field MRI. Table 4.1 and Figure 4.1 detail the structures and polarisation levels achieved across the range of materials that were examined.

4.1.1. Screening a large range of substrates to be used with SABRE.

Before deciding to optimise 5-methylpyrimidine, a range of substrates were screened with catalyst 2-c for SABRE activity, the results of these studies can be seen in Figure 4.1 and the corresponding enhancement levels at the optimum PTF summarised in Table 4.1. The corresponding ^1H NMR spectra for these substrates can be found in the Experimental Section. Even though the substrates imidazole and pyrazole show good levels of polarisation they were not chosen for further optimisation as their proton relaxation times are shorter than that of 5-methylpyrimidine.

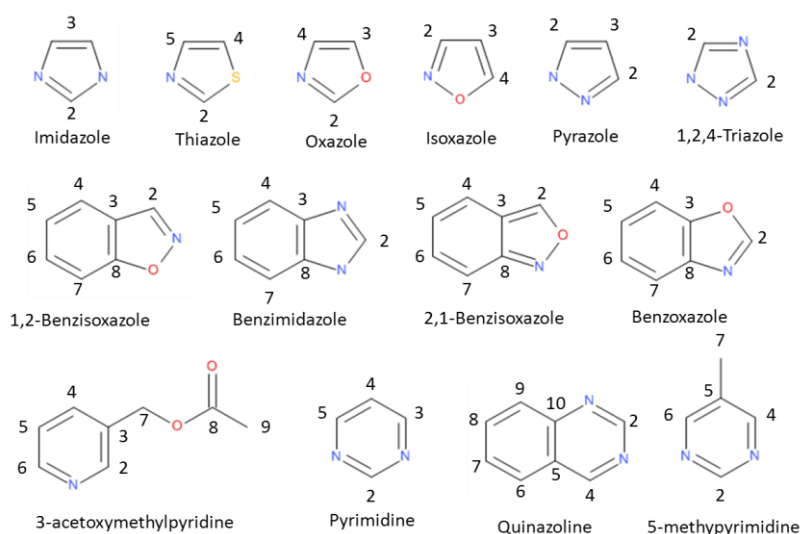


Figure 4.1 Range of substrates screen using catalyst 2-c to test the activity in a SABRE measurement

Substrate	Field / G	Proton Position / Enhancement							
		2	3	4	5	6	7	8	9
Imidazole	65	-198	-124	-	-	-	-	-	-
Thiazole	60	-100	-67	-56	-	-	-	-	-
Oxazole	65	-150	-149	-120	-	-	-	-	-
Isoxazole	60	-67	-53	-64	-	-	-	-	-
Pyrazole	50	-137	-200	-	-	-	-	-	-
1,2,4-triazole	60	-2.9	-	-	-	-	-	-	-
1,2-benzisoxazole	0	0	-	0	0	0	0	-	-
Benzimidazole	60	-48	-	-90	30	-	-	-	-
2,1-benzisoxazole	0	0	-	0	0	0	0	-	-
Benzoxazole		-58	-	-130	-57	-57	-89	-	-
3-acetoxymethylpyridine	60	-47	-	-46	-73	-77	3	-	-2
Pyrimidine	60	-58	-115	-49	-	-	-	-	-
Quinazoline	65	-61	-	-74	-	-110	-97	-86	-94
5-methylpyrimidine	50	-200	-	-200	-	-	-55	-	-

Table 4.1 Enhancement levels of substrates investigated with catalyst 2-c for SABRE, quoted as measured at the optimum PTF

The studies on quinazoline and 5-methylpyrimidine revealed some interesting behaviour which is discussed in more detail.

4.2. SABRE with 5-methylpyrimidine

4.2.1. Initial polarisation studies of 5-methylpyrimidine

To determine the most efficient SABRE catalyst for use with 5-methylpyrimidine, catalysts **2-a**, **2-b** and **2-c** were studied using method 1. Typical ^1H NMR spectra can be seen in Figure 4.2 and the associated signal enhancement levels are summarised in

Table 4.2. While all three catalysts polarise 5-methylpyrimidine, their catalytic activity follows the order **2-c** > **2-b** > **2-a**. They all produce emission type spectra at fields of 0.5 G and 65 G. The thermal ^1H NMR spectra recorded after activation produce only a single hydride resonance, which in the case of **x** appears -22.67 ppm. This indicates that the active complex $[\text{Ir}(\text{H}_2)(\text{NHC})(\text{substrate})_3]\text{Cl}$ (**5-c**) is formed in each case. Characterisation data for **5-c** are presented in the experimental section 7.4.

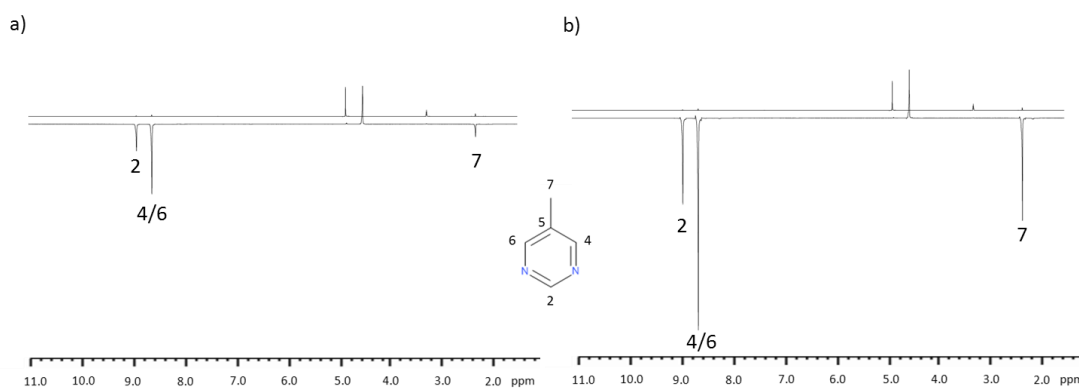


Figure 4.2 Observed ^1H NMR spectra of 5-methylpyrimidine after SABRE, detailing positions 2, 4 and 7, in conjunction with catalyst **2-c**. The corresponding thermal NMR spectra are presented on top and polarised NMR spectra on the bottom; a) at a PTF of 0.5 G and b) at a PTF of 65 G

Catalyst	¹ H Signal Enhancements 0.5 G			¹ H Signal Enhancements 65 G		
	2	4/6	7	2	4/6	7
ImMe ₂ NPri ₂ (2-a)	-10.5	-8.7	-2.8	-50.8	-60.4	-15.8
BzIMes (2-b)	-14.7	-21.5	-5.4	-60.8	-61.5	-25.1
IMes (2-c)	-40.67	-41.8	-7.2	-200.6	-198.5	-60.5

Table 4.2 Comparison of the levels of ¹H NMR signal enhancement observed for 5-methylpyrimidine using catalysts 2-a, 2-b and 2-c according to the shake method

Considering the long activation periods of greater than 48 hours needed for catalysts **2-a** and **2-b** for 5-methylpyrimidine, and the relative poor performance for SABRE at room temperature, the optimisation of 5-methylpyrimidine was completed with catalyst **2-c**.

Using catalyst **2-c**, the rate constant and thermodynamic parameters for ligand exchange, can be determined using a 1D NOESY method, as shown in Table 4.3. The raw data can be found in section 7.1.5.

Hydride Exchange			
Rate Constant / s ⁻¹ (300 K)	ΔH [‡] / kJ mol ⁻¹	ΔS [‡] / JK ⁻¹ mol ⁻¹	ΔG ₃₀₀ [‡] / kJ mol ⁻¹
5.4 ± 0.2	86.2 ± 2.3	62.4 ± 8.1	67.5 ± 0.09
5-methylpyrimidine Exchange			
Rate Constant / s ⁻¹ (300 K)	ΔH [‡] / kJ mol ⁻¹	ΔS [‡] / JK ⁻¹ mol ⁻¹	ΔG ₃₀₀ [‡] / kJ mol ⁻¹
1.85 ± 0.1	60.3 ± 0.9	33.2 ± 3.1	70.2 ± 0.05

Table 4.3 Activation parameters for the loss of 5-methylpyrimidine ligand and loss of hydride ligand when catalyst 2-c precursors are used

The rate of 5-methylpyrimidine ligand loss is 1.85 s⁻¹ at 300 K and lower than that reported for **2-c** with pyridine. This slow exchange accounts for the weak SABRE effect. Given the pK_a of 5-methylpyrimidine (9.45) and that of pyridine (5.25), a stronger iridium-nitrogen bond is expected for **2-c** and 5-methylpyrimidine. These data support this deduction.

When **2-c** is acting as a polarisation transfer catalyst, it does so by redistributing magnetisation at a molecular level. As mentioned previously, this is an equilibrium process, and hence might also be expected to be visible as an enhanced rate of signal relaxation. It is therefore necessary to quantify the T₁ relaxation for the proton spins of 5-

methylpyrimidine. Four experiments were carried out with catalyst **2-c** and 5-methylpyrimidine present at standard concentration and the results are outlined in Table 4.4.

5-methylpyrimidine / Site H	T ₁ Relaxation (s)		
	H (2)	H (4/6)	H (7)
Substrate/methanol/ air	7.30	7.05	4.24
Substrate/methanol/degassed	76.92	38.71	8.11
2-c /Substrate/methanol/degassed	50.46	31.30	7.59
2-c /Substrate/methanol/H ₂	22.52	20.92	6.02

Table 4.4 T₁ values for 5-methylpyrimidine resonances obtained experimentally at 298 K

It is evident from these data that the T₁'s times are affected by the presence of catalyst, air and H₂. If we consider the T₁ for H (2), it starts out at ~ 77 seconds which would be long relative to any injection time of 6-20 s¹⁶⁰ (dependent on injection site and tissue). The time taken for a signal to fall by 3 half-lives would be 163 s. This means that after injection, it could realistically be possible to measure a signal after 163 s. Hence, 5-methylpyrimidine is a potential molecular contrast agent. When **2-c** is added, there is evidence of an interaction with the catalyst because of the reduction of T₁, **2-c** is 16e⁻ and weak binding of 5-methylpyrimidine would therefore result in an 18e⁻ complex. When activated by H₂, the drop in T₁ is increased, giving a measured value of approximately 23 s. This is consistent with **5-c** acting as a SABRE catalyst. This means that 10 s bubbling in method 2 could be extended to ca. 3T₁ with the expectation that the signal strength might increase by ~12-fold, if first order behaviour is assumed. Similar results were observed for positions 2 (*ortho*), 3 (*meta*) and 4 (*para*) of pyridine¹⁵², here the corresponding T₁ values are 19.6, 14.6 and 12.6 respectively. The implication is that pyridine polarises more rapidly and that regardless of toxicity, its T₁ means it is a less suitable imaging probe than 5-methylpyrimidine.

4.2.2. Optimising 5-methylpyrimidine for SABRE with catalyst 2-c

4.2.2.1. Polarisation Transfer Field Plot

5-methylpyrimidine was then examined using method 2 in order to seek an optimum PTF value. The resulting ^1H NMR spectra are shown in Figure 4.3 and maxima are observed when a PTF value of 50 G is used. It is less sensitive to this change than pyridine in Chapter 3.

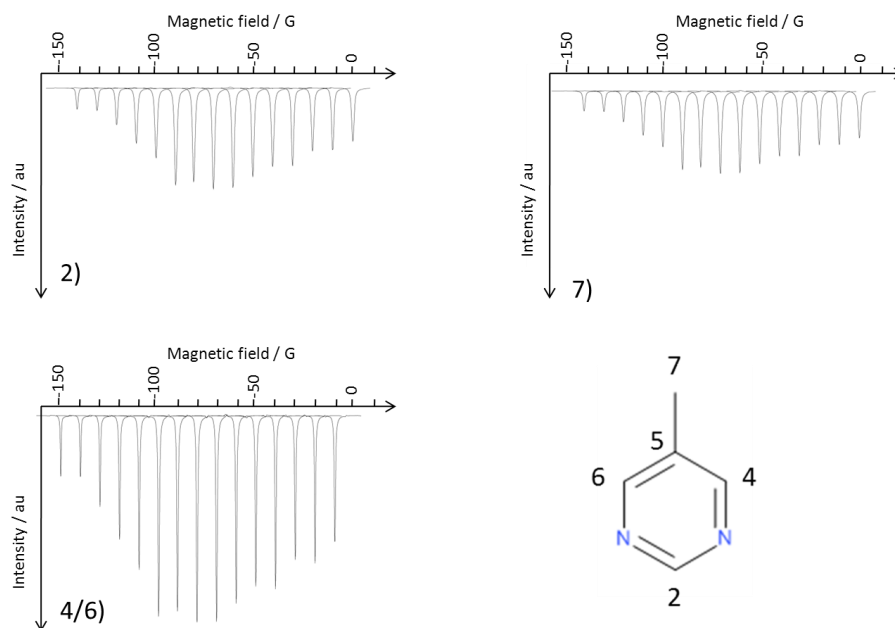


Figure 4.3 Observed ^1H NMR signal intensity field profiles for 5-methylpyrimidine resonances as a function of changing PTF, over the range 0 to -140 G, using 2-c

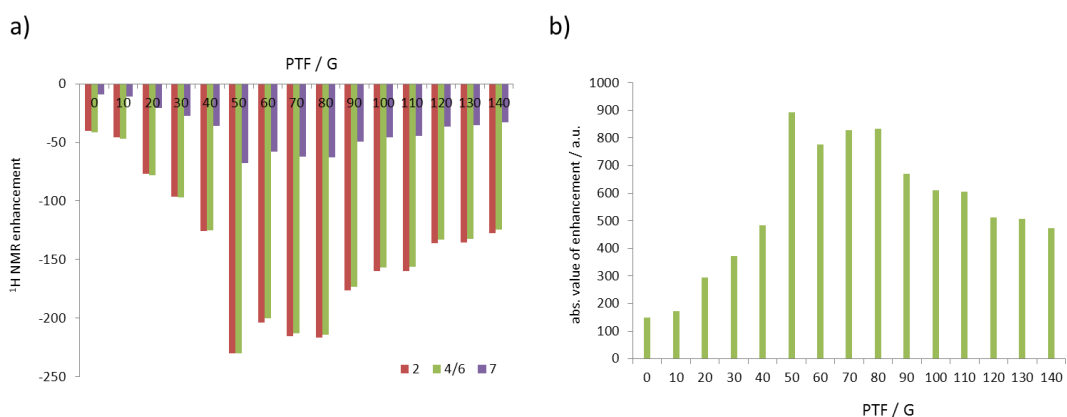


Figure 4.4 a) Graphical representation of the observed ^1H NMR signal enhancement of 5-methylpyrimidine using catalyst 2-c as a function of PTF over the range of 0 – 140 G b) total ^1H NMR signal enhancement

At this maximum, an absolute enhancement level of 892-fold is recorded (Figure 4.4). It can be seen that the ^1H NMR signals all contain emission type character under PTF values of between 0 and 140 G. Consequently, they do not contain any complicated antiphase signals as demonstrated previously in Chapter 3. This benefit is important if the technique is to be used for imaging, due to the fact that magnetisation will be cancelled due to signals containing both absorption and emission type character.

Polarisation of aliphatic groups by SABRE has received less attention than aromatic protons. It can be seen that whilst the enhancement levels are low, significant time savings are available compared to obtaining a thermal spectrum. The reason for the fall in the observed hyperpolarisation is due to the small coupling that connects the group into the aromatic spin system with $J_{\text{HH}} = 1.1 \text{ Hz}^{150}$. A polarisation enhancement of -68-fold is observed for the methyl group. When this is compared to 3-methylpyridine and 4-methylpyridine studied previously, under standard conditions and at room temperature, it is the most efficient seen for SABRE.

The effect of changing the PTF on the signal intensity of the resulting ^1H OPSYdq spectra was investigated and results are shown in Figure 4.5. It is revealed that the maximum I_{zS_z} magnetisation used for SABRE is found at a PTF of 70 G for the aromatic protons and at a PTF of 90 G for the methyl signal.

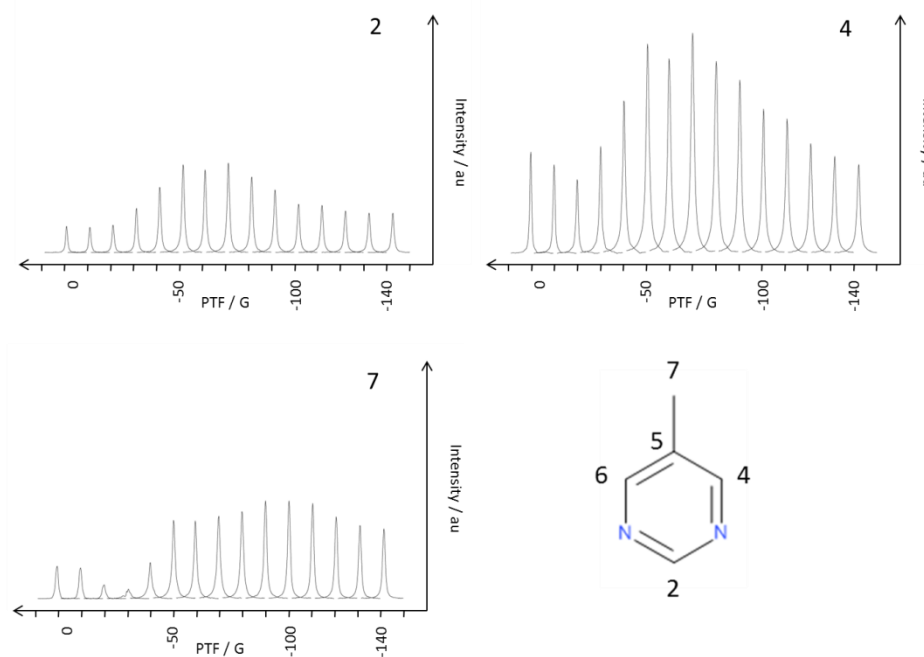


Figure 4.5 ^1H OPSYdq NMR signal intensity profiles for the 5-methylpyrimidine resonances as a function of PTF

In 2014, Fekete *et al.* reported a catalyst system which contained both NHC and phosphine ligands which acted to reduce the number of bound substrate molecules during SABRE¹⁶¹. The addition of acetonitrile- d_3 leads to the formation of $[\text{Ir}(\text{IMes})(\text{MeCN})_2(\text{PCy}_3)]\text{BF}_4$ (**7-d**) (Figure 4.16), but the more dominant product is $[\text{Ir}(\text{H})_2(\text{IMes})(\text{MeCN})(\text{Py})(\text{PCy}_3)]\text{BF}_4$ (**6-d**). This is reported as a good complex for polarisation transfer to pyridine.

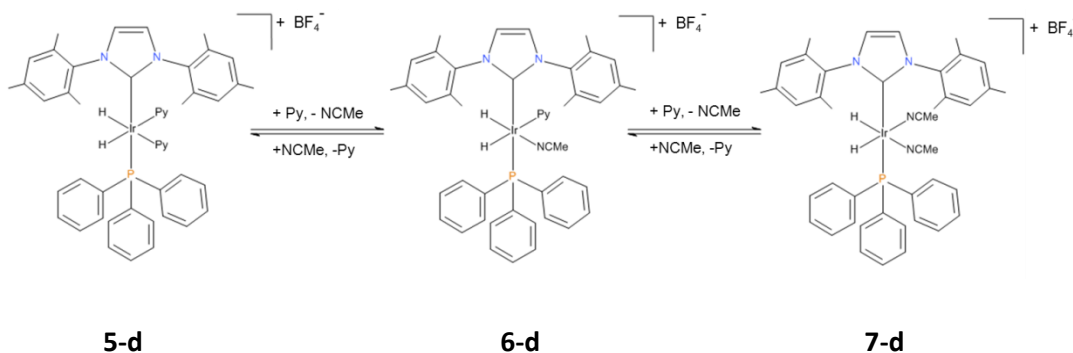


Figure 4.6 Schematic of equilibrium of complex **5-d**, with addition of pyridine and H_2 to form the more efficient complex **6-d**, reported by Fekete *et al.* 2014¹⁶¹

The effect of acetonitrile on this sample was therefore studied. A stock solution containing catalyst **2-c** (5 mM, 0.031 mmol) and 5-methylpyrimidine (100 mM, 0.062 mmol) in methanol- d_4 was made. Two aliquots of 0.6 ml were taken, with the first transferred to a J-Young's tap NMR tube (sample 1). To the second, a stoichiometric amount of acetonitrile- d_3 (1.2 μl) was added prior transfer to a similar NMR tube (sample 2). The samples were then examined using the standard procedure for method 1, out-lined in the Experimental Section 7.2.

The ^1H NMR spectra that were obtained for a hyperpolarised 5-methylpyrimidine sample, shaken at 50 G, can be seen in Figure 4.7. It has been shown that acetonitrile polarises under the same conditions¹⁶², therefore acetonitrile- d_3 is used to maximise SABRE transfer into 5-methylpyrimidine.

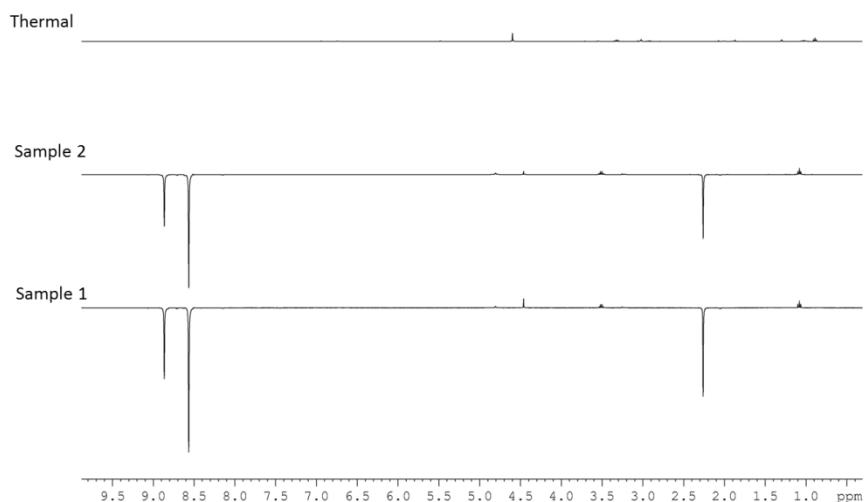


Figure 4.7 Observed ^1H NMR spectra for 5-methylpyrimidine resonances. The thermal is represented on top, polarised sample 2 containing acetonitrile in the middle and polarised sample 1 on the bottom shaken at approximately 50 G

The absolute enhancements observed for sample 1 and sample 2 are 897 and 799-fold respectively. Although there is no PPh_3 in this system, Figure 4.8 shows the ^1H NMR spectra for the hydride region of sample 2 confirms that the dominant species in this SABRE measurement is complex **6-d** with 5-methylpyrimidine and acetonitrile *trans* to the hydride, which resonate at -20.9 ppm and -22.2 ppm respectively. In this study, the addition of acetonitrile to the sample mixture does not improve the polarisation level achieved by SABRE, but more importantly it does not diminish the polarisation level. This will become important when considering catalyst loading.

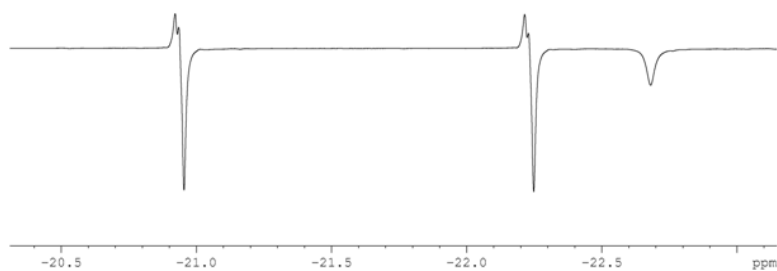


Figure 4.8 ^1H NMR spectra of the hydride region for sample 2 containing 5-methylpyrimidine and acetonitrile

4.2.2.2. Temperature

When the effect of temperature was investigated with 5-methylpyrimidine and catalyst **2-c**, the information presented in Figure 4.9 was obtained. It can be seen that optimum SABRE efficiency is observed at temperatures of 303 K and 293 K when PTFs of 0.5 G and 65 G are used respectively. The results at a PTF of 65 G are comparable to those presented earlier for the pyridine type substrates using **2-a** described in section 3.5.

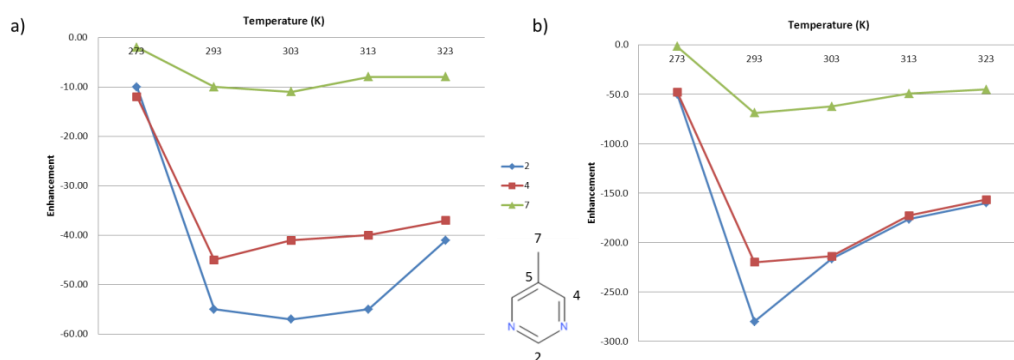


Figure 4.9 Graphical representation of the ¹H NMR signal enhancements seen for 5-methylpyrimidine using catalyst **2-c** as a function of temperature at a PTF of a) 0.5 G and b) 65 G

It can be concluded that the ligand exchange rates of Table 4.3 are optimal for 5-methylpyrimidine. This means that catalyst design cannot be undertaken without considering the impact of the substrate.

4.2.3. Concentration

In 2009, Atkinson *et al.*⁷⁹ reported on the effect of catalyst loading, where the amount of catalyst [Ir(COD)(PCy₃)(py)]BF₄ was varied to saturation point, with 20 mol % achieving the greatest observable polarisation⁷⁹. The effect of catalyst loading with **2-c** and pyridine has also been reported in a publication by Cowley *et al.*¹⁴⁹. For this system, the catalyst loading was varied from 0.1 mol % to 10 mol % and found, like the previous literature, that the higher the catalyst loading was, the higher the observed enhancement. This is represented graphically in Figure 4.10.

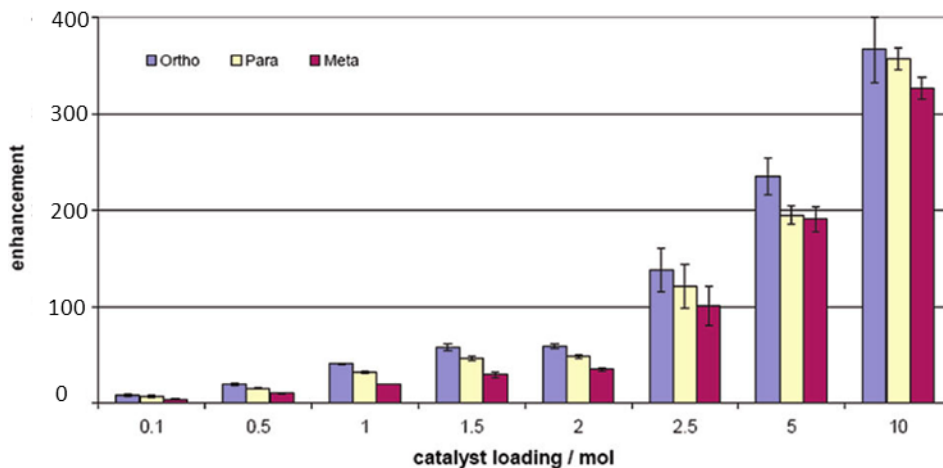


Figure 4.10 ^1H NMR enhancements obtained for catalyst loading of **2-c** as reported by Cowley *et al* 2011⁹³

Recent publications by Mewis *et al.* 2014¹⁵⁶ and Lloyd *et al.* 2012¹⁶³, have described the concentration dependence of SABRE of **2-c** with nicotinamide and quinoline respectively. The first study uses various different catalyst loadings of **2-c** and probes different spin states of nicotinamide using the OPSY pulse sequence. The second describes the detection of quinoline at 0.6 mM concentration level in both 1D and 2D NMR measurements, which equates to detecting 0.052 mg of substrate in a 600 μl sample.

Both publications mention using SABRE to observe hyperpolarisation signals in ^{13}C NMR spectroscopy. Lloyd *et al.* reports a newly developed decoupled ^{13}C INEPT pulse sequence, which was adapted for SABRE by the addition of a refocusing step. The resulting spectra for the quinoline sample can be seen in Figure 4.11 at the concentration of 0.6 mM.

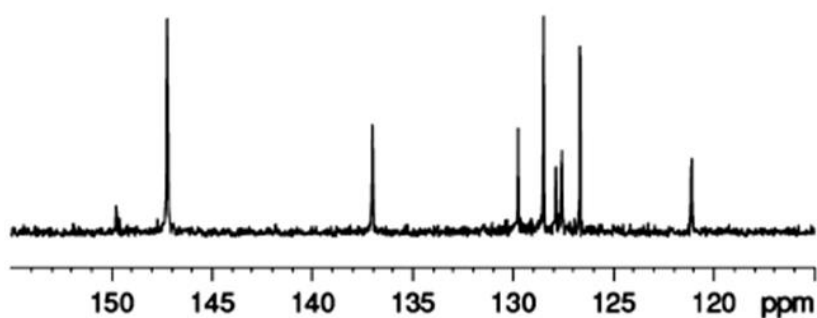


Figure 4.11 Corresponding ^{13}C NMR INEPT spectrum for a quinoline sample at a concentration of 0.6 mM¹⁶³

4.2.3.1. The effect of concentration during polarisation when the ratio of 5-methylpyrimidine to catalyst stays the same

This study was initially carried by making stock solution at concentration of; 300 mM 5-methylpyrimidine (0.186 mmol, 17.48mg) with 15 mM **2-c** (0.0093 mmol, 6 mg), where the substrate to catalyst ratio remains at the defined standard at 20:1. The samples were made by series dilution and are outlined in Table 4.5.

	Substrate to Catalyst Ratio	2-c		5-Methylpyrimidine	
		[2-c] (mM)	Mass (mg)	[5-Methyl pyrimidine] (mM)	Mass (mg)
Sample 1	20:1	15	6	300	17.5
Sample 2	20:1	12.5	5	250	14.6
Sample 3	20:1	10	4	200	11.6
Sample 4	20:1	7.5	3	150	8.75
Sample 5	20:1	5	2	100	5.83
Sample 6	20:1	2.5	1	50	2.92
Sample 7	20:1	0.5	0.2	10	0.58
Sample 8	20:1	0.05	0.02	1	0.058

Table 4.5 The amounts of **2-c** and substrate used in the corresponding concentration experiments with each made up with 0.6ml methanol-d₄

These data show that hyperpolarised signals can be obtained at very low concentration, represented in sample 8, where proton 2 produces a maximum enhancement of -134-fold. This corresponds to detecting 0.058 mg of 5-methylpyrimidine in a single scan (Figure 4.12). Sample 7 gives the best overall absolute enhancement of -1357-fold. One observation is that proton 4, generally gives the highest level of enhancement, followed by proton 2 and 7. This could start to explain the importance of proton 4 for the transfer of polarisation within the 5-methylpyrimidine molecule.

If the equipment were able to sustain 3 bars of *parahydrogen*, as indicated earlier by bubbling for longer, we might expect this to further increase the level of hyperpolarisation. This approach could be used to drop the concentration still further and increase the quality of the spectra.

	Proton Resonance / Enhancement			
	2	4	7	Total Enhancement
Sample 1	-157.4	-207.5	-54.6	736.6
Sample 2	-15.6	-97.4	-7.3	232.5
Sample 3	-123.0	-189.4	-43.5	632.5
Sample 4	-62.8	-164.2	-25.3	476.7
Sample 5	-47.1	-179.2	-31.7	500.8
Sample 6	-322.8	-36.2	-102.5	702.3
Sample 7	-297.3	-420.0	-73.1	1357
Sample 8	-134.7	-127.5	-36.3	498.9

Table 4.6 ^1H NMR signal enhancement levels of free 5-methylpyrimidine proton resonances that were obtained using concentrations listed in Table 4.5.

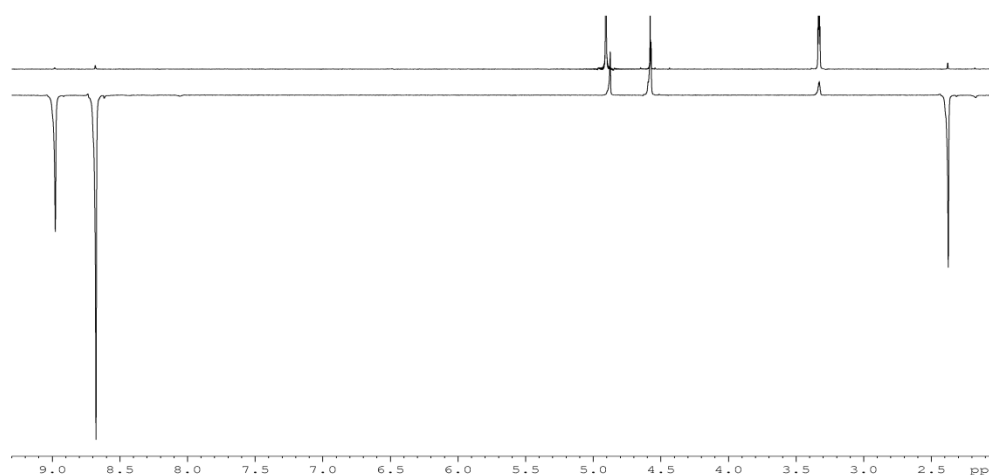


Figure 4.12 Thermal ^1H NMR spectrum of 5-methylpyrimidine (top) and a hyperpolarised spectrum of sample 8 (bottom) polarised with 2-c using shake and drop method (method 1) at 65G

It is much harder to record ^{13}C NMR spectra as the natural abundance of ^{13}C isotope is just 1.1 % of natural carbon. Figure 4.13 shows the resulting ^{13}C and ^{13}C INEPTrd spectra obtained at 0 G and 65 G respectively. These were collected in a single scan and sample 4 gave the maximum signal-to-noise ratio for each of the two spectra. These data are summarised in Table 4.7 and graphically in Figure 4.14.

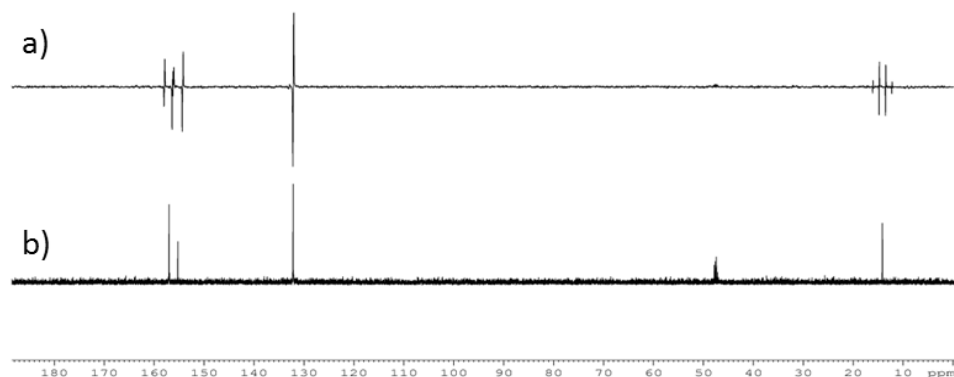


Figure 4.13 Two single scan spectra of hyperpolarised 5-methylpyrimidine with 2-c using ^{13}C (top) and ^{13}C INEPTrd NMR pulse sequence

NMR Experiment	Carbon position (signal-to-noise)			
	2	4	5	7
^{13}C	54.7	61.9	133.5	41.9
^{13}C INEPTrd	18.3	57.4	40.5	29.0

Table 4.7 Summary of signal-to-noise observed in the stated NMR experiment for sample 4 for the spectra represented in Figure 4.13

Figure 4.14 shows the graphs associated with the signal-to-noise ratio for 5-methylpyrimidine of samples 1-7 in Table 4.6. The ^{13}C measurement for sample 7 is able to detect positions 2, 4 and 5 with a signal-to-noise ratio of 2.87, 2.78 and 8.97 respectively. For the same measurement, sample 6 is the lowest concentration detectable for all four 5-methylpyrimidine carbon resonances 2, 4, 5 and 7 with good signal-to-noise ratio of 16.5, 15.7, 46.10 and 12.76. For ^{13}C INEPTrd pulse sequence the carbon resonances 2 and 4 are detectable in sample 7 with a signal-to-noise ratio of 9.94 and 19.0 respectively, but this time it is sample 5 to that is lowest concentration to be able to detect all four resonances, 2, 4, 5 and 7 with a good signal-to-noise ratio of 17.6, 9.25, 25.7 and 10.7 respectively.

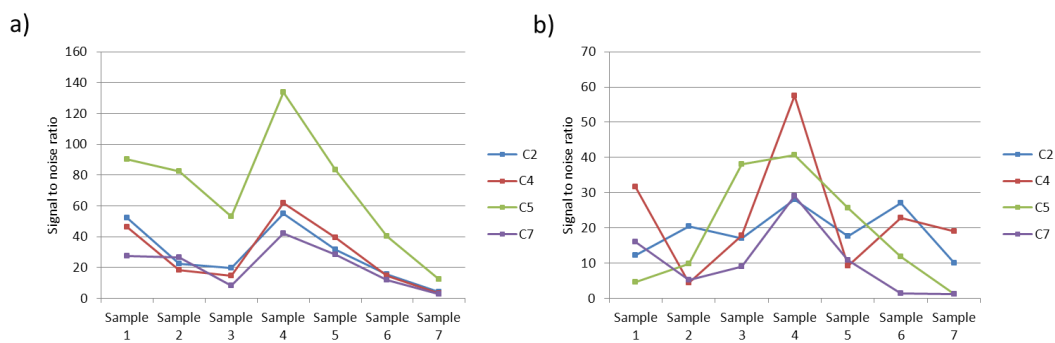


Figure 4.14 Signal-to-noise ratio graphs for sample 1-7 of Table 4.5 for the NMR measurement a) ^{13}C and b) INEPTTrd when the effect of concentration is studied and substrate to catalyst, 2-c, ratio remain constant at 20 : 1

To conclude that ^{13}C detection is possible down to 0.5 mM concentrations in a single scan. Signal averaging would drop this value even further. Interestingly, in this case, the detected resonances allow for characterisation.

4.2.3.2. The effect of concentration on polarisation transfer when the ratio of 5-methyl pyrimidine to catalyst changes.

For this concentration study, the addition of a stoichiometric amount of acetonitrile to catalyst is added to all the samples. This addition of acetonitrile becomes important when the substrate to catalyst ratio becomes less than a 3:1, as the catalyst would become unstable, degrade and therefore no longer transfer polarisation. Catalyst **2-c** (5 mM) remained constant, while varying the 5-methylpyrimidine concentration across a range of samples as outlined in Figure 4.6. These data maps onto those obtained with sample 5 in Section 4.3.3.1.

	Substrate to Catalyst Ratio	2-c		5-Methyl pyrimidine	
		[2-c] (mM)	Mass (mg)	[5-Methyl pyrimidine] (mM)	Mass (mg)
Sample 1	60:1	5	2	300	17.5
Sample 2	50:1	5	2	250	14.6
Sample 3	40:1	5	2	200	11.6
Sample 4	30:1	5	2	150	8.75
Sample 5	20:1	5	2	100	5.83
Sample 6	10:1	5	2	50	2.92
Sample 7	2:1	5	2	10	0.58

Table 4.8 The amounts of 2-c and substrate used in the corresponding concentration experiments with each made up with 0.6ml methanol- d_4

The maximum level of enhancement was achieved using a substrate to catalyst ratio of 2:1 (sample 7) which can be seen in Figure 4.15.

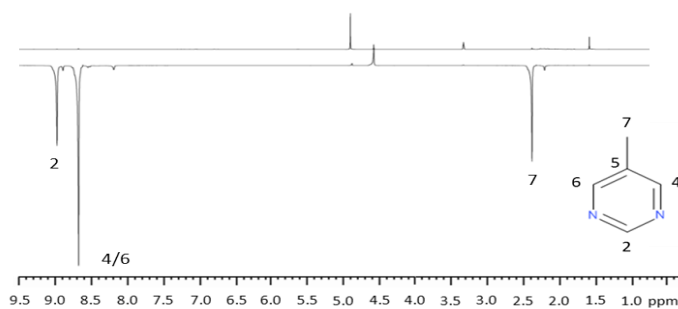


Figure 4.15 Observed ^1H NMR spectrum of 5-methylpyrimidine with thermal trace (top) and a hyperpolarised spectrum of sample 7 (bottom) with catalyst 2-c obtained at a PTF of 65G, with signal enhancements of -450, -582 and -149 respectively

	Substrate to Catalyst Ratio	Proton Resonance			
		2	4	7	Total Enhancement
Sample 1	60:1	-29.9	-36.7	-13.5	143.8
Sample 2	50:1	-81.1	-16.5	-24.7	188.2
Sample 3	40:1	-75.9	-35.64	-19.9	206.8
Sample 4	30:1	-34.0	-78.0	-0.19	190.6
Sample 5	20:1	-95.2	-254.8	-49.3	752.7
Sample 6	10:1	-893.9	-135.7	-107.4	1487
Sample 7	2:1	-450.8	-582.5	-149.2	2063

Table 4.9 ^1H NMR signal enhancement levels for 5-methylpyrimidine

These data follow the trend that has now been reported in the literature; that polarisation enhancement level increases as the catalyst loading increases^{92, 93, 152}. This is shown in graphically in Figure 4.16.

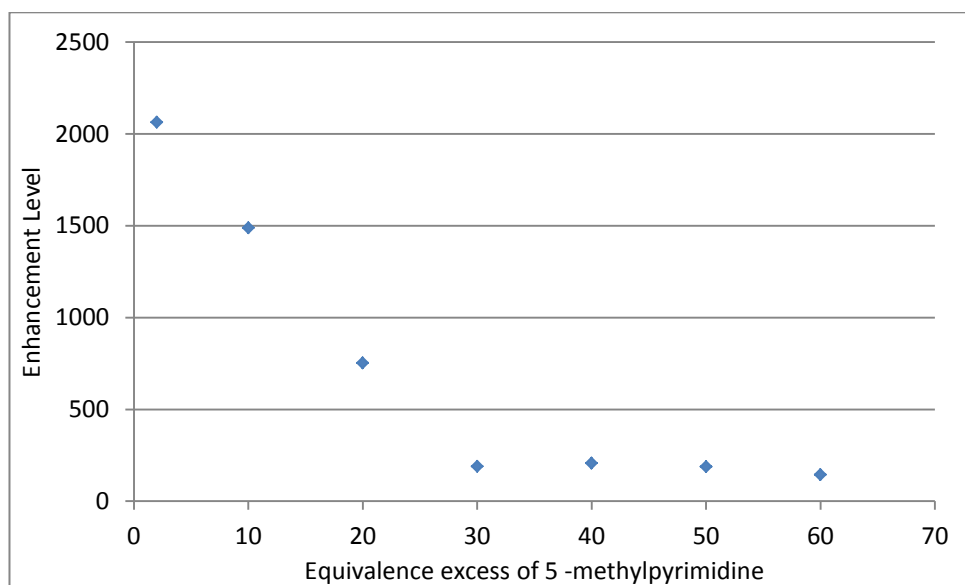


Figure 4.16 Effect of substrate to 2-c excess on the level of polarisation transfer for a metal concentration of 5 mM

A series of ^{13}C and ^{13}C INEPTrd signal-to-noise ratio spectra were then recorded. The results of this process can be viewed graphically in Figure 4.17. For the ^{13}C NMR measurement, the optimum catalyst loading ratio is 30:1. For the ^{13}C INEPTrd sequence, the signal is resonance dependent. For carbon 2 and 5, the maximum is observed with a ratio 30:1, while for carbon 4 and 7, it is at 20:1. Based on the smaller fluctuation of resonances 2 and 5, sample 2 would be chosen to run a ^{13}C INEPTrd measurement. The optimum signal-to-noise ratio for both NMR measurements are summarised in Table 4.10.

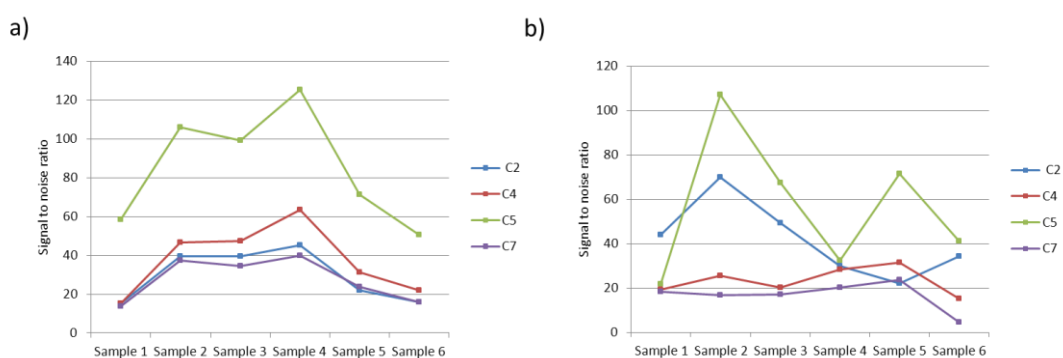


Figure 4.17 signal-to-noise ratio graphs for sample 1-7 of Table 4.5 for the NMR measurement a) ^{13}C and b) INEPTrd when the effect of concentration is studied, when catalyst 2-c concentration remains constant at 5 mM

NMR Experiment	Carbon position (SIGNAL-TO-NOISE)			
	2	4	5	7
^{13}C	45.2	63.57	125.4	39.89
^{13}C INEPTrd	69.80*	31.4 [#]	107.0*	18.59 [#]

Table 4.10 Summary of maximum signal-to-noise ratio observed the resulting NMR experiment were ^{13}C was from sample 4 and ^{13}C INEPTrd *sample 2 and [#] sample 5 taken from Figure 4.17

4.3. Imaging

There are many MRI experiments that could be used to acquire an image. High resolution images can take in the region of several hours to record, but this is not acceptable for medical applications. Instead, for contrast and angiography experiments, they consist of single shot and Echo Planar Imaging (EPI) experiments. For a SABRE experiment, time is an issue as the hyperpolarised signals decay rapidly. This makes 5-methylpyrimidine a good substrate to consider due to long relaxation of the proton signals in a ^1H NMR experiment. In this section, MRI sequences that have been employed to collect hyperpolarised images include:

- Fast Spin Echo / Rapid Acquisition with Refocused Echoes (FSE/RARE)
This consists of a spin echo being generated from a 90° r.f. pulse, followed by multiple 180° refocussing pulses, which are referred to as the echo train.
- Fast Low Angle Shot (FLASH)
This combines low flip angles ($10 - 80^\circ$) and echo gradients to produce a rapid image sequence. The higher the flip angle the greater T_1 weighting, the lower the angle the greater the T_2 weighting. This technique makes use of spoiler gradients to remove any transverse magnetisation at the end of an experiment. This type of experiment can be carried out in 20 to 30 ms, but as a result, poorer resolution can be observed.
- Fast Imaging with Steady State Precession (FISP)
This technique is used in cardiac images and angiography and is based on FLASH but uses a spoiler gradient at the end of the experiment. This sequence uses a repeat of small flip angles, which results in formation of magnetisation in the steady state.

The first published method for collecting a hyperpolarised MRI experiment was with hyperpolarised gases. The hyperpolarised states of these gases have a very short T_1 , which in turn requires a fast imaging technique. This must be ideally shorter than the T_1 so the maximum signal enhancement is observable before it decays. There have been many ways that MRI has been improved including stronger spoiler gradients, larger receiver band widths and fast imaging techniques, such as EPI, RARE, FSE or GRASE. Even still, the use of FLASH with a low flip angle is the most widely used, as this allows for many images in quick succession thus shows real-time tracking of physiological processes⁵¹.

This work was completed with help from a postdoctoral research colleague when collecting the MRI images and processing the information. This study uses the same samples which were presented for the concentration results to acquire hyperpolarised images. Prior to imaging, the samples were refreshed with three bar of *parahydrogen*, shaken at a PTF of 50-60 G and introduced into the magnet. The sample introduction differs from a conventional NMR experiment due to set up which can take considerably longer before acquisition.

Data collected in this way was processed as outlined in the Experimental. In order to estimate the signal enhancement for each solution, the average of the signal-to-noise ratio values obtained from the 5 shake-and-drop experiments was divided by the signal-to-noise ratio value extracted from the corresponding thermal images of the sample.

4.3.1. Imaging Results

A series of images have been acquired of SABRE polarised 5-methylpyrimidine. The ratio of **2-c** substrate was 20:1 and they mimic the NMR measurements in Table 4.5 of section 4.3.3.1. These MRI experiments used a RARE sequence. The resulting images are shown in Figure 4.18 of an NMR tube containing **2-c**, 5-methylpyrimidine and methanol- d_4 . A 5 mm slice was examined where the field of view (FOV) was 30 x 30 mm, and the matrix size 64 x 64. The echo time was 4 ms (TE/TR) and the total acquisition time 600 ms. A 90° pulse is employed in these measurements. A control thermal image was acquired using an 8 scan average with a long recycle time to account for the T_1 values described earlier. The results of this was that the control measurements take 7 minutes to perform whilst the hyperpolarised scan takes just 260 ms acquired using one scan.

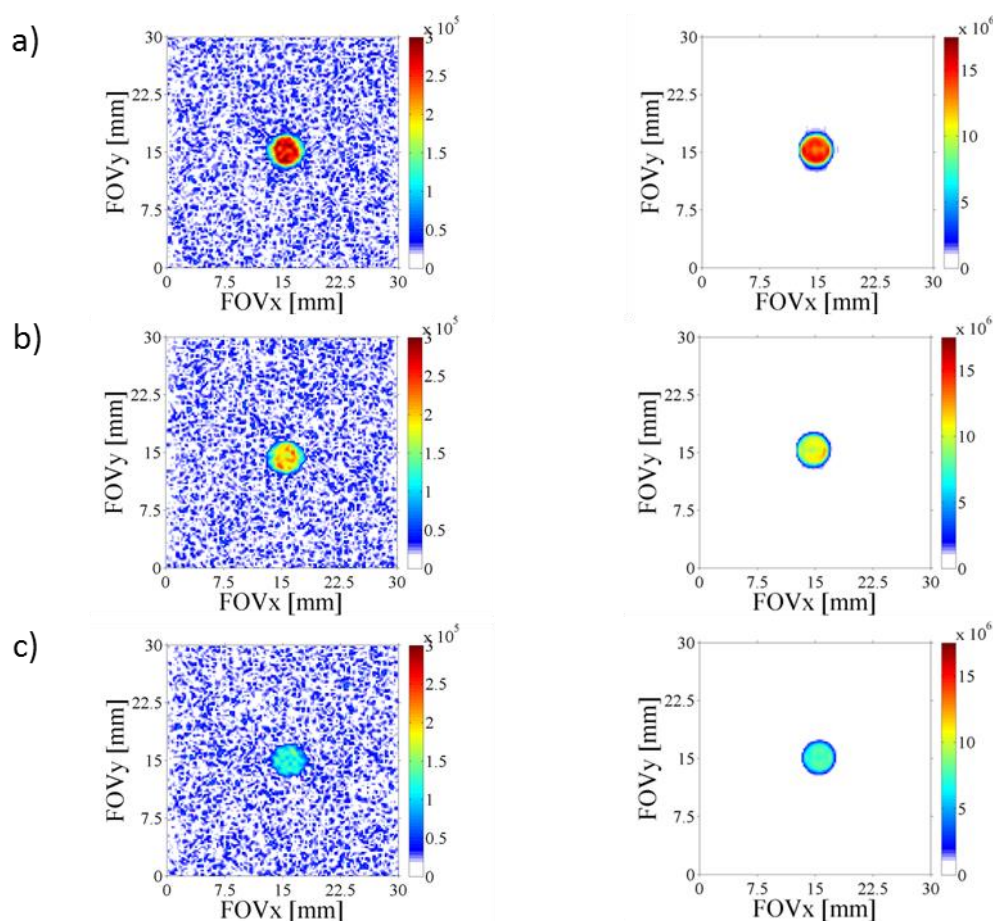


Figure 4.18 ^1H RARE MRI images for an NMR tube containing 5-methylpyrimidine and **2-c**, with the corresponding thermal images represented on the left and hyperpolarised images on the right at a PTF of 50 – 60 G with substrate ratio 20:1; the concentration of **2-c** is: a) 15 mM, b) 10 mM and c) 5 mM

The observed ^1H RARE MRI images reveal good polarisation of 5-methylpyrimidine and the signal is an order of magnitude greater when compared to the thermal image data. It is also observable that the signal-to-noise ratio has significantly increased in the hyperpolarised samples, with the images looking clearer and sharper than those of the thermal measurements. The images can be quantitatively examined for signal-to-noise ratio, as presented graphically in Figure 4.19. This shows that the best signal-to-noise ratio is observed when the concentration of **2-c** is 0.5 mM and 5-methylpyrimidine is 1 mM.

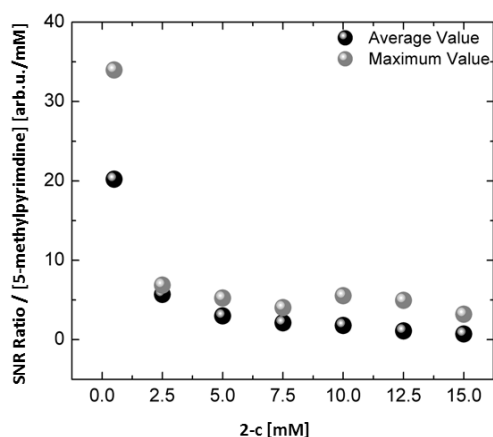


Figure 4.19 Influence of the amount of catalyst on the signal-to-noise ratio of 5-methylpyrimidine hyperpolarised/thermal images. In order to observe just the effect of **2-c**, each Signal-to-noise ratio has been normalized to the concentration of substrate used

These results demonstrate that the use of SABRE can not only reduce the experimental time, but also show a remarkable improvement in signal intensity. If this sample was to be considered as a contrast agent for *in-vivo* studies, it is important to determine an optimum concentration. This will involve a trade-off between high signal-to-noise values and the maximum amount of complex that can be administered under safe conditions. As the substrate is biocompatible, the concern remains with the catalyst.

The same ^1H RARE MRI measurements can be carried out to determine the optimum catalyst loading when the quantity of 5-methylpyrimidine is varied. This will determine the optimum quantity of substrate in terms of image quality and signal-to-noise. The results can be seen in Figure 4.20.

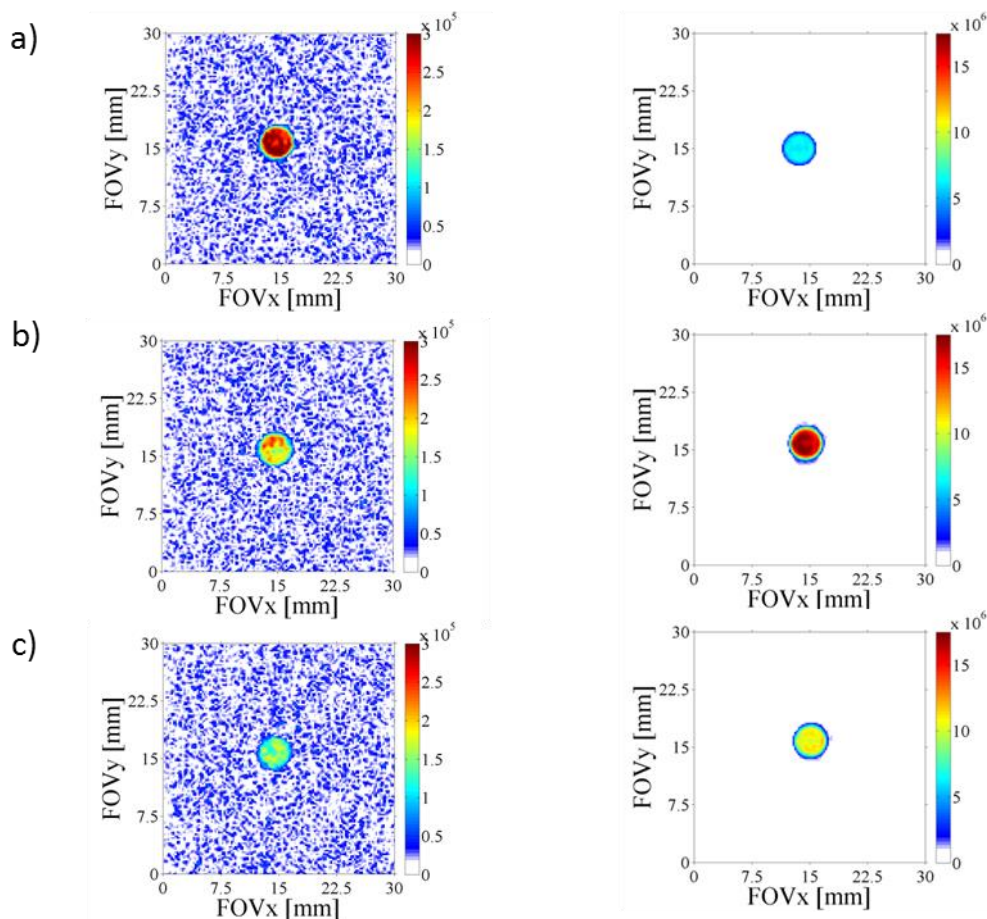


Figure 4.20 ^1H RARE MRI images for an NMR tube containing 5-methylpyrimidine and 2-c, thermal images shown on the left and hyperpolarised images on the right (collected for a PTF of 50 – 60 G, with substrate: catalyst ratio; a) 60:1 b) 40:1 and c) 20:1)

The analysis of the thermal results show a linear relationship between intensity and proton density, so increasing the amount of substrate leads to an increase in signal-to-noise ratio. However the hyperpolarised spectra do not seem to follow this trend, with the optimum signal intensity being observed when substrate to catalyst loading ratio is 40:1.

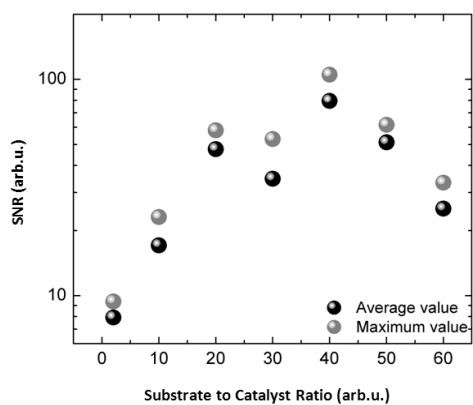


Figure 4.21 Influence of the substrate: catalyst ratio on the signal-to-noise ratio of 5-methylpyrimidine hyperpolarised/thermal images.

Figure 4.21 shows the graph of signal-to-noise ratio against catalyst loading and confirms that the optimum is at a ratio of 40:1. This is important from a clinical perspective as it proves that the best quality image and signal-to-noise was obtained when not using large amounts of substrate, and as a contrast agent a relatively low dosage could be administered.

Both sets of samples can now be compared to two standard phantom samples of water and oil. Water and oil are used to mimic the water and fat in the body, but their T_1 relaxation times are considerably quicker than that of human tissue⁵⁵. The arrangement of these samples for a MRI measurement is as shown in Figure 4.22.

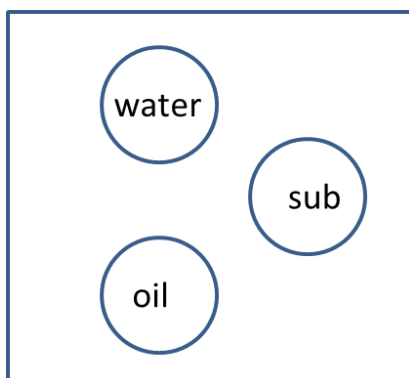


Figure 4.22 Arrangement of the phantoms and substrate (sub) in the bore of the magnet

These data have been acquired using MRI pulse sequences RARE, FLASH and FISP, which are three of the most common image acquisition strategies currently employed in preclinical and clinical imaging^{164, 165}. The purpose of these experiments was to assess the behaviour of the hyperpolarised complex when not only intensity, but also contrast is considered. All of the parameters were kept consistent throughout, with RARE parameters being: 5 mm slice, FOV 30 x 30 mm, matrix 64 x 64, TE/TR 4 ms/600 ms/ 90°. The FLASH parameters are: 5 mm slice, FOV 30 x 30 mm, matrix 64 x 64, TE/TR 4 ms/600 ms/ 5°. The FISP parameters are: 5 mm slice, FOV 30 x 30 mm, matrix 128 x 128, TE/TR 4 ms/600 ms/ 5°.

The resulting images can be seen in Figure 4.23 and Figure 4.27 with samples containing a 20:1 and 60:1 ratio of substrate to catalyst respectively. In the same way previously shown a graph of signal-to-noise ratio can be plotted, but instead of setting these against the thermal 5-methylpyrimidine signal, the hyperpolarised image can be set against the two phantom samples which are represented in d (water) and e (oil) of these figures.

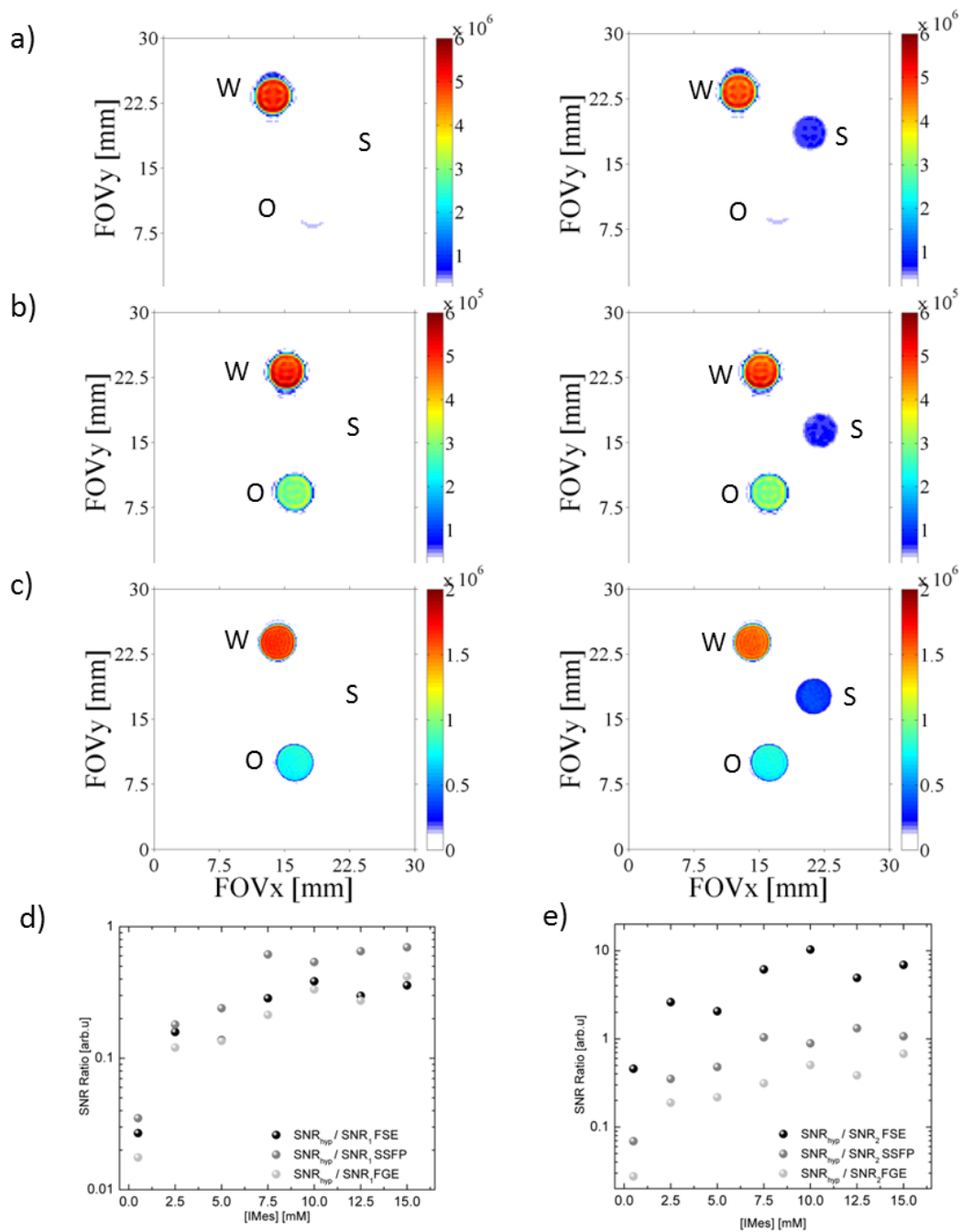


Figure 4.23 ^1H MRI images of three samples, where the MRI pulse sequences are: a) RARE, b) FLASH and c) FISP. The left images reflect the thermal traces whilst the right images reflect the hyperpolarised traces. The signal-to-noise ratio of the hyperpolarised 5-methylpyrimidine signal versus that of water and oil is shown in graphs (d) and (e) respectively. Substrate = S, water = W and oil = O. Catalyst loading 1:20

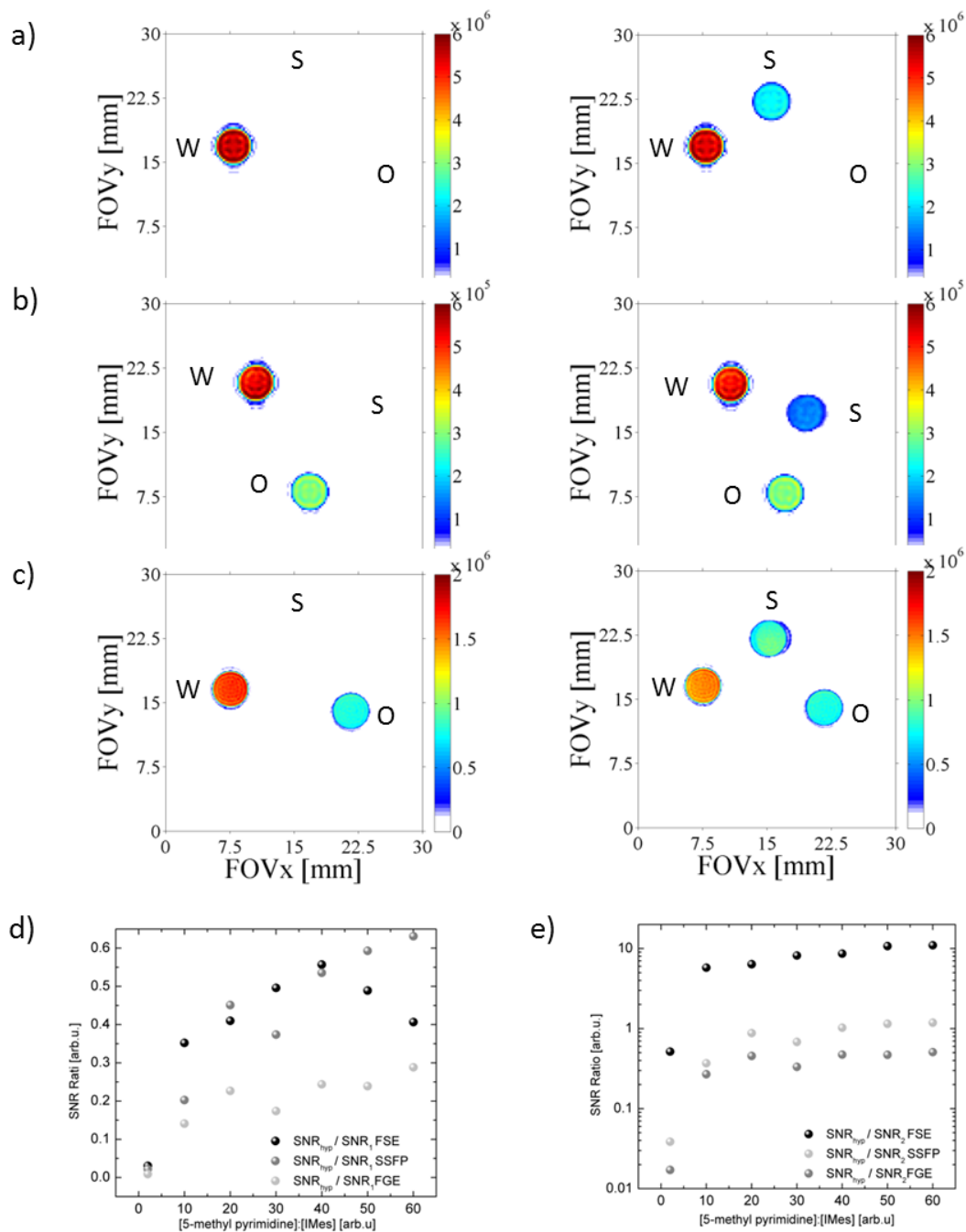


Figure 4.24 ^1H MRI images of three samples, where the MRI pulse sequences are: a) RARE, b) FLASH and c) FISP. The left images reflect the thermal traces whilst the right images reflect the hyperpolarised traces. The signal-to-noise ratio of the hyperpolarised 5-methylpyrimidine signal versus that of water and oil is shown in graphs (d) and (e) respectively. Substrate = S, water = W and oil = O. Catalyst loading 1:60

It can be seen from these data that the hyperpolarised image of 5-methylpyrimidine shows good signal intensity for all of the MRI pulse sequences. Figure 4.23 reveals the signal-to-noise ratio values of the hyperpolarised sample are comparable to those of pure water when using the FISP pulse sequence, when 2-c (7.5 mM) and 5-methylpyrimidine (150 mM) is employed. When an FSE pulse sequence is used, the signal-to-noise ratio values of the

hyperpolarised samples can be up to one order of magnitude higher than those of oil. The spin echo refocuses the hyperpolarised magnetisation and prevents it from decaying due to phenomena such as magnetic susceptibility of field in-homogeneities. Figure 4.24 reveals signal-to-noise ratio values that are about half when compared to the water and 10 times higher to that observed against the oil sample. The orientation of the sample images differ slightly, due to replacing the probe in a different alignment when carrying a SABRE experiment.

For high resolution MRI, longer acquisition times and multiple scans are required to achieve the desired image quality. Although this is still in the early stages of testing, due to the long T_1 relaxation time of 5-methylpyrimidine, it is possible to implement the FISP sequence with a total acquisition time of 9 seconds. The parameters for the experiment are as follows; 5 mm slice, FOV 30 x 30 mm, matrix 128 x 128, TE/TR₁/TR₂ 2 ms/ 4 ms / 600 ms/ 5°. This allowed the consecutive collection of eight images as shown in Figure 4.25 from a single polarisation step. A similar study with pyridine has been examined in the past¹⁶⁶. Initially, the corresponding data yielded similar signal-to-noise ratios to those obtained for 5-methylpyrimidine but it only proved possible to collect 2 - 3 images from one hyperpolarised sample due to the T_1 relaxation of pyridine being more facile.

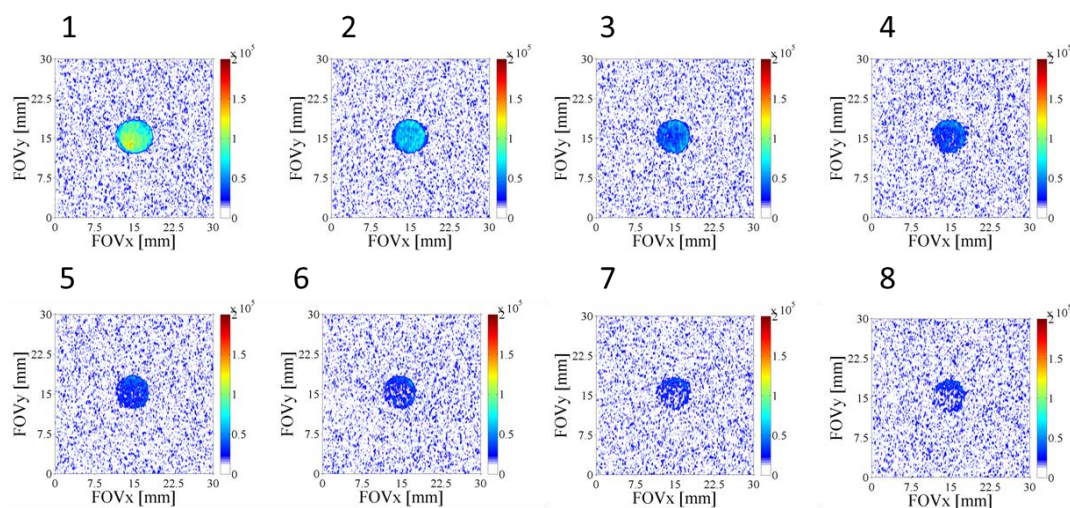


Figure 4.25 ¹H MRI images obtained for hyperpolarised 5-methylpyrimidine using FISP sequence in succession for a total acquisition of 9 s

This shows that the long T_1 relaxation time of 5-methylpyrimidine makes it a potentially suitable candidate to pursue MRI with *in-vivo* imaging. In conclusion, 5-methylpyrimidine is a good test compound for further *in-vivo* studies. This study has shown that it can be polarised, it has a long T_1 , and good phantom images can be obtained. If future work was to

be carried out, FISP or FLASH protocol should be employed in these studies, but FLASH may give fewer artefacts as it is less sensitive and works well with molecules with long T_1 . A 60 second *parahydrogen* SABRE transfer time was used to improve on the signal-to-noise ratio values.

4.4. Effect of deuterium labelling.

The effect of ^2H labelling has also been studied. It is known that incorporating ^2H into the substrate can lengthen T_1 and reduce the number of protons SABRE polarisation is distributed between. This means that larger hyperpolarisation levels might be achieved. A study of 2,6- d_2 -pyridine and 3,4,5- d_3 -pyridine was conducted with catalyst **2-a**. Typical ^1H NMR spectra are shown in Figure 4.26. The enhancement levels are summarised in Table 4.11.

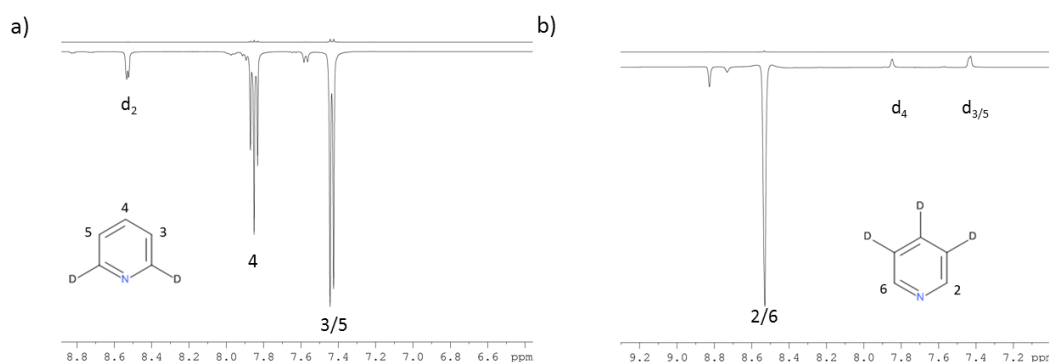


Figure 4.26 Hyperpolarised ^1H NMR for a) 2,6- d_2 -pyridine and b) 3,4,5- d_3 -pyridine with catalyst **2-a** at a PTF of 65 G

Substrate	Resonance	Enhancement level
2,6- d_2 -pyridine	<i>para</i> (4)	-141.59
	<i>meta</i> (3/5)	-104.96
3,4,5- d_3 -pyridine	<i>ortho</i> (2/6)	-403.36
Pyridine	<i>ortho</i> (2/6)	-113.56
	<i>para</i> (4)	-63.23
	<i>meta</i> (3/5)	-99.57

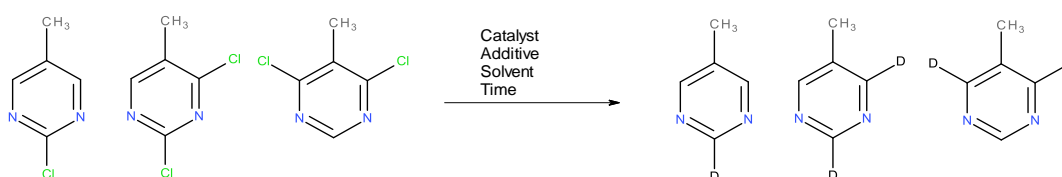
Table 4.11 Comparison of ^1H NMR signal enhancement levels (fold) observed for pyridine using catalyst **2-c**

The results show that 3,4,5- d_3 -pyridine has the greatest build-up of polarisation in the *ortho* position, nearly quadrupling the values seen in fully protonated pyridine. The 3,4,5-

d_3 -pyridine is also advantageous for MRI as the single resonance will prevent ghosting of the image¹⁶⁷. Based on these results for deuterated pyridine, it is a sensible idea to explore the effect of deuterating 5-methylpyrimidine.

4.4.1. Synthesis of deuterated 5-methylpyrimidine isotopomers

In order to do this, the synthesis of the deuterated 5-methylpyrimidine isotopomers shown in Scheme 4.1. was undertaken. Table 4.12 reveals the corresponding conversion data. The starting materials are readily available in the form of chlorinated precursors.



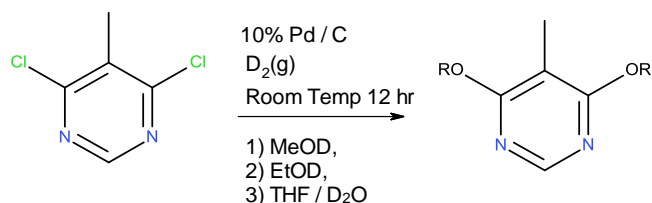
Scheme 4.1 Chlorinated precursors used in the synthesis of deuterium labelled 5-methylpyrimidine substrates. These were carried out as individual reactions to obtain the corresponding final product

Entry	Catalyst	Additive	Solvent	Time	Conversion	Isolated Yield
1	Zn	AcOD	THF/D ₂ O	12	0 %	0 %
2	Pd/C (10%)	Et ₃ N	MeOD	12	0 %	0 %
3	Pd/C (10%)	Et ₃ N	EtOD	12	2%	2 %
4	Pd/C (10%)	Et ₃ N	Et ₂ O	12	100 %	<10 %
5	Pd/C (10%)	Et ₃ N	THF/D ₂ O	12	4 %	2 %
6	Pd/C (10%)	Et ₃ N	THF	12	100 %	<15 %
7	Pd/C (10%)	K ₂ CO ₃	Et ₂ O	72 h	76 %	<50 %
8	Pd/C (10%)	K ₂ CO ₃	THF	72 h	95 %	< 30 %
9	Pd(OH) ₂ /C	K ₂ CO ₃	THF	72 h	85 %	< 50 %
10	Pd/C (5%)	K ₂ CO ₃	THF	72 h	100 %	98 % *

Table 4.12 Corresponding experimental conditions for the proposed Scheme 4.1 and conversion rates (* Isolation as the HCl salt)

Initial attempts to introduce deuterium into 2,4-chloro-5-methylpyrimidine focused on the use of transfer hydrogenative conditions with Zn (entry 1, Table 4.12). The reaction profile unfortunately showed no conversion to the desired product. Instead, deuterium was incorporated into all sites. Subsequent studies focused on the heterogeneous reductive

dechlorination utilising palladium on carbon in the presence of $D_{2(g)}$. When the reaction was attempted in the presence of protic solvents (entries 2, 3, and 5, Table 4.12) poor conversion was observed, with a major side reaction involving S_NAr addition of the protic solvent into the aryl halide bond (Scheme 4.2).



Scheme 4.2 Proposed side reaction with protic solvent leads to ethers 2, 3 of Table 4.12

Upon moving to the ethereal aprotic solvents (entries 4 and 6, Table 4.12), excellent conversion was observed. However, isolation of the desired product proved difficult due to the presence of the Et_3N which co-eluted under flash chromatography and formed an azeotrope with the product, resulting in the significant loss of yield upon isolation. Upon transferring to an inorganic base, the reaction times increased dramatically, with THF found to be a better solvent choice than Et_2O , most likely due to the increased solubility of both the base and D_2 . Upon changing the palladium catalyst, small improvements were found by changing to Pd/C with 5% loading. Subsequent purification relied on the formation of a salt of HCl in order to avoid similar azeotrope effects when removing the reaction solvent. These conditions were applied to the remaining chlorinated starting materials to allow access to the full range of isotopomers (Scheme 4.1). These reactions were followed by LC-MS.

4.4.1.1. 4,6- d_2 -5-methylpyrimidine

The resulting 1H NMR spectra associated with the formation of 4,6- d_2 -5-methylpyrimidine can be seen Figure 4.27 and deuterium incorporation is confirmed according to

Table 4.13. The deuterium exchange into the 4 / 6 positions has not been fully accomplished, giving 13 % hydrogen incorporation at these sites. It is also evident that deuterium exchange has taken place at the 2 position with 55 % incorporation. The methyl groups remain unchanged. The 1H NMR of the starting material showed 4 % hydrogen incorporation. This can arise from loss of enrichment of the $D_{2(g)}$ or from H_2 exchange from palladium on carbon, as this is a surface mediated reaction and the palladium on carbon catalytic surface can contain up to 50 % water. Attempts were made to minimise this effect by washing the catalyst in D_2O prior to starting the reaction.

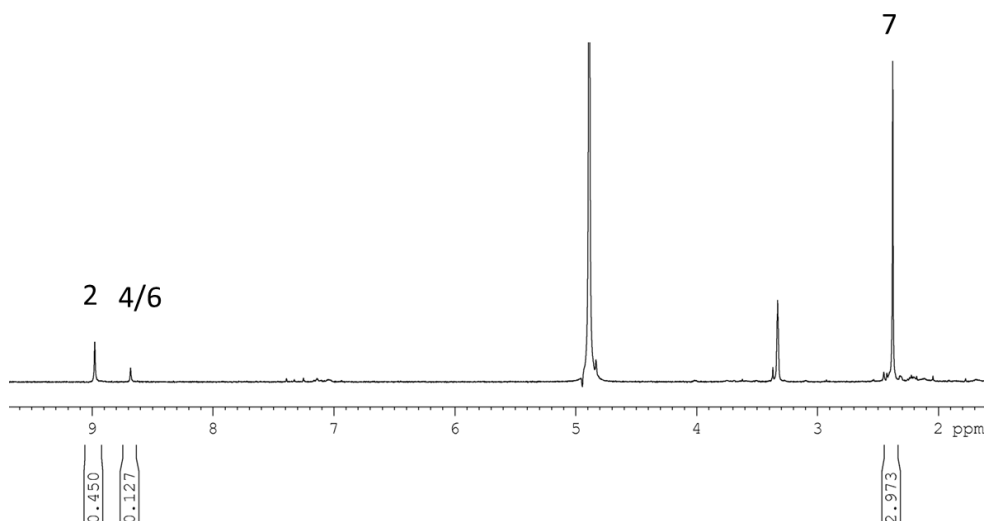


Figure 4.27 ^1H NMR spectrum of 4,6- d_2 -5-methylpyrimidine in methanol- d_4

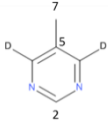
Substrate	Resonance	Deuterium incorporation (%)
	H_2	55 %
	$\text{H}_{4/6}$	87 %
	H_7	0 %
	H_2	55 %

Table 4.13 ^2H labelling of 4,6- d_2 -5-methylpyrimidine, and percentage label incorporation

4.4.1.2. 2-d-5-methylpyrimidine

The ^1H NMR spectrum of 2-d-5-methylpyrimidine can be seen in Figure 4.28 and deuterium incorporation is detailed in Table 4.14. Again it is evident that there is 15 % hydrogen incorporation in the 2 position. The ^1H NMR spectrum of the starting material revealed 2 % hydrogen in the same position. Unfortunately, the reaction has proceeded to incorporate 32 % deuterium into the hydrogen 4 / 6 of the final product as well as the desired deuteration site.

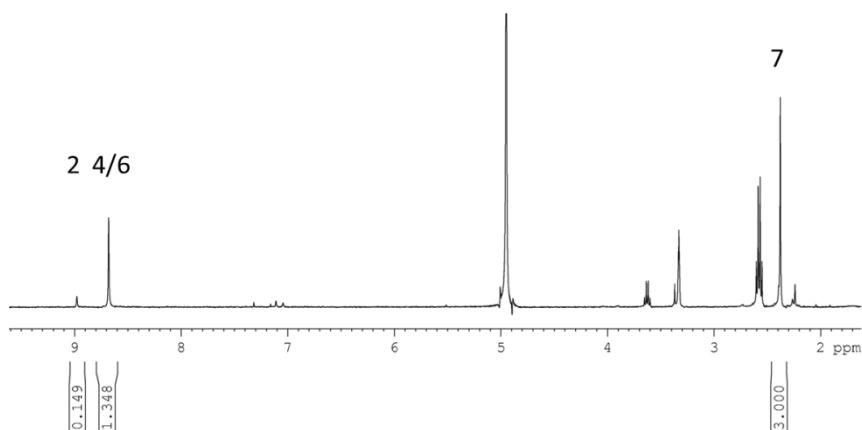


Figure 4.28 ^1H NMR spectrum of 2-d-5-methylpyrimidine in methanol- d_4

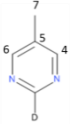
Substrate	Resonance	Deuterium incorporation (%)
	H_2	85 %
	$\text{H}_{4/6}$	42 %
	H_7	0 %
	H_2	85 %

Table 4.14 ^2H labelling of 2-d-5-methylpyrimidine, and percentage incorporation

4.4.1.3. 2,4- d_2 -5-methylpyrimidine

The ^1H NMR of 2,4- d_2 -5-methylpyrimidine can be seen in be seen in Figure 4.29 and deuterium incorporation in Table 4.15. Again, it is evident there is a 4 % hydrogen incorporation in the 2 position. The NMR spectra of the starting material revealed 1.5 % hydrogen in the same position. Unfortunately, the reaction has proceeded to incorporate an extra 34% deuterium at hydrogen 4 of the final product.

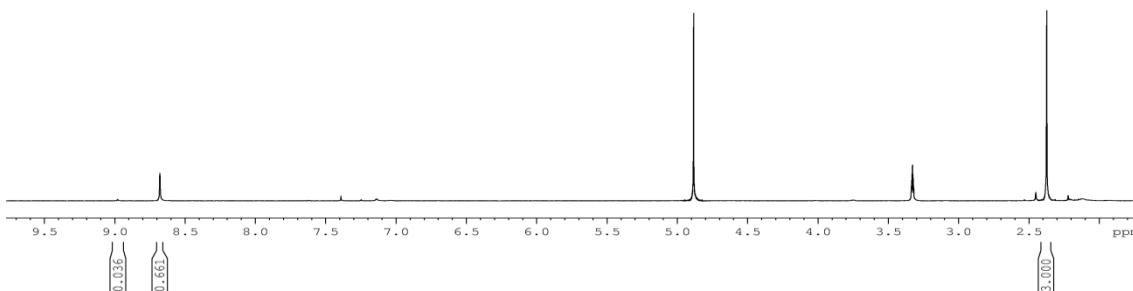


Figure 4.29 ^1H NMR spectrum for 2,4- d_2 -5-methylpyrimidine in methanol- d_4

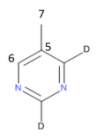
Substrate	Resonance	Deuterium incorporation (%)
2,4- d_2 -5-methylpyrimidine 	H ₂	96 %
	H ₄	100 %
	H ₆	34 %
	H ₇	0 %

Table 4.15 ^2H labelling of 2,4- d_2 -5-methylpyrimidine, and percentage incorporation

The deuterium labelled substrates and their precursors were then tested for SABRE activity.

4.4.2. Testing chlorinated and deuterated 5-methylpyrimidine analogues with SABRE

SABRE was investigated firstly with the chlorinated precursors and catalyst **2-c**. These exhibit poor polarisation transfer with resonances 4 and 6 of 2-chloro-5-methylpyrimidine giving the greatest enhancement level of -1.1-fold. The poor activity is possibly due to steric hindrance of the precursor (chlorine vs. proton), and consequently not being able to freely exchange with the catalyst. The study continued on to investigate the deuterium labelled substrates synthesised in the previous section. The hyperpolarised ^1H NMR spectra for each of these substrates can be seen in Figure 4.30.

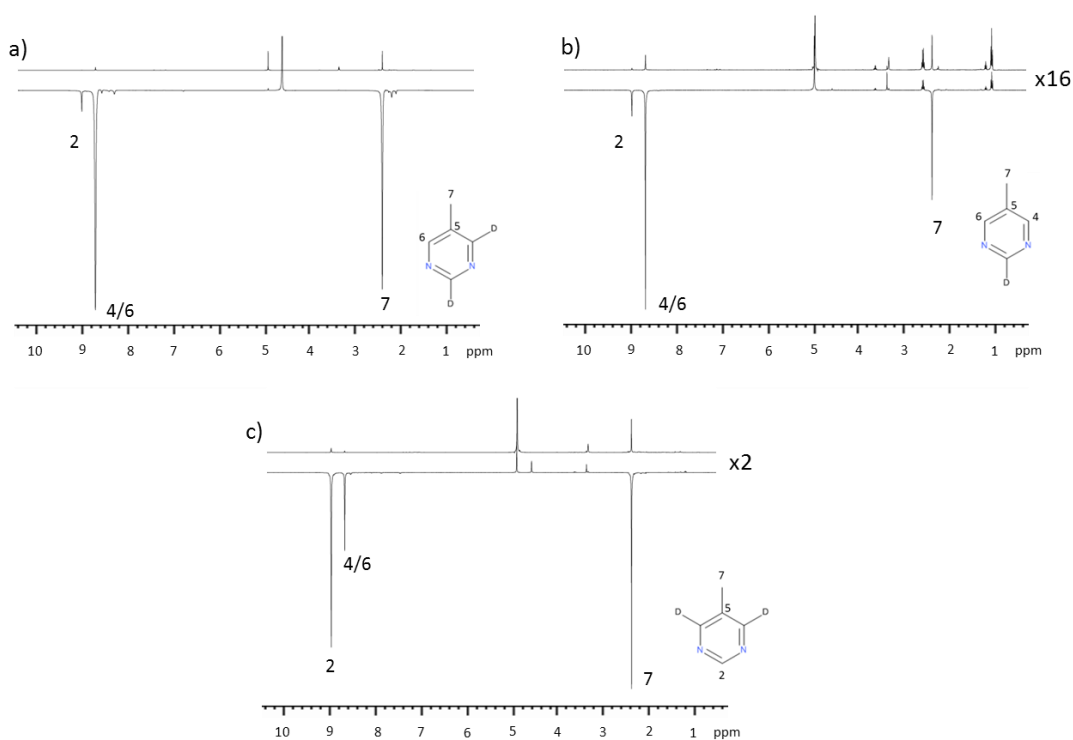


Figure 4.30 Observed ^1H NMR spectra for SABRE experiments with catalyst 2-c for a) 2,4-d₂-5-methylpyrimidine, b) 2-d-5-methylpyrimidine and c) 4,6-d₂-5-methylpyrimidine. The vertical expansion of b (x16) and c (x2) is based on spectra obtained for a.

The results for the SABRE revealed that 2,4-d₂-5-methylpyrimidine was the most efficient for polarisation transfer with resonances 6 and 7 yielding a 354 and 55-fold enhancement levels obtained at a PTF of 65 G. There is a large amount of polarisation observed for the deuterium labelled position 2, with 315-fold enhancement based on the thermal integral for 4 % hydrogen incorporation. All of the deuterium labelled substrates are summarised in Table 4.16.

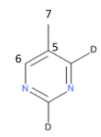
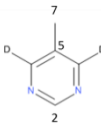
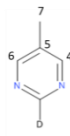
Substrate	Resonance	Deuterium incorporation (%)	Enhancement level
2,4-d ₂ -5-methylpyrimidine 	H ₂	96 %	-316
	H ₄	100 %	0
	H ₆	34 %	-354
	H ₇	0 %	-55.0
4,6-d ₂ -5-methylpyrimidine 	H ₂	55 %	-50.1
	H _{4/6}	87 %	-73.0
	H ₇	0 %	-7.12
2-d-5-methylpyrimidine 	H ₂	85 %	-49.9
	H _{4/6}	42 %	-72.2
	H ₇	0 %	-7.1

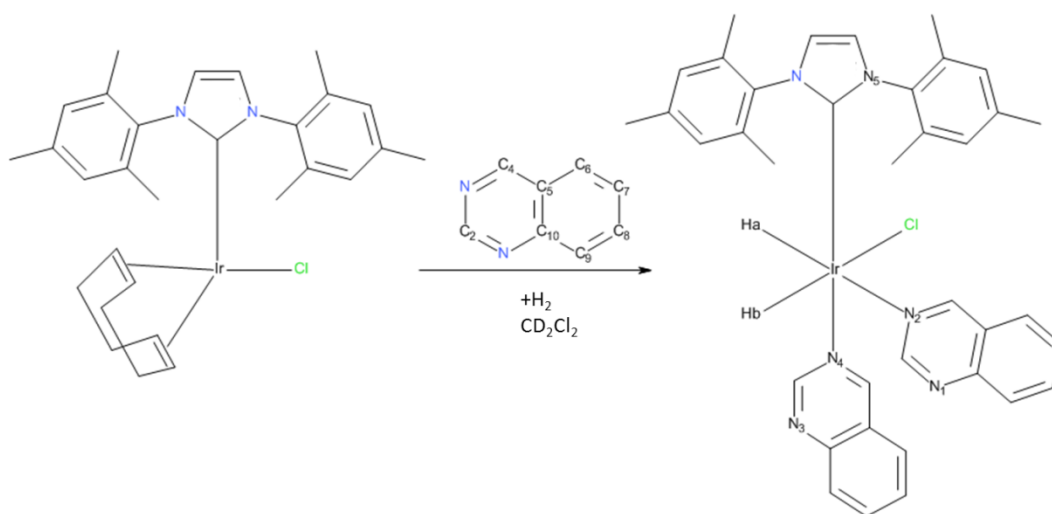
Table 4.16 Summarised ¹H NMR enhancements levels observed for the ²H labelling of 5-methylpyrimidine, and percentage incorporation

These data reveal that a large percentage of the polarisation could possibly be due to the small percentage of hydrogen incorporation at the specific sites for deuterium labelling. Therefore, it is difficult to determine the transfer process employed in SABRE for 5-methylpyrimidine. Protio 5-methylpyrimidine originally gave enhancement values of 200, 198 and 60-fold for H₂, H_{4/6} and H₇ respectively. We can see here that the levels observed for 2,4-d₂-5-methylpyrimidine significantly greater for H₂ and H₆ resonances. This could be linked to similar effects to those observed with concentration as the H concentration at H₂ site is relatively low compared to catalyst loading. Therefore, it seems wise to conduct a concentration study of 2,4-d₂-5-methylpyrimidine. The H₇ resonance remains unchanged, but does decrease when investigating the two other ²H labelled substrates. It cannot be clearly established, but a larger incorporation of ²H at the H_{4/6} position seems to present poor enhancement values, thus this site could be important in the transfer of polarisation of 5-methylpyrimidine. Until a more rigorous synthetic approach to labelling these substrates is found, no further work was continued for SABRE or MRI studies.

4.5. Conversion of Quinazoline to 3,4-dihydroquinazoline followed by SABRE

One further molecule that has been investigated was quinazoline. During this study the unexpected conversion of quinazoline to 3,4-dihydroquinazoline was observed in the presence of catalyst **2-c** in methanol- d_4 solution. This first was observed when testing quinazoline under standard conditions for a SABRE experiment. Both the product and reactant are SABRE active and consequently the metal catalyst not only mediates polarisation transfer but facilitates hydrogenation thereby enabling the examination of this transformation through hyperpolarised NMR.

In order to probe this reaction further a sample containing **2-c**, quinazoline (quin) in a dichloromethane- d_2 was prepared and this sample was then placed under H_2 . The product of this reaction was expected to form $[Ir(\mathbf{2-c})(H)_2(Quin)_3]Cl$, for which analogous complexes have been demonstrated in section 2.2.6. Instead this reaction (Scheme 4.3) proceeded to form a product which yields two inequivalent hydride ligands signals at δ -22.77 ppm and δ -23.78 ppm at 298 K, and corresponds to $[Ir(\mathbf{2-c})(H)_2(Quin)_2]Cl$.



Scheme 4.3 Reaction leading to the formation of $[Ir(\mathbf{2-c})(H)_2(Quin)_2]Cl$ in dichloromethane- d_2 solution

The hydrides are relatively broad and have slightly different line widths, where δv is 16.7 and 16.3 Hz respectively. Consequently upon cooling these two hydrides resonances sharpen, and resolve into two pairs of doublets that share a splitting of -7.9 Hz at 226 K (Figure 4.31).

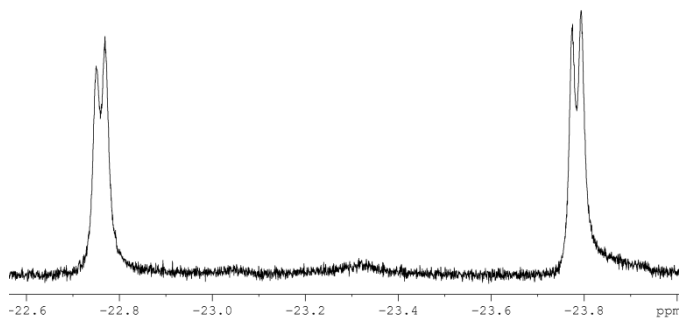


Figure 4.31 ^1H NMR spectra showing the inequivalent hydride as a pair of doublets for $[\text{Ir}(\mathbf{2-c})(\text{H})_2(\text{Quin})_2\text{Cl}]$ in dichloromethane- d_2 at 226 K

The detailed NMR characterisation of $[\text{Ir}(\mathbf{2-c})(\text{H})_2(\text{Quin})_2\text{Cl}]$ was undertaken using a series of 1D nOe measurements to locate the 6 distinct ^1H signals of the quinazoline ligand. Further ^{15}N NMR measurements provided 5 chemical shifts of δ 192.9, 226.2, 246.5, 282.9 and 283.3. The site at δ 192.9 proved to correspond to N_5 site of catalyst $\mathbf{2-c}$, which is connected to the ^1H singlet at δ 6.83 of the imidazole backbone. The δ 246.5 signal N_2 displays a strong coupling of 14 Hz to the H_a proton, thus indicating *trans* orientation. The N_1 signal appears at δ 283.6 which proved to connect to the aromatic resonance at δ 9.40. The ^{15}N chemical shifts of the free quinazoline appear at δ -291.8, therefore on binding to the iridium centre the ^{15}N shifts moves to lower field by approximately 45 ppm. This is similar to what is observed when catalyst $\mathbf{2-c}$ is examined when pyridine bound *trans* to hydride¹⁶⁸. The iridium N_3 and N_4 resonances for the axial quinazoline ligand appear at δ 226.2 and 282.9 respectively. Full characterisation of the $[\text{Ir}(\mathbf{2-c})(\text{H})_2(\text{Quin})_2\text{Cl}]$ can be found in the experimental. Confirmation of the presence of the directly bound, but NMR silent, chloride ligand was obtained by the addition of AgBF_4 which resulted in the formation of the initially predicted *tris*-substituted cation $[\text{Ir}(\text{H})_2(\text{IMes})(\text{Qu})_3]\text{BF}_4$.

The quinazoline ligand and hydride loss rate constants were determined for $\mathbf{2-c}$ in dichloromethane- d_2 solution at 300 K as 10 s^{-1} and 41 s^{-1} respectively. The associated rate data extracted from a series of variable temperature studies, led to ΔH^\ddagger and ΔS^\ddagger values of $87.8 \pm 1 \text{ kJ mol}^{-1}$ and $75 \pm 3 \text{ J K}^{-1} \text{ mol}^{-1}$ for quinazoline loss. ΔH^\ddagger and ΔS^\ddagger values of $80 \pm 2 \text{ kJ mol}^{-1}$ and $50 \pm 7 \text{ J K}^{-1} \text{ mol}^{-1}$ were determined for the H_2 loss process. These processes have $\Delta\text{G}^\ddagger_{(300)}$ values of $65.4 \pm 0.5 \text{ kJ mol}^{-1}$ and $61.2 \pm 0.2 \text{ kJ mol}^{-1}$ respectively. There is therefore little difference between these values and those reported for $[\text{Ir}(\mathbf{2-c})(\text{Py})_3(\text{H})_2]\text{Cl}$ ⁹³. Where ΔH^\ddagger , ΔS^\ddagger and $\Delta\text{G}^\ddagger_{(300)}$ for ligand loss are $93.4 \pm 3.1 \text{ kJ mol}^{-1}$, $97 \pm 13 \text{ J K}^{-1} \text{ mol}^{-1}$ and $64.4 \pm 2.2 \text{ kJ mol}^{-1}$ respectively and ΔH^\ddagger , ΔS^\ddagger and $\Delta\text{G}^\ddagger_{(300)}$ for hydride loss being $79.2 \pm 0.2 \text{ kJ mol}^{-1}$, $41.0 \pm 3.0 \text{ J K}^{-1} \text{ mol}^{-1}$ and $66.4 \pm 0.3 \text{ kJ mol}^{-1}$ respectively.

Upon the addition of methanol- d_4 to the $[\text{Ir}(\mathbf{2-c})(\text{H})_2(\text{Quin})_2\text{Cl}]$ solution further reactivity was evident as over a period of 24 hour the signals for quinazoline were replaced by those of a new material. This change is shown clearly in Figure 4.32 which presents an expansion of the aromatic region of the resulting ^1H NMR spectra. The material produced in this reaction is 3,4-dihydroquinazoline, as confirmed by ^1H and ^{13}C NMR data¹⁶⁹⁻¹⁷¹. This is the sole product of the reaction and no evidence for 1,2-dihydroquinazoline¹⁷² is seen.

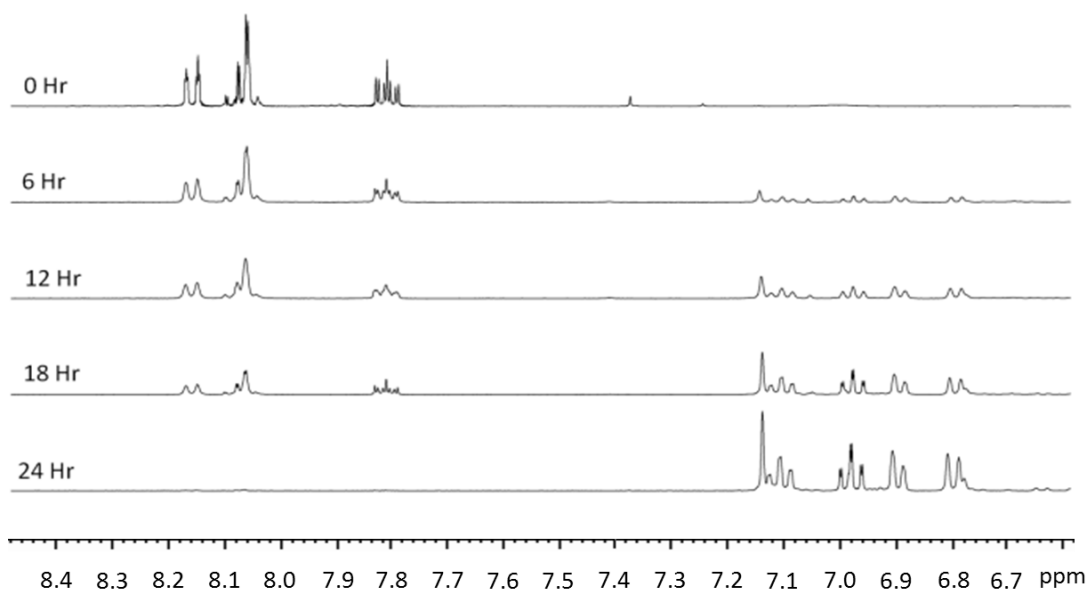


Figure 4.32 Series of ^1H NMR spectra following the conversion of quinazoline into 3,4-dihydroquinazoline by the addition of methanol- d_4 to the sample $[\text{Ir}(\mathbf{2-c})(\text{H})_2(\text{Quin})_2\text{Cl}]$ in dichloromethane- d_2

Remarkably both quinazoline, and the product 3,4-dihydroquinazoline, exhibit SABRE and this reaction can be followed by tracking the change in the corresponding enhanced signals. The SABRE enhanced resonances of 3,4-dihydroquinazoline correspond to all seven ring protons with no visible enhancement seen for the exchangeable NH proton. The signal gains for the H_2 and $\text{H}_{4/5}$ that are located next to the binding site are around 5 times larger than those of the remaining sites. The ^1H NMR spectra observed for both hyperpolarised reactant and product can be seen in Figure 4.33.

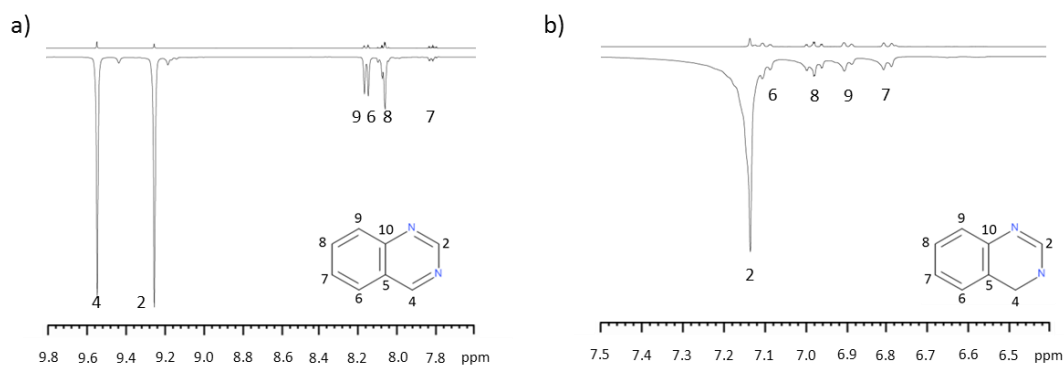


Figure 4.33 Observed ^1H NMR spectra of a) quinazoline when $[\text{Ir}(\mathbf{2-c})(\text{H})_2(\text{Quin})_2\text{Cl}]$ in dichloromethane- d_2 b) the product 3,4-dihydroquinazoline $[\text{Ir}(\mathbf{2-c})(\text{H})_2(\text{Quin})_3\text{Cl}]$ after the addition of methanol to the dichloromethane- d_2 in the presence of H_2 . The thermal trace is represented on top, and the polarised trace on the bottom, under transfer a PTF of 65 G

The hydrogenation reaction observed here seems specific to quinazoline as pyrimidine, 5-methylpyrimidine, isoquinoline and quinoxaline have been investigated using SABRE and no side reactions were noted. In order to probe whether direct hydrogenation or transfer hydrogenation operates here, a methanolic sample containing quinazoline and **2-c** was prepared and activated by hydrogen. Upon starting to observe the conversion of quinazoline to 3,4-dihydroquinazoline, the hydrogen-rich atmosphere was changed to nitrogen. The sample was then monitored for 24 hour. No further hydrogenation of the starting material occurred. The addition of ammonium formate, a known proton source for transfer hydrogenation¹⁷³⁻¹⁷⁵, in conjunction with heating the sample to 323 K also failed to promote further hydrogenation, thus conclude that dihydrogen is necessary for this transformation.

Examination of the literature reveals an outsphere hydrogenation mechanism of methylquinoline by Dobereiner *et al* 2011¹⁴⁸. This mechanism is shown in Figure 4.34.

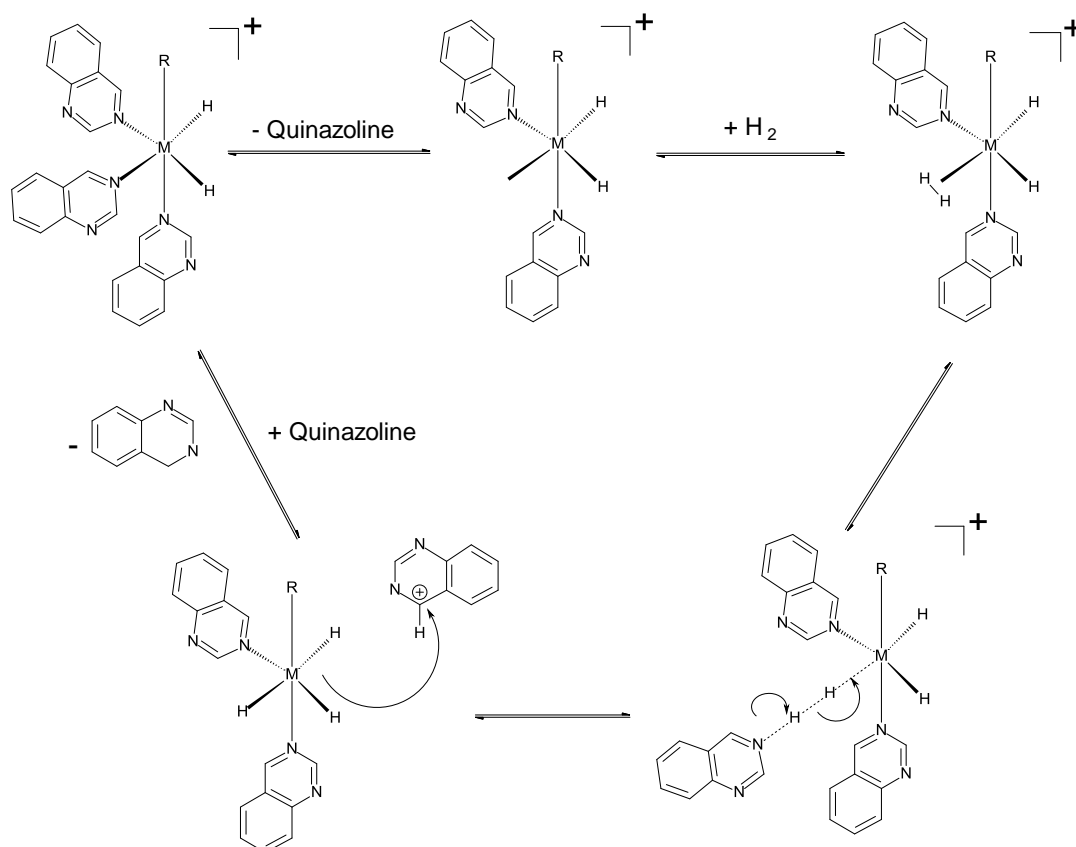


Figure 4.34 Proposed stepwise outer-sphere mechanism for the hydrogenation of quinolines as reported by Dobereiner et al 2011¹⁴⁸

4.6. Summary

In this chapter catalyst **2-c** has been employed to prove and extend the array of materials than can be examined by SABRE at room temperature. It showed good polarisation into the substrates; imidazole, pyrazole and oxazole, with total ¹H signal enhancements of 322, 337 and 419-fold respectively. The substrate 5-methylpyridimine has been shown to exhibit good polarisation and the long T₁, needed for an *in-vivo* probe, which the other substrates failed to display.

The optimisation of 5-methylpyridimine revealed that for a ¹H NMR measurement a PTF of 50 G should be employed. At this maximum, an absolute enhancement level of 892-fold is recorded under standard conditions (**2-c** (5 mM), 5-methylpyridimine (100 mM) and 0.6 ml methanol-d₄). The effect of catalyst loading and concentration was studied. This revealed when optimum conditions (**2-c** (0.5 mM), 5-methylpyridimine (1 mM), 0.6 ml of methanol-

d_4) are applied, an absolute enhancement level of 2063-fold is observed. At this maximum the substrate to catalyst ratio is 2:1, and the addition of acetonitrile- d_3 , is needed. This leads to the formation of $[\text{Ir}(\mathbf{2-c})(\text{H})_2(5\text{-methylpyrimidine})_2(\text{MeCN})]^+$, as the active species.

By working at the optimal concentrations, ^{13}C data can be recorded that is necessary for substrate characterisation. These data exhibit a strong field dependence which suggests that detailed investigations will always be necessary. If a substrate is to be screened, it is clear that catalyst optimisation must play a role in this process.

The initial ^1H RARE MRI images, reveal good polarisation of 5-methylpyrimidine with an order of magnitude greater signal intensity when compared the thermal trace. The optimal signal-to-noise ratio was observed when the concentration of $\mathbf{2-c}$ is 0.5 mM and 5-methylpyrimidine is 1 mM in 0.6 ml of methanol- d_4 , and when catalyst loading ratio 40:1. These conditions would be recommended for obtaining a ^1H RARE NMR image. On comparison with the other pulse sequences used, FISP and FLASH generate an order of magnitude greater signal intensity than that produced in the corresponding RARE MRI image. The FLASH sequence should be considered for further studies, as it works particularly well with molecules with long T_1 , with a 60 second *parahydrogen* SABRE transfer time to improve signal-to-noise values.

The synthesis of labelled 5-methylpyrimidine isotopomers, to lengthen the T_1 value and to reduce the number of protons, to increase larger hyperpolarisation levels was in theory a good idea. The synthesis proved difficult due to a high percentage of deuterium incorporation into the other sites of the molecule. Of the three molecules examined, it was 2,4- d_2 -5-methylpyrimidine which showed the greatest levels of polarisation, with an absolute total signal enhancement of 835-fold, which is comparable to a standard sample of 5-methylpyrimidine. The results with quinazoline reveal that even when the system is thought to be well understood unexpected observations can be made in this case for the conversion to 3,4-dihydroquinazolinone. Both the product and reactant are SABRE active and consequently the metal catalyst not only mediates polarization transfer but also facilitates substrate hydrogenation. It has been shown that NMR and SABRE can be used to follow this reaction, with theoretical calculations being used to confirm that hydrogenation of the substrate proceeds through a rare outer-sphere pathway.

5. Chapter 5 Heterogeneous and Water Soluble NHC Catalysts used for SABRE

5.1. Introduction

The use of hyperpolarised methods in conjunction with MRI imaging techniques is receiving significant attention because of the possibility to collect *in-vivo* images that may prove diagnostic of health¹⁷⁶. The successful collection of *in-vivo* data has already been demonstrated for a variety of hyperpolarisation routes, which include PHIP but not yet SABRE^{71, 157, 177}. The final goal of the research group that I worked in is to use SABRE to collect a human *in-vivo* image. To achieve this, two problems present themselves as illustrated by the work carried out in Chapter 2¹⁵². Firstly the catalyst must be removed before injection and secondly a biocompatible medium is required. The reason for removing the catalyst reflects the very expensive assessment that would be needed prior to human use. SABRE is currently routinely carried out in methanol, which also cannot be injected. The enzyme, alcohol dehydrogenase (ADH) within the liver metabolises methanol into toxic compounds via the oxidization of formaldehyde¹⁷⁸. This process can result in the destruction of the optic nerve, leading to blindness and hypoxia within cells¹⁷⁹. A better solvent would be ethanol, which cannot be injected as a neat solvent, but if the ethanol is diluted to a level below 30 %, the solution can be injected¹⁸⁰.

This chapter aims to address these two main problems and will be further split as follows.

- Heterogeneous Catalysis

Studies to immobilise an NHC catalyst on a variety of supported materials are described. The reasons for this stem from the resulting ability to remove the catalyst from the solution before injection and additionally, the ease of recycling. Two potential problems exist with such studies. The relative catalytic activity of heterogeneous vs homogeneous systems for SABRE is unknown, and the potential for, and extent of, catalyst leaching may be important. A paper on an immobilised catalyst with SABRE has appeared whilst this study was in progress¹⁸¹. This took advantage of a different approach to form a polymer bound derivative of $[\text{Ir}(\text{IMes})(\text{COD})(\text{py-polymer})]\text{PF}_6$.

- Water Soluble SABRE Catalyst

Studies to progress to a more biocompatible solution such as water are important. Water as a solvent is safer to use with regards to injecting solutions and from a green chemistry prospective, is cheaper and cleaner¹⁸². However, the solubility of H₂, and therefore *parahydrogen*, in water is reported to be 14 – 15 times lower than in methanol¹⁸³, which suggests that H₂ may become the limiting reagent. The extent of solubilisation of a precursor and active NHC complex in a medium such as water needs to be ensured. Furthermore, water is better able to solubilise charged species through solvent dipole orientation. This process can stabilise the precursor thereby reducing the ligand exchange rates that are necessary for SABRE to operate.

5.2. Heterogeneous Catalysis

5.2.1. Introduction

There are currently four major methodologies which feature in the generation of heterogeneous catalysts. These are adsorption¹⁸⁴, encapsulation¹⁸⁵, covalent tethering¹⁸⁶ and electrostatic interaction¹⁸⁷.

Catalysts which are immobilized by adsorption rely only on van der Waals interactions between the catalyst and the support. This is a weak interaction but the stability of the support can be improved by modifying both the catalyst and support to allow hydrogen bonding to occur. In 2014, Jesionowski *et al.*¹⁸⁸ described the immobilisation of lipase on to a glutaraldehyde-modified silica surface. This catalyst was then used in the esterification of ethanol and ferulic acid. It was noted that by supporting these lipases, increased catalytic activity could be achieved and it was possible to obtain 5 reaction cycles before deactivation.

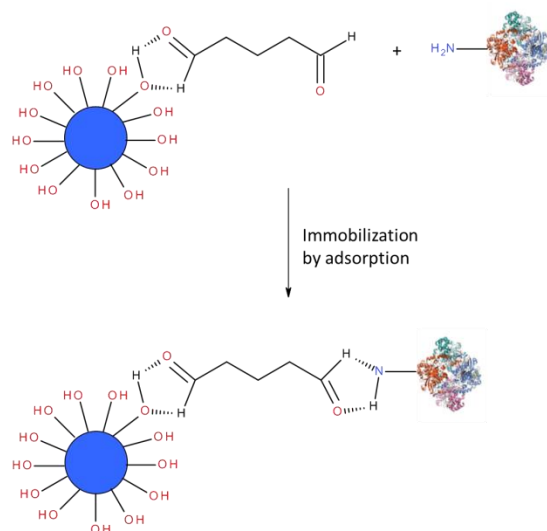


Figure 5.1 Immobilisation of lipase on to glutaraldehyde-modified silica surface by the adsorption method¹⁸⁸

Encapsulation reflects a different process that does not require any interaction between the catalyst and the support, and thus this method most closely mimics homogeneously catalysed reactions. To satisfy the method of encapsulation, the catalyst must be larger than the pores of the support material in order to prevent the loss of catalyst into solution during the course of the reaction or the recovery process. As the catalyst complex is necessarily larger than the pores of the support, techniques such as impregnation cannot be used to synthesise these catalysts¹⁸⁹. In 2003, Seelan *et al.*¹⁹⁰ reported the encapsulation of a vanadium phthalocyanine complex within a zeolite framework (Figure 5.2). They report difficulty in homogeneously distributing the catalyst under encapsulation, leading to a reduction in the size of the pores.

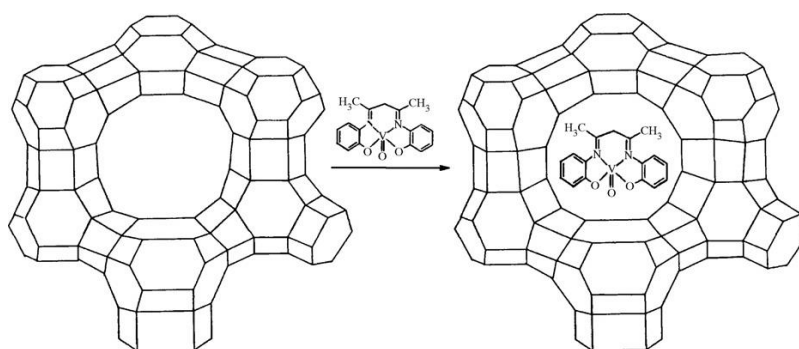


Figure 5.2 Structure of vanadium complex encapsulated by zeolite frame work¹⁹¹

Covalent tethering implies a modification of the ligand, which when applied to SABRE, may influence its electronic character and/or its conformation. Physisorption and ion-exchange methods result in the catalyst being in close proximity to the support which may also affect the electronic properties and ligand conformation. A supported catalyst can be prepared by

either assembling the catalyst within the pores of the support or assembling the support around the catalyst¹⁹¹. In 2011, Tyrrell *et al.* reported the successful tethering of a palladium carbene complex *via* an organic linker to a silica surface (Figure 5.3) and then used it for Suzuki coupling reactions¹⁹².

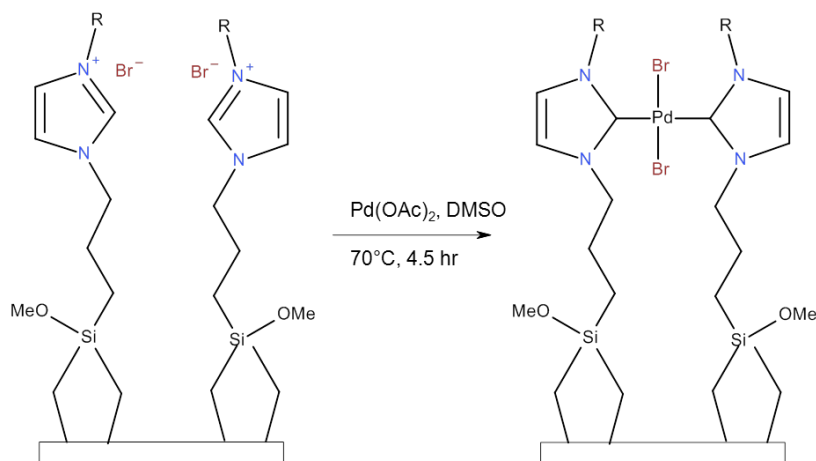
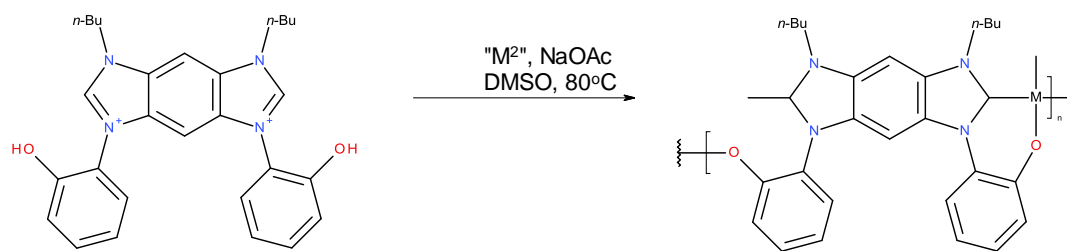


Figure 5.3 Formation of palladium carbene complex tethered to a silica support¹⁹²

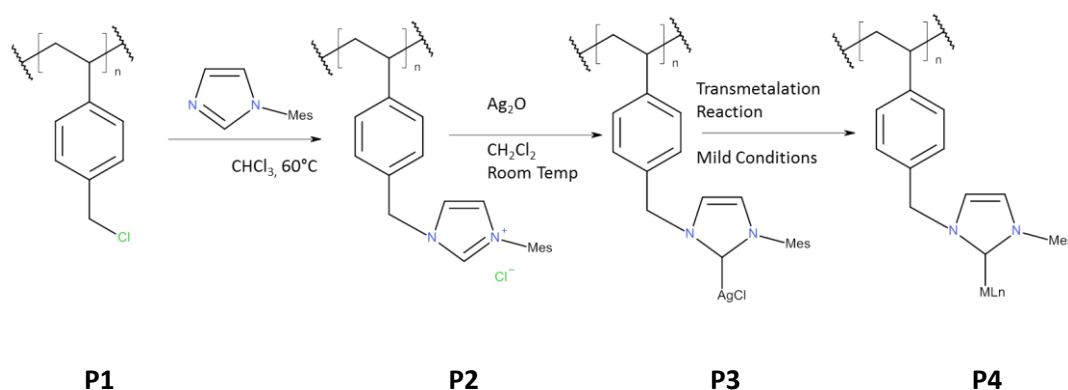
5.2.2. Immobilization on Polymer Supports

There have been various examples of immobilization of vanadium, palladium and ruthenium complexes reported in the literature^{191, 193, 194}. Many of these complexes are supported on cross linked polymers, which are non-reactive, but can be made reactive by adding functionality. These functionalized polymers have been used extensively to support homogenous catalysis through covalent bonding¹⁹⁵. Since the discovery of stable carbenes by the groups of Bertrand and Arduengo, NHCs have attracted considerable interest in both coordination chemistry and catalysis, with NHCs having components that readily allow the construction of organometallic polymeric materials. Bielawski's group has carried out work using NHCs as key components in the synthesis of novel organometallic macromolecules, which enabled the incorporation of transition metals into the main chain, and subsequently they were located in the backbone of the polymer (Scheme 5.1)¹⁹⁶.



Scheme 5.1 Polymerisation reaction to form an organometallic polymer, which can contain various transition metals within the backbone¹⁹⁶

The use of Ag(I)-NHC complexes in the construction of tailored organometallic hybrid mesostructured materials has been reported by Zeng *et al.*¹⁹⁵. The Ag(I)-NHC is readily produced by treatment of the imidazolium salt with silver oxide under mild conditions, and can be complexed with metals such as palladium(II), rhodium, iridium, copper, ruthenium, nickel and platinum^{139, 197-199}. Using this synthetic approach (Scheme 5.2) they describe a method for achieving the post polymerisation modification of a brush polymer (P2) and an Ag-NHC based side chain polymer (P3) and finally they produce a functional palladium-NHC containing polymer (P4), which they use for the catalysis of a Suzuki reaction¹⁹⁵.



Scheme 5.2 Synthetic approach for the preparation of imidazolium salts containing a brush polymer and an NHC-based organometallic polymer¹⁹⁵

5.2.2.1. Synthesis of an Iridium Supported Polymer

Described here is how to prepare iridium supported polymer. This synthesis follows the steps illustrated in Scheme 5.2

The preparation of **P2** starts by grafting 1-mesitylimidazole onto polychloromethylstyrene which is stirred in chloroform at 60°C for 4 days. The solution was cooled, the volume reduced by half and excess ether added to yield the white precipitate, **P2**, in a good yield. A

signal at 10.57 ppm in the corresponding ^1H NMR spectrum corresponds to the 2H-imidazolium proton of the NHC.

A mixture of **P2** and silver oxide, in chloroform, was then stirred at room temperature for 4 days. The solution was again reduced by half, and excess ether added to yield a white precipitate of **P3**. The ^1H NMR data for the polymeric silver salt **P3** shows the absence of any 2H-imidazolium proton signal.

The synthesis of **P3** follows the transmetalation procedure of Section 2.2.2. $[\text{Ir}(\text{COD})\text{Cl}]_2$ was added into a solution containing the polymeric silver salt and stirred for 5 days at room temperature until a yellow precipitate formed, (**P4**, 5 %). This step deviated from the literature method, as the precipitate should have formed immediately. Currently, no optimised method has been found for a higher yielding synthesis of **P4**.

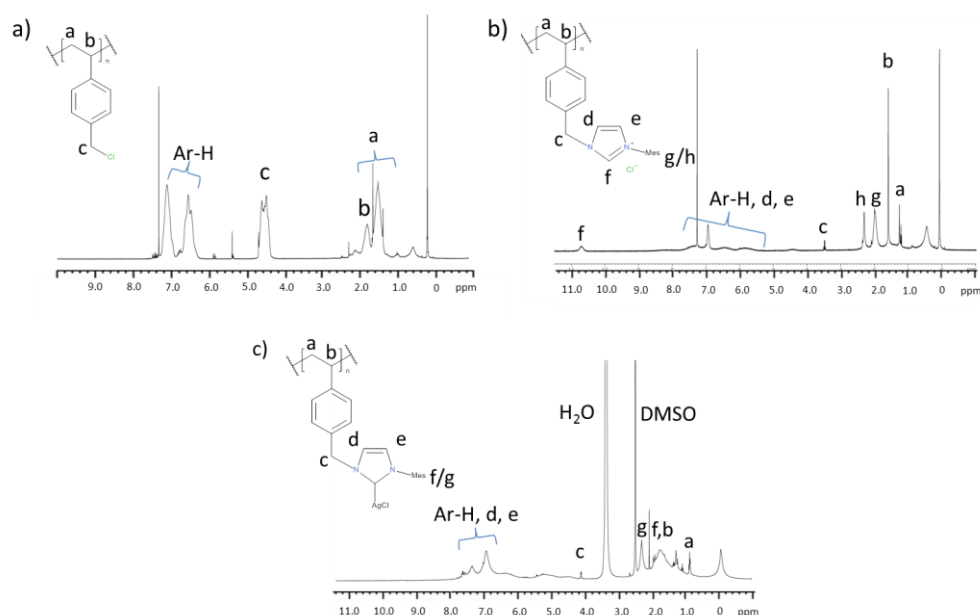


Figure 5.4 ^1H NMR spectra of a) **P1** b) **P2** c) **P3**, as using in the synthesis of **P4**

5.2.2.2. Exemplifying the SABRE Method with an Iridium Supported Polymer P4

A sample containing 5 mg of **P4**, 5 μl of pyridine and 0.6 ml of methanol- d_4 was prepared. The solution was degassed and activated with H_2 . A typical ^1H NMR spectrum obtained from the resulting SABRE hyperpolarised pyridine sample can be seen in Figure 5.5. The observed resonances are labelled as shown. The sample was shaken at 65 G to achieve SABRE.

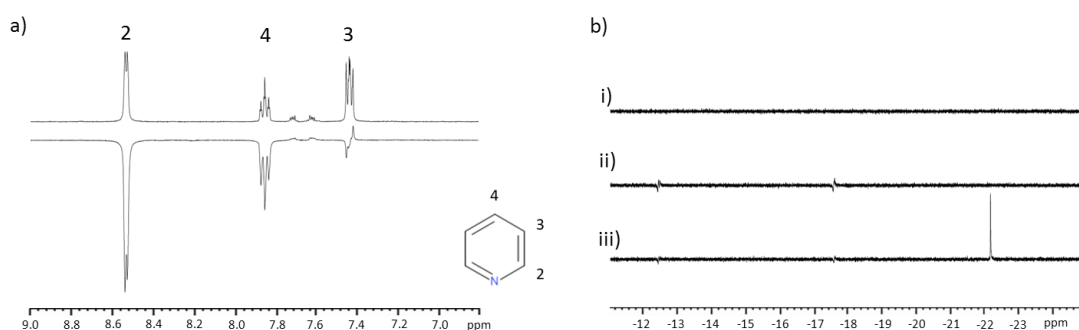


Figure 5.5 Observed ^1H NMR spectra for pyridine resonances, a) the thermal is represented on top and polarised on the bottom shaken in PTF of 65 G, b) corresponding hydride region i) thermal ii) one minute after activating iii) 5 minutes after activating

The thermal trace and hyperpolarised trace show small signals for the *meta* and *para* bound resonances of pyridine in activated **P4**. The corresponding hydride region shows evidence for the activation of the catalyst as a weak set of hydride signals in Figure 5.5 (ii) and (iii). The hydride signal at -22.25 ppm suggests that a symmetric product of the type $[\text{Ir}(\text{H}_2)(\text{NHC})(\text{py})_3]\text{Cl}$ is formed. The levels of signal gain are weak and no further measurements were made with this material.

5.2.3. Encapsulation of a SABRE catalyst.

Encapsulated catalysts can also be classed as single-site heterogeneous catalysts, where catalytic activity is well defined and evenly distributed, within the chemical environment one would expect for a homogeneous catalyst. Recent studies have shown that transition metal complexes trapped in macromolecules may be useful as catalysts, sensors, optical devices and liquid crystals¹⁹⁵. These can be made up of inorganic, organic or composite matrices²⁰⁰⁻²⁰⁴. In the case of inorganic systems, we deal with typically oxidic solids such as silicates, aluminosilicates and aluminophosphates, with a generally high porosity and a large surface area. Examples of this are found in crystallographically ordered microporous molecular sieves (zeolites) or non-ordered mesoporous materials²⁰⁰. When organic, we see a carbon backbone, based on a polymeric material with side functionalities²⁰⁵. Composites are combinations of inorganic and organic matrices in variable proportions.

In this study, it is the incorporation of a transition metal catalyst within an organic polymer bead that has been explored. There have been recent reports by Cavarzan *et al.* 2013²⁰⁶, on the encapsulation of an NHC-Au catalyst within a self-assembled host (Figure 5.6).

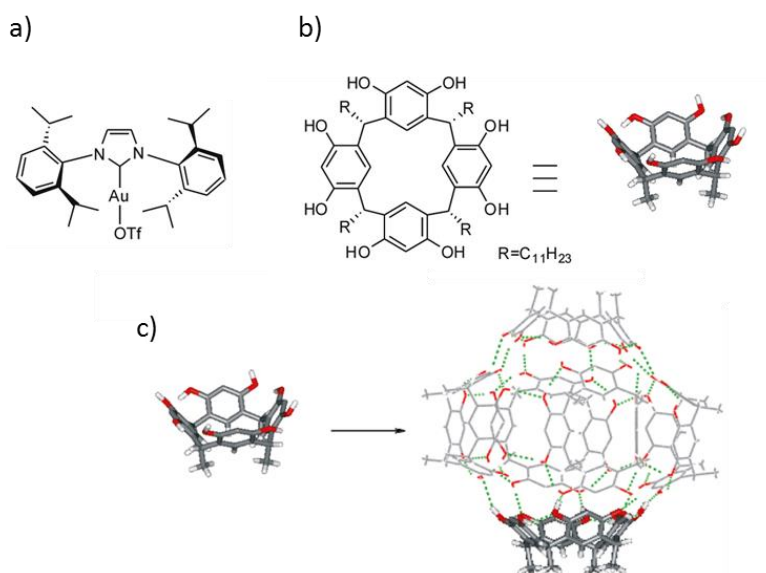
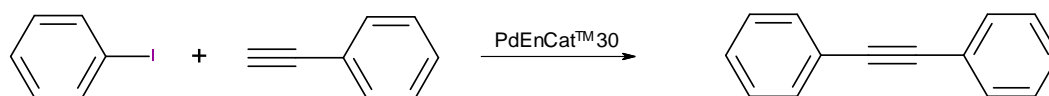


Figure 5.6 Chemical structure of the transition metal catalyst a) *i*Pr-Au-OTf, and the polymer matrices b) resorcin-4-arene, which in wet organic solvent self-assembles to form the encapsulated NHC catalyst, c) a hexameric host. Image taken from literature²⁰⁶

Furthermore Reaxa[®] has developed a range of EnCat[™] catalysts, which can contain a variety of transition metals such as Pd, Pt, Ni and Os. These can be tailored to meet the individual needs of the consumer by altering ligand types, porosity, crosslink density and

metal and ligand loading. Their use has been reported in literature, for a range of reactions including in cross coupling and hydrogenation reactions²⁰⁷⁻²¹⁴. In 2011, Barros *et al.*, used the PdEnCat™ 30 for Sonogashira coupling between haloarenes and acetylenes (Scheme 5.3). It was found that a 0.4 mmol % loading of palladium was optimal and a conversion level of 99 % achieved. Upon recycling of the catalyst, 90 % conversion levels were still achieved for three runs. It has been shown possible to lower levels of leaching by replacing the solvents DMF and toluene with either ethanol or isopropanol¹⁸⁵.



Scheme 5.3 Sonogashira coupling reaction between iodobenzene and phenylacetylene in the presence of PdEnCat™ 30¹⁸⁵

In collaboration with Reaxa®, catalyst **2-c** has been prepared and homogeneously distributed within a polyurea matrix, named IrEnCat. These matrices are made by the high shear mixing of a polyisocyanate monomer and the NHC catalyst (**2-c**), in an organic phase with stabilisers and surfactants in an aqueous phase. The result of this is a fine yellow powder which contains encapsulated **2-c**.

5.2.3.1. Exemplifying the SABRE method with an Encapsulated 2-c Catalyst

The IrEnCat produced in this way was washed with 1 ml of methanol-d₄ to remove any non-encapsulated material present on the solid. A sample containing 10 mg IrEnCat, 5 μl pyridine (0.062 mM) and 0.6 ml of methanol-d₄ was then used to study SABRE. No hyperpolarisation was observed in the corresponding ¹H or OPSYdq NMR measurements for the first 24 hours but after this time, signals are observed. A typical ¹H NMR and OPSYdq spectrum obtained for a hyperpolarised pyridine sample under these conditions can be seen in Figure 5.7.

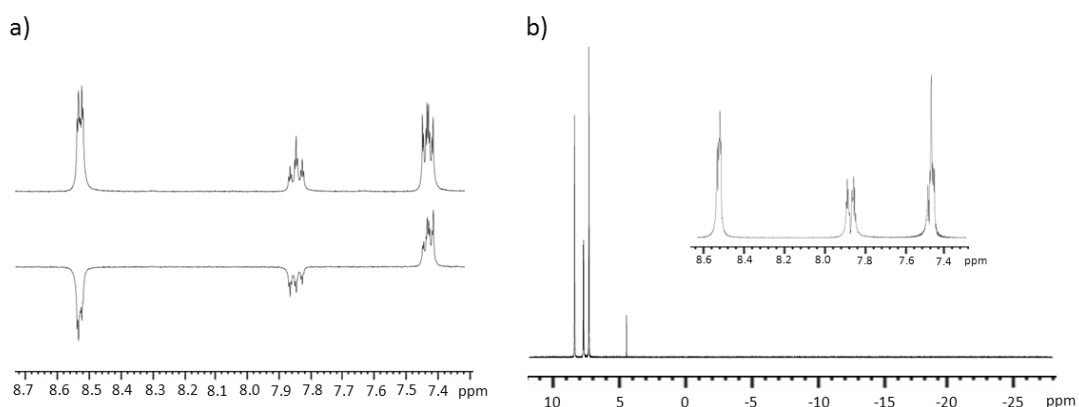


Figure 5.7 Observed NMR signals a) ¹H signals b) OPSYdq (including expansion) for the pyridine resonances under a PTF of 0.5 G

These spectra now show:

- Signal enhancements for resonances 2, 4 and 3 of pyridine as -0.59, -0.62 and 0.53 fold respectively when a PTF of 0.5 G is used.
- No bound pyridine signals or hydride signals are observed for the sample
- The absence of these signals indicates that the catalyst is still encapsulated and has not leached into solution. It was observed in Chapter 2 that activated **2-c** would give rise to hydride signals at -22 ppm in a ¹H NMR measurement.

Since the polarisation enhancement is low in comparison to that achieved with a homogeneous catalyst **2-c**, further SABRE ¹H NMR measurements were made at regular intervals other a further 60 hour period (Figure 5.8). The polarisation enhancements that resulted are summarised in Table 5.1.

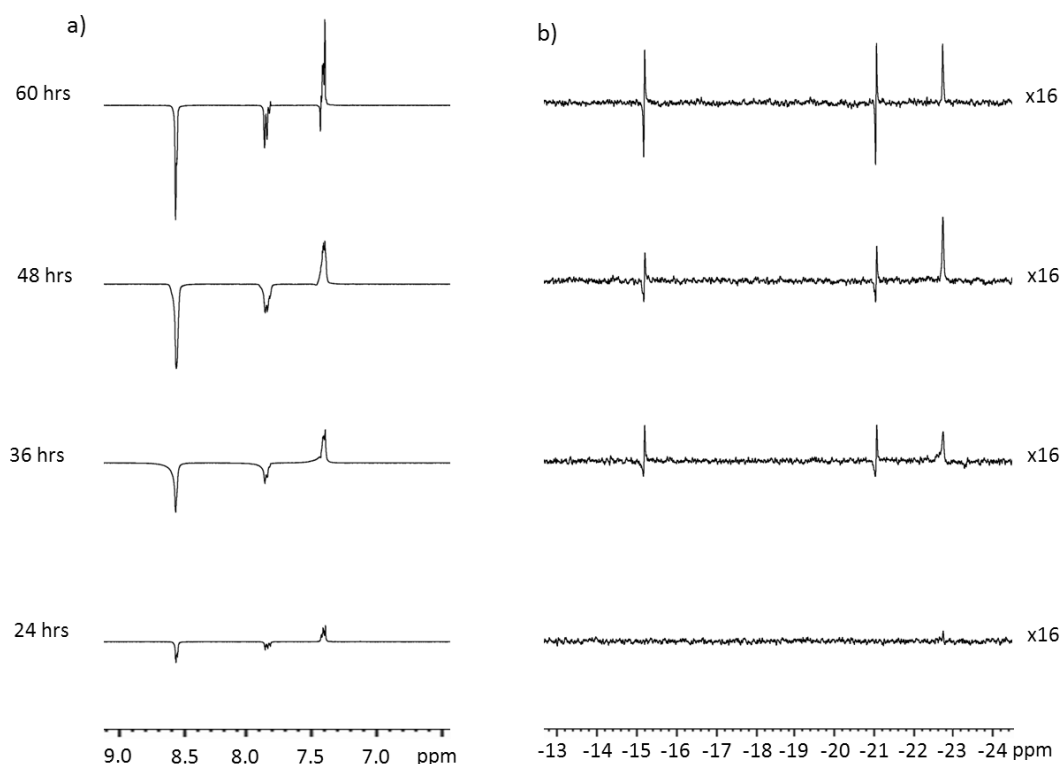


Figure 5.8 Observed ^1H NMR signals observed for pyridine as a function of time a) aromatic region b) hydride region

Catalyst (10 mg)	Time (hours)	^1H Signal Enhancements 0.5 G (position)			^1H Signal Enhancements 65 G (position)		
		2	4	3	2	4	3
IrEnCat	24	-0.59	-0.62	0.53	-4.65	-4.50	-3.01
	36	-2.58	-2.56	1.47	-4.01	-3.58	-4.94
	48	-3.58	-3.47	2.08	-13.37	-12.70	-7.77
	60	-2.47	-2.33	1.75	-9.23	-8.96	-5.43

Table 5.1 Comparison of ^1H NMR signal enhancement levels (fold) observed for pyridine using IrEnCat as a function of time

The 24 hour data confirms that very limited activation has taken place. After 36 hours the formation of both $[\text{Ir}(\text{H}_2)(\text{COD})(\text{IMes})]\text{Cl}$ (**2-c**) and $[\text{Ir}(\text{H})_2(\text{IMes})(\text{py})_3]\text{Cl}$ (**5-c**) is indicated in the hydride region. Over time it can be seen **2-c** converts to **5-c** and hence activation is very slow. The IrEnCat catalyst is not stable as evidenced by the signal for **5-c** also falling with time. The maximum enhancement matches the position where **5-c** is dominant. Based on

previous studies in Section 2.2.7, H_2 can get into the catalyst readily, but when **2-c** is free in solution, it does not add H_2 readily, activating rapidly only in the presence of a suitable substrate such as pyridine and H_2 in under 2 minutes. It can therefore be concluded that pyridine does not enter the polymer bead efficiently.

After 60 hours, the sample was split into two portions, separating the solution and solid of the first cycle for a second cycle. To achieve this, the catalyst was recovered by filtration, used for sample 2 (see later) and the methanol solution retained and placed into a clean Young's Tap capped NMR tube and degassed (sample 1). For Sample 2, the IrEnCat beads were washed 4 times with methanol and then dried in a low temperature oven for 5 hours. A new sample at standard concentrations was then made up containing the dried IrEnCat beads, pyridine and methanol. Both samples were studied using the SABRE method. The corresponding 1H and OPSYdq NMR spectra for sample 1 can be seen in Figure 5.9.

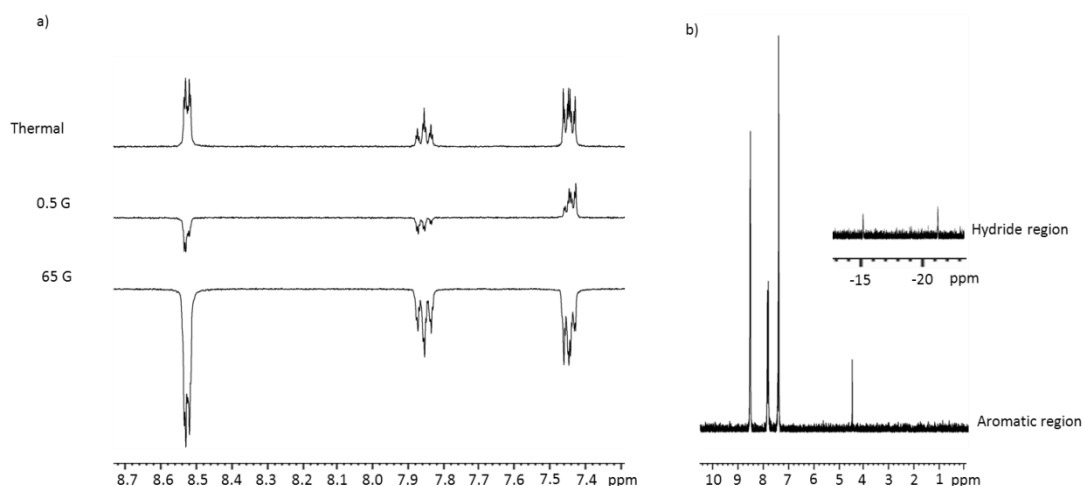


Figure 5.9 Observed NMR signals of sample 1 a) 1H signals b) OPSYdq (including expansion) for the pyridine resonances under PTF of 0.5 G, using Sample 1

Sample 1, which contains only the solution from the previous IrEnCat study, should give an idea to the level of leached material. If polarisation of pyridine is observed, then an amount of catalyst has come out of the encapsulation. 1H NMR signal enhancements are seen for pyridine resonances 2, 4 and 3 of -0.45, -0.51 and 0.59 at a PTF of 0.5 G, and -2.80, -2.64 and -1.51 at a PTF of 65 G respectively. This OPSYdq measurement confirms that I_2S_2 magnetisation is observed experimentally at a PTF of 0.5 G. These enhancement levels suggest that a small amount catalyst **2-c** has leached out from the polyurea matrix.

SABRE was then applied to sample 2. No ^1H or OPSYdq NMR signals were observed for the pyridine resonances over a time period of 60 hours. This suggests that the pore size of the IrEnCat system is too small for the substrate to move freely and that the observable polarisation comes from loosely encapsulated **2-c**, near to the surface of the polyurea bead or the catalyst has all leached out.

A sample containing the IrEnCat, pyridine and deuterium oxide was made to standard concentrations and investigated for SABRE. This test was to see if the encapsulated catalyst was able to work in a biologically compatible solvent. This produced no observable polarisation to the pyridine resonances over a period of 60 hours.

The concept for encapsulation works, but the pore size is too small to allow one of the smallest substrates, pyridine, to pass through to interact with the catalyst. Future work to solve this solution maybe to increase the pore size of the polymer bead and in turn would increase the catalyst size so it can be retained within the pores.

5.2.4. Immobilization of NHC complexes on silica supports.

5.2.4.1. Introduction

Figure 5.10 shows some of the earlier developed silica-supported complexes containing the transition metal ruthenium. In 2001, Kingsbury *et al.* introduced the first silica-supported NHC complex (**S1**)²¹⁵. They used a porous sol – gel material that allowed removal of their catalyst after the reaction yielding a pure product. They studied ring closing metathesis of over 15 diene reagent reactions with high yields of 98 %. However, some loss of ruthenium was detected after each cycle. In 2002, Centinkaya *et al.*²¹⁶, synthesised a different ruthenium silica-supported NHC (**S2**). This was used for furan formation and showed similar activity as the homogeneous catalyst. It could be used for up to five cycles which gave greater than 90 % conversation. In 2002, Mayr *et al.*²¹⁷, reported anchoring a catalyst through the NHC carbene ligand (**S3** and **S4**). An activity of 90 % for these catalysts was reported for ring closing metathesis, but the immobilisation of the second Grubbs catalyst in exchange for a chloride prove to give better stability resulting in lower ruthenium leaching. Fischer *et al.*²¹⁸ reported the anchoring of the catalyst through a phenyl – ether, *meta* to the Schrock carbene. This gave high activity, but recycling of the catalyst showed slow leaching of the ruthenium into the reaction solution. In 2005, Li and Shi.²¹⁹ reported anchoring of the catalyst through one of the side arms of the NHC. This was found to stop

decomposition under reaction conditions. They tested over fifteen ring closing metathesis reactions with five recycles of the catalyst giving greater than 95 % conversion. These catalysts show good development for supporting NHC ligands, and good catalytic activity.

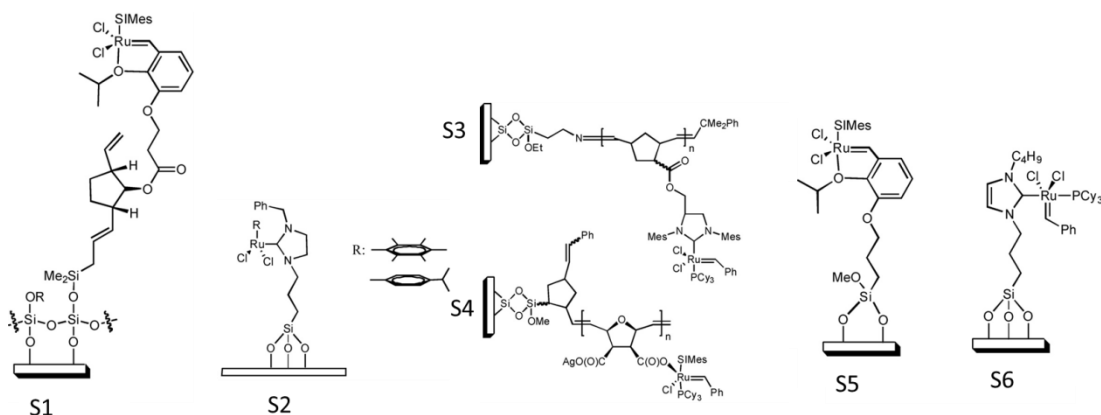


Figure 5.10 Silica-supported S1) second generation Grubbs-Hoveyda, developed by Kingsbury *et al.*, 2001²¹⁵ S2) Ruthenium complex, by Cetinkaya *et al.*, 2002²¹⁶, S3-S4) second generation Grubbs, by Mayr *et al.*, 2002 and Krause *et al.*, 2003²²⁰, S5) second generation Grubbs-Hoveyda by Fischer *et al.*, 2005²¹⁸ and S6) second generation Grubbs-Hoveyda by Li and Shi 2005²¹⁹

More recent developments have considered mesoporous silica, with the most common methodology for the preparation of functionalised materials consists of grafting organosilane precursors onto oxide surfaces²²¹⁻²²⁴. This method provides a suitable way of introducing various organic moieties into the solids, but does not control their distribution in the final material or the nature of the surface species, by formation of mono-, di-, and tripodal species (Figure 5.11 a)²²⁵. This uneven distribution of the final product can explain poor activity compared to the homogeneous catalysis. In contrast to these, recent advances by Maishal *et al.*, 2008²²⁵ have reported the generation of highly mesostructured functionalised materials containing regularly distributed organic moieties along their channel pores (Figure 5.11 b). This method was obtained by condensation of tetraethylorthosilicate (TEOS) and an organotriethoxysilane in a hydrolytic sol-gel process with a surfactant present for obtaining regular distribution of ordered organic structure.

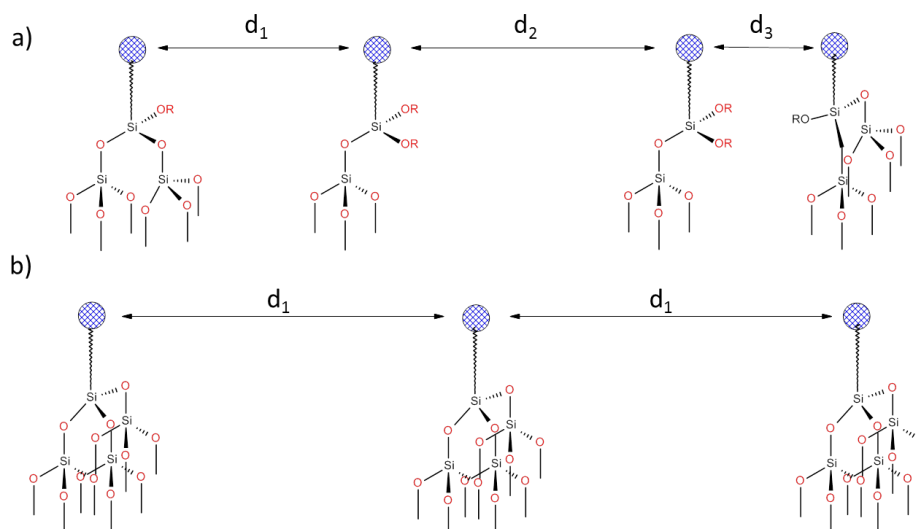
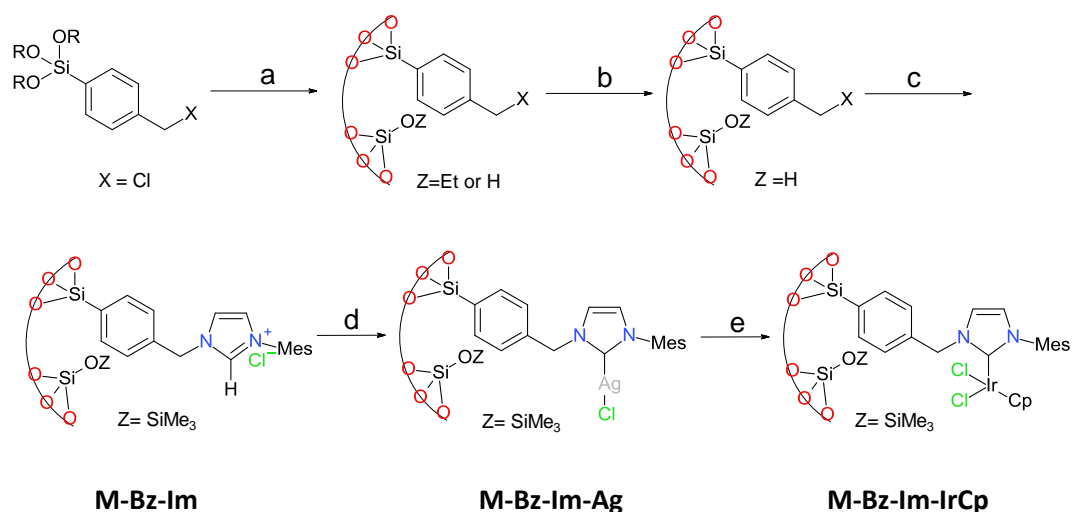


Figure 5.11 A simplified view of grafted oxide material after the grafting reaction (top), and a view of the inner surface of the channel pores of the mesostructured organic-inorganic material²²⁵

The grafting of immobilized catalyst on to mesoporous silica's has advantages over the encapsulation of such materials. The disadvantage due to this size restriction, is that it is difficult to encapsulate larger complexes, and in fact it is difficult for substrates to freely move and exchange with the catalyst centre¹⁹¹.

Here a well-defined single-site Ir-based heterogeneous catalyst has been developed from a tailored hybrid organic-inorganic material, which has been characterised at the molecular level. The preparation of these materials can be seen in Scheme 5.4. They start with a material containing benzyl chloride, which is used to prevent the active site from interacting with the silica surface. The material is then treated with the mesitylimidazole which is grafted to the silica surface through covalent bonds. In most cases, it is necessary to protect the free silanol groups on the surface of the silica, by reacting it with trimethylsilylbromide, thus giving the organic linker sufficient conformational rotation to act as a homogenous catalyst even when it is still anchored to the solid surface.



Scheme 5.4 Preparation of silica-supported material M-Bz-Im-IrCp, a) TEOS, HCl, pluronic P123, room temperature; b) 2 M HCl/H₂O, 45°C; c) mesitylimidazole, toluene, reflux, 2 days, then TMSBr, Et₃N, toluene, room temperature, 48 hour; d) AgOC(CF₃)₃, CH₃CN, 14 h, room temperature; e) [(Cp*IrCl₂)₂], 24 h, 60°C²²⁵

The catalyst activity was measured for H/D exchange reactions between methanol-d₄ and acetophenone, and proved to display similar activity to the homogenous homologues. It was shown that the deuteration occurred selectively at the methyl substituent of acetophenone to yield PhCOCD₃. It was also shown that the solid supported iridium-based material could be reused three times without significant loss of activity and conversion level of 95 % was achieved.

It has been reported by Skovpin et al.²²⁶, that silica-immobilized rhodium complexes, have been used in PHIP heterogeneous hydrogenation reactions. They report the observation of PHIP in the gas-phase and liquid-phase for hydrogenation reactions of propyne and propylene, catalysed by silica-immobilized rhodium complexes which were synthesised by anchoring Wilkinson's complex, RhCl(PPh₃)₃, to a phosphine-modified silica gel.

A ¹H NMR spectrum obtained during the hyperpolarised hydrogenation of propyne is shown in Figure 5.12. The Wilkinson's immobilized catalyst produced stereo-selective *cis* addition of the two hydrogen atoms to the substrate, which is characteristic of the homogeneous form. The NMR results that correspond to the vinyl fragment of the reaction product propylene show antiphase PASADENA NMR signals at 4.74 ppm (H_c) and 5.54 ppm (H_b). The NMR signal at 4.87 ppm (H_d) shows no polarization which would have been indicative of *trans* addition of the dihydrogen, thus the reaction proceeds stereo-selectively through *cis* formation.

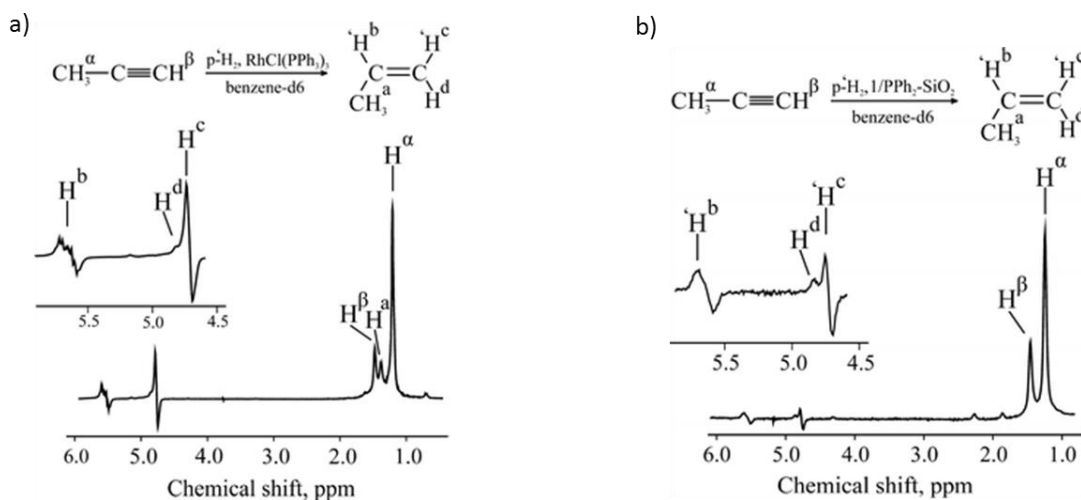


Figure 5.12 PASADENA ^1H NMR spectrum acquired for hydrogenation of propyne by a) homogeneous Wilkinson's catalyst in benzene- d_6 solution at $T = 50^\circ\text{C}$ b) immobilized Wilkinson's catalyst ($1/\text{PPh}_2\text{-SiO}_2$) in benzene- d_6 solution at $T = 70^\circ\text{C}$. Taken from literature reported by Skovpin *et al.*²²⁶.

It is also noted that the homogenous catalyst was more active in comparison to heterogeneous catalyst as the NMR signal for the methyl group of the propylene (H_a) can be seen. The activity was achieved at 50°C for homogenous catalyst but the temperature had to be raised to 70°C for the heterogeneous catalyst to achieve comparable activity. The method for the construction of the heterogeneous material was followed as described in the procedure by Shyu *et al.*²²⁷. It was here, by using this method of anchoring, that the leaching of the rhodium complex from the solid support was minimal, so that all the catalysis proceeds on the immobilized complex.

5.2.4.2. Synthesis of Iridium-NHC complexes supported to mesostructured silica material.

It was therefore decided to investigate synthetic routes to obtaining the two mesostructured silica-based heterogeneous catalysts **M-Pr-Im-Ir** and **M-Bz-Im-Ir** (where **M**=silica support, **Bz** or **Pr** = linker group, **Im**=mesitylimidazole and **Ir**= $[\text{Ir}(\text{COD})\text{Cl}]$), which differ according to the organic linker (Figure 5.13). This work was completed in collaboration with the Thieuleux group, CPE Lyon, where time was spent learning to synthesise these materials before testing them using SABRE.

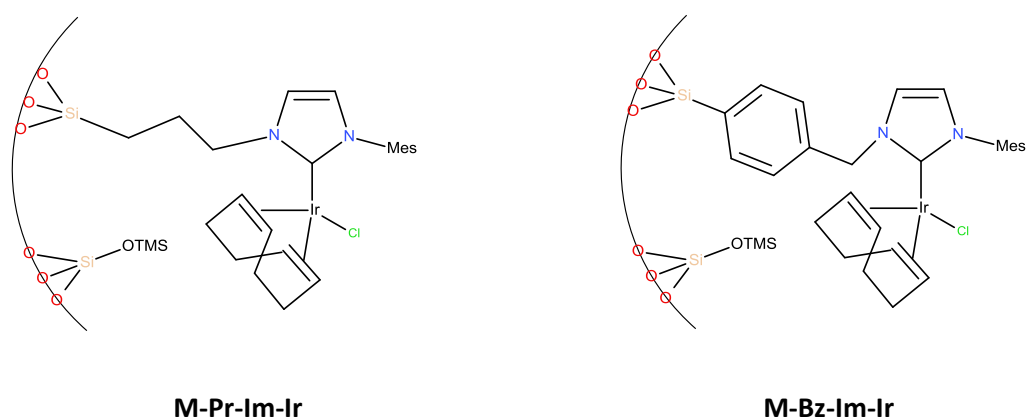
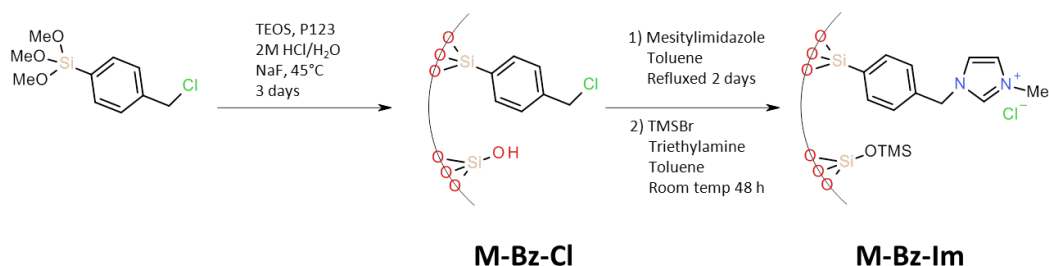


Figure 5.13 Heterogeneous mesoporous silica-supported iridium-NHC catalyst with different linker groups a) propyl: **M-Pr-Im-Ir** b) benzyl: **M-Bz-Im-Ir**

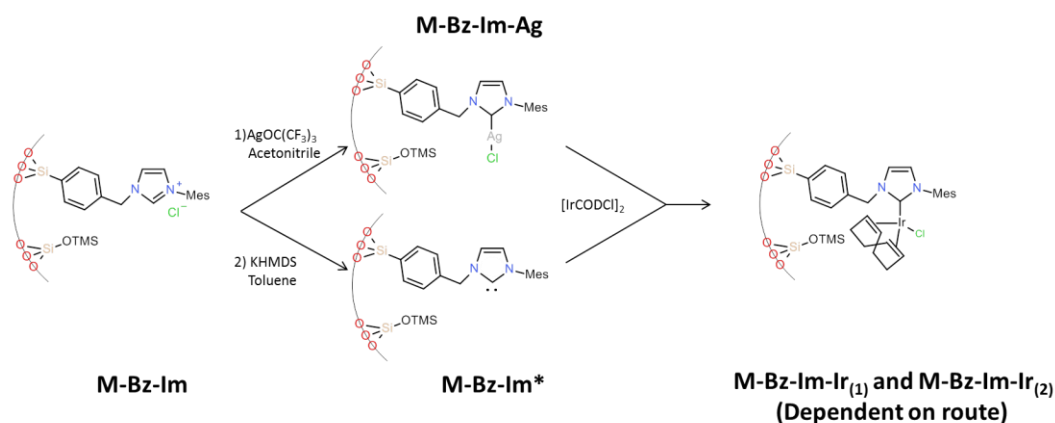
The synthetic method follows that reported by Maishal *et al.*, 2008²²⁵ which can be seen in Scheme 5.5. To an acidic solution containing chlorobenzyltriethoxysilane, pluronic P123 and tetraethyl orthosilicate (TEOS) were added. The reaction mixture was then stirred for 90 minutes until it became transparent. The reaction mixture is heated to 45°C and a small amount of sodium fluoride added whilst stirring for a period of 76 hours. The solid was filtered and washed three times with acetone. The solid was placed in a soxhlet extractor and ethanol used to remove the surfactant over a period of 24 hours. The white solid (**M-Bz-Cl**) was dried at 140°C and under vacuum (10^{-5} mm Hg) and obtained in a yield of 80 %.



Scheme 5.5 Synthesis of materials **M-Bz-Cl** and **M-Bz-Im**

The synthesis of material **M-Bz-Im** involves two steps, 1) addition of NHC, and 2) protecting the unreacted silanol groups. A toluene solution containing **M-Bz-Cl** and mesitylimidazole was refluxed for a period of 52 hours. The solid was filtered and washed three times successively with toluene, methanol and diethyl ether, and then dried under vacuum for 24 hours (140°C , 10^{-5} mm Hg). This produced a white solid which was suspended in a toluene solution with trimethylsilylbromide (TMSBr) and stirred at room temperature for a period of 24 hours. The solid was filtered and washed three times successively with toluene, methanol and diethyl ether, then dried under vacuum for 24 hours (140°C , 10^{-5} mm Hg).

The synthesis of material **M-Bz-Im-Ir** (Scheme 5.6) follows the methods discussed in section 2.23. It can be achieved by method 1 using silver alkoxide ($\text{AgOC}(\text{CF}_3)_3$) to form a supported mono-NHC silver intermediate. This step was followed by transmetalation with $[\text{Ir}(\text{COD})\text{Cl}]_2$ to form a grey solid, **M-Bz-Im-Ir** in a good yield. Alternatively, method 2 can be followed where KHMDS is used to deprotonate the carbene, followed by the addition of $[\text{Ir}(\text{COD})\text{Cl}]_2$ to form a yellow solid, **M-Bz-Im-Ir**, again a good yield was achieved.



Scheme 5.6 Synthetic approach for the preparation of imidazolium salts containing mesoporous silica and the NHC-based organometallic material **M-Bz-Im-Ir₍₁₎** via a) $\text{AgOC}(\text{CF}_3)_3$ and **M-Bz-Im-Ir₍₂₎** b) KHMDS

The mesoporous silicas were analysed (at CPE Lyon) by recording nitrogen adsorption-desorption isotherms to estimate the pore size of the silica and ^{13}C CP-MAS NMR data. Figure 5.14 shows the corresponding ^{13}C CP-MAS NMR data for a) material **M-Bz-Im**, b) **M-Bz-Im-Ir** and c) **M-Bz-Im-IrCp**, the final products of Scheme 5.4 (spectrum taken from literature reported by Maishal *et al.* 2008²²⁵). The broad peak at 140 ppm for the material **M-Bz-Im** corresponds to the imidazolium carbon (NCN), which is absent in the final product. The NMR data are comparable to the data obtained for the homogenous catalyst and that mentioned in literature²²⁵. Further characterisation data can be found in the Experimental Section 7.3.17.

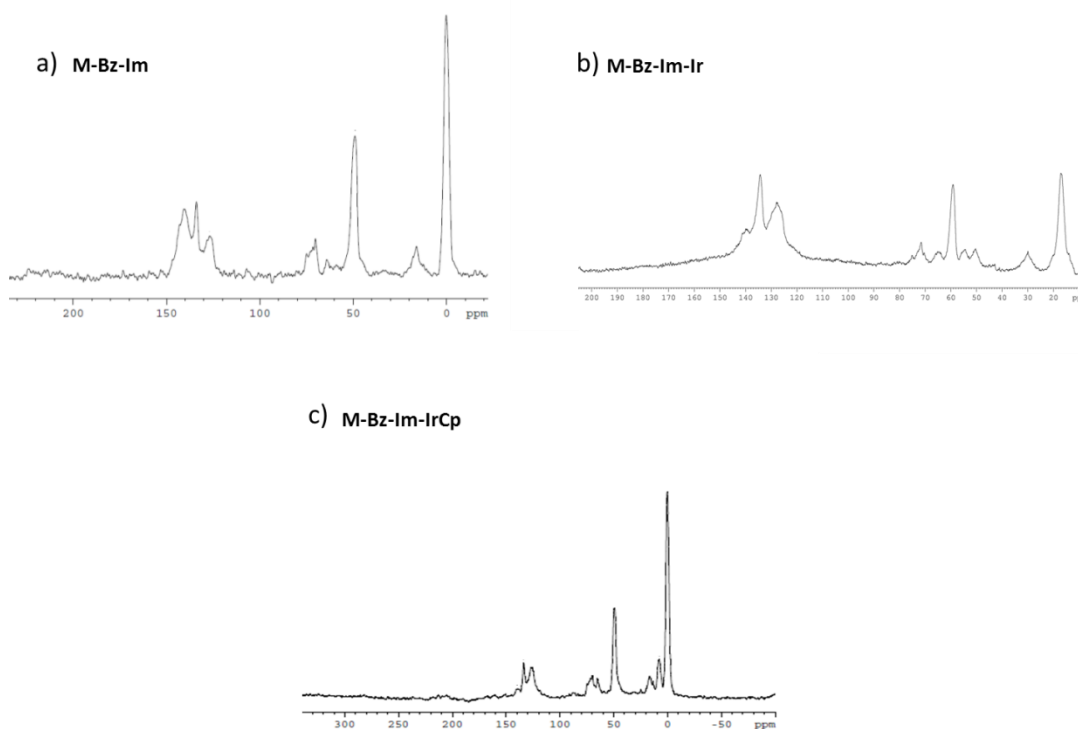


Figure 5.14 Observed ^{13}C CP-MAS NMR data for a) material **M-Bz-Im** b) **M-Bz-Im-Ir** and c) **M-Bz-Im-IrCp**, the final product from Scheme 5.4 which has been taken from literature reported by Maishal *et al.*, 2008²²⁵, for comparison.

5.2.4.3. Exemplifying the SABRE method with an iridium complex supported on mesoporous silica.

This section will investigate three iridium supported mesoporous silica catalysts:

1. **M-Bz-Im-Ir₍₁₎** made via AgOC(CF₃)₃
2. **M-Bz-Im-Ir₍₂₎** made via KHMDS
3. **M-Pr-Im-Ir** made via KHMDS

Catalyst **M-Pr-Im-Ir**, produced no observable ¹H NMR polarisation throughout this study. It has been reported Thomas *et al.*, 2014²²⁸ that the propyl chains fold the imidazolium onto the silica and that it promotes interactions between the transition metal and the surface of the siloxane as shown in Figure 5.15, thus catalyst activity is decreased significantly.

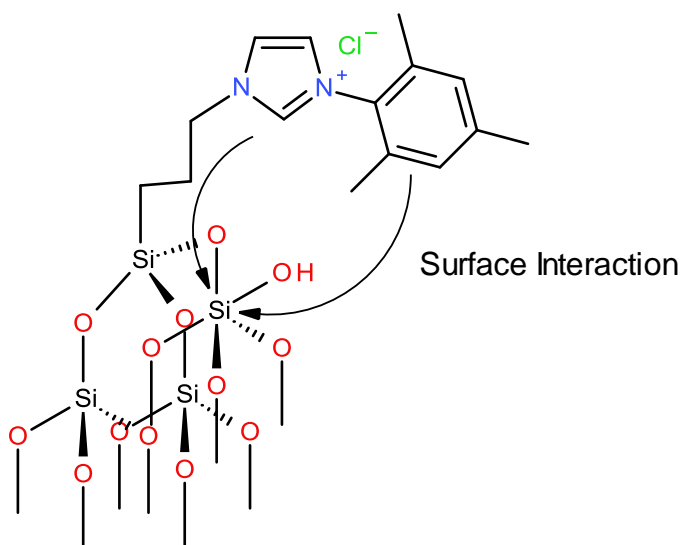


Figure 5.15 Structure of silica material, showing interaction with surface of siloxane bridges²²⁸

A typical ¹H NMR spectrum obtained for a SABRE experiment was obtained using pyridine and catalyst **M-Bz-Im-Ir₍₁₎**, can be seen in Figure 5.16. The spectrum shows no polarisation in the pyridine resonances, but the presence of the antiphase hydrogen signal indicates the *parahydrogen* must undergo reversible interactions with the catalyst, but no polarisation transfer is achieved through the J-coupling into the pyridine protons. Similar activity is observed for **M-Bz-Im-Ir₍₂₎** catalyst. No hydride resonances are observed for either catalyst.

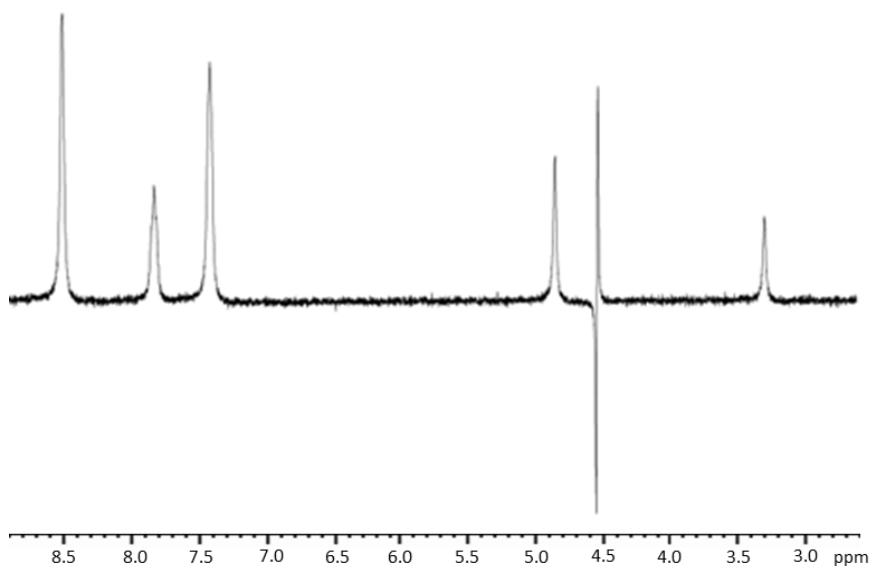


Figure 5.16 Observed ^1H NMR spectrum for pyridine using catalyst $\text{M-Bz-Im-Ir}_{(1)}$, at PTF of 0.5 G. Spectrum shows the antiphase hydrogen signal at δ 4.57 ppm

Further to the initial result, temperature and concentration studies of both catalyst and pyridine were investigated, but no positive results for the polarisation of pyridine resonances were observed. It was noted that after a period of 4 hours, the methanol solution turned from clear and colourless to a cloudy brown/orange colour with further ^1H NMR experiments yielding no antiphase hydrogen signals, thus concluding that the catalyst had destabilised.

A range of substrates were screened (Chapter 4, Table 4.1) using both M-Bz-Im-Ir catalysts. Only nicotinamide produced a positive result for SABRE, indicated by emission-type signals. Figure 5.17 shows observable ^1H NMR signals obtained for nicotinamide using catalyst $\text{M-Bz-Im-Ir}_{(2)}$ at PTF of 65 G. This was obtained by heating the sample to 314 K for a period of 25 minutes prior to the NMR measurement. The enhancement levels for the nicotinamide resonances 2, 6, 4 and 5 are -0.69, -0.13, 0.072 and 0.23 respectively.

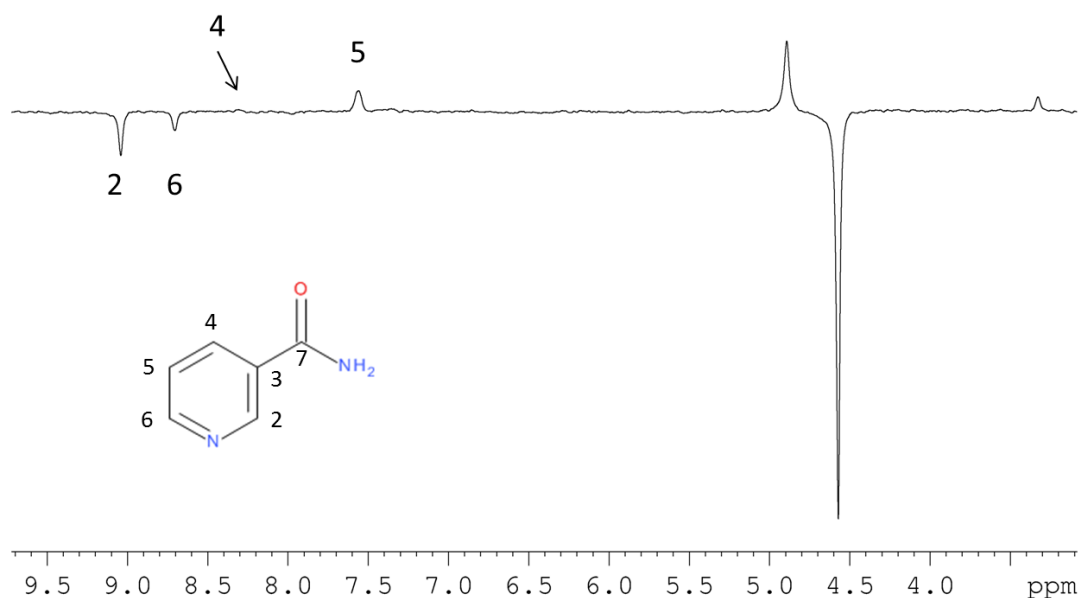


Figure 5.17 Observed ^1H NMR Spectra of nicotinamide using catalyst **M-Bz-Im-Ir₍₂₎**, PTF undertaken at 65 G

The results observed for SABRE activity using mesoporous silica has been minimal. As a control, a sample containing both **2-b** and **M-Bz-Im-Ir₍₂₎** were examined and the resulting ^1H NMR spectra can be seen in Figure 5.18.

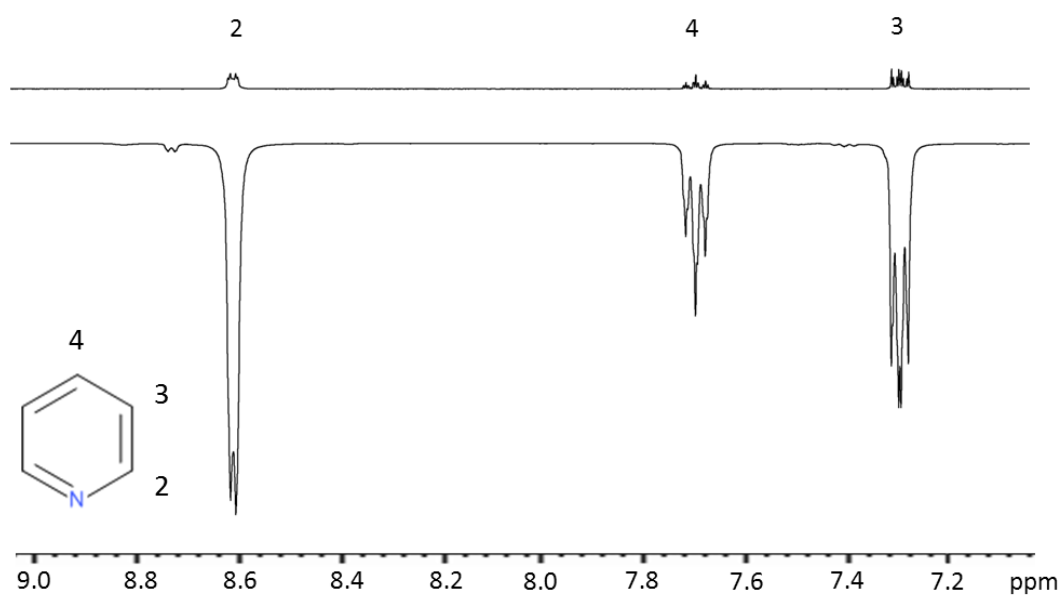
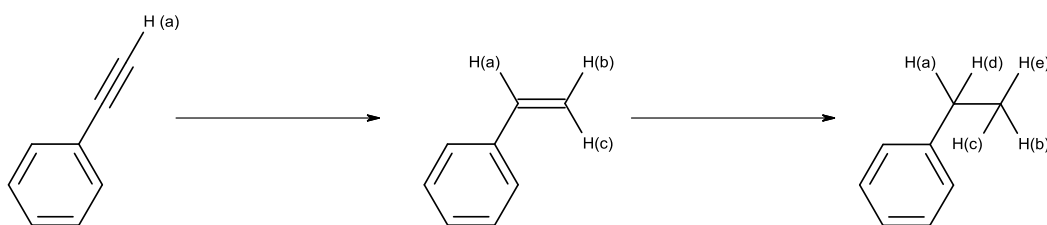


Figure 5.18 Observed ^1H NMR spectra for pyridine resonances when a control sample containing both catalyst **2-b** and **M-Bz-Im-Ir₍₂₎** were shaken in a PTF of 65 G

The ^1H NMR measurements now showed pyridine resonances 2, 4 and 3 that were -32.2, -28.7 and -26.1 fold enhanced respectively. This result is lower to that observed in chapter 3 for catalyst **2-c** alone under identical conditions. Speculatively, **2-c** could be interacting with the surface thereby deactivating the homogenous catalyst.

5.2.4.4. Exemplifying PHIP heterogeneous hydrogenations reactions with an iridium supported mesoporous silica.

Catalyst **M-Bz-Im-Ir₍₂₎** has proven not very active for SABRE, but could be active towards PHIP^{229, 230}. Within this section, and the wider context of producing hyperpolarised compounds, the hydrogenation of the triple carbon – carbon bonds of phenylacetylene (Scheme 5.7) using a catalysts **2-b** (control) and **M-Bz-Im-Ir₍₂₎** would reflect a sensible test. PHIP ¹H NMR experiments are investigated for the catalysts in methanol-d₄ and dichloromethane-d₂ solution.



Scheme 5.7 Mechanism for the hydrogenation of phenylacetylene

Figure 5.19 shows the controlled PHIP ¹H NMR experiment for the hydrogenation of phenylacetylene with catalyst **2-b** in methanol and dichloromethane, which are represented on the same vertical scale. These spectra were obtained by shaking each sample in the stray field of the magnet and interrogating it by ¹H NMR using a 45° r.f. pulse. For the methanol sample, in-phase magnetisation is observed as in Figure 5.19, indicative of ALTADENA. This implies the observed signals were derived from *parahydrogen* predominantly added outside the magnet. In the DCM sample, a different profile is observed, with antiphase magnetisation as shown in Figure 5.20, indicative of PASADENA. This implies the observed signals were derived from *parahydrogen* predominantly added inside the magnet. These data imply that methanol promotes hydrogenation as the reaction begins before the sample is placed into the magnet. As a consequence, in methanol-d₄, it is also possible to observe SABRE-derived signals on the phenyl ¹H NMR resonances of the substrate, where the polarisation is transferred from the *parahydrogen*-derived protons that are now incorporated into the substrate.

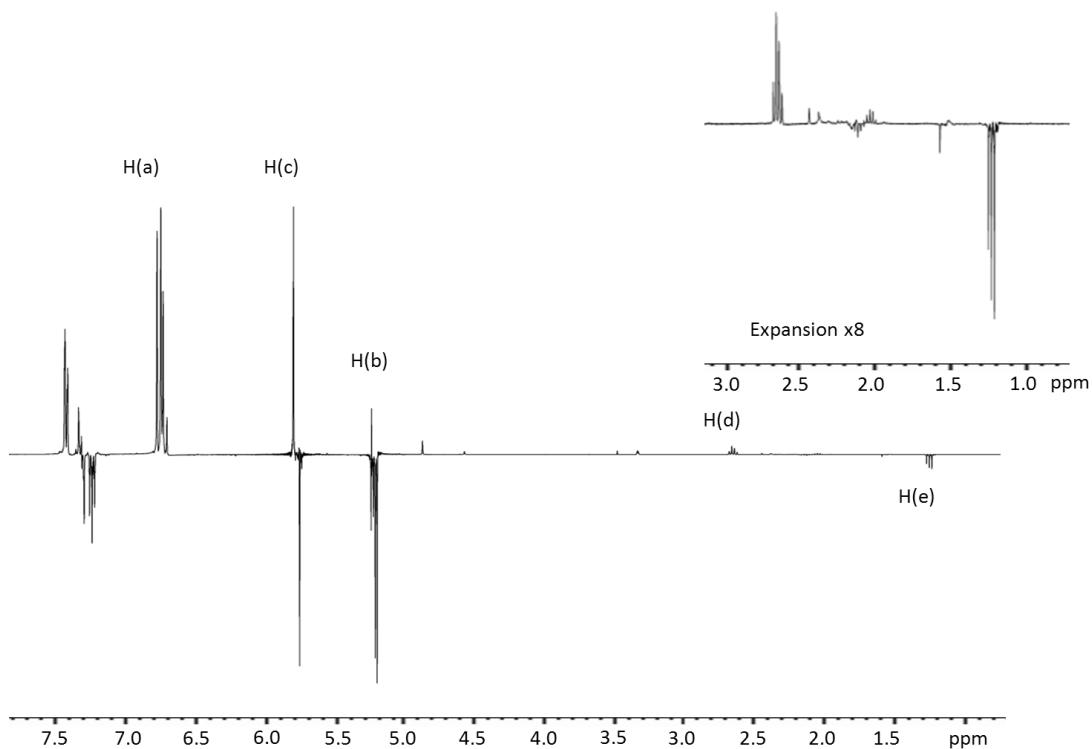


Figure 5.19 Observed ^1H NMR spectra for the hydrogenation of phenylacetylene using catalyst 2-b in methanol- d_4

Polarisation of the olefinic resonances in methanol- d_4 is observable at δ 6.74 (H_a) and 5.21 ppm (H_b), and the H-H coupling constant is 10.92 Hz, which is comparable to the value obtained in dichloromethane solution. The resonance at δ 6.74 ppm shows absorption type character, and the δ 5.21 ppm contains emission type character, which can be seen in Figure 5.19. The resonance at δ 5.78 ppm shows antiphase character and an H-H coupling of 17.78 Hz. The ethylbenzene product is also observable at resonances δ 2.64 (H_d) and 1.23 ppm (H_e).

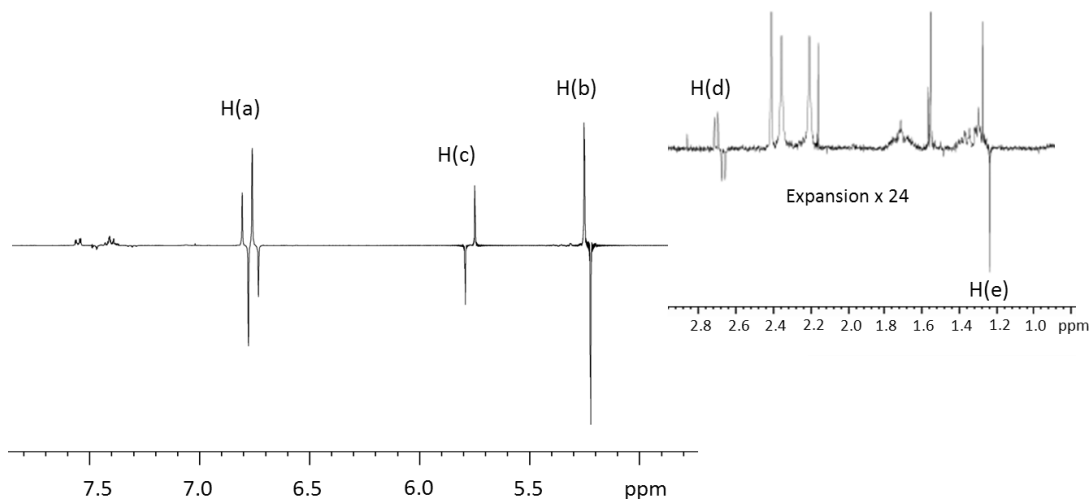


Figure 5.20 Observed ^1H NMR spectra for the hydrogenation of phenylacetylene using catalyst 2-b in dichloromethane- d_2

The sample in dichloromethane- d_2 , also produces polarised olefinic resonances at δ 6.71 (H_a) and 5.24 ppm (H_b) and agrees with what has been reported previously²³¹ indicating that PHIP arises from *cis*-addition of *para*hydrogen to the phenylacetylene triple bond. The δ 6.71 ppm resonances is an antiphase doublet of doublets, and the δ 5.24 ppm antiphase doublet with a have H-H coupling of 10.93 Hz, this is characteristic of *cis* olefinic protons splitting.

The proton at δ 5.78 due to H_c shows a coupling of 17.46 Hz to the proton *trans* to it which resonates at δ 6.71 ppm. This proton comes from the original phenylacetylene substrate and is therefore not strongly enhanced. The hydrogenation of the styrene product to ethylbenzene is evident through the appearance of the resonances at δ 2.67 (H_d) and 1.26 ppm (H_e). Although their signal intensity is weaker than those of the olefinic resonances they are clearly visible.

The comparison of the results obtained in Figure 5.19 and Figure 5.20 reveals:

- ALTADENA and PASADENA type signals are observable for the double hydrogenation product ethylbenzene.
- Greater polarisation is transferred to the aromatic protons in methanol.
- A combination of magnetic states are observable, I_z (H_a , H_b , H_d and H_e) and $I_z S_z$ (H_c) in methanol.
- The dominant magnetic state, $I_z S_z$, is converted to observable antiphase states under a 45° pulse in dichloromethane.

A publication by Harthun *et al.* in 1996, describes the pairwise proton exchange mechanism in styrene during homogeneous hydrogenation with a rhodium and palladium catalyst²³². The spectrum shown in Figure 5.21 are the results of PHIP enhanced proton signals, which exchange through the germinal positions of the terminal alkenes using the rhodium catalyst.

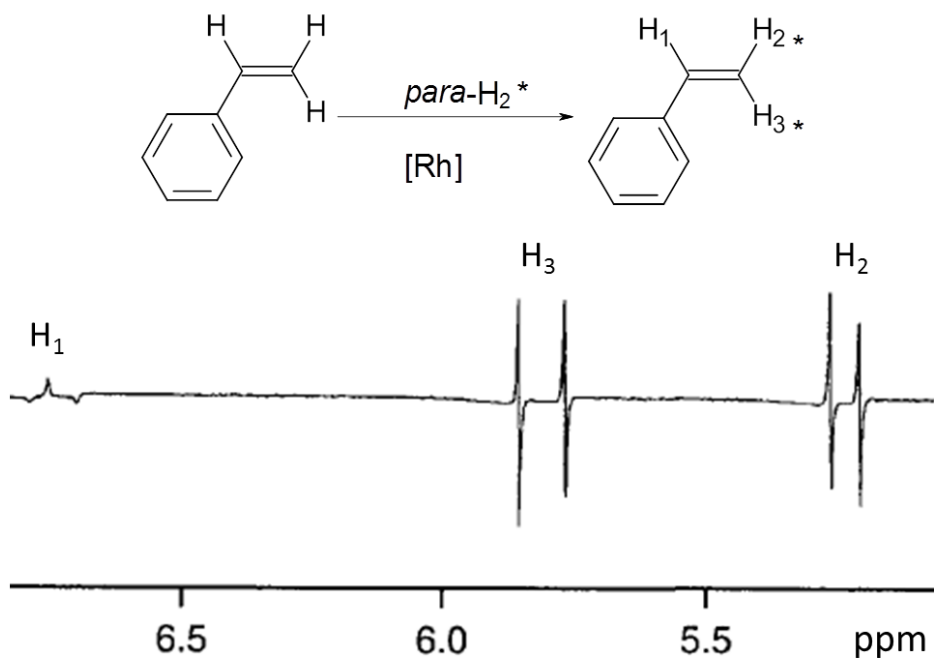


Figure 5.21 ¹H NMR polarisation spectrum of hydrogenation of styrene by a rhodium complex [Rh(COD)(dppb)]BF₄. Spectrum taken from literature reported by Harthun *et al.* 1996²³²

The resulting NMR spectrum that they obtained for the hydrogenation of phenylacetylene with *para*hydrogen can be seen in Figure 5.22 (a). The remaining NMR spectra are from a computer simulation programme, PHIP, which reveals both a pairwise *cis* and geminal hydrogenation occurs.

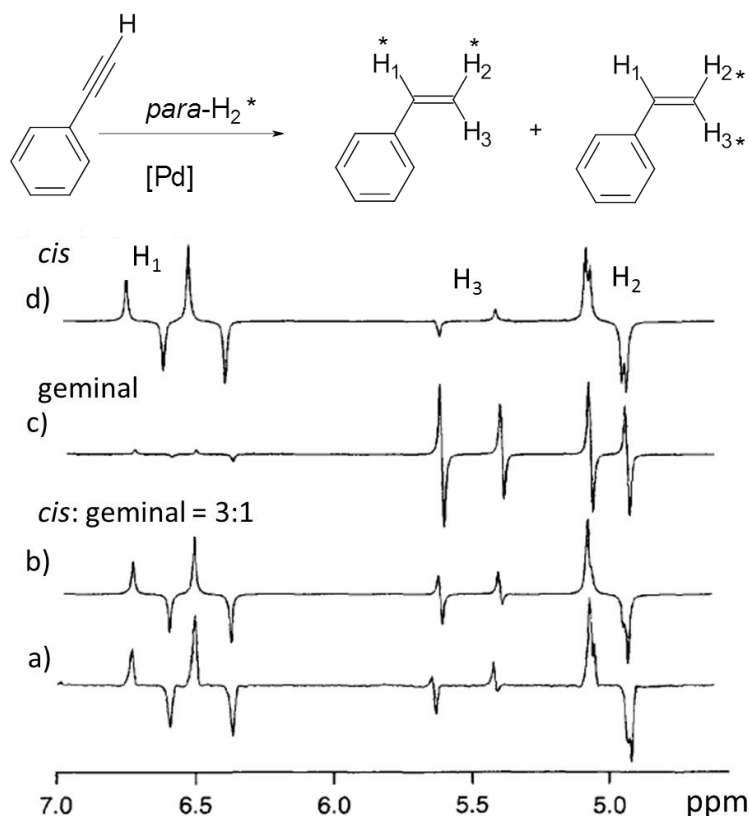


Figure 5.22 ^1H NMR polarisation spectrum of hydrogenation of phenylacetylene by a palladium complex a) experimental spectrum, b) simulation spectrum considering *cis* and geminal-hydrogenation in 3:1 ratio, c) simulation of spectrum of geminal *parahydrogen* into positions H^1 and H^3 , d) simulation spectrum of a *cis parahydrogen* transfer into positions H_1 and H_2 . Spectra taken from literature reported by Harthun *et al.*²³² 1996

The PHIP results obtained using catalyst **2-b** (Figure 5.20) are comparable to the results obtained via *cis* and geminal hydrogenation of phenylacetylene reported by Harthun *et al.*²³²

The heterogeneous catalyst **M-Bz-Ir-Ir₍₁₎** has been examined for the same hydrogenation reaction of phenylacetylene under the same conditions in both methanol and dichloromethane. The results that were obtained in a methanol solution, shown in Figure 5.23, showed signs of some catalytic activity, but it is very limited when compared to the homogeneous catalyst **2-b**. Only resonances at δ 6.74 and 5.21 ppm, corresponding to H_a and H_b respectively, are visible. They appear as antiphase singlets, which is very different to that seen for the homogeneous route. The H_c resonance that was observed at δ 5.78 ppm is not observable. The reaction is therefore much slower and much more selective.

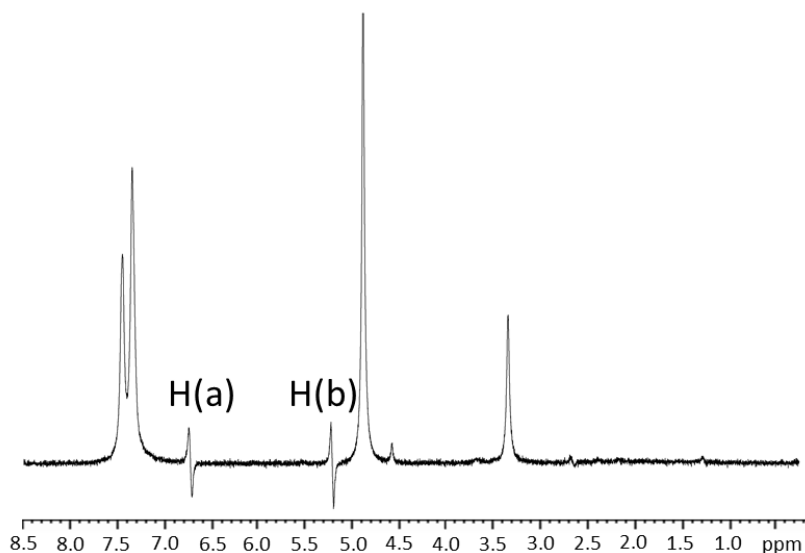


Figure 5.23 Observed ^1H NMR spectra for the hydrogenation of phenylacetylene using material catalyst **M-Bz-Im-Ir₍₁₎** in methanol solution

The **M-Bz-Im-Ir₍₂₎** catalyst was also examined in dichloromethane- d_2 and the resulting spectra can be seen in Figure 5.24. It produced similar results to those observed when using the homogeneous catalyst **2-b**. The polarised olefinic resonances at δ 6.71 (H_a) and 5.24 ppm (H_b) have visible H-H couplings of 10.98 Hz and are antiphase doublet of doublets and antiphase doublets respectively, which is characteristic of *cis* olefinic protons splitting. The H_c resonance at δ 5.78 ppm is an antiphase doublet, which show H-H coupling of 17.76 Hz with the proton *trans* to it at δ 6.71 ppm and agrees with what has been reported previously^{231, 233}. Signals for the ethylbenzene are observable and much weaker than those previously observed for **2-b**. The noticeable difference between the heterogeneous and homogeneous catalyst is that the homogeneous system produces hydride signals at δ -13.60 and -17.93, which are characteristic of a reaction intermediate originating from the activation of the catalyst, which is seen when using **2-b** catalyst when applying SABRE measurement. The lack of hydride signals in the heterogeneous measurements is a good indication that the catalyst is supported on the silica and not leaching off the support.

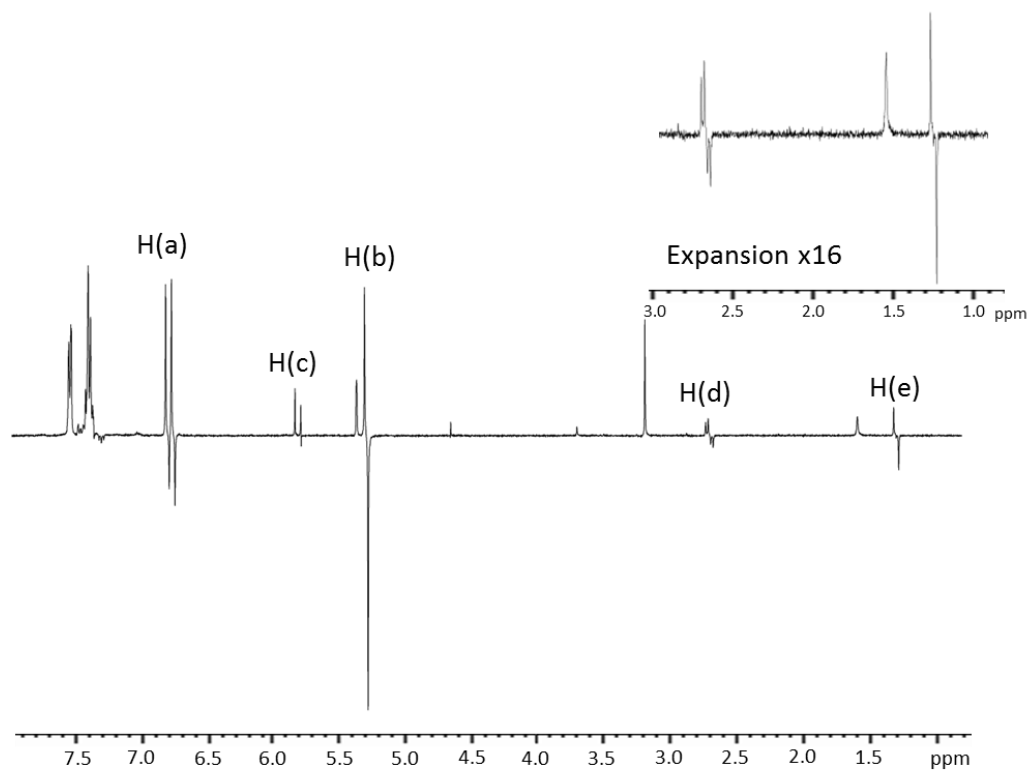


Figure 5.24 Observed ^1H NMR spectra for the hydrogenation of phenylacetylene using material catalyst M-Bz-Im-Ir₍₂₎ in dichloromethane-d₂ solution

5.3. Iridium NHC catalyst used for SABRE in a biocompatible solvent.

The aim of this study was to produce an iridium NHC catalyst to be used for SABRE in a more biocompatible medium. In 2004, Tyagi *et al.*¹⁸⁰ used a 30 % ethanol solution in saline to administer drugs intravenously. A good starting point would be a sample containing 30 % ethanol and 70 % water solution. The studies of the iridium-bound NHC catalyst in this thesis contain either aliphatic or aromatic substituents which increase the hydrophobic properties rather than increase hydrophilic properties thereby increasing water solubility. These catalysts have been tested and found to produce poor solubility in the desired ethanol / water solution²³⁴.

In 2013, Schaper *et al.* published a review containing many synthetic routes to obtaining water soluble carbenes²³⁵. It has been described that by changing the functionality of these NHC substituents, by adding ionic or strongly polar groups, the solubility of these catalysts in water can be increased. The most common ionic groups are sulfonate, carboxylate, phosphonate and ammonium^{236, 237}. Alternative non-ionic methods which can be used include adding hydrophilic ligands or using carbohydrates and polymers^{238, 239}. Examples of these can be seen in Figure 5.25.

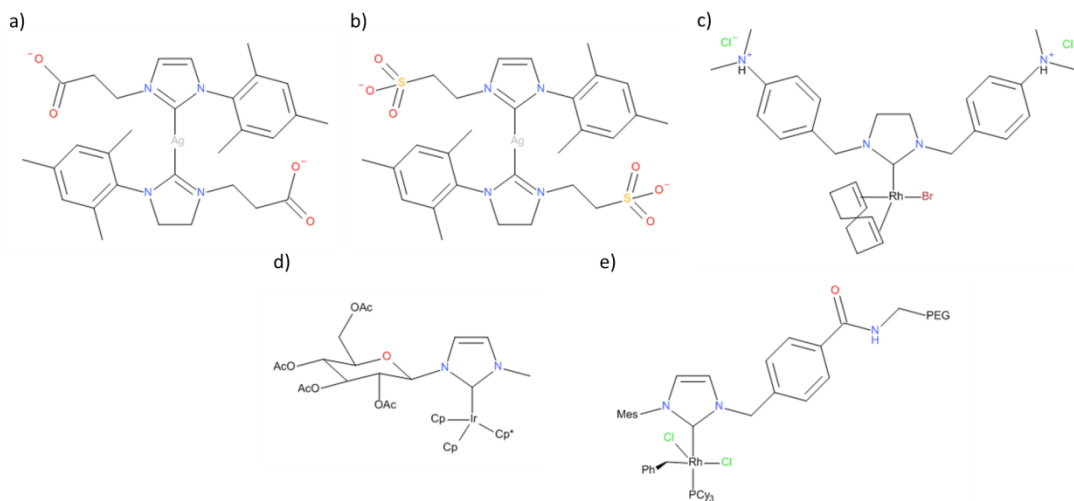


Figure 5.25 Examples catalyst designed to increase solubility by changing the of functionalised NHC substituent group to: - a) carboxylate, b) sulfonate, c) ammonium, d) carbohydrate and e) polymer

In 2011, Bhattacharya *et al.* reported using a 30 % ethanol solution in a PHIP experiment for the hydrogenation of a 2,2,3,3-tetrafluoropropyl 1-¹³C-acrylate-d_{2,3,3} (TFPA). This was used for collecting a hyperpolarised *in-vivo* MR receptor image of the atheroma of a mouse (Figure 5.26)¹⁵⁷.

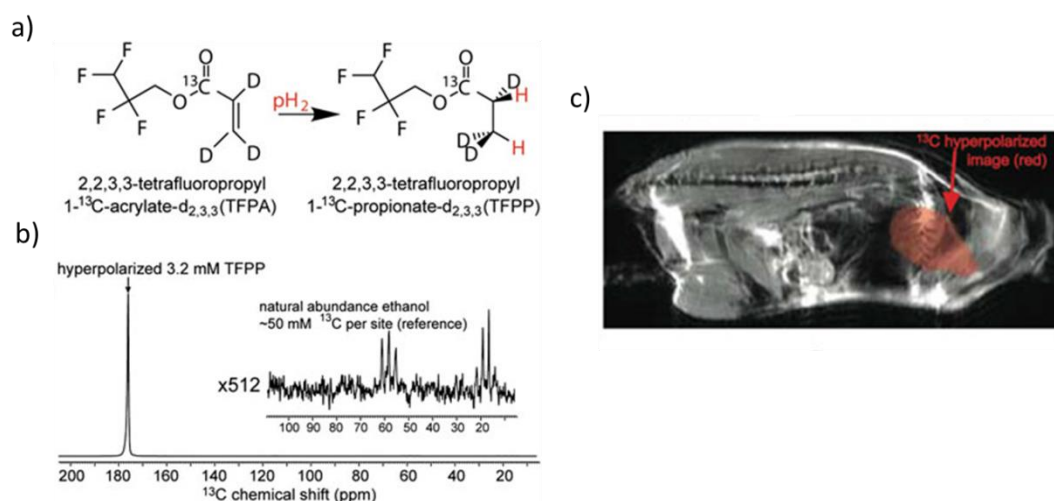


Figure 5.26 PHIP reaction for hydrogenation of (TFPA) in a 30 % ethanol solution, a) scheme of the *cis* addition of *parahydrogen*, b) ¹³C NMR enhanced spectra with 17 % polarisation level obtained on a 4.7 T scanner, including a reference sample of natural abundance ¹³C ethanol, c) *in-vivo* PHIP enhanced ¹³C NMR image using rapid acquisition with relaxation enhancement (RARE) sequence. Images taken from literature reported by , Bhattacharya *et al.* 2011¹⁵⁷

Since research for this thesis began, two publications by Hövener and Zeng have reported low field ¹H NMR and high field ¹H NMR hyperpolarisation of substrates using SABRE in a water solution respectively. In 2014, Hövener *et al.*¹⁷⁶ reported the detection of a pyridine sample in a 90 % water, 10 % ethanol solution for an *in situ* low field ¹H NMR measurement. They quote a 0.02 % polarisation level for the pyridine substrate which was measured on a 7 Telsa spectrometer; this would represent approximately 8 fold absolute signal enhancement level.

Also in 2014, Zeng *et al.* reported 1% polarisation of 3-amino-1,2,4-triazine (ATZ) in a 90 % water, 10 % methanol solution on a 17.6 Telsa spectrometer. This equates to ¹H NMR signal enhancement of 170 fold. This was achieved by activating the sample by bubbling H₂ through the methanol solution for 2 hours. Water was then added and the methanol is removed *in vacuo*. This is then added to the polariser which contained 10 % methanol, bubbled with *parahydrogen* under a PTF of 65 G and a ¹H NMR spectrum recorded (Figure 5.27). They also reported trying to polarise pyridine, isoniazid and pyrazinamide with SABRE under the same conditions, but no enhancements were observed²⁴⁰.

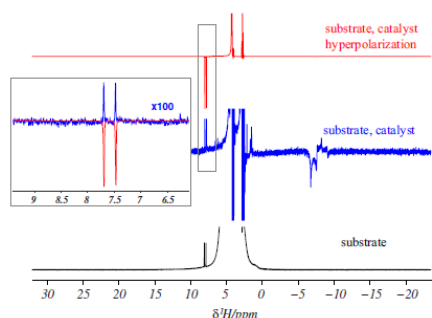
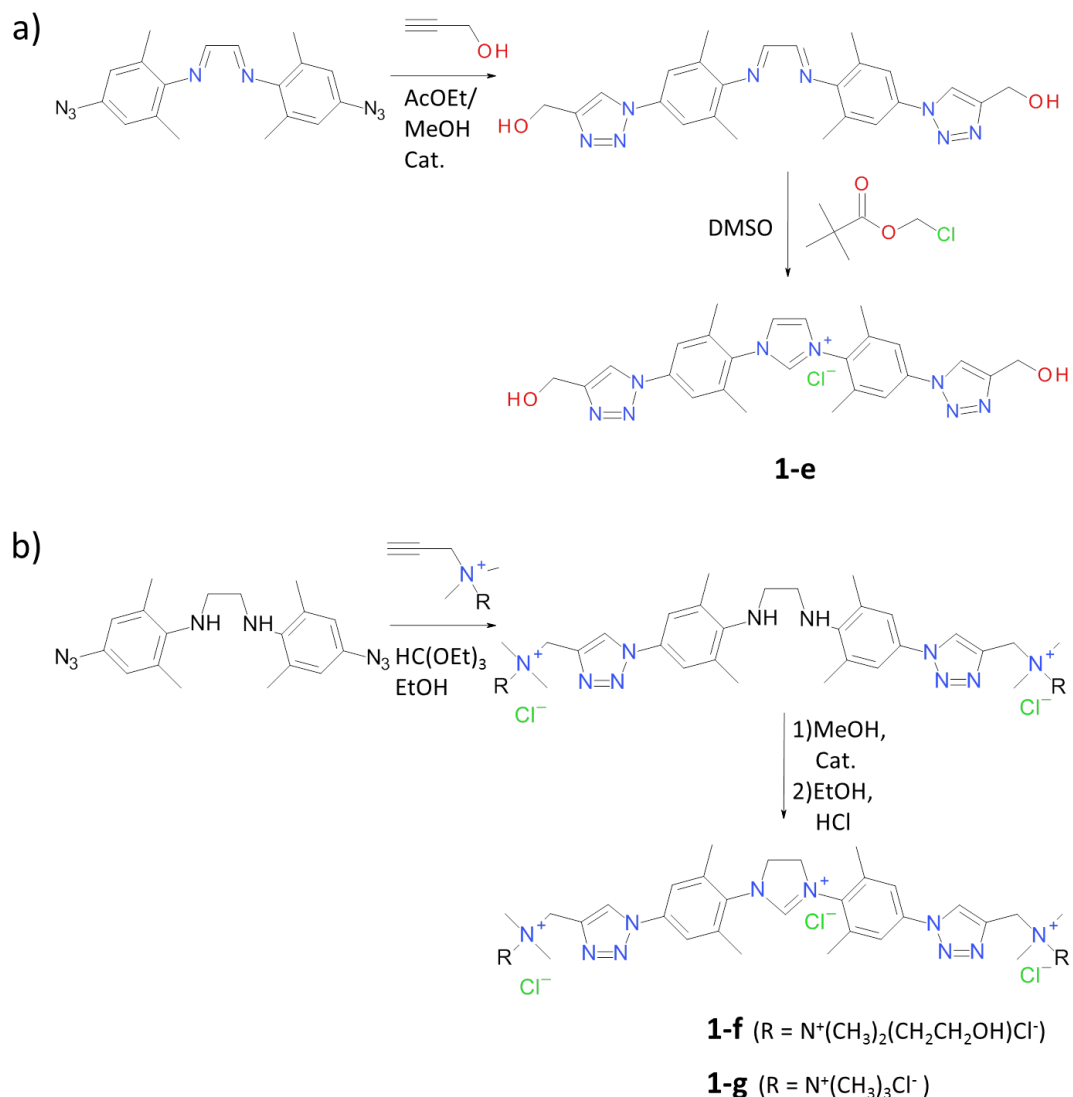


Figure 5.27 ^1H NMR enhancement of ATZ in 90 % water, 10 % methanol at 54.4°C (top), compared to thermal polarisation (middle). The bottom spectrum is of the substrate without catalyst (16 scans). Image taken from literature reported by Zeng *et al.* 2014²⁴⁰

In 2012, Gaulier *et al.* describes a synthetic route to a series of water soluble azolium salts that act as NHC ligand precursors, wherein the common NHC motif is functionalised at the periphery by a triazole ring carrying a protic or a charged group (Scheme 5.8)²⁴¹. The functionalization step involves a copper-catalysed azide alkyne cycloaddition (CuAAC) reaction. This reaction was performed efficiently under Click conditions via a stable and active copper(I)-NHC complex^{242, 243} on synthetically accessible diamine²⁴⁴ or diimine precursors.

After introduction of the hydrophilic moieties, cyclisation was performed by reaction with pivaloyloxymethyl chloride (POMCl, IMes-like backbone) as in our previous reports and for other hydrophilic compounds classically¹¹⁷ with triethyl orthoformate (SIMes-like backbone; SIMes). Preliminary experiments showed that CuAAC could also be performed on the diimine precursor with alkynes bearing ammonium salts. However, no efficient cyclisation conditions could be found in that case (attempted cyclisation's with POMCl resulted in decomposition of the diimine group). In any case, changing from unsaturated IMes to saturated SIMes backbone is well-known to have a limited effect on the behaviour of the NHC ligand²⁴⁵.

Here, the SIMes form bears a cationic quaternary ammonium groups that is derived from choline (SIMesCh²⁺) or trimethylammonium (SIMesTrimet²⁺)²⁴⁴.



Scheme 5.8 Synthesis of azolium salts a) IMesOH – (**1-e**) and b) where R = -N⁺(CH₃)₂(CH₂CH₂OH)Cl⁻ = SIMesCh – (**1-f**) and R = -N⁺(CH₃)₃Cl⁻ = SIMesTrimet (**1-g**)

Starting from these hydrophilic NHC salts, **1-e**, **1-f** and **1-g**, the necessary [Ir(NHC)(COD)Cl] complexes could be synthesised under basic condition. The NHC salt and sodium methoxide were dissolved in a DMSO / ethanol solution and stirred for 18 hours at room temperature. The solvent was removed *in vacuo* to obtain a yellow brown solid at a 60-65 % yield. Full reaction details can be found in the Experimental Section. Figure 5.28 show catalysts **2-e**, **2-f** and **2-g** that will be explored using SABRE in a biocompatible solution.

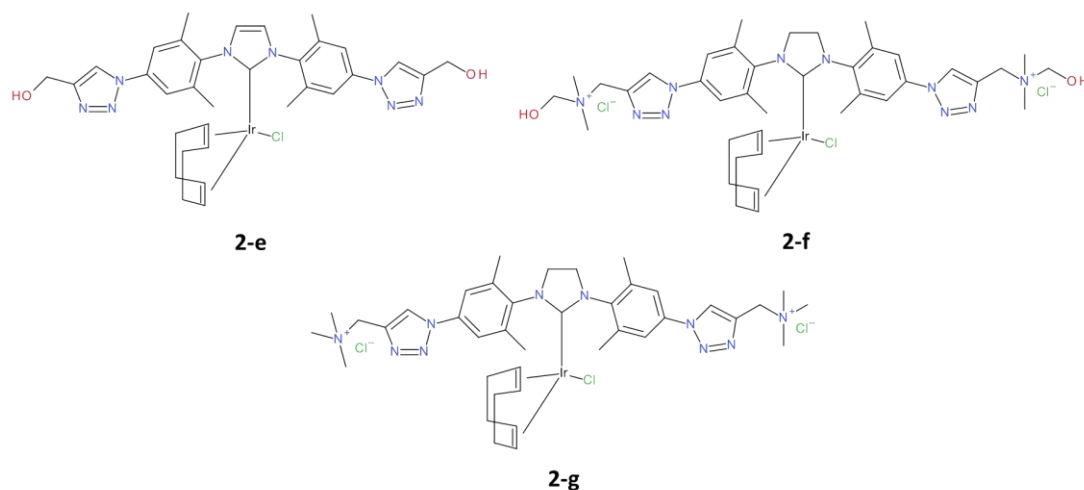


Figure 5.28 Water soluble iridium NHC complexes **2-e**, **2-f** and **2-g** to be tested for SABRE activity in a biocompatible medium

5.3.1. Exploring SABRE efficiency with catalyst **2-e**, **2-f** and **2-g**.

Control measurements for catalysts **2-e**, **2-f** and **2-g** have been employed in a series of SABRE reactions with pyridine and *para*hydrogen in methanol, using method 2. Figure 5.29 shows the ^1H NMR enhancement levels for the three resonances of pyridine (left) and the absolute enhancement level (right) at selected concentration studies of catalyst : pyridine ratio, as a function of PTF.

Catalysts **2-e**, **2-f** and **2-g** produce a hydride resonance in the corresponding ^1H NMR spectra at δ -22.66 , δ -22.54 and δ -22.72 respectively for these species. The pyridine ligand loss rate constant was determined for **2-g** in methanol- d_4 solution at 300 K as 1.2 s^{-1} , whilst that for **2-f** proved to be 0.043 s^{-1} . These two ligand loss rate constants are therefore smaller than that of **2-c** ($[\text{Ir}(\text{IMes})(\text{py})_3(\text{H})_2]\text{Cl}$) but comparable to those of **2-b** ($[\text{Ir}(\text{BzIMes})(\text{py})_3(\text{H})_2]\text{Cl}$). Catalyst **2-e** proved difficult to obtain rate data, due from the exchange process being too slow.

Under standard conditions (19 fold pyridine excess), the most efficient magnetisation transfer for the catalysts is achieved under a PTF of 70 G for catalyst **2-f** and **2-g** and a PTF of 130 G for **2-e**. When comparing the absolute pyridine ^1H NMR signal enhancement, catalyst **2-f** proved to have an enhancement of 791 fold. This is not greatly affected upon changing from 2-fold to 34-fold pyridine ligand excess. Under the same conditions catalyst **2-f** exceeds that of **2-c** which produced the highest absolute signal enhancement of 555-

fold in Section 3.3. It can be seen that **2-g** and **2-e** are relatively poor in comparison only producing a total ^1H NMR signal enhancement of 27 and 10 fold respectively.

In all cases, the *meta* position still remains complex when compared to the results in Chapter 3, although for catalyst **2-f**, presents more ^1H NMR signals in the same phase than the others.

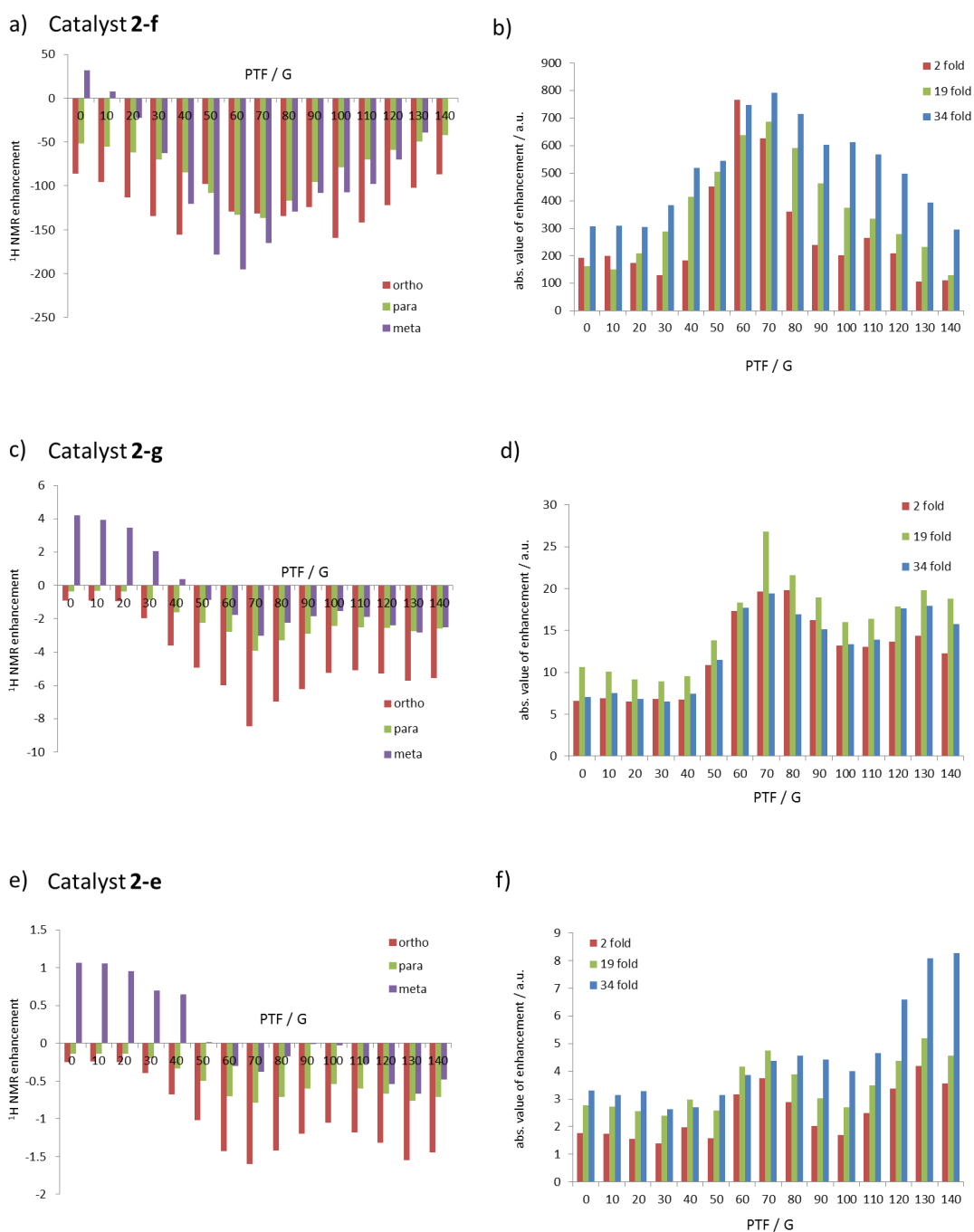


Figure 5.29 Graphical representation of the observed ^1H NMR signal enhancement profile of pyridine (left) and total ^1H NMR signal enhancement (right) obtained in methanol solution using catalyst as a function of PTF using catalyst 2-e, 2-f and 2-g

These complexes were then examined in a 67 % D₂O, 3 % DMSO and 30 % ethanol solution mixture. The resulting ¹H NMR spectra for catalyst **2-f** (Figure 5.30) and graphical representations for catalyst **2-f** and **2-g** can be seen in Figure 5.31 and Figure 5.32 respectively. No SABRE activity was observed for catalyst **2-e**.

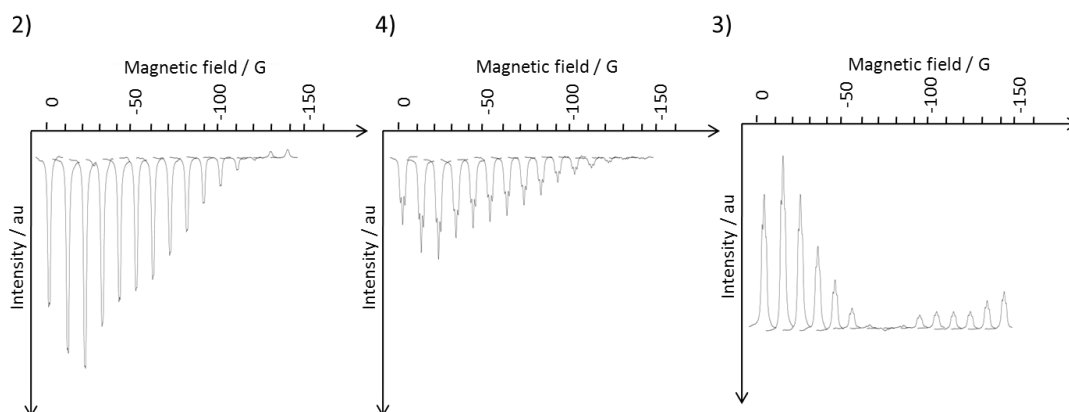


Figure 5.30 Observed ¹H NMR signal intensity changes for pyridine resonances 2, 3 and 4 as a function of the PTF using catalyst **2-f** and method 2 in a 67 % D₂O, 3 % DMSO and 30 % ethanol solution

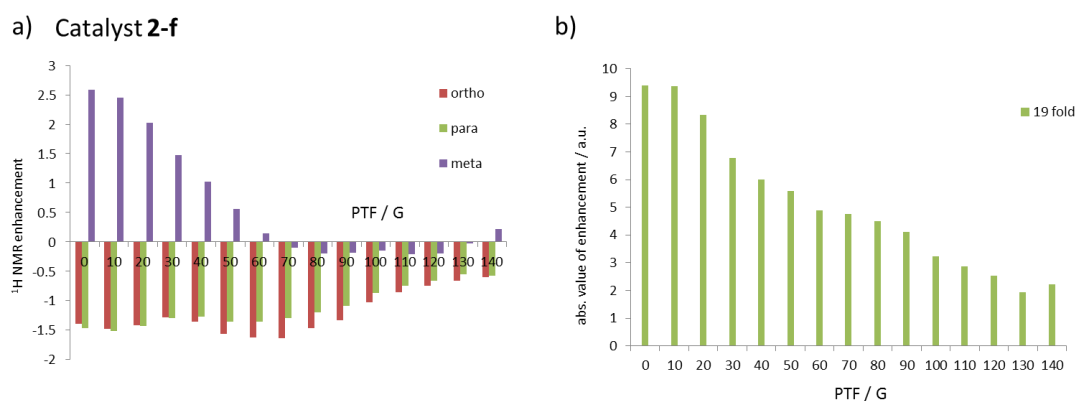


Figure 5.31 a) Graphical representation of the observed ¹H NMR signal enhancement of pyridine using catalyst **2-f** as a function of PTF over the range of 0 – 140 G b) total ¹H NMR signal enhancement, in a 67 % D₂O, 3 % DMSO and 30 % ethanol solution

These data of Figure 5.31 for catalyst **2-f**, show that the *meta* proton delivers optimal SABRE enhancement at PTF of 0.5 G with 2.58-fold, followed by *ortho* under PTF of 70 G with 1.63-fold and *para* under PTF of 10 G with 1.51-fold. The absolute ¹H NMR signal level was achieved at a PTF of 0.5 G with 9.4-fold enhancement. It is also noted that there is little variance in polarisation between the *ortho* and *para* resonances, but as seen previously the *meta* position remains complex, changing phase at a PTF of 60 G from absorption to emission.

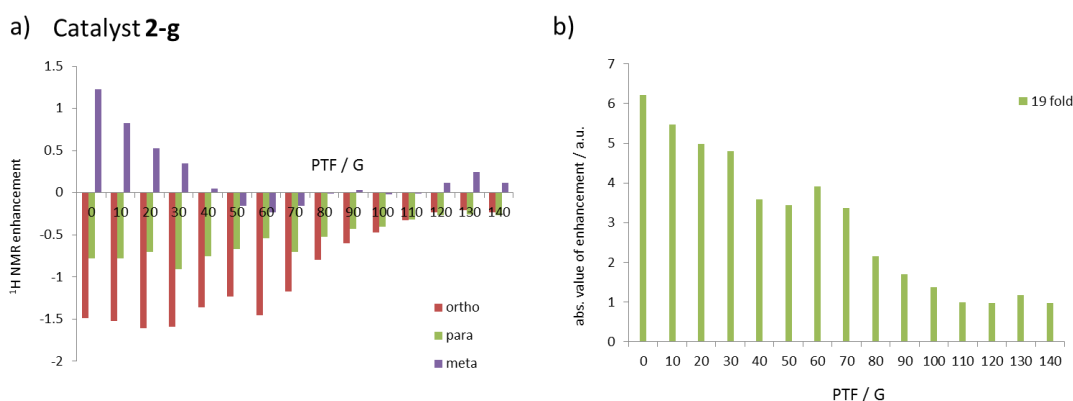


Figure 5.32 a) Graphical representation of the observed ¹H NMR signal enhancement of pyridine using catalyst 2-e as a function of PTF over the range of 0 – 140 G b) total ¹H NMR signal enhancement, in a 67 % D₂O, 3 % DMSO and 30 % ethanol solution

Figure 5.32, for catalyst **2-g**, reveals that the *ortho* position presents the most efficient SABRE activity at a PTF of 20 G with 1.62-fold enhancement level. This is followed by *meta* and *para* positions at PTF of 0.5 G and 30 G with enhancement levels of 1.2 and 0.7-fold respectively. The maximum absolute enhancement level is again achieved at PTF of 0.5 G with 6.2 fold. It is noticeable that the absolute values for both catalysts in the 67 % D₂O, 3 % DMSO and 30 % ethanol solution mixture follow a similar trend, with the polarisation level decreasing as field is increased.

The observed levels of polarisation for pyridine in this biocompatible solution exhibit poor solvent tolerance for SABRE. Even still, these results obtained for water soluble NHC with pyridine are comparable to the results obtained by Hövener who obtained a 8 fold absolute signal enhancement level¹⁷⁶, and better than that reported by Zeng as no SABRE activity was achieved. Fekete *et al.*¹⁶¹ has explored iridium phosphine complexes in the formation of [Ir(H)₂(NCMe)(py)(IMes)(L)]BF₄, where L can be either triphenylphosphine (PPh₃), 3,3',3''-phosphinetriylbenzenesulfonate (*mtppts*) or 3-diphenylphosphinobenzenesulfonate *mtppps*. Pyridine samples measured under the same experimental conditions in a water / ethanol solution, failed to produce any SABRE activity. The study concluded that catalyst containing ligand *mtppps* showed good polarisation into 3-hydroxypyridine producing a 62 fold enhancement under PTF of 140 G.

Pyridine has a relatively poor polar surface area in comparison to the ATZ substrate studied by Zeng²⁴⁰, therefore it is a sensible idea to screen a larger range of more hydrophilic substrates using catalyst **2-e**, **2-f** and **2-g** in the same solvent ratio mixture.

Two substrates oxazole and 3-hydroxypyridine showed activity for SABRE but were only observed when using catalyst **2-f**. The resulting ^1H NMR spectra at the optimum for oxazole can be seen in and graphically in Figure 5.33 and 3-hydroxypyridine in Figure 5.34.

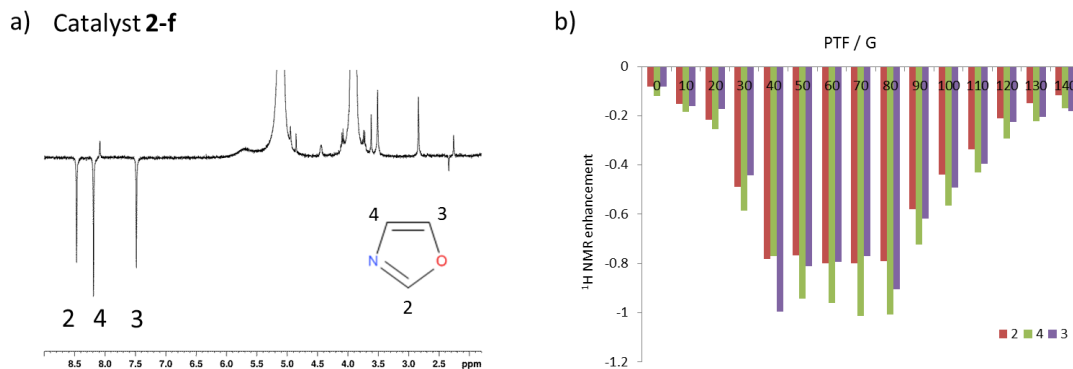


Figure 5.33 SABRE with Oxazole, catalyst **2-f** in a 30 % ethanol solution a) Observed ^1H NMR spectra obtained at the maximum PTF of 80 G, b) graphical representation of the observed ^1H NMR signal enhancement of oxazole as a function of PTF over the range of 0 – 140 G

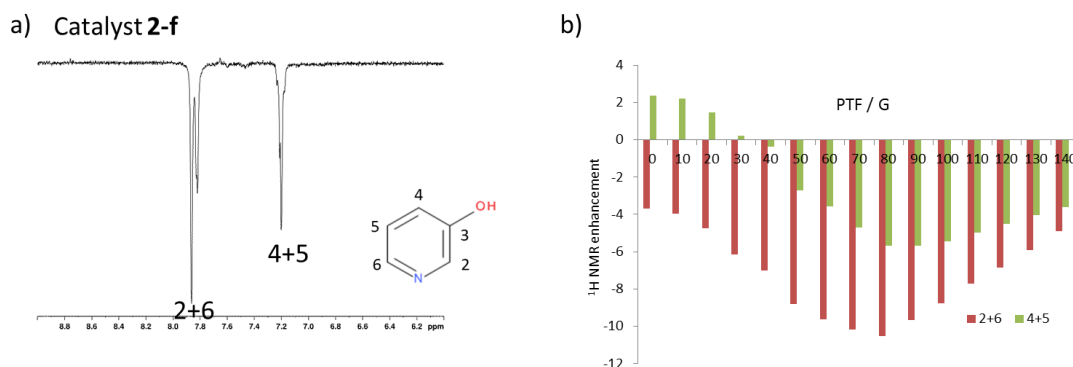


Figure 5.34 SABRE with 3-hydroxypyridine, catalyst **2-f** in a 30 % ethanol solution a) Observed ^1H NMR spectra obtained at the maximum PTF of 80 G, b) graphical representation of the observed ^1H NMR signal enhancement of 3-hydroxypyridine as a function of PTF over the range of 0 – 140 G

It can be observed that the signal intensity of the oxazole sample shows limited SABRE activity producing approximately 1 fold for each of the corresponding proton resonances. This has been tested by the same catalyst in methanol- d_4 producing 8 fold enhancements for each proton resonance. The 3-hydroxypyridine sample has achieved greater polarisation in this medium producing a maximum absolute enhancement level at a PTF of 80 G of 22 fold. The results obtained in the methanol- d_4 solution gave absolute enhancement level of 50 fold. With the addition of the hydroxyl group it has only decreased by half compared to the control hyperpolarised sample, but the hydroxyl group fails to polarise. A comparison

of the absolute signal enhancement for the samples investigated in the 30 % ethanol and 70 % water can be seen in Figure 5.35.

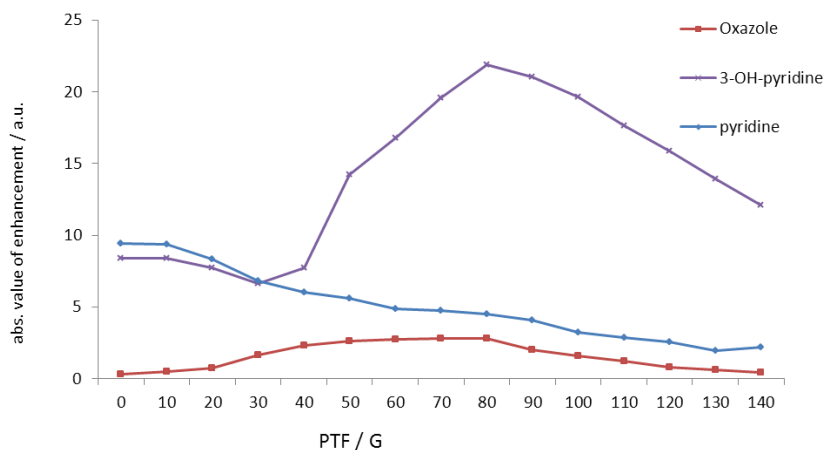


Figure 5.35 Graphical representation of the enhancement levels achieved for oxazole, 3-hydroxypyridine and pyridine for SABRE with catalyst 2-f as a function of PTF over a range 0 – 140 G

5.4. Summary

In conclusion, significant effort has been made to produce a hyperpolarisable mixture that is biocompatible. This was attempted in two ways, firstly to produce a solid-supported catalyst that could be removed from the solution prior to injection. This removes the need to test the toxicity of the catalyst. Secondly, a water soluble catalyst preparation was attempted, as a biocompatible solvent is required for injection, and methanol is not suitable. In an ideal world, these two concepts would be combined to produce a solid-supported catalyst that is effective in either water or ethanol.

With respect to the solid supported catalysts, many different approaches were investigated, including encapsulation, polymer support and mesoporous scaffold. In most cases, significant leaching and poor recycling was observed.

The encapsulation of **2-c** within a polyurea matrix showed promising signs of good polarisation to pyridine, however over a 60 hour period, it was the homogeneous species; $[\text{Ir}(\text{H})_2(\text{IMes})(\text{py})_3]\text{Cl}$ (**5-c**), which had leached that proved SABRE active. It is thought that loosely encapsulated **2-c** near the surface was the component that had leached and the remaining material was still encapsulated, but the pore size of the polyurea matrix was

too small as to allow one of the smallest substrates pyridine to pass through and interact with the catalyst. Polymer **P4**, also showed signs of leaching.

The results obtained using the silica supported material; **M-Bz-Im-Ir₍₂₎** confirmed weak SABRE activity. However the same catalyst displayed PHIP activity for the hydrogenation of phenylacetylene in dichloromethane-d₂, which was comparable to that of **2-b**. **M-Bz-Im-Ir₍₂₎** therefore reflects a suitable catalyst for further study, possibly with a ¹³C labelled material, which could also be used as a substrate for MRI purposes, as it is now ease to remove the catalyst by filtration.

Catalyst **2-e**, **2-f** and **2-g** functioned well in methanol and ethanol solution, but **2-f** performed most efficiently for SABRE, producing an absolute enhancement level of 791-fold. This surpasses that achieved for early work obtained for **2-a**, **2-b**, and **2-c** at room temperature and should be considered for future work. However, upon changing to a biocompatible solvent mixture of 67 % D₂O, 3 % DMSO and 30 % ethanol, the catalytic activity significantly reduced. This can be explained by the low solubility of H₂ in water. This reduction in SABRE activity was also noted for more polar substrates of oxazole and 3-hydroxypyridine, with the latter achieving a maximum absolute enhancement level at a PTF of 80 G of 22-fold with **2-f**. It is worth considering the possibility of widening the substrate tested to include a more polar molecular, ATZ, which was recently reported in literature by Zeng *et al*²⁴⁰. Polarisation in ethanol where H₂ solubility is high followed by dilution with water is the most likely route to establish a viable SABRE process to deliver biocompatibility.

6. Chapter 6 Conclusions and Future Work

6.1. Conclusion

This thesis has demonstrated and expands on previous work for the application of SABRE within high resolution NMR and MRI spectroscopy. The study started by investigating two new catalytic systems, **2-a** and **2-b**, and further expansion of **2-c**, of that has previously reported^{149, 156, 163}. The synthetic approaches have been established for homogeneous and heterogeneous catalysis. Analysis of the activation parameters reveal, that the key factors that affect the SABRE process are the electronic and steric effects of the NHC, which has an influence in the promotion of ligand exchange. The efficiency of polarisation transfer is dependent on the catalyst contact time with the substrate, with an optimum contact time for each catalyst, but no direct correlation can be made versus the TEP or buried volume values for these catalysts.

This work demonstrates that optimisation of key components, catalyst, PTF, temperature and concentration, should be studied when endeavouring to polarise a new substrate. **2-a**, **2-b** and **2-c** have demonstrated their ability to polarise a good selection of biological relevant compounds which have been studied in Chapters 2 and 3 for ¹H and ¹³C NMR measurements. For a ¹³C measurement of any potential new or existing substrate, catalyst **2-c** would be the preferable choice, as the SABRE activity of **2-a** and **2-b**, becomes very poor when moving away from just testing a pyridine sample. For a ¹H NMR measurement of a pyridine, at room temperature, the catalyst order catalyst order for enhancement would be **2-c** > **2-a** > **2-b**, but if temperature could be control more accurately using the mixing chamber, then at higher temperature catalyst **2-b** would be the catalyst choice. **2-b** performs at its optimum at approximately 330 K which can produce an absolute enhancement level in excess of 800-fold enhancement, under standard concentrations. When this is extended to pyridine type ligands such as 3-methylpyridine, 4-methylpyridine and nicotinamide a similar trend is noted, producing absolute total enhancements of 739, 1643 and 985-fold respectively, which greatly surpasses the SABRE activity of the two other catalysts. Initially these results for **2-b** were surprising given the fact that the complex should be more stable and hence undergo slower ligand exchange, but mentioned previously optimum contact time is dependent on the catalyst chosen. If the temperature of a sample containing **2-b** could be raised further beyond the limitations of the methanol solvent, then the possibility of increasing polarisation to the substrate could be achieved.

The effect of PTF plays significant role in achieving the optimum enhancement levels when studying these pyridine type substrates, especially the *meta* position, as this was found to be quite complex. A SABRE experiment generates both single spin longitudinal (I_z) order and multiple spin longitudinal order (I_2S_z) terms and later which has now become observable due to the possible fact that a slight imperfect 90° pulse has been applied. Given that the amplitude of these states is not equal, the detected signals can therefore be complex. Care therefore needs to be taken when examining *meta* proton signals, and a PTF of 80 G would be a good choice to study these substrates. This may not be at the maximum enhancement level but it would produce a good overall representation and moves away from any complicated antiphase signals at arise between field of 0.5 and 50 G. The relevance of these enhancement levels that SABRE generates, can save time and money, when trying to generate a similar measurement under thermal conditions. A signal enhancement of 10-fold obtained for pyridine would take 14 hours to record a similar spectrum under thermal conditions (when $T_1 = 10$ seconds, and to fully relax $5 \times T_1$).

A future application for the SABRE technique is to be able to make an *in-vivo* MRI measurement. The challenge with making a MRI measurement is lifetime of the ^1H hyperpolarised signal that is to be detected. 5-methylpyrimidine is a good candidate for such measurement, as it possesses a long T_1 value, and time required for the polarised state to return to thermal equilibrium is in the order of 150 seconds. The optimum conditions which would be recommended for ^1H , ^{13}C , ^{13}C INEPTrd NMR measurement and for RARE, FLASH and FISP MRI measurements are summarised in the table below.

Measurement	2-c [mM]	5-methylpyridine [mM]	PTF (G)	Absolute Signal-to-noise
^1H	0.5	1	70	2063 [^]
^{13}C	7.5	150	65	294
^{13}C INEPTrd	7.5	150	0	145
RARE	5	200	65	105
RARE vs Phantoms	10	200	65	0.6 [#] , 10.0 [*]
FLASH vs Phantoms	7.5	150	65	0.6 [#] , 1.2 [*]
FISP vs Phantoms	15	300	65	0.5 [#] , 0.9 [*]

Table 6.1 Recommended optimal conditions for the desired NMR or MRI measurement, including catalyst and substrate concentration and PTF. Listed in the table is the absolute signal-to-noise values achieved at these optimum conditions. [^]absolute signal enhancement, signal-to-noise ratio of the hyperpolarised 5-methylpyrimidine signal versus that of [#]water and ^{*}oil

For high resolution MRI, longer acquisition times and multiple scans are required to achieve the desired image quality. Preliminary results used the FISP sequence with a total 9 second acquisition, which allowed the consecutive collection of eight images from a single polarisation step. FLASH protocol would also be recommended for these studies as it may give fewer artefacts as it is less sensitive and works well with molecules with a long T_1 .

The results from quinazoline revealed that it is possible to use SABRE and NMR to follow the unexpected hydrogenation reaction of quinazoline to form 3,4-dihydroquinazoline. Both the product and reactant proved to be SABRE active and consequently the metal catalyst not only mediates polarization transfer but also facilitates substrate hydrogenation. Combined with DFT calculations, it was able to confirm the proposed substrate hydrogenation reaction occurred through a rare outer-sphere pathway.

Whilst the thesis has shown good progress for the application of SABRE, the biggest challenge in progression to obtaining an *in-vivo* MRI image, which would include the removal of the catalyst and secondly a more biocompatible medium is required. This thesis as shown some possible routes to anchoring NHCs to a variety of supported material. The results here are not fully conclusive as they all exhibit poor activity for SABRE, and high leaching of catalyst, with the exception to the latter for that of the mesoporous silica material. However these mesoporous material **M-Bz-Im-Ir**, proved to be active for PHIP hydrogenation of phenylacetylene and showed good activity compared to the homogenous catalyst **2-b**.

As SABRE is routinely carried out in methanol, the work in this thesis attempts to move from this solvent to a more biocompatible solution of 70 % water and 30 % ethanol. This included the design of water soluble NHCs, which was achieved by changing the functionality of these NHC substituents, by adding ionic or strongly polar groups. It was found that catalyst **2-f** surpasses the SABRE activity found when **2-a**, **2-b**, or **2-c** for a pyridine and in methanol, under standard conditions. Upon moving to a 70 % water and 30 % ethanol solution, the enhancement levels fall, which can be explained due to the lower H_2 solubility in water. The observed levels of polarisation for pyridine in this biocompatible solution exhibit poor solvent tolerance for SABRE. Even still, these results obtained for water soluble NHC with pyridine are comparable to the results obtained by Hövener who obtained a 8 fold absolute signal enhancement level¹⁷⁶, and better than that reported by Zeng²⁴⁰ as no SABRE activity was achieved. It is worth considering the possibility of

widening the substrates tested to include a more polar molecular as **2-f**, showed an increase in polarisation when 3-hydroxypyridine was tested.

6.2. Future Work

Since completing this thesis, a new technical piece of equipment has been purchased, which is a temperature control unit for the mixing chamber. This will enable to investigate the array of catalyst which has been developed to study the temperature and magnetic field dependence values with greater accuracy. This would conclude the good SABRE activity exhibited by catalyst **2-b** at higher temperatures, which could be further tested with an array of other substrates, including 5-methylpyrimidine with greater ease. Another advantage of this temperature unit is that if being used for *in-vivo* studies then optimum working temperature for the catalyst would have to be approximately 35°C, which is close to internal body temperature. Catalyst **2-b** would be a good candidate as it achieved greater SABRE activity when compared to catalyst previously examined.

The key areas which have already continued work, is with the development of 5-methylpyrimidine. To date this has presented itself as a suitable substrate for *in-vivo* imaging. If the synthesis of the deuterating these substrates could be improve, then it would increase the T_1 of these molecules, maximising time given to achieving an *in-vivo* image following injection.

If the heterogeneous route was to be continued, then the challenge to overcome the relaxation and the bulkiness of these catalyst would have to be addressed, which lead to the poor SABRE activity. This could be achieved by trying new catalysts, and other possible routes to anchoring through the iridium.

An area of interested is the development to remove the catalyst from the solution. It is understood that a bi-pyridine disulfonic acid molecule will deactivate the catalyst complex by binding tightly. If the pH is increase then the catalyst would precipitate, and be able filtered out of solution. The challenges here would be able to achieve this in a time scale before an *in-vivo* measurement and secondly the biocompatibility process, with another suggested route to polarise in 100 % ethanol then dilute the sample with D_2O . These reasons add to why 5-methylpyrimidine with a long T_1 is crucial to this operation.

Moving to more of pharmaceutical application, it would be advantageous to be able to probe a mixture of substrates in a sample. The work here has concentrated on obtaining maximum enhancements which has been desired for certain applications and is only good if the substrate is known. If a much more active catalyst was studied, this would lead to a weaker Ir-substrate bond. This in turn would lower the polarisation levels, but early indications in testing a mixture of substrates, it doesn't bind the substrate tightly to all the substrates, but it will polarise everything with a similar level of enhancement.

7. Chapter 7 Experimental

7.1. Instrumentation

NMR measurements of substrates and characterisation of active complexes have been carried out on various Bruker spectrometers. These instruments included an Avance III 400 (400.13 MHz), Avance III 500 (500.13 MHz), Avance III 600 (600.13 MHz), Avance II 700 (700.13 MHz). ^{13}C frequency measured at 100 MHz, 125 MHz, 150 MHz and 175 MHz respectively. ^{15}N frequency measured at 40 MHz, 50 MHz, 60 MHz and 70 MHz respectively. NMR software which has been used to acquire and process data are Topspin version 2.0⁺ and Topspin version 3.2⁺.

7.2. Standard Methods

7.2.1. Preparation of *parahydrogen*

Parahydrogen was produced by cooling hydrogen down to 25 K over Fe_2O_3 where it was possible to obtain 99% *parahydrogen* conversion. *Parahydrogen* has been used from two different sources throughout this PhD thesis. The first coming from generator designed at the University of York which used a source of hydrogen from a cylinder. This was used for all shake method experiments and for early work for the flow method. The second was a *parahydrogen* generator that was provided by Bruker, which used an H-cube for the production of hydrogen.

7.2.2. Shake Method (method 1)

This method makes use of a 5mm J Young's Tap NMR tube (which was reported as Young's Tap NMR tube) with its contents made to standard concentrations as reported for the whole range of substrates tested in this thesis, so that a direct comparison can be made. An example of a standard sample would comprise of 2mg IMes (0.0031 mmol, 5 mM), 5 μl pyridine (0.062 mmol, 100 mM) and 0.6 ml of deuterated solvent, unless otherwise stated. The samples were degassed using a high vacuum line, by freeze thaw method, until there was no pressure drop. The headspace was then filled with 3 bar of hydrogen or *parahydrogen* and the sample left to allow the catalyst to activate. The sample was then introduced into the NMR spectrometer where general procedures were followed, and a thermal ^1H NMR spectrum was recorded. This was used to calculate the levels of polarisation transferred to the substrate. To the Young's Tap NMR tube, 3 bar of

parahydrogen was added and shaken vigorously, in an up-down motion for 10 seconds at either 0.5 G or 65 G, placed back into the NMR spectrometer and interrogated by a range of 1D and 2D NMR methods. Before each reading, the headspace of the NMR tube was evacuated and, 3 bar of *parahydrogen* replenished.

7.2.3. Flow Method (method 2)

This method used a sample prepared by dissolving catalyst (0.015 mmol, 5 mM), substrate (0.31 mmol, 100 mM) in deuterated solvent (3 mL), unless otherwise stated. The sample was then injected into the mixing chamber where it was shuttled into a Bruker Avance III series 400 MHz spectrometer equipped with a flow probe head for a thermal ^1H NMR. The solution was returned, and can then be activated in the mixing chamber by bubbling *parahydrogen* through the solution *via* a series of valves. *Parahydrogen* was then regulated to deliver 3 Bar for 6 seconds before being shuttled back to the probe head for NMR interrogation of the hyperpolarised sample. The carrier gas used to shuttle the sample was either helium or nitrogen. For samples that take longer to activate, for example **2-a** ($\text{ImMe}_2\text{NPr}_2^j$) and **2-c** (BzIMes), the complexes must be pre-activated. An ampoule was charged with the sample solution and degassed as per protocol for the solvent and 3 bar *parahydrogen* was introduced into the ampoule and shaken for a period of 5 minutes and stored at room temperature until the catalyst was activated and ready to be injected into the mixing chamber.

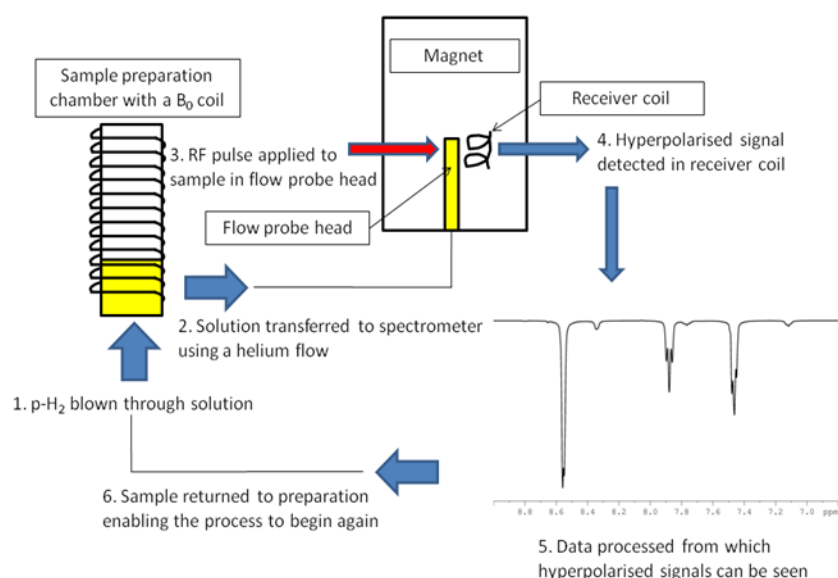


Figure 7.1 Schematic representation of polariser and flow system

Two polarisers were used in measurements by method 2, the MKII and MKIII. The field ranges of the automated equipment MKII and MKIII are -150 to 150 G and -140 to 140 G respectively. This was achieved as the mixing chamber was surrounded by a B_0 coil, through which a current was passed and therefore control of the magnetic field in the z direction can be achieved. The MKII polariser was used with a TXO probe and MKIII was used with either a TXO or TXI probe.

7.2.3.1. Reproducibility of method 2

A series of ^1H NMR spectra were collected for a sample of **2-c** with pyridine at standard concentrations, collected at 65G to avoid complications arising from the antiphase nature of the *meta* position. The results of these experiments were presented in Table 7.1 and Figure 7.2 below.

	Position 2		Position 4		Position 3	
	Integral	Enhancement	Integral	Enhancement	Integral	Enhancement
Run 1	-22183191	-112.98	-9515740	-92.34	-11140641	-54.92
Run 2	-21608165	-110.06	-9563696	-92.80	-11082411	-54.63
Run 3	-21219980	-108.08	-9548655	-92.66	-11281286	-55.61
Run 4	-22139379	-112.76	-9564910	-92.81	-10992202	-54.19
Run 5	-21674794	-110.40	-9492575	-92.11	-10863504	-53.55
Run 6	-21510220	-109.56	-9300026	-90.24	-10767635	-53.08
Mean	-21722622	-110.63	-9497600	-92.15	-11021280	-54.33
S.E	141316	0.777	38133	0.399	70844	0.377
S.D	373888	1.904	100891	0.979	187436	0.923
Confidence Limit 95%	267794	1.36	72262	0.701	134249	0.672

Table 7.1 Detailing the statistics estimating the reproducibility of method 2

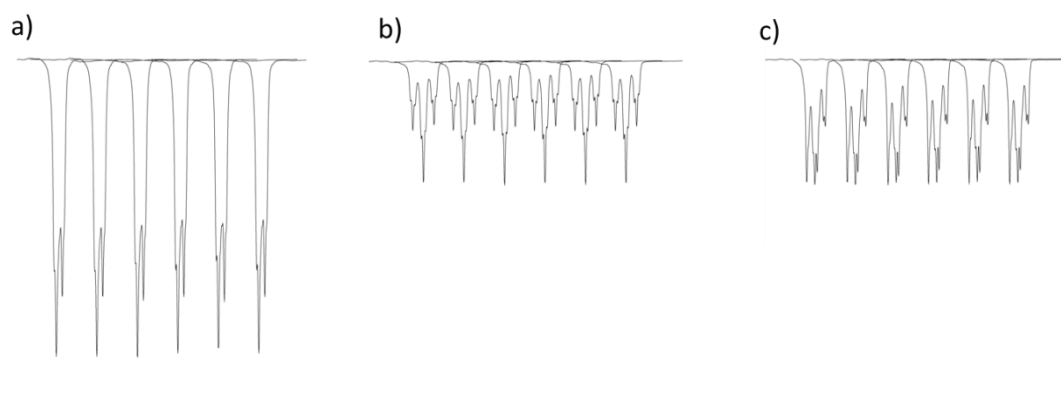


Figure 7.2 Comparing 6 ^1H NMR spectra measured consecutively using the polariser

This data showed a very high level of reproducibility and was observed for the polariser, with results reproducible to within 2 %.

7.2.4. Calculation of ^1H NMR enhancement factors

For calculation of the ^1H NMR signal enhancement, the following formula was used:

$$E = \frac{S_{pol}}{S_{unpol}}$$

Figure 7.3 when E = enhancement, S_{pol} = signal of polarised sample measured by integral, and S_{unpol} = signal of thermally polarised (reference) sample measured by integral

Experimentally, reference spectra were acquired with the same sample that was used for the hyperpolarised measurement after it had fully relaxed in the magnet (typically 5-10 minutes at high magnetic field). Reference and polarised spectra were collected using identical acquisition parameters, in particular the receiver gain. The raw integrals of the relevant resonances in the polarized and thermal spectra were then used to determine the enhancement level using equation in Figure 7.3.

7.2.5. Total Enhancement

For comparison of overall SABRE activity of a catalyst system, it was advantageous to calculate the total enhancement, which was the sum enhancement calculated for each proton.

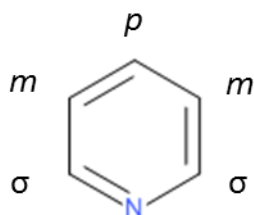


Figure 7.4 Labelled structure of pyridine with proton resonances labelled as *ortho* (σ), *para* (ρ) and *meta* (m)

Figure 7.4 showed the labelled structure of pyridine, when calculating the total enhancement, the number of proton environments must be considered, and the sign of the enhancement value (negative or positive). The total enhancement for pyridine resonances was calculated:

$$\text{Total Enhancement (E)} = |\sigma \times 2| + |\rho| + |m \times 2|$$

7.2.6. Calculation of ^1H MRI enhancement factors

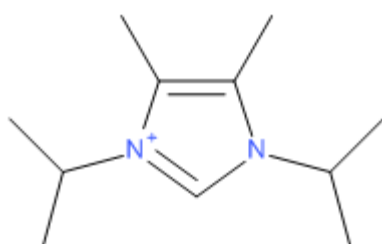
All raw data were Fourier transformed and zero-filled once, using a routine included in the NMRI package of Prospa (Magritek LTD.). For calculating the signal-to-noise ratios of every image, an algorithm has been designed that selects circular regions of interest (ROIs) containing signal and noise, and calculates the signal-to-noise ratio values using the mathematical description of Rice white noise. With the exception of the high-resolution images presented at the end of this chapter 4 (on which a sinebell squared noise filter was applied to the k-space data prior to the FT), no noise filtering was performed as part of the data processing. In order to estimate the signal enhancement for each solution, the average of the signal-to-noise ratio values obtained from the 5 shake-and-drop experiments was divided by the SNR value extracted from the corresponding thermal images of the samples. Contrast enhancement was evaluated using the ratio of the signal-to-noise ratio of the hyperpolarised images and the signal-to-noise ratio of the images recorded on the water and oil phantoms respectively.

7.2.7. Chemicals and Solvents

All materials for synthetic procedures were purchased from Aldrich, Alfa Aesar and fluorochem. All materials were used as received unless otherwise stated. The solvents used were of general purpose or HPLC grade and were purchased from Fisher Scientific. TLC analysis was performed using aluminium-backed silica gel 60 F₂₅₄, 0.2 (Merck plates) or aluminium-backed aluminium oxide 60 F₂₅₄, (Merck plates). Silica gel chromatography was performed with silica gel 60 (Davisil). When required, diethyl ether, dichloromethane, acetonitrile and acetic acid were dried as follows; diethyl ether was dried over sodium metal and benzophenone followed by distillation; dichloromethane and acetonitrile were dried over calcium hydride for 24 h followed by distillation; acetic acid was dried by adding acetic anhydride (3% w/v) and distilling (b.p. 118°C). All other solvents required were dried using an Innovative Technology anhydrous solvent engineering system. High purity gases were obtained from BOC.

7.3. Reactions

7.3.1. Synthesis of ImMe₂NPrⁱ₂ (1-a)



1-a

Figure 7.5 Structure of 1-a (ImMe₂NPrⁱ₂)

Step 1

Diisopropylthiourea (16.03 g, 100 mmol), 3-hydroxybutanone (9.69 g, 110 mmol) and pentan-1-ol (65 ml) were added to a round bottom flask equipped with a magnetic stirrer, dean stark trap and reflux condenser. The solution was heated in an oil bath for 48 hours at 142 °C, at which point no more water was produced indicating complete conversion. The mixture was allowed to cool overnight. The solution was then filtered under vacuum and

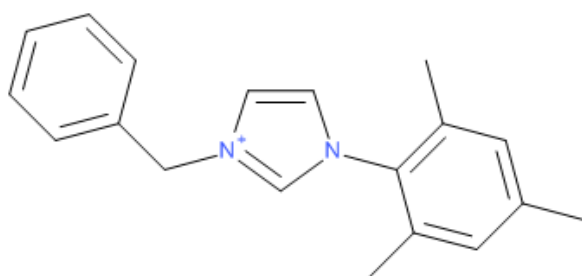
washed several times with cold methanol (-20 °C). The product was further dried in a Schlenk tube tube for 48 hours. Yield =13.0 g (61 %). Only mass spectrometry recorded (ESI m/z= 213.1)

Step 2

To the product obtained in step 1 (1.06 g, 5 mmol), dimethoxyethane (DME) (30 ml) was added under a nitrogen atmosphere. The reaction vessel was bathed in dry ice prior to the addition of potassium (0.5 g, 12.79 mmol) in small quantities. Once potassium addition was complete, the mixture was heated at reflux for 4 hours at 88 °C and allowed to cool overnight. The mixture was then filtered through a cannula to a clean Schlenk tube tube and evaporated to dryness to afford an orange/brown powder. Dry hexane (45 ml) was added to the powder and stirred for 1.5 hours. The solution was then removed by pipette and evaporated to dryness. This process afforded yellow crystals of **1-a** (ImMe₂iPr₂), which was immediately transferred to a glove box for storage. Yield = 0.81 g (90 %).

¹H NMR (400 MHz, DMSO-d₆, 298 K): 4.95 (sept, 2H, N(1,3)-CH(CH₃)₂, ³J= 6.74 Hz), 2.40 (s, 6H, C(4,5)-CH₃), 1.61 (d, 12H, N(1,3)-CH(CH₃)₂). ¹³C{¹H} NMR (CDCl₃, 101 MHz, 298 K): δ=209.27 (C(2)), 126.6 (C(4,5)), 50.40 (N(1,3)-CH(CH₃)₂), 22.03 (N(1,3)-CH(CH₃)₂), 7.72 [C(4,5) – CH₃]. MS (ESI+): m/z 181.2 (M+Cl)

7.3.2. Synthesis of BzIMes (1-b)



1-b

Figure 7.6 Structure of 1-b (BzIMes)

Aqueous formaldehyde (3 mL), aqueous glyoxal (4.7 mL) and glacial acetic acid (10 mL) were added to a 75 mL round bottom flask and heated up to 70°C. A solution made up of glacial acetic acid (10 mL), ammonium acetate (3.00 g in 2.1 mL) and mesitylamine (5.6 mL) was added dropwise over a period of 30-40 minutes. The solution was stirred continually at 70°C throughout the addition followed by a further 18 hours. The solution was then cooled to room temperature and then added dropwise to a solution of NaHCO₃ (29.4 g) in water (300 mL). Upon the addition, a precipitate formed, which was filtered to obtain a beige solid product. This was purified by recrystallization in ethyl acetate to obtain beige shard crystals of 1-mesitylimidazole. (4.99 g, 67%)

¹H NMR (CDCl₃, 400 MHz, 297 K): δ 7.40 (m, 1H), 7.20 (m, 1H), 6.95 (m, 2H), 6.82 (m, 1H), 2.33 (s, 3H), 1.96 (s, 6H).

1-mesitylimidazole (1.0g, 0.0053 mol, 1.0 e.q) and toluene (25 mL) were added to a Schlenk tube and stirred for 30 min. Benzylchloride (3.5 ml, 0.026 mol, 6.0 e.q) was added dropwise to the mixture over a 20 minute period and heated at reflux (135°C) for a further 12 hours after the addition was complete. Hot pentane was added to the solution and a white precipitate formed. The solution was cannula filtered, the precipitate washed 3 times with hot pentane, and dried *in vacuo* to produce a white powder (1.68 g, 97%).

¹H NMR (400 MHz, CD₃OD, 298 K): δ 11.12 (t, 1H, NCHN), 7.93 (t, 1H, NCHCHN), 7.65-7.35 (m, 5H, Ph-CH), 7.23(t, 1H, NCHCHN), 6.99 (s, 2H, CH^{mes}), 5.86 (s, 2H, Ph-CH₂-N), 2.32 (s, 3H, *p*CH^{mes}), 2.03 (s, 6H, *o*CH^{mes}). **¹³C{¹H} NMR** (101 MHz, CD₂Cl₂, 298 K): δ 141.1 (NCHN), 138.9 (Q *p*C^{mes}), 134.4 (Q *o*C^{mes}), 134.3-129 (ArCH), 123.3 (NCHCHN), 122.8 (NCHCHN), 52.8 (Ph-CH₂-N), 20.8 (*p*-CH₃^{mes}), 17.4 (*o*-CH₃^{mes}). **MS** (ESI+): m/z 277.2 (M+-Cl)

7.3.3. Synthesis of $[\text{Ir}(\text{COD})\text{Cl}]_2$

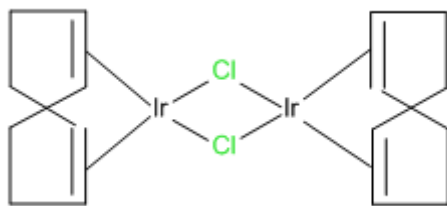


Figure 7.7 Structure of $[\text{Ir}(\text{COD})\text{Cl}]_2$.

Iridium (III) chloride (2.00 g, 6.69 mmol) was dissolved in a mixture of isopropanol (40 mL) and H_2O (20 mL). The mixture was degassed with N_2 for 30 minutes. 1,5-cyclooctadiene (6.5 mL) was added and was heated at reflux under N_2 for 48 hours. The reaction mixture was reduced by half volume which resulted in an intense red precipitate forming. The mixture was allowed to cool, and the red precipitate product was collected by vacuum filtration and washed with ice cold methanol to remove unreacted starting materials. Yield 55%.

$^1\text{H NMR}$ (400 MHz, DMSO-d_6 , 298 K): δ 4.10 (br, s, 4H, CH), 3.96 (br, s, 4H, CH), 2.16-2.35 (m, 8H, CH_2), 1.65-1.78 (m, 8H, CH_2). $^{13}\text{C}\{^1\text{H}\}$ NMR (101 MHz, DMSO-d_6 , 298 K) δ 73.8 (CH), 30.7 (CH_2). MS (ESI+): m/z 672.4

7.3.4. Synthesis of $[\text{Ir}(\mu\text{-OMe})(\text{COD})]_2$.

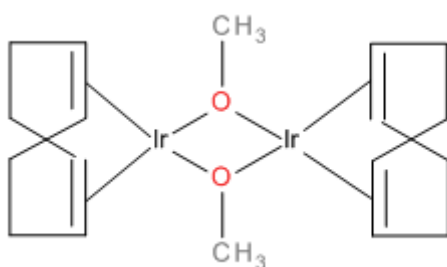


Figure 7.8 Structure of $[\text{Ir}(\mu\text{-OMe})(\text{COD})]_2$.

$[\text{Ir}(\text{COD})\text{Cl}]_2$ (1.01 g, 1.50 mmol) and KOH (0.17 g, 3 mmol) were placed in a separate Schlenk tube tubes under N_2 , then dry and degassed methanol (70 and 35 mL) was added to each Schlenk tube tube respectively. Once the solids had been dissolved, the KOH

solution was cannula transferred to $[\text{Ir}(\text{COD})\text{Cl}]_2$ solution, and stirred at room temperature for 30-60 minutes until the solution turned a golden yellow. Degassed H_2O was added to form a yellow precipitate product which was collected by vacuum filtration. (0.763 g, 1.16 mmol, 76%).

$^1\text{H NMR}$ (400 MHz, DMSO-d_6 , 298 K): δ 4.10 (br, s, 4H, $\underline{\text{CH}}$), 3.96 (br, s, 4H, $\underline{\text{CH}}$), 3.8 (s, 6H, CH_3), 2.16-2.35 (m, 8H, $\underline{\text{CH}_2}$), 1.65-1.78 (m, 8H, $\underline{\text{CH}_2}$). $^{13}\text{C}\{^1\text{H}\}$ NMR (101 MHz, DMSO-d_6 , 298 K) δ 73.8 ($\underline{\text{CH}}$), 65.1 ($\underline{\text{CH}_3}$), 30.7 ($\underline{\text{CH}_2}$). **MS** (ESI+): m/z 662.3

7.3.5. Synthesis of $[(\text{NHC})\text{AgCl}]$

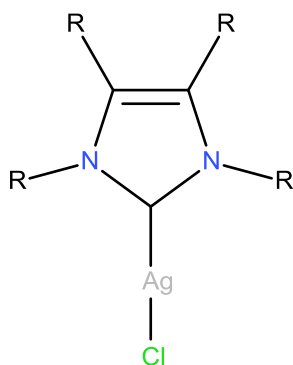


Figure 7.9 Structure of NHC.AgCl

1-(benzyl)-3-(mesityl)imidazol-2-ylidene.HCl (1 eq.), and dry, degassed DCM were added to a Schlenk tube tube and stirred for 20 minutes under N_2 . To a second Schlenk tube tube, Ag_2O (1.2 eq.) and DCM were added and stirred for 20 minutes. The Ag_2O solution was cannula transferred to the 1-(benzyl)-3-(mesityl)imidazol-2-ylidene solution and stirred for 18 hours in the absence of light. The solution was filtered through celite, washed with 3 portions of DCM and solvent removed *in vacuo* to produce an off white solid. Characterisation data for catalyst **2** (silver(1-(benzyl)-3-(mesityl)imidazol-2-ylidene) chloride)

$^1\text{H NMR}$ (400 MHz, CD_2Cl_2 , 298 K): δ 7.41-7.0 (m, 9H, Ar-CH), 5.39 (s, 2H, Ph- CH_2 -N), 2.35 (s, 3H, $p\text{CH}^{\text{mes}}$), 1.99 (s, 6H, $o\text{CH}^{\text{mes}}$). $^{13}\text{C}\{^1\text{H}\}$ NMR (101 MHz, CD_2Cl_2 , 298 K): δ 141 ($\underline{\text{NCN}}$), 139.6 (Q $p\text{C}^{\text{mes}}$), 136.0 (Q $o\text{C}^{\text{mes}}$), 135-127.5 (ArCH), 123.3 ($\underline{\text{NCHCHN}}$), 121.3 ($\underline{\text{NCHCHN}}$), 55.5 (Ph- $\underline{\text{CH}_2}$ -N), 20.8 ($p\text{-CH}_3^{\text{mes}}$), 17.4 ($o\text{-CH}_3^{\text{mes}}$). **MS** (ESI+): m/z 421

7.3.6. Synthesis of [Ir(NHC)(COD)Cl] (2-a, 2-b)

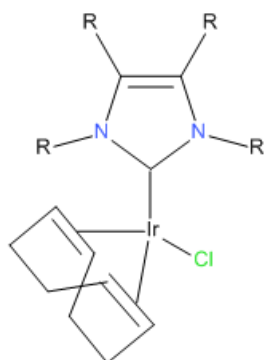


Figure 7.10 Structure of [Ir(NHC)(COD)Cl] (2-a, 2-b)

Method 1:

[(NHC)AgCl] (1 eq.) and [Ir(COD)Cl]₂ (0.5 eq.) and DCM were added to a Schlenk tube tube and degassed for 30 min with N₂. The solution was stirred for 5 hours at room temperature and the resulting solution was filtered through celite. The crude product was reduced *in vacuo* and purified by column chromatography with an eluent of DCM : Acetone (19:1) resulting in a yellow powder.

Method 2:

NHC.HCl (2.2 eq.) and potassium *tert*-butoxide (2.2 eq.) were added to a Schlenk tube tube. Dry degassed THF was added to the flask and the mixture was stirred for 45 min at room temperature. [Ir(COD)Cl]₂ (1 eq.) was dissolved in a minimum volume of dry THF, the resulting solution then added to the first Schlenk tube by cannula transfer and stirred for 2 hours at room temperature. The solvent was then removed under vacuum and the resulting solid was purified by column chromatography with an eluent of DCM : Acetone (19:1) resulting in a yellow/orange powder.

Characterisation data for **2-a**:

¹H NMR (700 MHz, CD₃OD, 278 K): δ 6.05 (sept, J=7.2 Hz, 2H, CH(CH₃)₂), 4.48 (b, 2H, CH-COD), 2.99 (b, 2H, CH-COD), 2.19 (b, 8H, CH₂-COD), 2.15 (s, 6H, NC(CH₃)C(CH₃)N), 1.61 (d, J=6.92 Hz, 6H, CH(CH₃)₂), 1.47 (d, J=6.92 Hz, 6H, CH(CH₃)₂). ¹³C{¹H} NMR (175 MHz, CD₃OD, 278 K): δ 177.39 (N_CN), 124.63 (N_CCN), 82.70 (CH-COD), 53.33 ((CH₃)₂CH-N), 51.00 (CH-COD), 33.70 (CH₂-COD), 29.40 (CH₂-COD) 22.77 ((CH₃-C-CH₃), 21.77 (CH₃-C-CH₃), 10.30 (C-

$\underline{\text{C}}\text{H}_3$). $^{15}\text{N}\{^1\text{H}\}$ NMR (70 MHz, CD_3OD , 278 K): δ 197.8 (Carbene N). MS (ESI+): m/z 522 ($\text{M}^+ - \text{Cl} + \text{acetonitrile}$), 481 ($\text{M}^+ - \text{Cl}$)

Characterisation data for **2-b**:

^1H NMR (400 MHz, CD_3OD , 298 K): δ 7.45-7.35 (m, 5H, Ph-CH), 7.29 (CH-COD), 7.07 (s, 1H, $m\text{CH}^{\text{mes}}$), 6.96 (d, $J=1.97$ Hz, 1H, NCHCHN), 6.95 (s, 1H, $m\text{CH}^{\text{mes}}$), 6.78 (d, $J=1.97$ Hz, 1H, NCHCHN), 6.25 (d, $J=15.12$ Hz, 1H, Ph- $\text{CH}_2\text{-N}$), 5.51 (d $J=15.16$ Hz, 1H Ph- $\text{CH}_2\text{-N}$), 4.48 (b, 2H, CH-COD), 3.01 (m, 1H, CH-COD), 2.75 (m, H, CH-COD) 2.4 (s, 6H, $o\text{CH}^{\text{mes}}$), 1.96 (s, 3H, $p\text{CH}^{\text{mes}}$), 2.03-1.2 (m, 8H, $\text{CH}_2\text{-COD}$)

$^{13}\text{C}\{^1\text{H}\}$ NMR (100 MHz, CD_3OD , 298 K): δ 180.49 (NCN), 138.64 (Q N-C^{mes}) 137.4 (Q Ph- $\underline{\text{C}}\text{-CH}_2\text{-N}$), 136.83 (Q $o\text{C}^{\text{mes}}$), 135.50 (Q $p\text{C}^{\text{mes}}$) 129.42 ($m\text{-ArCH}$), 128.58 (ArCH-Ph), 128.03 ($m\text{-ArCH}$), 123.04 (NCHCHN), 120.73 (NCHCHN), 84.10 (CH-COD), 55.00 (Ph- $\underline{\text{C}}\text{H}_2\text{-N}$), 52.20 (CH-COD), 51.03 (CH-COD), 34.12 ($\text{CH}_2\text{-COD}$), 32.59 ($\text{CH}_2\text{-COD}$), 29.30 ($\text{CH}_2\text{-COD}$), 28.71 ($\text{CH}_2\text{-COD}$), 21.13 ($o\text{-CH}_3^{\text{mes}}$), 19.62 ($o\text{-CH}_3^{\text{mes}}$), 17.91 ($p\text{-CH}_3^{\text{mes}}$). MS (ESI+): m/z 577.21 ($\text{M}^+ - \text{Cl}$)

7.3.7. Synthesis of $[\text{Ir}(\mathbf{1-a})(\text{CO})_2\text{Cl}]$ (**3-a**)

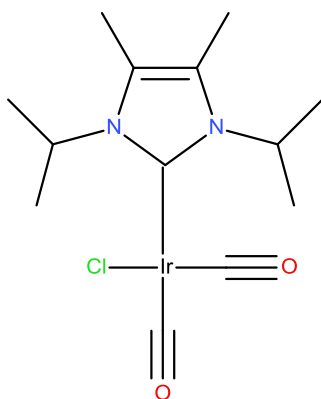


Figure 7.11 Structure of $[\text{Ir}(\mathbf{1-a})(\text{CO})_2\text{Cl}]$ (**3-a**)

$[\text{Ir}(\text{COD})(\mathbf{1-a})\text{Cl}]$ was added to DCM in round bottom flask under N_2 atmosphere. The headspace was purged with CO gas and the reaction stirred for 30 minutes until a pale yellow precipitate was formed. The solution was removed and the product dried *in vacuo* and immediately transferred to a glove box for storage. Yield = 0.81 g (90 %).

Characterisation data for **3-a**:

$^1\text{H NMR}$ (400 MHz, CD_3OD , 298 K): 6.05 (sept, 2H, N(1,3)-CH(CH $_3$) $_2$), 2.40 (s, 6H, C(4,5)-CH $_3$), 1.65 (d, 12H, N(1,3)-CH(CH $_3$) $_2$). $^{13}\text{C}\{^1\text{H}\}$ NMR (100 MHz, CD_3OD , 278 K): δ 181.74 (IrCO), 169.01 (N $\underline{\text{C}}\text{N}$), 168.32 (IrCO), 126.2 (N $\underline{\text{C}}\text{C}\text{N}$), 54.05 ((CH $_3$) $_2$ CH-N), 20.70 ((CH $_3$ -C-CH $_3$), 14.1 (C-CH $_3$). MS (ESI+): m/z 470.2. FTIR: cm^{-1} 2054, 1982, 1965

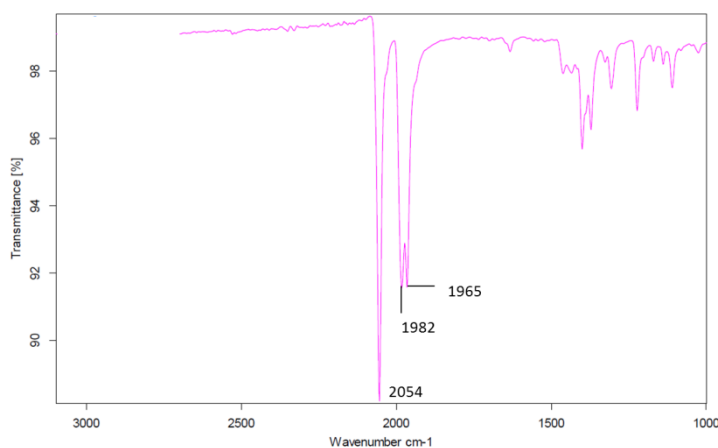
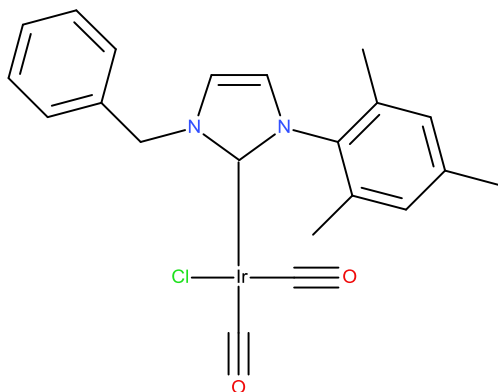


Figure 7.12 IR spectrum corresponding to the addition of CO to complex **3-a**

7.3.8. Synthesis of [Ir(**1-b**)(CO) $_2$ Cl] (**3-b**)



[Ir(COD)(**1-b**)Cl] was added to DCM in round bottom flask under N_2 atmosphere. The headspace was purged with CO gas and the reaction stirred for 30 minutes until a pale yellow precipitate was formed. The solution was removed and the product dried *in vacuo* and immediately transferred to a glove box for storage. Yield = 0.75 g (87 %).

$^1\text{H NMR}$ (400 MHz, CD_3OD , 298 K): δ 11.12 (t, 1H, NCHN), 7.93 (t, 1H, NCHCHN), 7.65-7.35 (m, 5H, Ph-CH), 7.23 (t, 1H, NCHCHN), 6.99 (s, 2H, CH $^{\text{mes}}$), 5.86 (s, 2H, Ph-CH $_2$ -N), 2.32 (s, 3H, $p\text{CH}^{\text{mes}}$), 2.03 (s, 6H, $o\text{CH}^{\text{mes}}$). $^{13}\text{C}\{^1\text{H}\}$ NMR (100 MHz, CD_2Cl_2 , 298 K): δ 180.21 (IrCO), 149.15

(Ir $\underline{C}O$) 141.1 (NCHN), 138.9 (Q pC^{mes}), 134.4 (Q oC^{mes}), 134.3-129 (ArCH), 123.3 (NCHCHN), 122.8 (NCHCHN), 52.8 (Ph- $\underline{C}H_2$ -N), 20.8 (p - CH_3^{mes}), 17.4 (o - CH_3^{mes}). **MS** (ESI+): m/z 497 (M+Cl) **FTIR**: cm^{-1} 2057, 1978

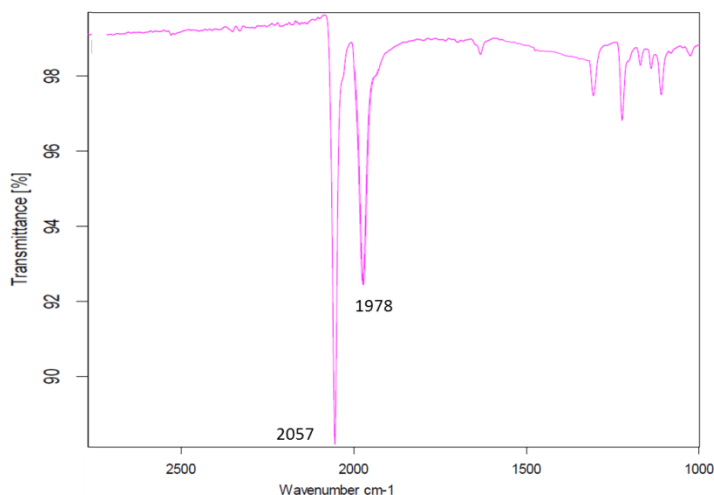


Figure 7.13 IR spectrum corresponding to the addition of CO to complex 3-b

7.3.9. Synthesis of $LiOC(CF_3)_3$

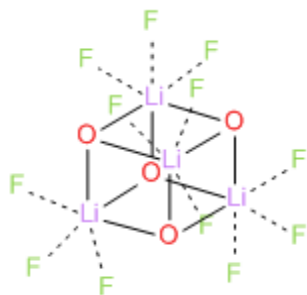


Figure 7.14 Structure of $LiOC(CF_3)_3$

Lithium hydride (0.167 g, 20.9 mmol) and Et_2O (50 mL) was added to a Schlenk tube tube and stirred for 10 minutes. To the white suspension, nonafluoro-tert-butanol (2.9 mL, 20.9 mmol) was added dropwise over a 20 minute period. After H_2 formation was complete, the reaction mixture was stirred for 1 hour at room temperature, then heated at reflux for a further 2 hours. The solvent was removed to produce a white solid which was dried *in vacuo*. (4.50 g, 89 %)

7.3.10. Synthesis of $\text{AgOC}(\text{CF}_3)_3$.

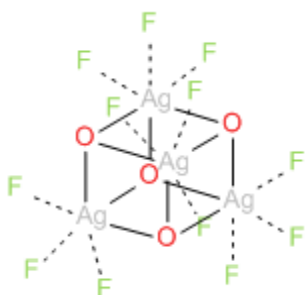


Figure 7.15 Structure of $\text{AgOC}(\text{CF}_3)_3$.

In a double Schlenk tube, $\text{LiOC}(\text{CF}_3)_3$ (1.10 g, 4.13 mmol) and AgBF_4 (0.801 g, 4.13 mmol) were mixed in a glovebox. Dry degassed DCM was added to this mixture and stirred for 18 hour in the absence of light. The solution was filtered through a glass frit into the second half of the Schlenk tube and all the solvent removed and quickly dried *in vacuo*, as prolonged drying resulted in decomposition of the white product. (0.9 g, 63%).

7.3.11. Synthesis of 3-acetoxymethylpyridine

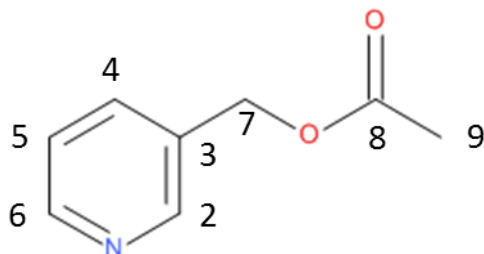
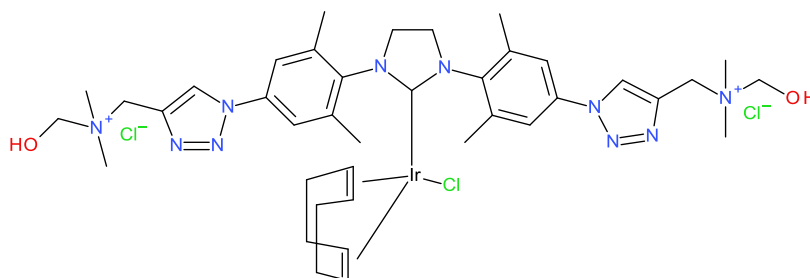


Figure 7.16 Structure of 3-acetoxymethylpyridine

3-hydroxypyridine (1.00 g, 10.51 mmol) and triethylamine (2.13 g, 21 mmol) were added to a Schlenk tube tube and dissolved in degassed DCM (15 mL). Under N_2 conditions at room temperature acetyl chloride (0.91 g, 11.23 mmol) was added and stirred for 3 hours. The solvent was removed *in vacuo* and purified by column chromatography with an eluent of DCM : methanol (97:3) to produce a pale yellow / brown oil.

$^1\text{H NMR}$ (400 MHz, CD_3OD , 298K): δ 8.62 (s, 1H, H2), 8.55 (br, 1H, H6), 7.71-7.67 (m, 1H, H4), 7.30 (dd, $J=7.8$ Hz, 4.8 Hz, 1H, H5). 5.11 (d, $J=1$ Hz, 2H, H7), 2.10 (s, 3H, H9). **MS** (ESI+): m/z 151

7.3.12. Synthesis of [Ir(SIMesCh)(COD)Cl] 2-f



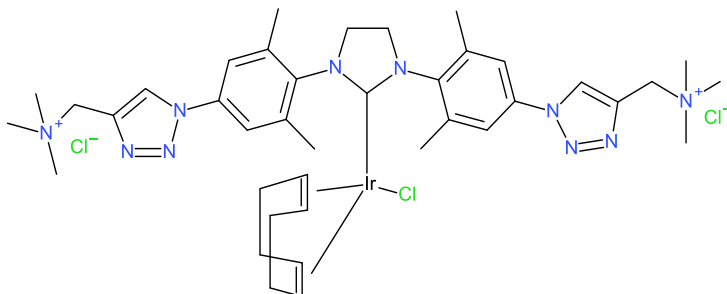
2-f

Figure 7.17 Structure of [Ir(SIMesCh)(COD)Cl] 2-f

SIMesCh.HCl (**1-f**) (0.22 g, 0.337 mmol), sodium-methoxide (0.03g, 0.555 mmol) and [IrCl(COD)]₂ (0.1 g, 0.149 mmol) were added to a Schlenk tube and dissolved in a mixture of 10 mL DMSO and 10 mL ethanol. The solution was stirred 16.5 hours at room temperature and solvent removed *in vacuo* to produce a pale yellow solid product (0.185 g, 65 %).

¹H NMR (400 MHz, CD₃OD, 298 K): δ -22.54 (2H, hydrides), 2.57-2.53 (br, 24H, CH(CH₃)₂), 2.70 (m, 4H, CH(CH₃)₂), 4.89 (d, J_{HH} = 5.95 Hz), 5.29 (br, 2H, OH), 7.14 (t, 1H, *para* proton of pyridine in axial position), 7.65 (t, 2H, *meta* proton of pyridine in axial position), 7.74 (t, 1H, *para* proton of pyridine molecules in equatorial position) 7.77 (s, 2H, H_{Ar}), 7.83 (s, 2H, H_{Ar}), 7.95 (s, 2H, NCH-CHN), 8.17 (t, 1H, *para* proton of pyridine in axial position), 8.40 (d, 2H, *ortho* proton of pyridine molecules in equatorial position), 8.70 (d, 2H, *ortho* proton of pyridine in axial position), 8.98 (s, 1H, H_{triazole}), 9.03 (s, 1H, H_{triazole}). ¹³C{¹H} NMR (125 MHz, d₆-DMSO, 298 K): δ 163.41 (Ir-C_{tmx}), δ 138.90 (-C=,tmx), δ 136.98 (-C=, tmx_{triazole}), 131.50 (-C=, tmx), 131.10 (2 -C(CH₃)-, tmx), 128.60 (-CH=, triazol), 120.00 (-CH=, aril), 62.70 (NCH₂CH₂N), 59.48 (-CH₂-N), 52.5 (N(CH₃)₃), 62.5 (-CH=, COD), 49.38 (-CH=, COD), 46.4 (-CH=, COD), 31.40 (-CH₂-, COD), 17.8 (CH₃-C=). **MS** (ESI): m/z 1022

7.3.13. Synthesis of [Ir(SIMesTrimet)(COD)Cl] (2-g)



2-g

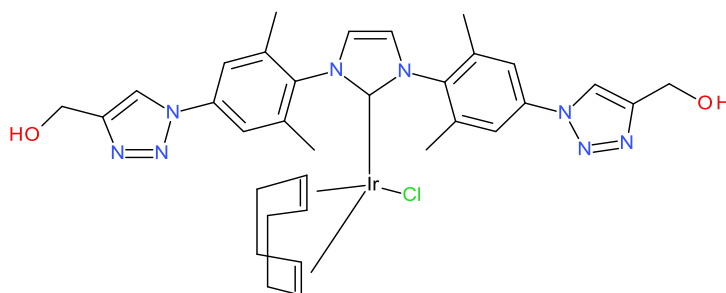
Figure 7.18 Structure of [Ir(SIMesTrimet)(COD)Cl] (2-g)

SIMesTrimet.HCl (**1-g**) (0.50 g, 0.755 mmol), sodium-methoxide (4.2 mg, 0.755 mmol) and [IrCl(COD)]₂ (0.25 g, 0.378 mmol) were added to a Schlenk tube and dissolved in the mixture of 15 mL DMSO and 15 mL ethanol. The solution was stirred 18 hours at room temperature and solvent removed *in vacuo* to yield a yellow brown solid (0.234 g, 62 %).

¹H NMR (400 MHz, DMSO-*d*₆, 298 K): δ 9.20 (br, 0.33H, H_{triazole}), δ 9.16(br, 0.66H, H_{triazole}), 8.97 (s, 1H, H_{triazole}), 8.43(s, 2H, -CH=, COD), 8.18(s, 2H, -CH=, COD), 7.87(s, 1H, H_{Ar}), 7.77(s, 1H, H_{Ar}), 7.50(s, 2H, H_{Ar}), 4.81(s, 2H, CH₃N-CH₂-C_{triazole}), 4.77(s, 2H, CH₃N-CH₂-C_{triazole}), 4.62 (br, 4H, NCH₂-CH₂N), 3.72 – 3.97 (m, -CH₂-, COD), 3.15(s, 12H, N-CH₃), 3.13(s, 12H, N-CH₃), 2.21 – 2.34(m, 12H, Ar-CH₃)

¹³C{¹H} NMR (125 MHz, DMSO-*d*₆, 298 K): δ 162.17 (Ir-C_{tmx}), δ 138.90 (-C=, tmx), δ 136.98 (-C=, tmx_{triazole}), 133.50 (-C=, tmx), 133.10 (2 -C(CH₃)-, tmx), 127.60 (-CH=, triazol), 120.61 (-CH=, aril), 62.70 (NCH₂CH₂N), 59.48 (-CH₂-N), 52.5 (N(CH₃)₃), 62.5 (-CH=, COD), 49.38 (-CH=, COD), 46.4 (-CH=, COD), 31.40 (-CH₂-, COD), 17.8 (CH₃-C=). **MS** (ESI): m/z 962

7.3.14. Synthesis of [Ir(IMesOH)(COD)Cl] (2-e)



2-e

Figure 7.19 Structure of [Ir(SIMesTrimet)(COD)Cl] (2-e)

[Ir(IMesOH)(COD)Cl] 0.144 g (0.215 mmol) of [Ir(COD)Cl]₂ was dissolved in 10 mL acetonitrile. 0.230 g (0.43 mmol) of IMesOH·HCl and 0.049 g (0.44 mmol) of K₂CO₃ were dissolved in a mixture of 5 mL degassed H₂O and 10 mL NCMC under N₂. The aqueous solution was added into the NCMC solution of the iridium dimer, and stirred at room temperature for 4 hours. The solvent was removed by vacuum and a beige brown powder remained as the product. Yield was: 0.277 g (85%).

¹H NMR (500 MHz, D₂O, 298 K): δ 1.78-2.25 (*m*, -CH₂-, COD), 2.84 (4H, -CH₂-imid), 2.31 (*s*, 12H, CH(CH₃)₂), 4.49 (*s*, 4H, -CH_v, COD), 4.85 (*s*, 4H, -CH₂-triazole), 7.80 (*s*, 2H, -CH_v, H_{Ar}), 8.04 (*s*, 2H, -CH_v, H_{triazole}), 8.49 (*s*, 2H, -CH_v, H_{imid}). ¹³C{¹H} NMR (125 MHz, D₂O, 298 K): δ 16.9 (CH₃,), 24.9 (-CH₂-, COD), 50.9 (-CH₂-imid), 57.0 (-CH₂-C_{triazole}), 79.7 (-CH_v, COD), 121.1 (-CH_v, Ar), 122.4 (-CH_v, imid), 124.9 (-CH_v, triazole), 133.4, 137.5, 138.3 (-C_v, Ar), 147.5 (-C_v, imid) 173.6 (Ir-C). MS (ESI⁺): Data didn't match expected value.

7.3.15. Synthesis of 2-d-5-methylpyrimidine.HCl

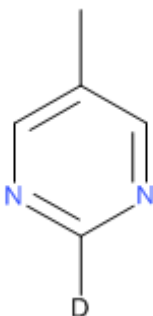


Figure 7.20 Structure of 2-d-5-methylpyrimidine

2-Chloro-5-methylpyrimidine (0.90 g, 0.70 mmol), 5 % palladium carbon (0.10 g), triethylamine (2.07 g, 2 mmol) and THF (100 mL) were added to a 150 mL round bottom flask and stirred for 10 minutes under N_2 . The N_2 atmosphere was removed and then replaced by a deuterium gas atmosphere and the mixture was stirred for 18 hours. The solution was passed through celite to remove the palladium on carbon. 4 M HCl in dioxane (1 mL) was added dropwise over a 5 minute period to produce a white precipitate and the solvent was removed *in vacuo* (0.60g, 65%).

1H NMR (400 MHz, CD_3OD , 298K): δ 8.97 (s, 0.15 H, NDN), 8.68 (s, 1.34 H, NCHC), 2.39 (s, 3H, CH_3). $^{13}C\{^1H\}$ NMR (100 MHz, CD_3OD , 298K): δ 157.60 (NDN), 155.60 (QC), 131.70 (NCHC), 14.00 (CH_3). MS (ESI+): 95.13

7.3.16. Synthesis of 2,4-d-5-methylpyrimidine

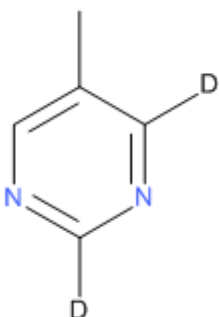


Figure 7.21 Structure of 2,4-d-5-methylpyrimidine.

2,4-Chloro-5-methylpyrimidine (0.90 g, 0.54 mmol), 5 % palladium carbon (0.15 g), triethylamine (2.07 g, 2 mmol) and THF (100 mL) were added to a 150 mL round bottom

flask and stirred for 10 minutes under N₂. The N₂ atmosphere was removed and then replaced by a deuterium gas atmosphere and the mixture was stirred for 48 hours. The solution was passed through celite to remove the palladium on carbon. 4 M HCl in dioxane (1 mL) was added dropwise over a 5 minute period to produce a white precipitate and the solvent was removed *in vacuo* (0.70g, 75%).

¹H NMR (400 MHz, CD₃OD, 298K): δ 8.97 (s, 0.04 H, NDN), 8.68 (s, 0.66 H, NCHC + NCDC), 2.39 (s, 3H, CH₃). ¹³C{¹H} NMR (100 MHz, CD₃OD, 298K): δ 157.60 (NDN), 155.60 (QC), 131.70 (NCHC), 14.00 (CH₃). MS (ESI+): 96.08

7.3.17. Synthesis of 4,6-d-5-methylpyrimidine

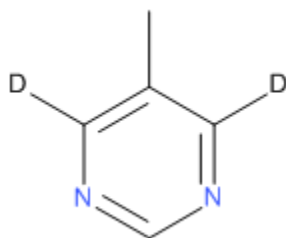


Figure 7.22 Structure of 4,6-d-5-methylpyrimidine

4,6-Chloro-5-methylpyrimidine (2.01 g, 1.2 mmol), 5 % palladium carbon (0.3 g), triethylamine (4.07 g, 4 mmol) and THF (150 mL) were added to a 50 mL round bottom flask and stirred for 10 minutes under N₂. The N₂ atmosphere was removed and then replaced by a deuterium gas atmosphere and the mixture was stirred for 48 hours. The solution was passed through celite to remove the palladium on carbon. 4 M HCl in dioxane (2.5 mL) was added dropwise over a 10 minute period to produce a white precipitate and the solvent was removed *in vacuo* (95%).

¹H NMR (400 MHz, CD₃OD, 298K): δ 8.97 (s, 0.45 H, NHN), 8.68 (s, 0.13 H, NCDC), 2.39 (s, 3H, CH₃). ¹³C{¹H} NMR (100 MHz, CD₃OD, 298K): δ 157.60 (NHN), 155.60 (QC), 131.70 (NCDC), 14.00 (CH₃). MS (ESI+): 96.21

7.3.18. Synthesis of silica material M-Bz-Im

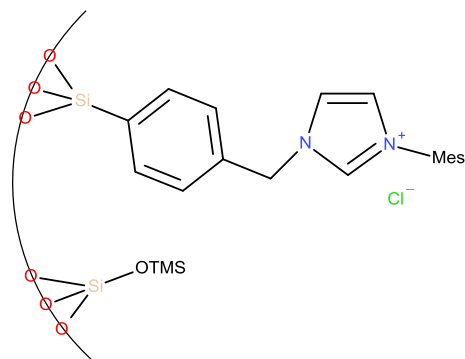


Figure 7.23 Structure of M-Bz-Im

M-Bz-Cl (1.5g) was suspended in 300 ml of 2M aqueous HCl and heated at 50°C for 3 hours. The solid was filtered and washed several times with water and acetone, and material dried under vacuum for 18 hours. A solution mesitylimidazole (2.45g, 0.014 mmol) in toluene (30 ml) was heated at reflux for 52 hours. The solid was filtered and washed three times successively with toluene, methanol and diethyl ether, dried under vacuum for 24 hours (140°C, 10⁻⁵ mm Hg). This produced a white solid (1.6 g) which was suspended in a toluene solution (140 ml) containing trimethylamine (22 ml) and trimethylsilylbromide (TMSBr, 10 ml), which was stirred at room temperature for 24 hours. The solid was filtered and washed three times successively with toluene, methanol and diethyl ether, then was dried under vacuum for 24 hours (140°C, 10⁻⁵ mm Hg). This was isolated as a white solid (1.4 g) M-Bz-Im.

¹H Solid State NMR (500 MHz) δ 7.6-7.0 (ArH), 3.3 (Si-OMe), 0.0 (Si-OTMS)

¹³C Solid State NMR (125 MHz) δ 141 (NCN), 140-127 (ArC), 49 (Si-OMe), 0 (Si-OTMS).

7.3.19. Synthesis of silica material **M-Bz-Im-Ir₍₁₎**

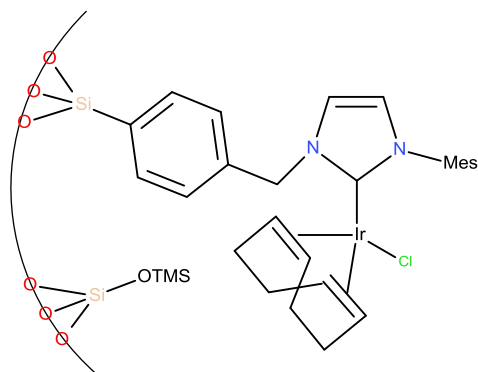


Figure 7.24 Structure of M-Bz-Im-Ir

Protected benzylimidazolium silica (**M-Bz-Im**) (500 mg, 0.023 mmol) was added to a schlenk tube tube and heated at 60°C under vacuum for a period of 2 hours. Under inert conditions AgOC(CF₃)₃ (134 mg, 0.37 mmol) and acetonitrile (8 ml) was added and stirred for 12 hours in the absence of light at room temperature. The solid was filtered and washed several times with acetonitrile and DCM and the material dried under vacuum for 5 hours. To this material a solution of acetonitrile (7ml) containing [IrCODCl]₂ (75mg, 0.112 mmol) was added and stirred at room temperature for 18 hours. The reaction mixture was cannula filtered and the solid washed several times with acetonitrile, DCM and methanol, until the filtrate was colour less and finally dried under vacuum for 8 hours, to produce a beige solid (**M-Pr-Im-Ir₍₁₎**, 490 mg).

¹H Solid State NMR (500 MHz) δ 7.3-6.7 (ArH), 3.3 (Si-OMe), 0.3 (Si-OTMS).

¹³C Solid State NMR (125 MHz) δ 140* (NCN), 134- 127 (ArC), 60 (Si-OMe), 5 (Si-OTMS).

*This region is considerably less compared to the starting material M-Bz-Im.

7.3.20. Synthesis of silica material **M-Pr-Im-Ir₍₂₎**

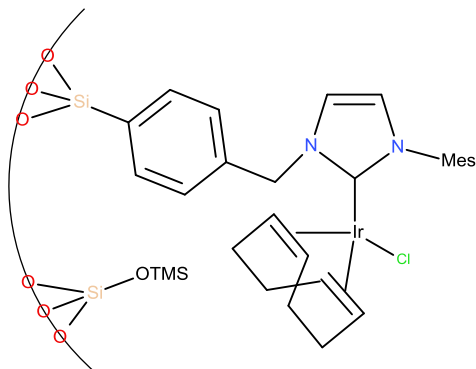


Figure 7.25 Structure of M-Bz-Im-Ir

Protected benzylimidazolium silica (**M-Bz-Im**) (500 mg, 0.023 mmol) was added to a schlenk tube and heated at 60°C under vacuum for 8 hours. The schlenk tube was removed from the heat and cooled. To the schlenk tube toluene (4 ml) was added and stirred for 10-15 minutes. A solution of Potassium *bis*(trimethylsilyl)amide (KHMDs, 0.5ml, 0.027 mmol) in toluene (1.5 ml) was added dropwise to the **M-Bz-Im** suspension, under argon and stirred for 1 hour. The reaction mixture was cannula filtered and the solid washed several times with toluene, to remove excess KHMDs. [Ir(COD)Cl]₂ (0.0906 g, 0.135 mmol) was dissolved in 5 ml toluene was added to the solid and stirred for 18 hours under argon and at room temperature. The reaction mixture was cannula filtered and the solid washed several times with toluene and DCM, until the filtrate was colour less and finally dried under vacuum for 8 hours, to produce a pale yellow solid (**M-Pr-Im-Ir₍₂₎**, 480 mg).

¹H Solid State NMR (500 MHz) δ 7.4-6.4 (ArH), 3.3 (Si-OMe), 0.3 (Si-OTMS). ¹³C Solid State NMR (125 MHz) δ 140* (NCN), 137- 120 (ArC), 60 (Si-OMe), 5 (Si-OTMS). *This region is considerably less compared to the starting material M-Bz-Im.

7.3.21. Synthesis of 3,4-dihydroquinazoline

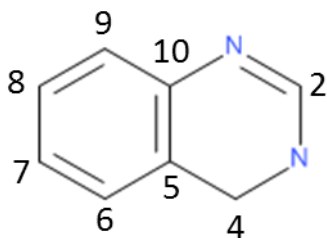


Figure 7.26 Structure of 3,4-dihydroquinazoline

o-Aminobenzylamine (4.0 g, 33 mmol) was dissolved in anhydrous triethylorthoformate (20 ml, 120 mmol). The reaction was heated at reflux, 120°C for 14 hours and then allowed to cool to room temperature. The reaction mixture was concentrated under reduced pressure to give a beige solid. The crude product was obtained and recrystallized from toluene to give 2.8 g (21 mmol, 64.7 %) cream coloured product and stored under inert conditions.

$^1\text{H NMR}$ (400 MHz, CD_2Cl_2 , 243K): δ 10.54 (vb, 1H, NH), 7.16 (s, 1H, H2), 7.13 (m, $J=5.7$ Hz, 1H, H7) 7.01 (m, $J=2.3$ Hz, 1H, H8), 6.9 (m, $J=5.7$ Hz, 1H, H6), 6.86 (dt, $J=8.1$ Hz, 1.1 Hz, 1H, H9), 4.63 (s, 2H, H4). $^{13}\text{C}\{^1\text{H}\}$ NMR (100 MHz, CD_2Cl_2 , 243K): δ 147.11 (C2), 139.05 (C5), 127.82 (C7), 126.02 (C6), 124.21 (C8), 120.6 (C10), 119.93 (C9), 43.9 (C4). MS (ESI+): m/z 132

7.4. Characterisation of Catalyst Precursors and Their Active Analogues

7.4.1. [Ir(IMes)(COD)Cl] (2-c)

Collected characterisation data agreed with that in literature⁹³

7.4.2. [Ir(IMes)(pyridine)₃(H)₂]Cl (5-c)

¹H NMR (CD₃OD, 500 MHz, 243 K): 8.34 (d, J = 4.98 Hz, 4H, *ortho*H, py *trans* to hydride), 8.09 (d, J = 5.43 Hz, 2H, *ortho*H, py *cis* to hydride), 7.79 (tt, J = 7.53 Hz, 1.46 Hz, 2H, *para*H, py *trans* to hydride), 7.69 (t, J = 7.67 Hz, 1H, *para*H, py *cis* to hydride), 7.18 (s, 2H, N-CH-CH-N), 7.14 (m, 4H, *meta*H, py *trans* to hydride), 6.99 (m, 2H, *meta*H, py *cis* to hydride), 6.67 (s, 4H, CH^{mes}), 2.20 (s, 6H, *p*CH₃^{mes}), 2.06 (s, 12 H, *o*CH₃^{mes}), -22.52 (s, 2H, hydrides).

¹³C{¹H} NMR (CD₃OD, 151 MHz, 243 K): 194.0 (NCN), 167.5 (N-C^{mes}), 155.3 (*ortho*C, py *cis* to hydride), 154.3 (*ortho*C, py *trans* to hydride), 138.2 (C^{ar}), 136.3 (*para*C, py *cis* to hydride), 135.8 (*para*C, py *trans* to hydride), 135.1 (C^{ar}), 128.4 (CH^{ar}), 125.3 (*meta*C, py *cis* to hydride), 125.2 (*meta*C, py *trans* to hydride), 122.4 (NCHCHN), 19.7 (*para*CH₃^{mes}), 17.7 (*ortho*CH₃^{mes}).

¹⁵N{¹H} NMR (CD₃OD, 50.6 MHz, 253 K): 194.5 (Carbene N), 255.6 (py *trans* to Hydride), 239.1 (py *cis* to hydride).

7.4.3. [Ir(IMes)(Benzimidazole)₃(H)₂]Cl (5-c)

¹H NMR (400 MHz, CD₃OD, 298 K): δ -21.22 (2H, hydride), 8.78 (s, 2H, NCHN *trans* benz), 7.54 (s, 1H, NCHN *cis* benz), 7.48 (d, Aryl CH *trans* benz), 7.42 (t, Aryl CH *trans* benz), 7.37 (t, Aryl CH *cis*), 7.30 (Aryl CH *trans* benz), 7.21 (d, Aryl CH *cis* benz), 7.08 (s, Aryl CH^{mes}), 6.99 (t, Aryl CH *trans* benz), 6.92 (s, Aryl CH^{mes}), 6.53 (t, Aryl CH *cis* benz), 6.26 (s, NCHCHN), 2.12 (CH₃^{mes}), 1.80 (CH₃^{mes}), 1.73 (CH₃^{mes}).

¹³C{¹H} NMR (100 MHz, CD₃OD, 298 K): δ 155.9 (Ir-NCN), 146.33 (NCHN *cis* benz), 143.51 (NCHN *trans* benz), 143.20 (Q C *trans* benz), 142.10 (Q C *cis* benz), 137.6 (Q C^{mes}), 134.6 (Q C^{mes}), 132.48 (Q C *cis* benz), 131.46 (Q C *trans* benz), 128.99 (Q C^{mes}), 128.82 (Q C^{mes}), 128.8 (Aryl C *cis* benz), 127.53 (NCHCHN), 124.0 (Aryl C *cis* benz), 123.7 (Aryl C *cis* benz), 122.7 (Aryl C *trans* benz), 122.10 (Aryl C *trans* benz), 121.61 (Aryl C *trans* benz), 120.3 (Aryl C *trans* benz), 19.8 (CH₃^{mes}), 17.8 (CH₃^{mes}), 16.6 (CH₃^{mes}).

$^{15}\text{N}\{^1\text{H}\}$ NMR (50.6 MHz, CD_3OD , 253 K): 196.5 (Carbene N), 186.7 (benz *trans* to Hydride), 153.7 (benz *cis* to hydride), 147.8 (benz *trans* to Hydride), 147.5 (benz *cis* to Hydride)

7.4.4. $[\text{Ir}(\text{IMes})(\text{Quinazoline})_3(\text{H})_2]\text{Cl}$ (5-c)

^1H NMR (400 MHz, CD_3OD , 243 K): δ -21.87 (2H, hydride), 9.59 (s, 1H, *trans* $\text{NCH}^{4'}$ quin), 9.30 (s, 1H, *cis* $\text{NCH}^{4'}$ quin), 9.18 (s, 1H, *cis* NCHN quin), 9.16 (s, 1H, *trans* NCHN quin), 8.15 (t, 1H, *trans* Aryl H quin), 8.12 (d, 1H, *trans* Aryl H quin), 8.07 (d, 1H, *trans* Aryl H quin), 7.97 (t, 1H, *cis* Aryl H quin), 7.89 (d, 1H, *cis* Aryl H quin), 7.84 (t, 1H, *trans* Aryl H quin), 7.60 (d, 1H, *cis* Aryl H quin), 7.54 (t, 1H, *cis* Aryl H quin), 7.25 (s, 2H, NCHCHN), 6.33 (s, 2H, Aryl H^{mes}), 6.27 (s, 2H, Aryl H^{mes}), 2.21-1.83 (m, 18H, mes- CH_3).

$^{13}\text{C}\{^1\text{H}\}$ NMR (100 MHz, CD_3OD , 243 K): δ 179.59 (Ir-NCN), 164.69 (*trans* NCN quin, J_{CH} 186.32Hz), 164.4 (*cis* NCN quin, J_{CH} 186.32Hz), 160.74 (*cis* $\text{NCH}^{4'}$ quin, J_{CH} 208.68Hz), 158.05 (*trans* NCN quin, J_{CH} 207.63Hz), 158.01 (Q C *trans* quin), 149.30 (Q C *cis* quin), 147.44 (Q C *cis* quin), 147.40 (Q C *trans* quin), 138.65 (Q C-mes), 136.76 (Q C-mes), 136.20 (Q C-mes), 135.90 (*cis* Aryl C quin), 134.76 (Q C-mes), 129.09 (*trans* Aryl C quin), 129.05 (*cis* Aryl C quin), 128.06 (*trans* Aryl C quin), 127.51 (*trans* Aryl C quin), 127.37 (*cis* Aryl C quin), 127.3 (*trans* Aryl C quin), 126.99 (*trans* Aryl C quin), 128.3 (2xmes Aryl C), 122.86 (NCHCHN), 19.89 (mes- CH_3), 19.58 (mes- CH_3), 17.78 (mes- CH_3).

$^{15}\text{N}\{^1\text{H}\}$ NMR (50.6 MHz, CD_3OD , 243 K): 194.87 (Carbene N), 225.30 (*cis* quin N), 237.81 (*trans* quin N, 9 Hz), 282.5 (*trans* quin N), 285.1 (*cis* quin N,)

7.4.5. $[\text{Ir}(\text{IMes})(\text{Quinazoline})_2(\text{DCM})(\text{H})_2]\text{Cl}$ (5-c)

^1H NMR (400 MHz, CD_2Cl_2 , 273 K): δ -23.78 (1H, hydride), -22.78 (1H, hydride), 10.08 (s, 1H, *trans* $\text{NCH}^{4'}$ quin), 9.76 (s, 1H, *cis* $\text{NCH}^{4'}$ quin), 9.40 (s, 1H, *cis* NCHN quin), 9.20 (s, 1H, *trans* NCHN quin), 8.05 (d, 1H, *trans* Aryl H quin), 7.97 (d, 1H, *cis* Aryl H quin), 7.94 (d, 1H, *trans* Aryl H quin), 7.79 (t, 1H, *trans* Aryl H quin), 7.74 (d, 1H, *cis* Aryl H quin), 7.70 (t, 1H, *trans* Aryl H quin), 7.66 (d, 1H, *cis* Aryl H quin), 7.44 (t, 1H, *trans* Aryl H quin), 6.83 (s, 2H, NCHCHN), 6.64 (s, 2H, Aryl H^{mes}), 6.64 (s, 2H, Aryl H^{mes}), 2.28-1.79 (m, 18H, mes- CH_3).

$^{13}\text{C}\{^1\text{H}\}$ NMR (100 MHz, CD_2Cl_2 , 273 K): δ 182.86 (Ir-NCN), 160.8 (*cis* NCN quin), 160.4 (*trans* NCN quin), 159.1 (*trans* $\text{NCH}^{4'}$ quin), 134.6 (*cis* Aryl C quin), 134.5 (*trans* Aryl C quin), 128.3 (*cis* Aryl C quin), 128.3 (*trans* Aryl C quin), 128.3 (2xmes Aryl C), 128.2 (*cis* Aryl C quin), 128.2 (*trans* Aryl C quin), 127.6 (*trans* Aryl C quin), 127.4 (*trans* Aryl C quin), 121.6 (NCHCHN), 20.5 (mes- CH_3), 18.1 (mes- CH_3), 18.0 (mes- CH_3).

$^{15}\text{N}\{^1\text{H}\}$ NMR (50.6 MHz, CD_2Cl_2 , 273 K): 198.8 (Carbene N), 226 (*cis* quin N), 246.5 (*trans* quin N, 14Hz), 282.9 (*cis* quin N), 283.6 (*trans* quin N, 16Hz)

7.4.6. $[\text{Ir}(\text{IMes})(3,4\text{-dihydroquinazoline})_3(\text{H})_2]\text{Cl}$ (5-c)

^1H NMR (400 MHz, CD_3OD , 243 K): δ -23.50 (2H, hydride), 7.12 (s, 1H, *cis* NCHN 3,4-dihydroquin), 7.06 (d, 1H, *cis* Aryl H 3,4-dihydroquin), 7.02 (t, 1H, *trans* Aryl H 3,4-dihydroquin), 6.99 (t, 1H, *cis* Aryl H 3,4-dihydroquin), 6.98 (s, 1H, *trans* NCHN 3,4-dihydroquin), 6.89 (d, 1H, *trans* Aryl H 3,4-dihydroquin), 6.83 (t, 1H, *cis* Aryl H 3,4-dihydroquin), 6.80 (t, 1H, *trans* Aryl H 3,4-dihydroquin), 6.79 (s, 2H, NCHCHN), 6.78 (s, 4H, Aryl H^{mes}), 6.64 (d, 1H, *trans* Aryl H 3,4-dihydroquin), 6.47 (d, 1H, *cis* Aryl H 3,4-dihydroquin), 4.57 (s, 2H, *trans* NCH_2 3,4-dihydroquin), 4.42 (s, 2H, *cis* NCH_2 3,4-dihydroquin), 2.19-2.02 (m, 18H, mes- CH_3).

$^{13}\text{C}\{^1\text{H}\}$ NMR (100 MHz, CD_3OD , 243 K): δ 160.2 (Ir-NCN), 155.53 (NCHCHN), 154.3 (*trans* NCN 3,4-dihydroquin), 144.2 (*cis* NCN 3,4-dihydroquin), 143.10 (Q C *cis* 3,4-dihydroquin), 143.0 (Q C *cis* 3,4-dihydroquin), 139.00 (Q C *trans* 3,4-dihydroquin), 138.40 (Q C^{mes}), 138.20 (Q C *trans* 3,4-dihydroquin), 137.10 (Q C^{mes}), 128.70 (Q C^{mes}), 125.8 (*trans* Aryl C 3,4-dihydroquin), 124.10 (*cis* Aryl C 3,4-dihydroquin), 124.00 (*trans* Aryl C 3,4-dihydroquin), 122.10 (Q C-mes), 120.80 (*cis* Aryl C 3,4-dihydroquin), 120.70 (*trans* Aryl C 3,4-dihydroquin), 120.5 (2*mes Aryl C), 120.10 (*cis* Aryl C 3,4-dihydroquin), 119.9 (*trans* Aryl C 3,4-dihydroquin), 117.5 (*cis* Aryl C 3,4-dihydroquin), 57.40 (*trans* NCH_2 3,4-dihydroquin), 45.40 (*cis* NCH_2 3,4-dihydroquin), 20.40 (2*mes- CH_3), 18.80 (mes- CH_3).

$^{15}\text{N}\{^1\text{H}\}$ NMR (50.6 MHz, CD_3OD , 243 K): δ 193.1 (Carbene N), 157.3 (*trans* 3,4-dihydroquin N), 141.1 (*cis* N 3,4-dihydroquin), (*trans* 3,4-dihydroquin N), (*cis* 3,4-dihydroquin N).

7.4.7. $[\text{Ir}(\text{IMes})(\text{oxazole})_3(\text{H})_2]\text{Cl}$ (5-c)

^1H NMR (400 MHz, CD_3OD , 243 K): δ -22.71 (2H, hydride), 8.18 (d, $J=0.68$ Hz, 1H, NCHO *cis* oxazole), 7.98 (d, $J=0.68$ Hz, 2H, NCHO *trans* oxazole), 7.91 (t, $J=1$ Hz, 2H, OCHCHN *trans* oxazole), 7.76 (t, $J=1$ Hz, 1H, OCHCHN *cis* oxazole), 7.11 (s, 2H, NCHCHN), 7.05 (d, $J=0.68$ Hz, 2H, OCHCHN *trans* oxazole), 6.81 (s, 4H, Aryl H^{mes}), 6.58 (d, $J=0.68$ Hz, 1H, OCHCHN *cis* oxazole), 2.30-2.02 (m, 18H, mes- CH_3).

$^{13}\text{C}\{^1\text{H}\}$ NMR (100 MHz, CD_3OD , 243 K): δ 156.99 (NCHO $J_{\text{CH}}=238$ Hz, *cis* oxazole), 156.83 (NCHO $J_{\text{CH}}=236.5$ Hz, *trans* oxazole), 150.67 (Ir-NCN), 140.72 (OCHCHN, $J_{\text{CH}}=214$ Hz *cis* oxazole), 140.13 (OCHCHN, $J_{\text{CH}}=214$ Hz *trans* oxazole), 138.58 (Q C^{mes}), 137.5 (Q C^{mes}), 135.4

(Q C^{mes}), 129.80 (OCHCHN, J_{CH}=200 Hz *trans* oxazole), 129.46 (OCHCHN, J_{CH}=200 Hz *cis* oxazole), 128.6 (Aryl CH^{mes}), 122.25 (NCHCHN), 19.79 (mes-CH₃), 17.53 (mes-CH₃).

¹⁵N{¹H} NMR (50.6 MHz, CD₃OD, 243 K): δ 202.90 (N *trans* oxazole), 193.58 (Carbene N), 189.40 (N *cis* oxazole).

7.4.8. [Ir(IMes)(isoxazole)₃(H)₂]Cl (5-c)

¹H NMR (400 MHz, CD₃OD, 243 K): δ -21.71 (2H, hydride), 8.75 (d, J=1.95 Hz, 2H, NCH *trans* isoxazole), 8.47 (d, J=1.95 Hz, 1H, NCH *cis* isoxazole), 8.19 (t, J=2.07 Hz, 1H, OCH *cis* isoxazole), 7.95 (d, J=1.95 Hz, 2H, OCH *trans* isoxazole), 7.11 (s, 2H, NCHCHN), 6.88 (s, 4H, Aryl H^{mes}), 6.47 (t, J=1.95 Hz, 2H, OCHCHCHN *trans* isoxazole), 6.38 (t, J=2.07 Hz, 1H, OCHCHCHN *cis* isoxazole), 2.0-1.58 (m, 18H, mes-CH₃).

¹³C{¹H} NMR (100 MHz, CD₃OD, 243 K): δ 159.30 (NCH, *cis* isoxazole), 159.28 (NCH, *trans* isoxazole), 154.05 (OCH, *trans* isoxazole), 153.95 (OCH, *cis* isoxazole), 148.30 (Ir-NCN), 138.28 (Q C^{mes}), 137.22 (Q C^{mes}), 135.25 (Q C^{mes}), 128.4 (Aryl CH^{mes}), 122.38 (NCHCHN), 106.24 (OCHCHCHN, *cis* isoxazole), 106.12 (OCHCHCHN, *trans* isoxazole), 26.27 (mes-CH₃), 19.78 (mes-CH₃), 16.9 (mes-CH₃).

7.4.9. [Ir(ImMe₂NPr₂)(COD)Cl] (2-a)

¹H NMR (700 MHz, CD₃OD, 278 K): δ 6.05 (sept, J=7.2 Hz, 2H, CH(CH₃)₂), 4.48 (b, 2H, CH-COD), 2.99 (b, 2H, CH-COD), 2.19 (b, 8H, CH₂-COD), 2.15 (s, 6H, NC(CH₃)C(CH₃)N), 1.61 (d, J=6.92 Hz, 6H, CH(CH₃)₂), 1.47 (d, J=6.92 Hz, 6H, CH(CH₃)₂). ¹³C{¹H} NMR (150 MHz, CD₃OD, 278 K): δ 177.39 (NCN), 124.63 (NCCN), 82.70 (CH-COD), 53.33 ((CH₃)₂CH-N), 51.00 (CH-COD), 33.70 (CH₂-COD), 29.40 (CH₂-COD), 22.77 ((CH₃-C-CH₃), 21.77 (CH₃-C-CH₃), 10.30 (C-CH₃). ¹⁵N{¹H} NMR (70 MHz, CD₃OD, 278 K): δ 197.8 (Carbene N).

MS (ESI⁺): m/z 522 (M⁺ -Cl +acetonitrile), 481 (M⁺ -Cl)

7.4.10. [Ir(ImMe₂NPr₂)(pyridine)(COD)]Cl (4-a)

¹H NMR (700 MHz, CD₃OD, 278 K): δ 8.89 (d, J=5.38 Hz, 2H, *o*-pyridine), 7.92 (b, 1H *p*-pyridine), 7.61 (d, J=6.78 Hz, 2H, *m*-pyridine), 6.05 (sept, J=7.21 Hz, 2H, CH(CH₃)₂), 3.95 (b, 2H, CH-COD), 3.76 (b, 2H, CH-COD), 2.40 (b, 4H, CH₂-COD), 1.94 (b, 4H, CH₂-COD), 2.22

(s, 6H, NC(CH₃)C(CH₃)N), 1.72 (d, J=6.92 Hz, 6H, CH(CH₃)₂), 1.45 (d, J=6.92 Hz, 6H, CH(CH₃)₂).
¹³C{¹H} NMR (150 MHz, CD₃OD, 278 K): δ 177.39 (NCN), 150.52 (C-*o*-pyridine), 137.2 (C-*p*-pyridine), 126.40 (C-*m*-pyridine), 124.63 (NCCN), 81.60 (CH-COD), 54.32 ((CH₃)₂CH-N), 53.51 (CH-COD), 32.08 (CH₂-COD), 29.40 (CH₂-COD) 21.23 ((CH₃-C-CH₃), 20.60 (CH₃-C-CH₃), 8.88 (C-CH₃).

¹⁵N{¹H} NMR (70 MHz, CD₃OD, 278 K): δ 198.8 (Carbene N) 240.30 (bound pyridine).

MS (ESI+): m/z 560.7 (M+), 481.5 (M+-C₅H₅N)

7.4.11. [Ir(ImMe₂NPr_i₂)(pyridine)₃(H)₂]Cl (5-a)

¹H NMR (500 MHz, CD₃OD, 298 K): δ 8.78 (d, J=4.26 Hz, 2H, *ortho*H, axial pyridine), 8.27 (d, J=4.26 Hz, 2H, *ortho*H, pyridine *trans* to H), 8.01 (m, 1H, *para*H, axial pyridine), 7.92 (m, 1H, *para*H, pyridine *trans* to H), 7.50 (m, 2H, *meta*H, axial pyridine), 7.25 (m, 2H, *meta*H, pyridine *trans* to H), 6.05 (sept, J=7.2 Hz, 2H, CH(CH₃)₂), 2.22 (s, 6H, NC(CH₃)C(CH₃)N), 1.72 (d, J=6.93 Hz, 6H, CH(CH₃)₂), 1.44 (d, J=6.93 Hz, 6H, CH(CH₃)₂), -22.77 (s, 2H, Hydrides)

¹³C{¹H} NMR (151 MHz, CD₃OD, 298 K): δ 176.3 (NCN), 155.93 (Ar-CH), 155.1 (Ar-CH), 138.2 (Ar-CH), 137.3 (Ar-CH), 126.3 (Ar-CH), 125.8 (Ar-CH), 125.7 (NCCN), 54. (CH), 20.1 (CH₃), 19.5 (CH₃), 9.68 (CH₃)

¹⁵N{¹H} NMR (50.6 MHz, CD₃OD, 253 K): δ 198.8 (Carbene N), 242.67 (axial pyridine N), 253.75 (equatorial pyridine N)

7.4.12. [Ir(ImMe₂NPr_i₂)(pyridine)₂(MeOH)(H)₂]Cl

¹H NMR (500 MHz, CD₃OD, 298 K): δ 8.78 (d, J=4.26 Hz, 2H, *ortho*H, axial pyridine), 8.27 (d, J=4.26 Hz, 2H, *ortho*H, pyridine *trans* to H), 8.01 (m, 1H, *para*H, axial pyridine), 7.92 (m, 1H, *para*H, pyridine *trans* to H), 7.50 (m, 2H, *meta*H, axial pyridine), 7.25 (m, 2H, *meta*H, pyridine *trans* to H), 6.05 (sept, J=7.2 Hz, 2H, CH(CH₃)₂), 2.22 (s, 6H, NC(CH₃)C(CH₃)N), 1.72 (d, J=6.93 Hz, 6H, CH(CH₃)₂), 1.44 (d, J=6.93 Hz, 6H, CH(CH₃)₂), -22.56 (hydride), -26.51 (MeOH, Hydride).

¹³C{¹H} NMR (151 MHz, CD₃OD, 298 K): δ 176.3 (NCN), 155.93 (Ar-CH), 155.1 (Ar-CH), 138.2 (Ar-CH), 137.3 (Ar-CH), 126.3 (Ar-CH), 125.8 (Ar-CH), 125.7 (NCCN), 54. (CH), 20.1 (CH₃), 19.5 (CH₃), 9.68 (CH₃)

¹⁵N{¹H} NMR (50.6 MHz, CD₃OD, 253 K): δ 198.8 (Carbene N), 242.67 (axial pyridine N), 253.75 (equatorial pyridine N)

7.4.13. [Ir(BzIMes)(COD)Cl] (2-b)

$^1\text{H NMR}$ (400 MHz, CD_3OD , 298 K): δ 7.45-7.35 (m, 5H, Ph-CH), 7.29 (CH-COD), 7.07 (s, 1H, $m\text{CH}^{\text{mes}}$), 6.96 (d, $J=1.97$ Hz, 1H, NCHCHN), 6.95 (s, 1H, $m\text{CH}^{\text{mes}}$), 6.78 (d, $J=1.97$ Hz, 1H, NCHCHN), 6.25 (d, $J=15.12$ Hz, 1H, Ph- $\text{CH}_2\text{-N}$), 5.51 (d $J=15.16$ Hz, 1H Ph- $\text{CH}_2\text{-N}$), 4.48 (b, 2H, CH-COD), 3.01 (m, 1H, CH-COD), 2.75 (m, H, CH-COD) 2.4 (s, 6H, $o\text{CH}^{\text{mes}}$), 1.96 (s, 3H, $p\text{CH}^{\text{mes}}$), 2.03-1.2 (m, 8H, $\text{CH}_2\text{-COD}$)

$^{13}\text{C}\{^1\text{H}\}$ NMR (400 MHz, CD_3OD , 298 K): δ 180.49 (NCN), 138.64 (Q N-C^{mes}) 137.4 (Q Ph- $\text{C-CH}_2\text{-N}$), 136.83 (Q $o\text{C}^{\text{mes}}$), 135.50 (Q $p\text{C}^{\text{mes}}$) 129.42 ($m\text{-ArCH}$), 128.58 (ArCH-Ph), 128.03 ($m\text{-ArCH}$), 123.04 (NCHCHN), 120.73 (NCHCHN), 84.10 (CH-COD), 55.00 (Ph- $\text{CH}_2\text{-N}$), 52.20 (CH-COD), 51.03 (CH-COD), 34.12 ($\text{CH}_2\text{-COD}$), 32.59 ($\text{CH}_2\text{-COD}$), 29.30 ($\text{CH}_2\text{-COD}$), 28.71 ($\text{CH}_2\text{-COD}$), 21.13 ($o\text{-CH}_3^{\text{mes}}$), 19.62 ($o\text{-CH}_3^{\text{mes}}$), 17.91 ($p\text{-CH}_3^{\text{mes}}$).

MS (ESI+): m/z 577.21 (M+ -Cl)

7.4.14. [Ir(BzIMes)(pyridine) $_3$ (H) $_2$]Cl (5-b)

$^1\text{H NMR}$ (400 MHz, CD_3OD , 298 K): δ 7.45-7.35 (m, 5H, Ph-CH), 7.07 (s, 1H, $m\text{CH}^{\text{mes}}$), 6.96 (d, $J=1.97$ Hz, 1H, NCHCHN), 6.95 (s, 1H, $m\text{CH}^{\text{mes}}$), 6.78 (d, $J=1.97$ Hz, 1H, NCHCHN), 6.25 (d, $J=15.12$ Hz, 1H, Ph- $\text{CH}_2\text{-N}$), 5.51 (d $J=15.16$ Hz, 1H Ph- $\text{CH}_2\text{-N}$), 3.01 2.4 (s, 6H, $o\text{CH}^{\text{mes}}$), 1.96 (s, 3H, $p\text{CH}^{\text{mes}}$),

8.36 (4H, *trans ortho* pyridine), 8.22 (2H, *cis ortho* pyridine), 7.80 (2H, *trans para* pyridine), 7.76 (4H, *trans meta* pyridine), 7.11 (4H, *cis meta* pyridine).

7.4.15. [Ir(SIMesCh)(COD)Cl] (2-f)

$^1\text{H NMR}$ (400 MHz, DMSO-d_6 , 298 K): δ 9.19 (s, 1H, $\text{H}_{\text{triazole}}$), 9.13 (s, 1H, $\text{H}_{\text{triazole}}$), 7.95 (s, 2H, NCH-CHN), 7.83 (s, 2H, H_{Ar}), 7.77 (s, 2H, H_{Ar}), 5.49 (br, 2H, OH), 4.87(d, $J_{\text{HH}} = 5.95$ Hz), 4.62 (s, 4H, $-\text{CH}=\text{COD}$), 2.70 (m, 4H, $\text{CH}(\text{CH}_3)_2$), 2.57-2.53 (br, 24H, $\text{CH}(\text{CH}_3)_2$), 1.60 – 1.97 (m, $-\text{CH}_2\text{-COD}$).

$^{13}\text{C}\{^1\text{H}\}$ NMR (101 MHz, $d_6\text{-DMSO}$, 298 K): δ 161.17 (Ir- C_{tmx}), 140.64 ($-\text{C}=\text{tmx}$), 139.65 (NCHN), 139.69 (2 $-\text{C}(\text{CH}_3)\text{-tmx}$), 138.57, 137.32, 137.01, 136.84, 135.79, 133.91 ($-\text{C}=\text{tmx}$), 127.32 (NCHCHN), 127.02 (NCHCHN), 120.95 ($-\text{CH}=\text{triazol}$), 120.51, 119.67 ($-\text{CH}=\text{aril}$), 83.55 ($-\text{CH}=\text{COD}$), 55.61 (CH_2OH), 51.01($-\text{CH}=\text{COD}$), 50.93 ($\text{N}(\text{CH}_3)_2$) 33.51 ($-\text{CH}_2\text{-COD}$), 30.13($\text{CH}(\text{CH}_3)_2$) 28.57 ($-\text{CH}_2\text{-COD}$), 22.79, 20.09 ($\text{CH}(\text{CH}_3)_2$).

7.4.16. [Ir(SIMesCh)(pyridine)₃(H)₂]Cl (5-f)

¹H NMR (400 MHz, CD₃OD, 298 K): δ -22.54 (2H, hydrides), 2.57-2.53 (br, 24H, CH(CH₃)₂), 2.70 (m, 4H, CH(CH₃)₂), 4.89 (d, J_{HH} = 5.95 Hz), 5.29 (br, 2H, OH), 7.14 (t, 1H, *para* proton of pyridine in axial position), 7.65 (t, 2H, *meta* proton of pyridine in axial position), 7.74 (t, 1H, *para* proton of pyridine molecules in equatorial position) 7.77 (s, 2H, H_{Ar}), 7.83 (s, 2H, H_{Ar}), 7.95 (s, 2H, NCH-CHN), 8.17 (t, 1H, *para* proton of pyridine in axial position), 8.40 (d, 2H, *ortho* proton of pyridine molecules in equatorial position), 8.70 (d, 2H, *ortho* proton of pyridine in axial position), 8.98 (s, 1H, H_{triazole}), 9.03 (s, 1H, H_{triazole}).

7.4.17. [Ir(SIMesTrimet)(COD)Cl] (2-g)

¹H NMR (400 MHz, DMSO-d₆, 298 K): δ 9.20 (br, 0.33H, H_{triazole}), δ 9.16 (br, 0.66H, H_{triazole}), 8.97 (s, 1H, H_{triazole}), 8.43 (s, 2H, -CH=, COD), 8.18 (s, 2H, -CH=, COD), 7.87 (s, 1H, H_{Ar}), 7.77 (s, 1H, H_{Ar}), 7.50 (s, 2H, H_{Ar}), 4.81 (s, 2H, CH₃N-CH₂-C_{triazole}), 4.77 (s, 2H, CH₃N-CH₂-C_{triazole}), 4.62 (br, 4H, NCH₂-CH₂N), 3.72 – 3.97 (m, -CH₂-, COD), 3.15 (s, 12H, N-CH₃), 3.13 (s, 12H, N-CH₃), 2.21 – 2.34 (m, 12H, Ar-CH₃)

¹³C{¹H} NMR (101 MHz, DMSO-d₆, 298 K): δ 162.17 (Ir-C_{tmx}), δ 138.90 (-C=, tmx), δ 136.98 (-C=, tmx_{triazole}), 133.50 (-C=, tmx), 133.10 (2 -C(CH₃)-, tmx), 127.60 (-CH=, triazol), 120.61 (-CH=, aril), 62.70 (NCH₂CH₂N), 59.48 (-CH₂-N), 52.5 (N(CH₃)₃), 62.5 (-CH=, COD), 49.38 (-CH=, COD), 46.4 (-CH=, COD), 31.40 (-CH₂-, COD), 17.8 (CH₃-C=).

7.4.18. [Ir(SIMesTrimet)(pyridine)₃(H)₂]Cl (5-g)

¹H NMR (400 MHz, CD₃OD, 253 K): δ -22.55 (2H, hydrides), 2.48-2.32 (m, 12H, Ar-CH₃), 3.24 (d, 18H, N-CH₃), 3.39 (br, 4H, NCH₂-CH₂N), 4.82 (d, 4H, CH₃N-CH₂-C_{triazole}), 7.84 (s, 4H, H_{Ar}), 9.07 (d, 2H, H_{triazole}), 9.22 (*trans ortho* Py), 8.12 (*trans meta* Py), 7.69 (*trans para* Py), 8.81 (*cis ortho* Py), 8.18 (*cis meta* Py), 7.70 (*cis para* Py)

¹³C{¹H} NMR (101 MHz, CD₃OD, 253 K): δ 170.2 (Ir-C_{tmx}), δ 138.40 (-C=, tmx), δ 137.2 (-C=, tmx_{triazole}), 130.8 (2 -C(CH₃)-, tmx), 126.9 (-C=, tmx), 126.70 (-CH=, triazol), 121.00 (-CH=, aril), 59.7 (-CH₂-N), 47.20 (NCH₂CH₂N), 52.0 (N(CH₃)₃), 153.2 (*trans ortho* Py), 137.9 (*trans meta* Py), 126.2 (*trans para* Py), 152.4 (*cis ortho* Py), 137.7 (*cis meta* Py), 125.7 (*cis para* Py).

¹⁵N{¹H} NMR (50.6 MHz, CD₃OD, 253 K): δ 358.22 (N, Mes-N_{triazol}), 357.58 (N, N_{triazol}), 257.3 (N, N_{triazol}), 252.2 (N, pyridine *trans* to hydride), 249 (N, pyridine *cis* to hydride), 130.7 (N, Ir-C-(NR)₂), 50.1 (N, N-(CH₃)₃).

7.5. Characterisation of Substrates and Associated Data

7.5.1. Pyridine

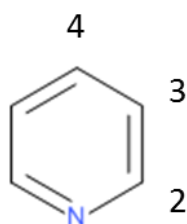


Figure 7.27 Labelled structure of pyridine.

^1H NMR (400 MHz, CD_3OD , 283K): δ 8.56 (dt, $J=4.35$ Hz, 1.63 Hz, 2H, **H2**), 7.89 (tt, $J=7.63$ Hz, 1.81 Hz, 1H, **H4**), 7.46 (m, $J=5.89$ Hz, 1.42 Hz, 2H, **H3**). $^{13}\text{C}\{^1\text{H}\}$ NMR (100 MHz, CD_3OD , 283K): δ 148.58 (**C2**), 137.12 (**C4**), 124.33 (**C3**).

7.5.1.1. Hyperpolarised spectra

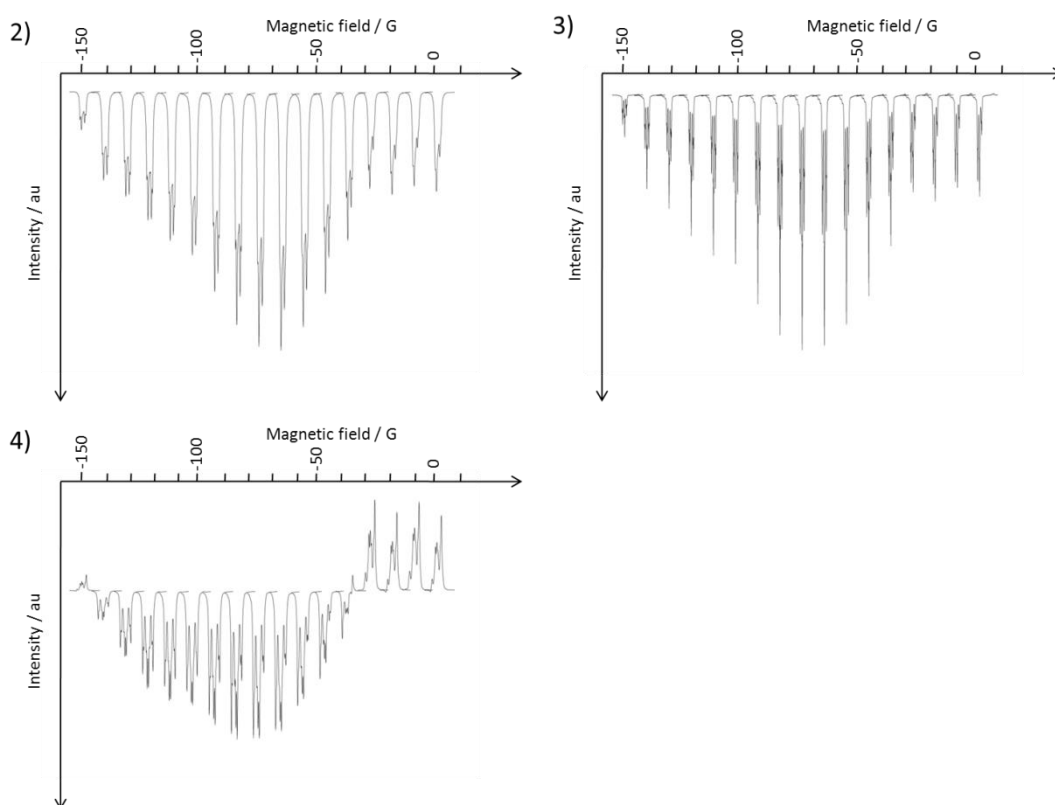


Figure 7.28 ^1H NMR field dependence spectra for hyperpolarised pyridine sample.

7.5.2. 3-methylpyridine

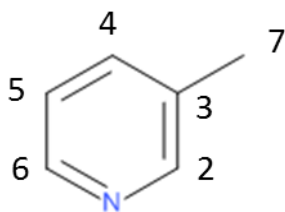


Figure 7.29 Labelled structure of 3-methylpyridine

^1H NMR (400 MHz, CD_3OD , 298K): δ 8.37 (s, 1H, **H2**), 8.31 (d, $J=4.5$ Hz, 1H, **H6**), 7.67 (d, $J=7.89$ Hz, 1H, **H4**), 7.32 (dd, $J=8.06$ Hz, 5.08 Hz, 1H, **H5**), 2.37 (s, 3H, **H7**). $^{13}\text{C}\{^1\text{H}\}$ NMR (100 MHz, CD_3OD , 298K): δ 148.87 (**C2**), 145.60 (**C6**), 137.36 (**C4**), 134.06 (**C3**), 123.33 (**C5**), 16.77 (**C7**).

7.5.2.1. Hyperpolarised spectra

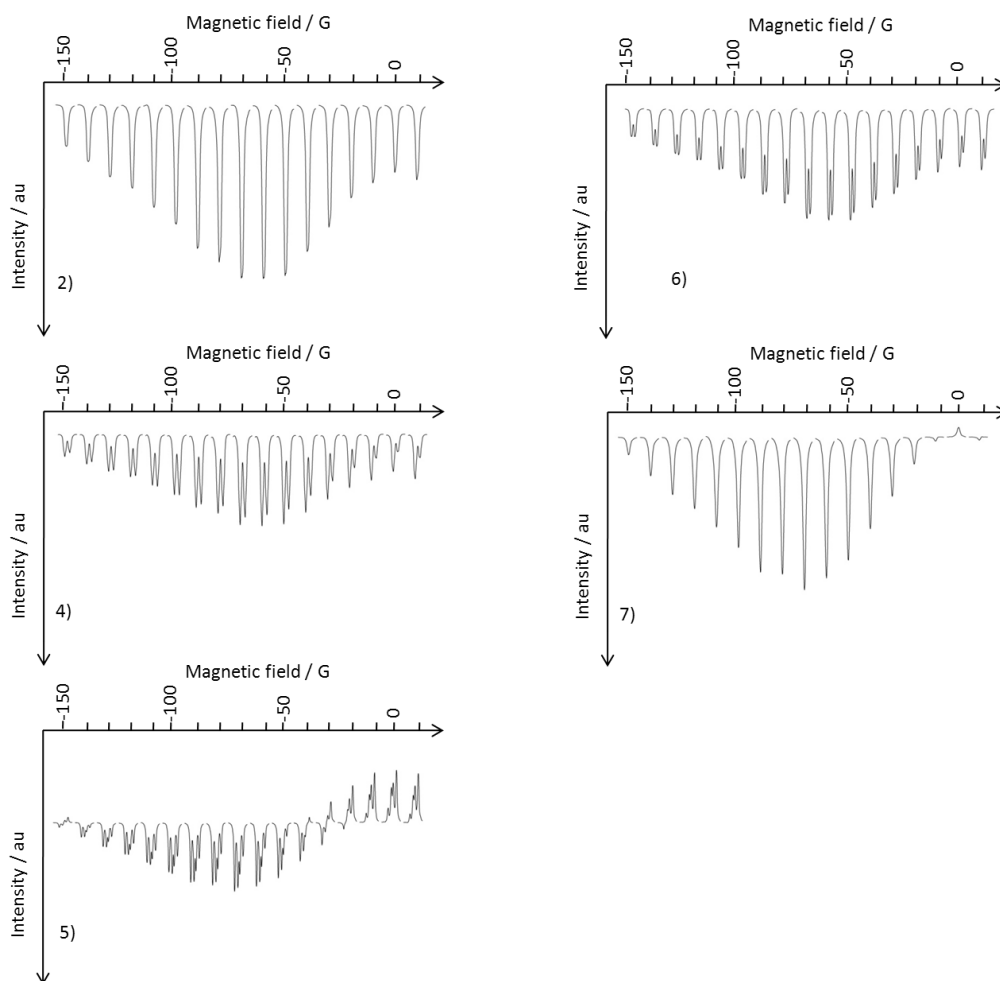


Figure 7.30 ^1H NMR field dependence spectra for hyperpolarised 3-methylpyridine sample.

7.5.3. 4-methylpyridine

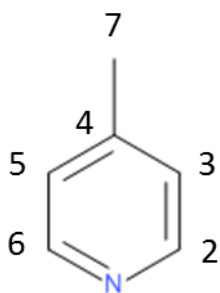


Figure 7.31 Labelled structure of 4-methylpyridine

$^1\text{H NMR}$ (400 MHz, CD_3OD , 298K): δ 8.36 (dd, $J=4.72$ Hz, 1.51 Hz, 2H, **H2&6**), 7.27 (d, $J=5.57$ Hz, 2H, **H3&5**), 2.39 (s, 3H, **H7**). $^{13}\text{C}\{^1\text{H}\}$ NMR (100 MHz, CD_3OD , 298K): δ 148.87 (**C2**), 147.40 (**C4**), 124.95 (**C3**), 20.89 (**C7**).

7.5.3.1. Hyperpolarised spectra

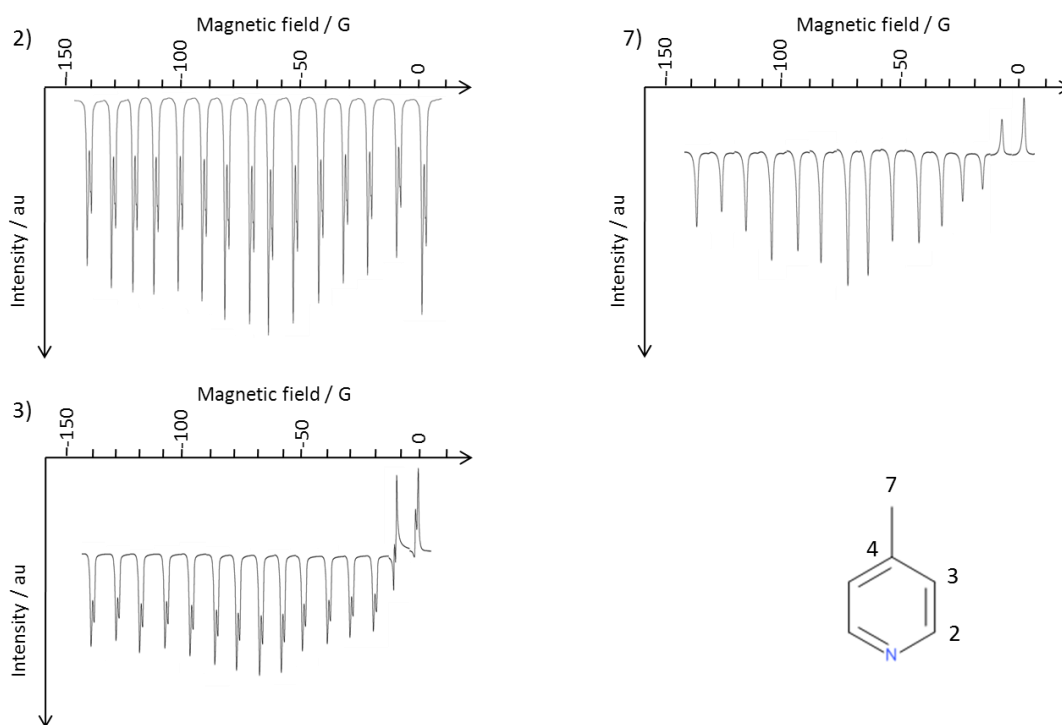


Figure 7.32 $^1\text{H NMR}$ field dependence spectra for hyperpolarised 4-methylpyridine sample.

7.5.4. Nicotinamide

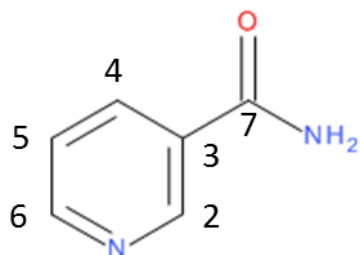


Figure 7.33 Labelled structure of nicotinamide.

^1H NMR (400 MHz, CD_3OD , 298K): δ 9.08 (d, $J=1.68$ Hz, 1H, **H2**), 8.71 (dd, $J=4.86$ Hz, 1.67 Hz, 1H, **H6**), 8.31 (dt, $J=8.12$ Hz, 1.67 Hz, 1H, **H4**), 7.57 (dd, $J=7.64$ Hz, 4.98 Hz, 1H, **H5**). $^{13}\text{C}\{^1\text{H}\}$ NMR (100 MHz, CD_3OD , 298K): δ 167.49 (**C7**), 151.47 (**C2**), 148.08 (**C6**), 136.01 (**C3**), 123.77 (**C5**).

7.5.4.1. Hyperpolarised spectra

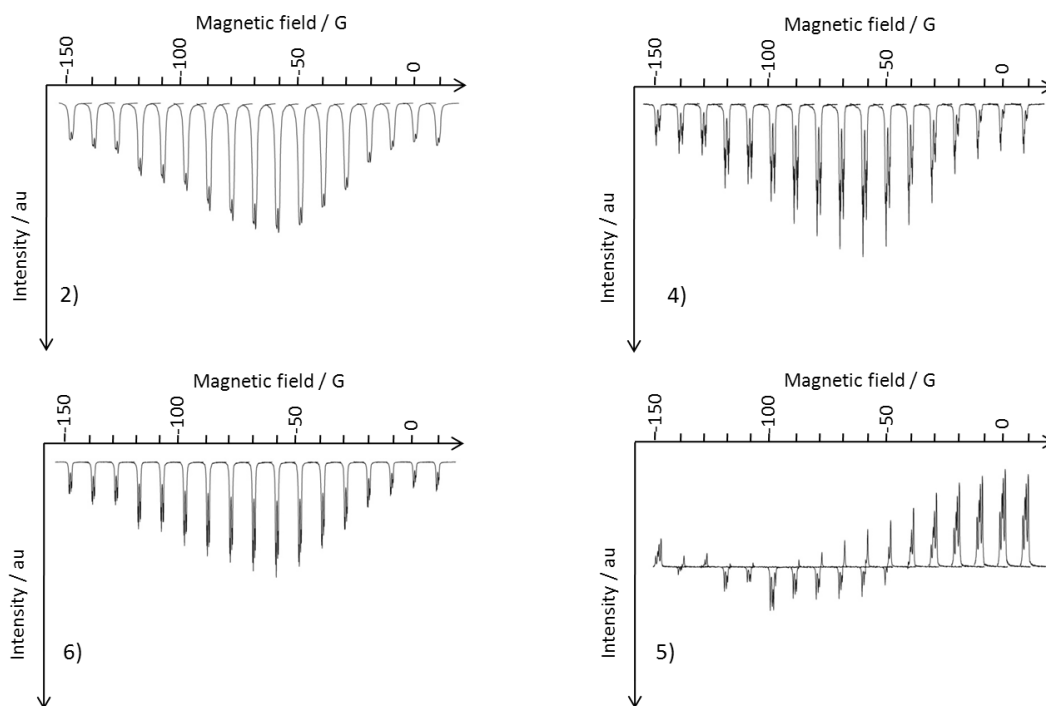


Figure 7.34 ^1H NMR field dependence spectra for hyperpolarised nicotinamide sample.

7.5.5. 3-acetoxymethylpyridine

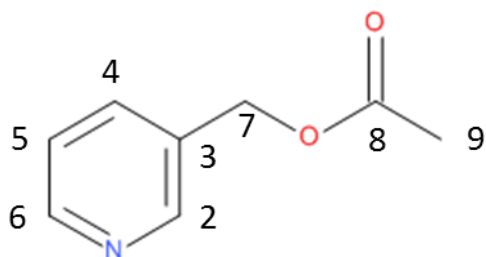


Figure 7.35 Labelled structure of 3-acetoxymethylpyridine

$^1\text{H NMR}$ (400 MHz, CD_3OD , 298K): δ 8.62 (s, 1H, **H2**), 8.55 (br, 1H, **H6**), 7.71-7.67 (m, 1H, **H4**), 7.30 (dd, $J=7.8$ Hz, 4.8 Hz, 1H, **H5**). 5.11 (d, $J=1$ Hz, 2H, **H7**), 2.10 (s, 3H, **H9**).

7.5.5.1. Hyperpolarised spectra

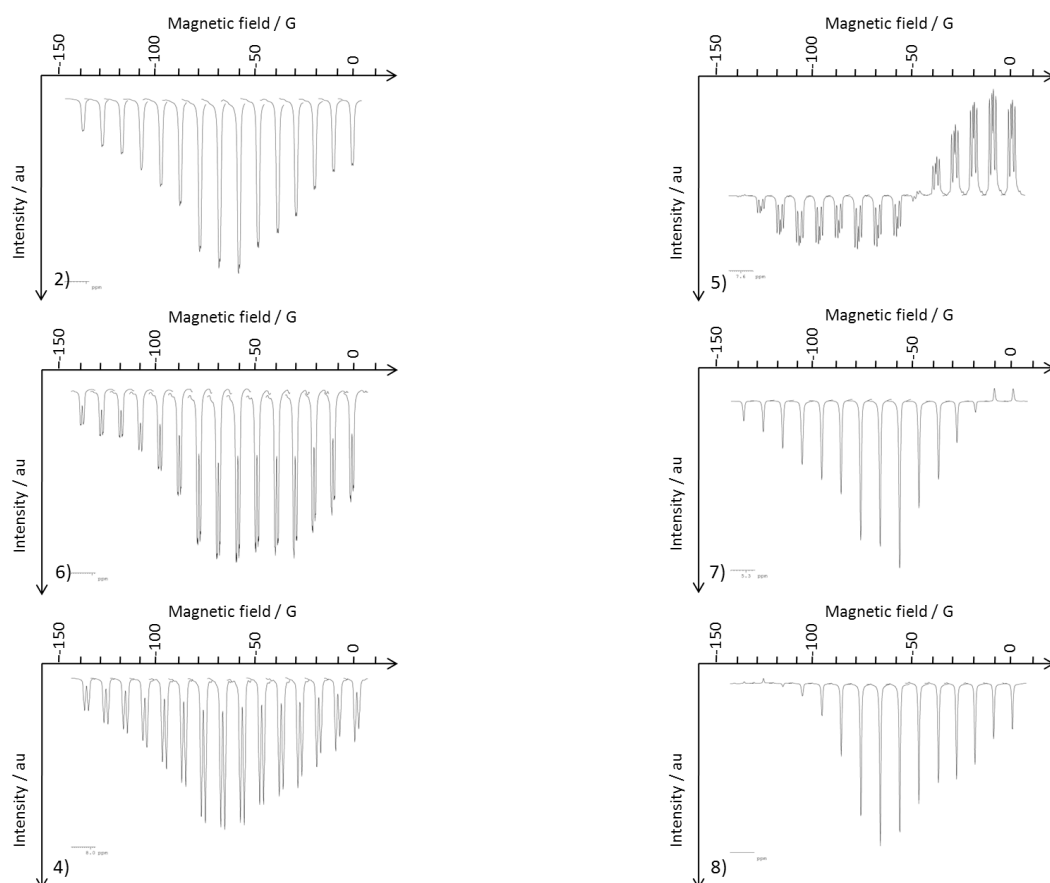


Figure 7.36 $^1\text{H NMR}$ field dependence spectra for hyperpolarised 3-acetoxymethylpyridine sample.

7.5.6. 5-methylpyrimidine

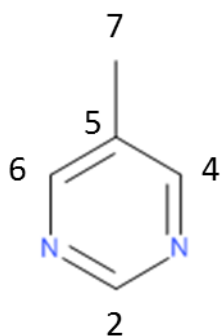


Figure 7.37 Labelled structure of 5-methylpyrimidine.

^1H NMR (400 MHz, CD_3OD , 298K): δ 8.97 (s, 1H, **H2**), 8.68 (s, 2H, **H4&6**), 2.39 (s, 3H, **H7**).

$^{13}\text{C}\{^1\text{H}\}$ NMR (100 MHz, CD_3OD , 298K): δ 157.60 (**C3**), 155.60 (**C5**), 131.70 (**C4**), 14.00 (**C7**).

7.5.6.1. Hyperpolarised spectra

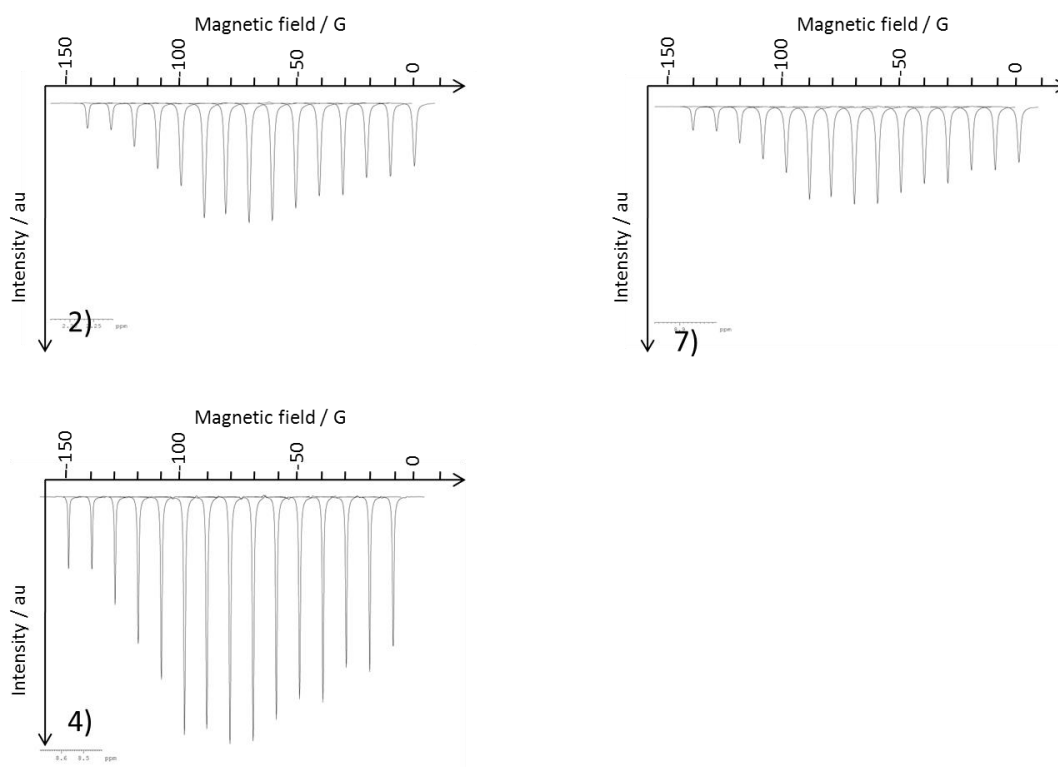


Figure 7.38 ^1H NMR field dependence spectra for hyperpolarised 5-methylpyrimidine sample.

7.5.7. Benzimidazole

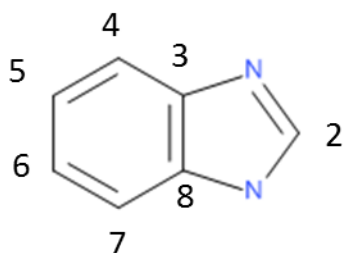


Figure 7.39 Labelled structure of benzimidazole.

^1H NMR (400 MHz, CD_3OD , 298K): δ 8.16 (s, 1H, **H2**), 7.62 (m, $J=3.17$ Hz, 1.03 Hz, 2H, **H4**), 7.28 (m, $J=3.17$ Hz, 1.36 Hz, 2H, **H5**). $^{13}\text{C}\{^1\text{H}\}$ NMR (100 MHz, CD_3OD , 298K): δ 141.90 (**C2**), 138.09 (**C3**), 121.78 (**C5**, **C6**), 115.31 (**C4**).

7.5.7.1. Hyperpolarised spectra

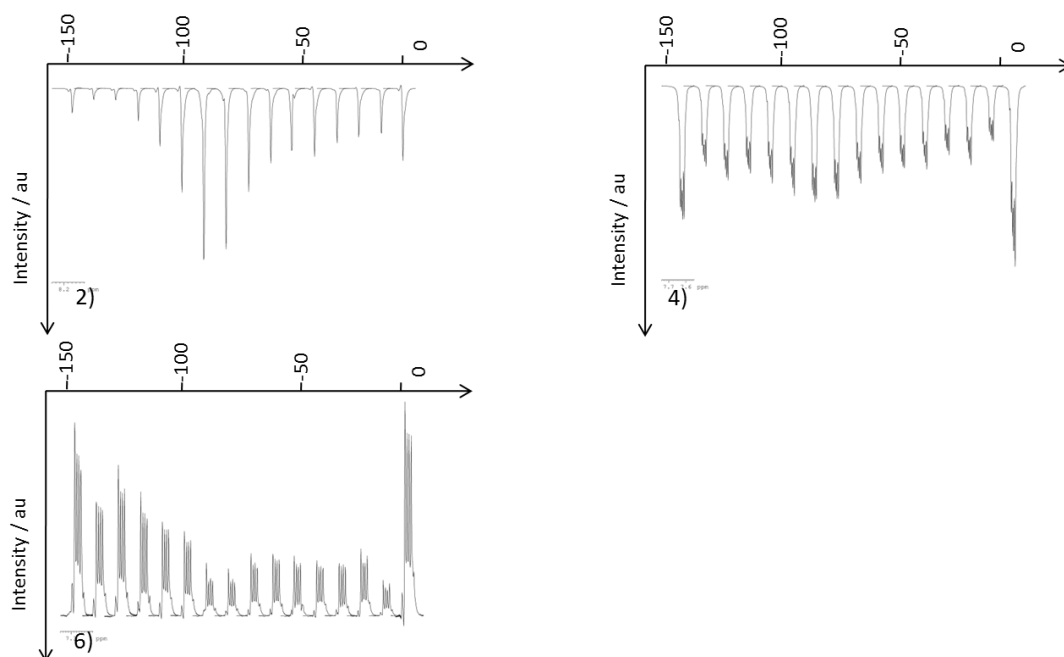


Figure 7.40 ^1H NMR field dependence spectra for hyperpolarised benzimidazole.

7.5.8. Imidazole

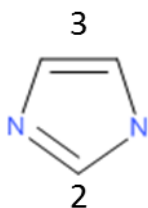


Figure 7.41 Labelled structure of imidazole.

^1H NMR (400 MHz, CD_3OD , 298K): δ 7.68 (s, 1H, **H2**), 7.05 (s, 2H, **H3**). $^{13}\text{C}\{^1\text{H}\}$ NMR (100 MHz, CD_3OD , 298K): δ 136.4 (**C2**), 122.9 (**C3**).

7.5.8.1. Hyperpolarised spectra

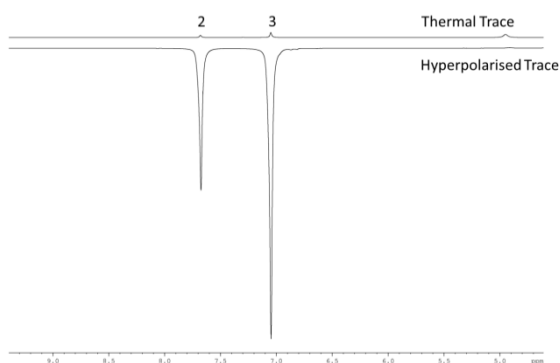


Figure 7.42 Hyperpolarised spectrum of imidazole.

7.5.9. Oxazole

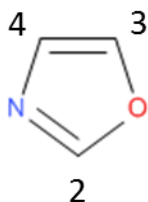


Figure 7.43 Labelled structure of Oxazole.

^1H NMR (400 MHz, CD_3OD , 253K): δ 8.37 (s, 1H, **H2**), 8.06 (t, $J=0.95$ Hz, 1H, **H4**), 7.29 (s, 1H, **H3**). $^{13}\text{C}\{^1\text{H}\}$ NMR (100 MHz, CD_3OD , 253K): δ 152.00 (**C2**), 139.86 (**C4**), 125.71 (**C3**).

7.5.9.1. Hyperpolarised spectra

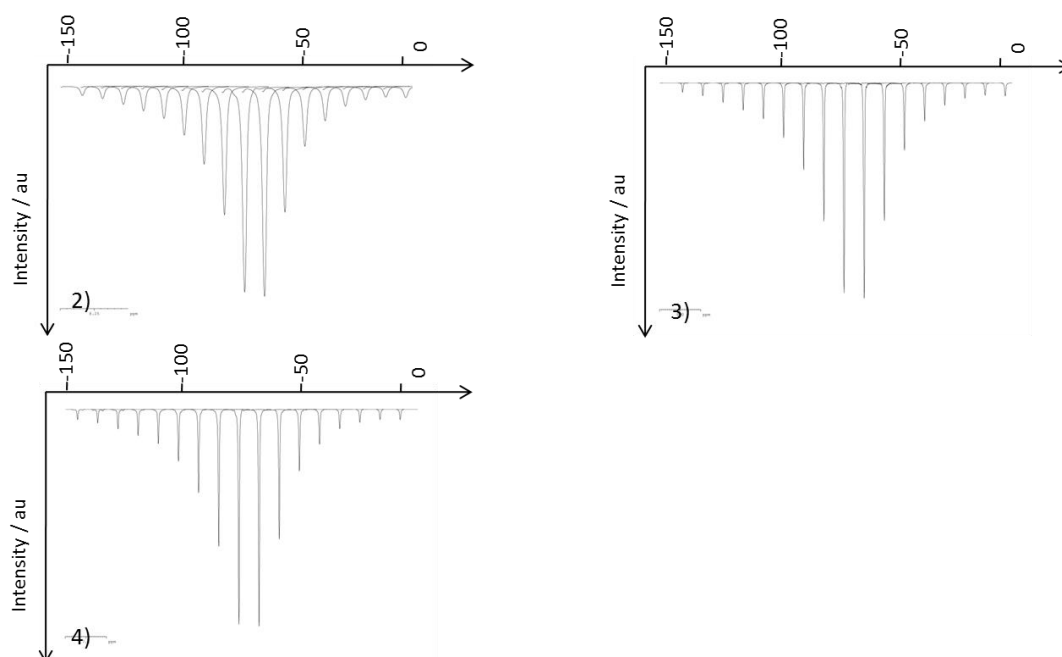


Figure 7.44 ^1H NMR field dependence spectra for hyperpolarised oxazole sample.

7.5.10. Isoxazole

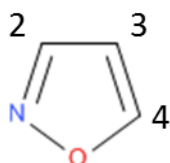


Figure 7.45 Labeled structure of isoxazole.

^1H NMR (400 MHz, CD_3OD , 263K): δ 8.78 (d, $J=1.77$ Hz, 1H, **H2**), 8.49 (d, $J=1.77$ Hz, 1H, **H4**), 6.55 (t, $J=1.77$ Hz, 1H, **H3**). $^{13}\text{C}\{^1\text{H}\}$ NMR (100 MHz, CD_3OD , 263K): δ 158.2 (**C2**), 148.9 (**C4**), 103.2 (**C3**).

7.5.10.1. Hyperpolarised spectra

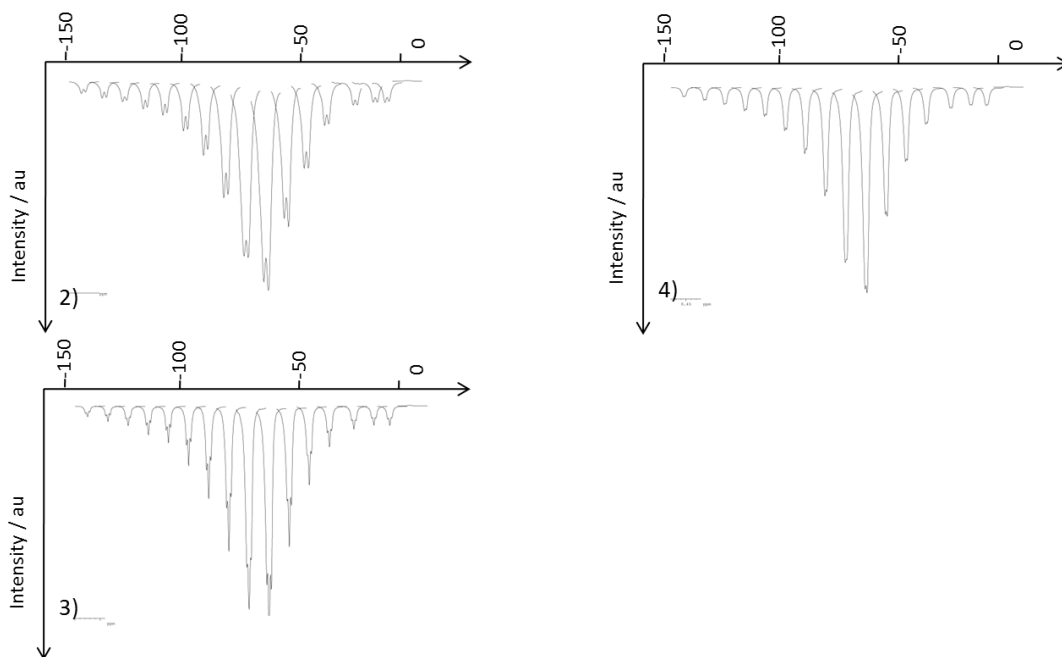


Figure 7.46 ^1H NMR field dependence spectra for hyperpolarised isoxazole sample.

7.5.11. Pyrazole

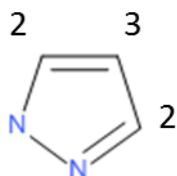


Figure 7.47 Labeled structure of pyrazole

^1H NMR (400 MHz, CD_3OD , 298K): δ 7.60 (s, 2H, **H2**), 6.33 (t, $J=2.4$ Hz, 1H, **H3**). $^{13}\text{C}\{^1\text{H}\}$ NMR (100 MHz, CD_3OD , 298K): δ 135.21 (**C2**), 105.20 (**C3**).

7.5.11.1. Hyperpolarised spectra

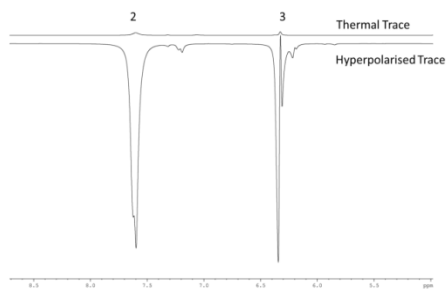


Figure 7.48 Hyperpolarised spectrum of pyrazole

7.5.12. Thiazole

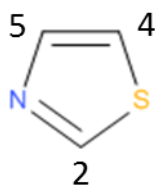


Figure 7.49 Labeled structure of Thiazole

$^1\text{H NMR}$ (400 MHz, CD_3OD , 298K): δ 9.05 (d, $J=1.73$ Hz, 1H, **H2**), 7.95 (d, $J=3.24$ Hz, 1H, **H5**), 7.68 (dd, $J=3.24$ Hz, 1.96, 1H, **H4**). $^{13}\text{C}\{^1\text{H}\}$ NMR (100 MHz, CD_3OD , 298K): δ 153.96 (**C2**), 142.57 (**C5**), 119.38 (**C4**)

7.5.13. 1,2,4-Triazole

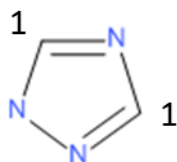


Figure 7.50 Labeled structure of 1,2,4-triazole

$^1\text{H NMR}$ (400 MHz, CD_3OD , 298K): δ 8.32 (s, 2H, **H1**). $^{13}\text{C}\{^1\text{H}\}$ NMR (100 MHz, CD_3OD , 298K): δ 147.30 (**C1**).

7.5.13.1. Hyperpolarised spectrum

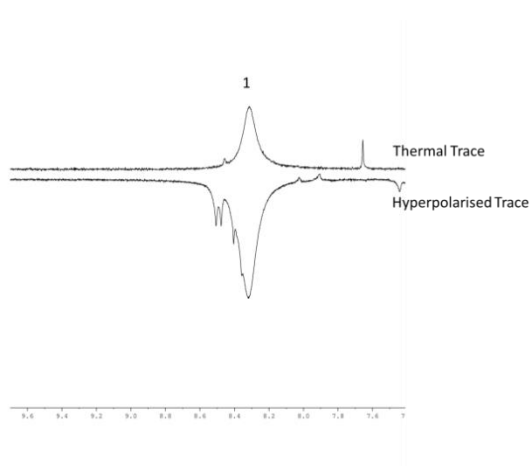


Figure 7.51 Hyperpolarised spectrum of 1,2,4-triazole.

7.5.14. Benzoxazole

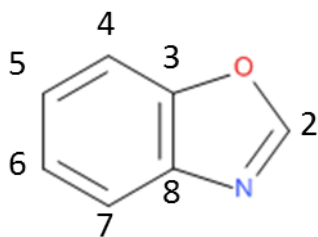


Figure 7.52 Labeled structure of benzoxazole.

$^1\text{H NMR}$ (400 MHz, CD_3OD , 298K): δ 8.10 (s, 1H, **H2**), 7.79 (1H, **H7**), 7.58 (dd, $J=7.12$ Hz, 1.75 Hz, 1H, **H4**), 7.41 (dd, $J=7.41$ Hz, 1.50 Hz, 1H, **H5**), 7.34 (dd, $J=7.41$ Hz, 1.50 Hz, 1H, **H6**).

$^{13}\text{C}\{^1\text{H}\}$ NMR (100 MHz, CD_3OD , 298K): δ 152.80 (**C2**), 150.10 (**C3**), 139.87 (**C8**), 125.60 (**C6**), 124.60 (**C5**), 120.49 (**C7**), 111.01 (**C4**).

7.5.14.1. Hyperpolarised spectra

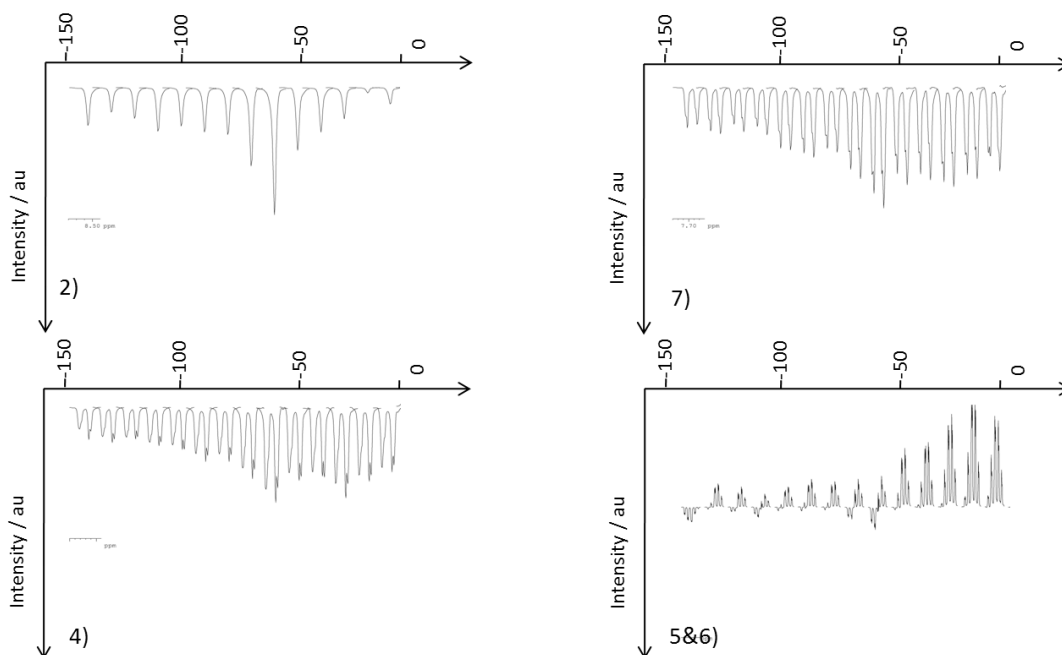


Figure 7.53 ^1H NMR field dependence spectra for hyperpolarised benzoxazole sample.

7.5.15. 2,1-Benzisoxazole

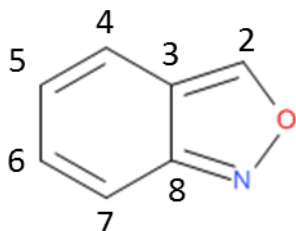


Figure 7.54 Labeled structure of 2,1-benzisoxazole

^1H NMR (400 MHz, CD_3OD , 298K): δ 9.46 (s, 1H, **H2**), 7.68 (d, $J=8.74$, 1H, **H6**), 7.57 (d, $J=9.16$ Hz, 1H, **H4**), 7.38 (dd, $J=9.0$ Hz, 6.6 Hz, 1H, **H5**), 7.06 (dd, $J=8.6$ Hz, 6.6 Hz, 1H, **H6**).

7.5.15.1. Hyperpolarised spectra

Did not show any of polarisation to the substrate.

7.5.16. 1,2-Benzisoxazole

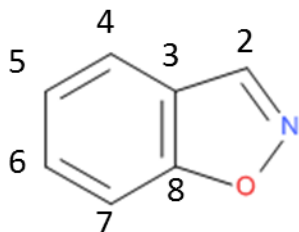


Figure 7.55 Labelled structure of 1,2-benzisoxazole.

$^1\text{H NMR}$ (400 MHz, CD_3OD , 298K): δ 7.50 (dd, $J=7.3$ Hz, 1H, **H2**), 7.45 (t, $J=7.3$ Hz, 1H, **H4**), 6.92 (dd, $J=8.1$ Hz, 5.9 Hz, 1H, **H7**), 4.95 (br, 2H, **H5&6**).

7.5.16.1. Hyperpolarised spectra

Did not show any enhancement to the substrate but it does show signals in the hydride region, which indicates the complex activates.

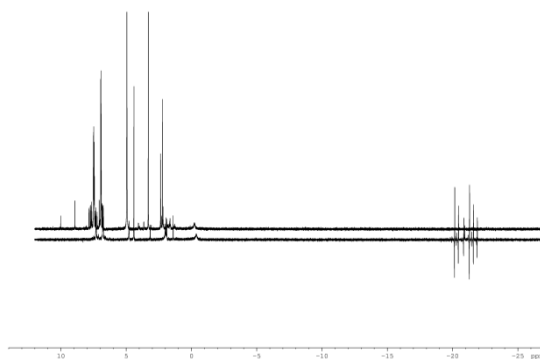


Figure 7.56 Hyperpolarised spectra of 1,2-benzisoxazole.

7.5.17. Quinazoline

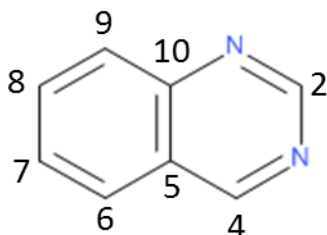


Figure 7.57 Labelled structure of quinazoline.

$^1\text{H NMR}$ (400 MHz, CD_2Cl_2 , 243K): δ 9.54 (s, 1H, **H4**), 9.24 (s, 1H, **H2**), 8.03 (dt, $J=8.5$ Hz, 1.0 Hz, 1H, **H9**), 8.01 (m, $J=6.0$ Hz, 1H, **H6**), 7.97 (m, $J=6$ Hz, 1H, **H7**), 7.79 (m, $J=2.2$ Hz, 1H, **H8**).
 $^{13}\text{C}\{^1\text{H}\}$ NMR (100 MHz, CD_2Cl_2 , 243K): δ 160.64 (**C4**), 155.34 (**C2**), 155.00 (**C10**), 150.10 (**C5**), 134.50 (**C7**), 128.40 (**C9** & **C8**), 127.6 (**C6**).

7.5.17.1. Hyperpolarised spectra

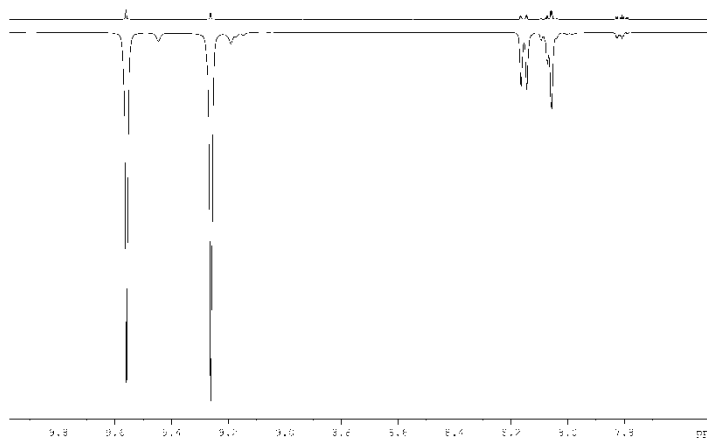


Figure 7.58 Hyperpolarised spectra of quinazoline

7.5.18. Pyrimidine

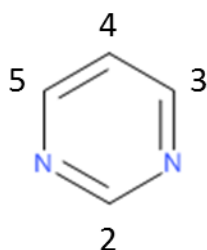


Figure 7.59 Labelled structure of pyrimidine.

^1H NMR (400 MHz, CD_3OD , 298K): δ 8.89 (s, 1H, **H2**), 8.52 (d, $J=5.32$ Hz, 2H, **H3&5**), 7.25 (td, $J=4.94$ Hz, 1.50 Hz, 1H, **H4**). $^{13}\text{C}\{^1\text{H}\}$ NMR (100 MHz, CD_3OD , 298K): δ 158.53 (**C2**), 156.59 (**C3**), 122.08 (**C4**).

7.5.18.1. Hyperpolarised spectra

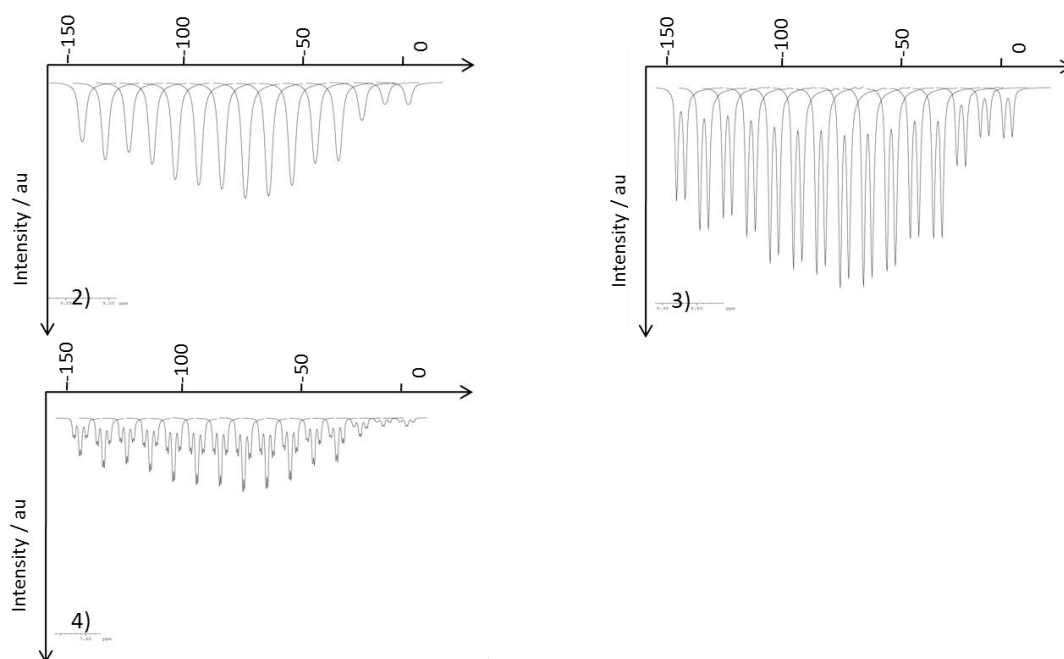


Figure 7.60 ^1H NMR field dependence spectra for hyperpolarised pyrimidine sample.

8. Appendices

8.1. Collection of NMR data for the calculation of exchange rates.

This section contains the entire rate data collected for the calculation of thermodynamic parameters.

8.1.1. Collection of NMR data for the calculation of exchange rates

A series of ^1H NOESY NMR spectra were collected, the hydride ligand is selectively excited after a short mixing time, a NMR spectrum recorded. The integral is taken, and the process is repeated for a different mixing time. The absolute integral is change into an a percentage of each other and then plotted as a function of mixing time as shown in

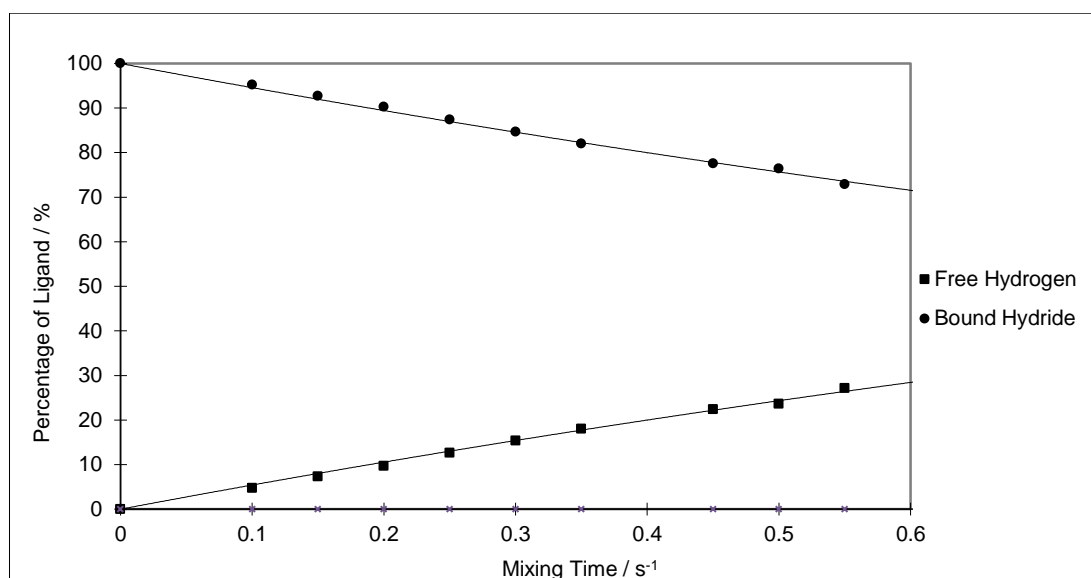


Figure 8.1 A plot of the percentage of bound hydride and free hydrogen derived from ^1H NOESY NMR spectra against the mixing time implemented. This data was collected at 300 K and monitored the loss of hydride ligands from 2-b to free hydrogen, when 5-methylpyrimidine is studied.

8.1.2. Calculation of thermodynamic activation parameters

The thermodynamic parameters of activation for each catalytic system were calculated through using the Eyring method. This involves plotting a graph of $(1/T)$ vs $\ln(2k/T)$ where T is temperature in Kelvin and k is the experimentally measured rate constants in s^{-1} . This

produces a straight line, the gradient and intercept of which can be used to derive the ΔH^\ddagger and ΔS^\ddagger according to Equation 8.1.

$$y = mx + c$$

$$\ln(k/T) = (-\Delta H^\ddagger/RT) + \ln(k_b/h) + (\Delta S^\ddagger/R)$$

Equation 8.1 Eyring equation

8.1.3. Collected rate constant and thermodynamic activation parameters of 2-a and with pyridine.

T / K	Observed rate constant / s ⁻¹	
	Loss of hydride	Loss of pyridine
267	-	0.153
271	-	0.271
276	0.181	0.590
280	0.264	0.590
285	0.505	1.88
290	0.91	0.153
295	1.49	3.90
300	2.87	8.11
305	5.00	14.14

Table 8.1 Rate constants for the loss of pyridine and hydride ligands from 2-a in the presence of pyridine at the indicated temperatures.

The data in Table 8.1 was used to produce the Eyring plots shown in Figure 8.2

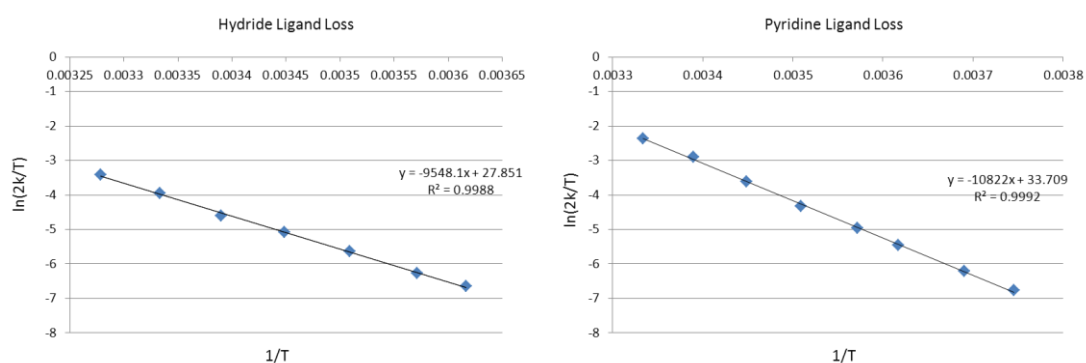


Figure 8.2 The Eyring plots for hydride ligands and pyridine ligands loss from 2-a in the presence of pyridine with associated equations, produced from the data presented in Table 8.1.

Figure 8.2 displays the equations which can then be used to calculate the thermodynamic parameters presented in Table 8.2

	Ligand Loss	
	Hydride	Pyridine
Rate Constant / s ⁻¹ (300 K)	5.0	14.4
ΔH^\ddagger / kJ mol ⁻¹	79.4 ± 3.2	89.9 ± 3.60
ΔS^\ddagger / JK ⁻¹ mol ⁻¹	34.0 ± 10.9	82.6 ± 12.9
ΔG_{300}^\ddagger / kJ mol ⁻¹	69.2 ± 0.003	65.2 ± 0.03

Table 8.2 Thermodynamic parameters of activation for the loss of hydride and pyridine ligands with catalyst 2-a, errors are quoted as 95% confidence limit.

A statistical approach of jack-knife was employed to determine average values and errors by resampling the data after removing one of the rate data points. For this data set the rate for a given temperature was removed then the values of ΔH^\ddagger , ΔS^\ddagger and ΔG_{300}^\ddagger recalculated. This was then repeated for each individual temperature and each sample. Errors are then given as 95 % confidence limit.

8.1.4. Collected rate constant and thermodynamic activation parameters of 2-b and with pyridine.

T / K	Observed rate constant / s ⁻¹	
	Loss of hydride	Loss of pyridine
290	0.15	1.37
295	0.3	3.15
298	0.41	5.69
300	0.56	7.29
305	1.09	23.6
310	2.13	42.0
332	-	987

Table 8.3 Rate constants for the loss of pyridine and hydride ligands from 2-b in the presence of pyridine at the indicated temperatures.

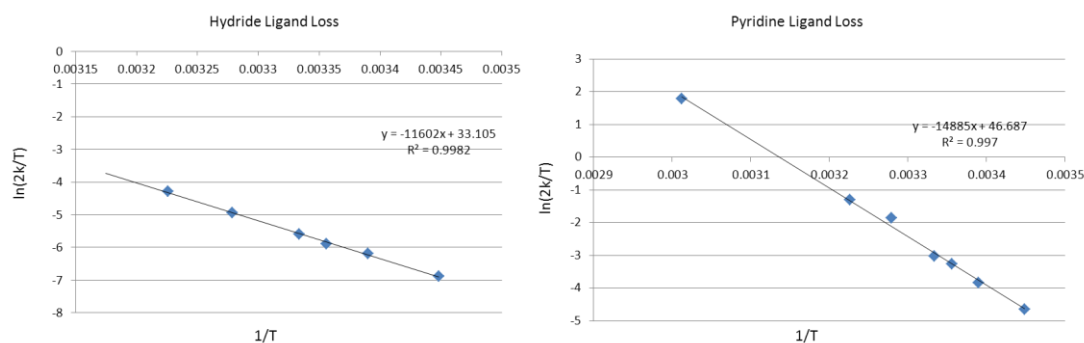


Figure 8.3 The Eyring plots for hydride ligands and pyridine ligands loss from 2-b in the presence of pyridine with associated equations, produced from the data presented in Table 8.3.

Figure 8.3 displays the equations which can then be used to calculate the thermodynamic parameters presented in Table 8.4

	Ligand Loss	
	Hydride	Pyridine
Rate Constant / s ⁻¹ (300 K)	0.56	7.29
ΔH^\ddagger / kJ mol ⁻¹	96.4 ± 1.01	130.5 ± 2.34
ΔS^\ddagger / JK ⁻¹ mol ⁻¹	77.5 ± 3.40	213.2 ± 7.9
ΔG_{300}^\ddagger / kJ mol ⁻¹	73.1 ± 0.01	66.5 ± 0.05

Table 8.4 Thermodynamic parameters of activation for the loss of hydride and pyridine ligands with catalyst 2-b, errors are quoted as 95% confidence limit.

8.1.5. Collected rate constant and thermodynamic activation parameters of 2-c and with 5-methylpyrimidine.

T / K	Observed rate constant / s ⁻¹	
	Loss of hydride	Loss of 5-methylpyrimidine
278	0.299	0.261
283	0.663	0.390
288	1.38	0.641
290	1.65	0.841
293	2.30	0.900
298	3.99	1.61
300	5.46	2.10

Table 8.5 Rate constants for the loss of pyridine and hydride ligands from 2-c in the presence of 5-methylpyrimidine at the indicated temperatures.

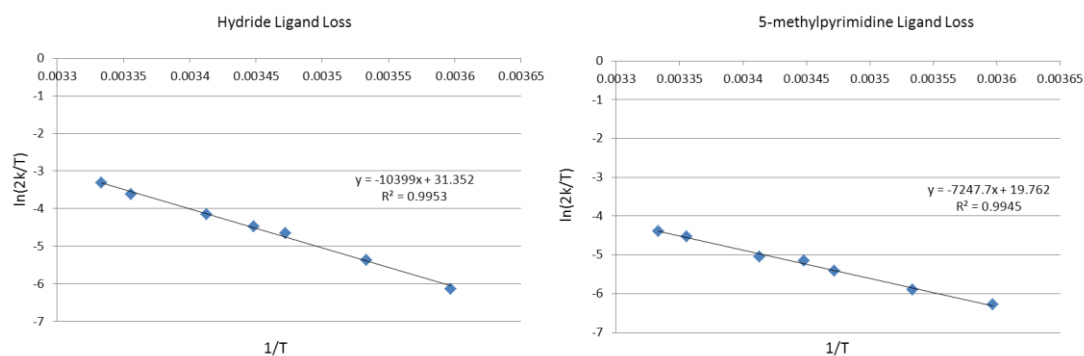


Figure 8.4 The Eyring plots for hydride ligands and pyridine ligands loss from 2-c in the presence of 5-methylpyrimidine with associated equations, produced from the data presented in Table 8.5.

Figure 8.4 displays the equations which can then be used to calculate the thermodynamic parameters presented in Table 8.6

	Ligand Loss	
	Hydride	5-methylpyrimidine
Rate Constant / s ⁻¹ (300 K)	0.56	7.29
ΔH^\ddagger / kJ mol ⁻¹	96.4 ± 1.01	130.5 ± 2.34
ΔS^\ddagger / JK ⁻¹ mol ⁻¹	77.5 ± 3.40	213.2 ± 7.9
ΔG_{300}^\ddagger / kJ mol ⁻¹	73.1 ± 0.01	66.5 ± 0.05

Table 8.6 Thermodynamic parameters of activation for the loss of hydride and 5-methylpyrimidine ligands with catalyst 2-c, errors are quoted as 95% confidence limit.

8.1.6. Collected rate constant and thermodynamic activation parameters of 2-c and with quinazoline in methanol-d₄.

T / K	Observed rate constant /	
	Loss of hydride	Loss of quinazoline
248	-	0.0805
253	-	0.1075
258	-	0.1329
263	-	0.1973
265	-	0.1946
268	-	0.2253
270	-	0.2528
273	-	0.2771
278	-	0.3525
276.5	0.18	-
280	-	0.3847
283	-	0.4296
280	0.264	-
285	0.505	-
290	0.91	-
295	1.49	-
300	2.87	-
305	5	-

Table 8.7 Rate constants for the loss of pyridine and hydride ligands from 2-c in the presence of quinazoline at the indicated temperatures in methanol-d₄.

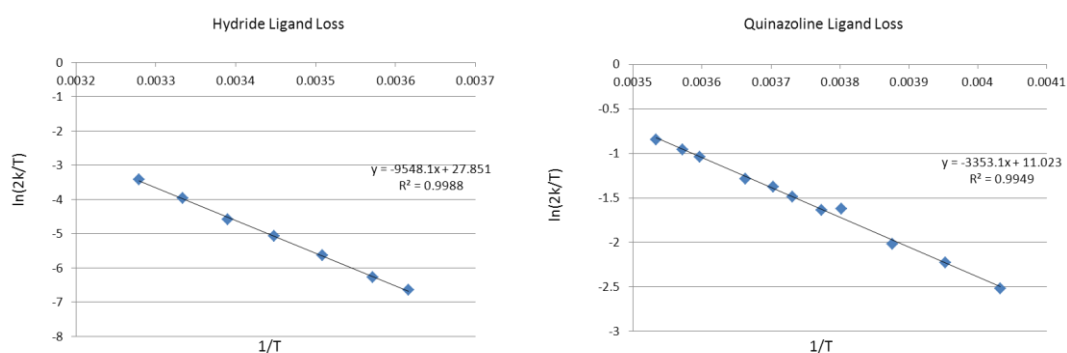


Figure 8.5 Eyring plots for hydride ligands and quinazoline ligands loss from 2-c in the presence of quinazoline with associated equations, produced from the data presented in Table 8.7.

Figure 8.5 displays the equations which can then be used to calculate the thermodynamic parameters presented in Table 8.8

	Ligand Loss / s ⁻¹	
	Hydride	Quinazoline
Rate Constant / s ⁻¹ (300 K)	2.87	0.32
ΔH^\ddagger / kJ mol ⁻¹	79.3 ± 1.04	27.8 ± 2.05
ΔS^\ddagger / JK ⁻¹ mol ⁻¹	34.2 ± 2.80	101 ± 4.02
ΔG_{300}^\ddagger / kJ mol ⁻¹	69.1 ± 0.5	59 ± 0.1

Table 8.8 Thermodynamic parameters of activation for the loss of hydride and quinazoline ligands with catalyst 2-c in methanol-d₄, errors are quoted as 95% confidence limit.

8.1.7. Collected rate constant and thermodynamic activation parameters of 2-c and with quinazoline in dichloromethane-d₂.

T / K	Observed rate constant /	
	Loss of hydride	Loss of 5-methylpyridine
263	0.708	-
267	-	0.153
268	1.28	-
271	-	0.271
273	2.48	-
278	5.35	-
276.5	-	0.59
280	-	0.973
283	7.96	-
285	-	1.88
290	-	3.9
295	-	8.11
300	-	10

Table 8.9 Rate constants for the loss of pyridine and hydride ligands from 2-c in the presence of quinazoline at the indicated temperatures in dichloromethane-d₂

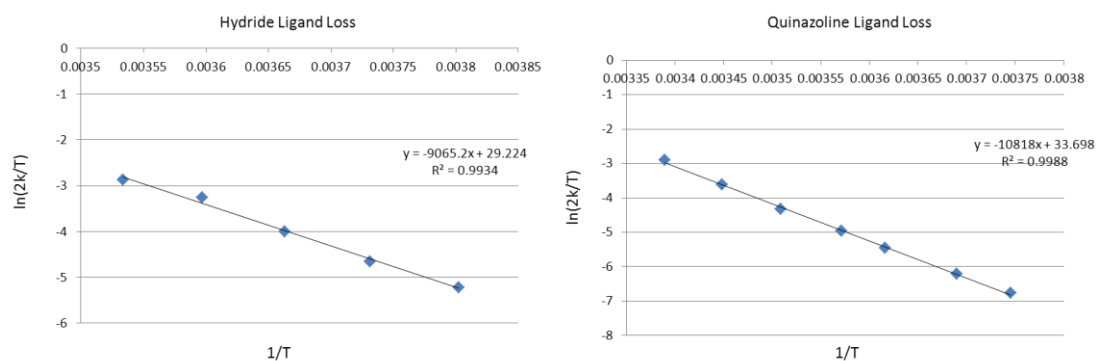


Figure 8.6 Eyring plots for hydride ligands and quinazoline ligands loss from 2-c in the presence of quinazoline with associated equations, produced from the data presented in Table 8.9.

Figure 8.6 displays the equations which can then be used to calculate the thermodynamic parameters presented in Table 8.10

	Ligand Loss / s ⁻¹	
	Hydride	Quinazoline
Rate Constant / s ⁻¹ (300 K)	49.5*	10.0
ΔH^\ddagger / kJ mol ⁻¹	80.0 ± 2	87.8 ± 1
ΔS^\ddagger / JK ⁻¹ mol ⁻¹	50.1 ± 7	75.3 ± 3
ΔG_{300}^\ddagger / kJ mol ⁻¹	61.2 ± 0.2	65.4 ± 0.5

Table 8.10 Thermodynamic parameters of activation for the loss of hydride and quinazoline ligands with catalyst 2-c in dichloromethane-d₂, errors are quoted as 95% confidence limit. *calculated value.

8.2. Calibration graphs for concentration studies.

To determine if the series dilution was accurate the thermal ^1H signal is proportional to the concentration of 5-methyl pyrimidine so a graph could be plotted of ^1H integral vs 5-methyl pyrimidine concentration and shown in Figure 8.7. These are for experiments when substrate : catalyst ratio remain 20 : 1 as indicated in Table 4.5

	Substrate to Catalyst Ratio	2-c		5-Methyl pyrimidine	
		[2-c] (mM)	Mass (mg)	[5-Methyl pyrimidine] (mM)	Mass (mg)
Sample 1	20:1	15	6	300	17.5
Sample 2	20:1	12.5	5	250	14.6
Sample 3	20:1	10	4	200	11.6
Sample 4	20:1	7.5	3	150	8.75
Sample 5	20:1	5	2	100	5.83
Sample 6	20:1	2.5	1	50	2.92
Sample 7	20:1	0.5	0.2	10	0.58
Sample 8	20:1	0.05	0.02	1	0.058

Table 8.11 The amounts of 2-c and substrate used in the corresponding concentration experiments with each made up with 0.6ml d4-methanol

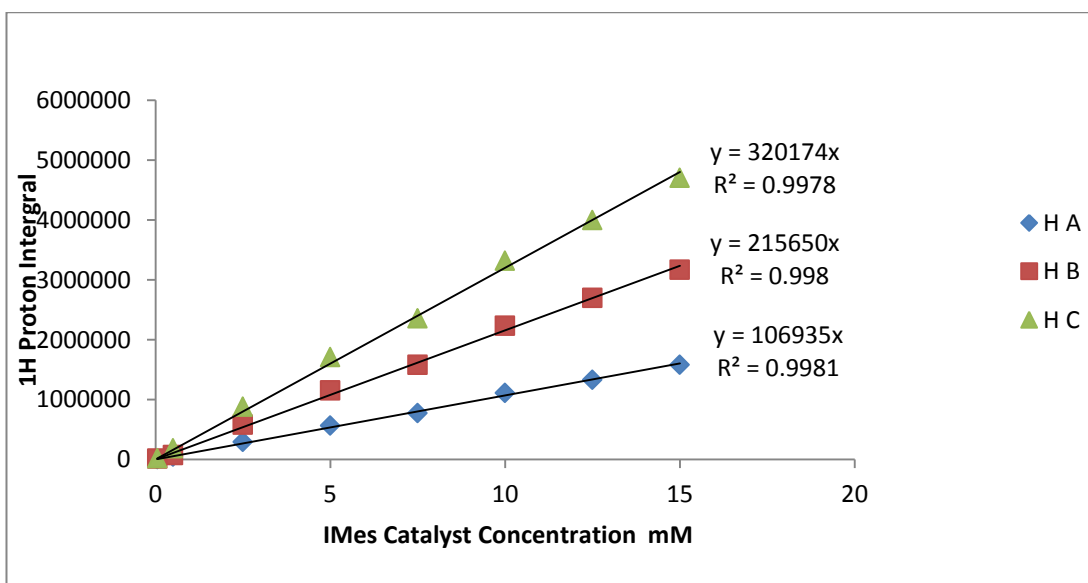


Figure 8.7 Graphical representation of the absolute integrals of the 5-methyl pyrimidine H A, H B and H C, obtained in a single scan ^1H NMR spectrum when 2-c catalyst concentration and substrate retain constant (mM),

To determine if the series dilution was accurate the thermal ^1H signal is proportional to the concentration of 5-methyl pyrimidine so a graph could be plotted of ^1H integral vs 5-methyl pyrimidine concentration and shown in Figure 8.7. These are for experiments when substrate : catalyst ratio remain change as indicated in Table 4.8.

	Substrate to Catalyst Ratio	IMes		5-Methyl pyrimidine	
		[IMes] (mM)	Mass (mg)	[5-Methyl pyrimidine] (mM)	Mass (mg)
Sample 1	60:1	5	2	300	17.5
Sample 2	50:1	5	2	250	14.6
Sample 3	40:1	5	2	200	11.6
Sample 4	30:1	5	2	150	8.75
Sample 5	20:1	5	2	100	5.83
Sample 6	10:1	5	2	50	2.92
Sample 7	2:1	5	2	10	0.58

Table 8.12 The amounts of 2-c and substrate used in the corresponding concentration experiments with each made up with 0.6ml d_4 -methanol.

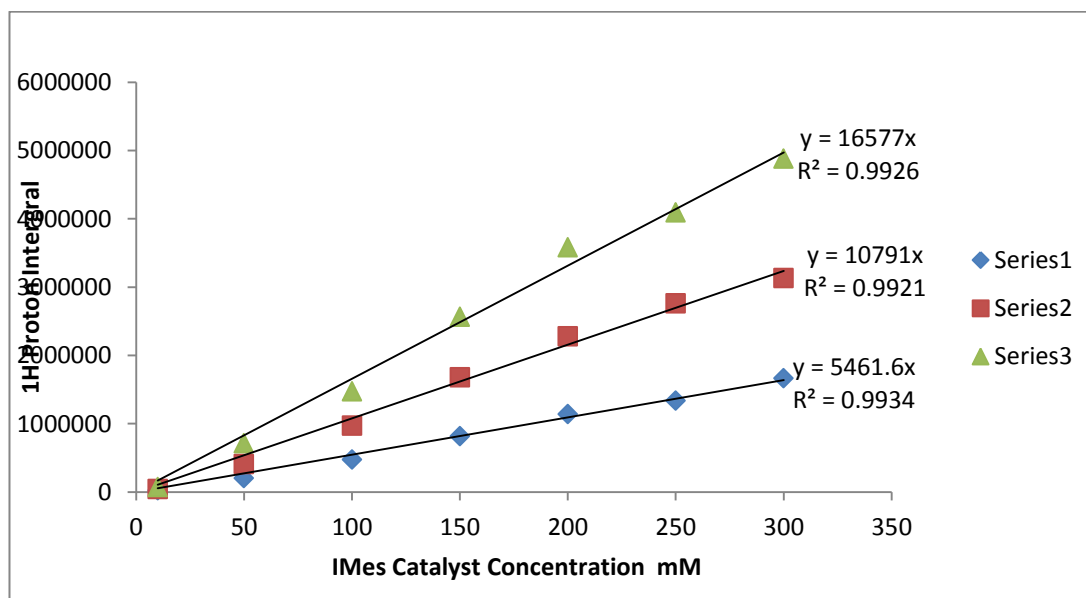


Figure 8.8 Graphical representation of the absolute integrals of the 5-methyl pyrimidine H A, H B and H C, obtained in a single scan ^1H NMR spectrum when IMes catalyst concentration and substrate (mM) contained different ratio amounts.

8.3. Adapted pulse sequences used within this thesis

During the development of SABRE for use of method 2, a series of new pulse sequences have been written to incorporate the commands and employed in NMR measurement. These are prefixed with 'ph_'.

8.3.1. Standard 90° pulse acquire sequence

This sequence completes a single 90° pulse followed by acquisition. It has been used for both ¹H and ¹³C acquisitions.

```

;ph_zg
;zg for use with parahydrogen polariser

#include <Avance.incl>
#include <Polariser.incl>

1 ze
2 1u
  subr POLARISE( d20, d21, d24 ) ;wait for sample and polarise; transfer when done
3 d1
  p0 ph1
  go=3 ph31
  30m wr #0
  TOPOL      ;transfer sample to polariser
  lo to 2 times l0
  POLPOS     ;wait for sample in polariser
exit

ph1=0 2 2 0 1 3 3 1
ph31=0 2 2 0 1 3 3 1

```

```

;d1 : relaxation delay; set to very short for hyperpolarisation experiments
;ns : number of scans: set to = 1 for hyperpolarisation experiments
;d20: bubble time for polarisation
;d21: stop bubbling, wait before transferring the sample
;d24: settling after transfer
;l0 : accumulate L0 scans; re-polarising between scans

```

8.3.2. ^1H OPSYdq NMR pulse sequence – ph_OPYdq

This sequence filters the double quantum magnetic states using gradients and transforms them into observable magnetisation. It can be altered to achieve zero quantum or single quantum filtration by changing the proportions of the gradients used.

```
;;start
```

```
;ph_OPYdq
```

```
;OPY with double quantum filter modified for use with the parahydrogen polariser
```

```
#include <Avance.incl>
```

```
#include <Grad.incl>
```

```
#include <Polariser.incl>
```

```
1 ze
```

```
2 d1
```

```
    subr POLARISE( d20, d21, d24 )
```

```
3 30m
```

```
  d1
```

```
  p1 ph1      ; pH MODIFIED
```

```
  50u UNBLKGRAD
```

```
  p16:gp1*-1
```

```
  d16
```

```
  20u BLKGRAD
```

```
  p1 ph2      ; pH MODIFIED
```

```
  50u UNBLKGRAD
```

```
  p16:gp1
```

```
  d16
```

```
  p16:gp1
```

```
  d16
```

```
  20u BLKGRAD
```

```
  go=3 ph31
```

```
  30m wr #0
```

```
  TOPOL ;transfer sample to polariser
```

```
  20u ze
```

```
  lo to 2 times l0
```

```
  ;POLPOS ;wait for sample in polariser
```

```
exit
```

```
ph1=1 1 1 1 0 0 0 0
```

```
ph2=0 0 0 0 1 1 1 1
```

```
ph31=0 0 0 0 1 1 1 1
```

```
;d1 : relaxation delay; set to very short for hyperpolarisation experiments
```

```
;d20: bubble time for polarisation
```

```
;d21: stop bubbling, wait before transferring the sample
```

```
;d24: settling after transfer
```

```
;l0 : accumulate L0 scans
;p11 : f1 channel - power level for pulse (default)
;p1 : f1 channel - 90 degree high power pulse
;p2 : f1 channel - 180 degree high power pulse
;p16: homospoil/gradient pulse
;d16: delay for homospoil/gradient recovery
;NS: 1 * n, total number of scans: NS * TD0
;use gradient ratio: gpz1= from 80 to 100 %
;p16= 1-3 ms
; increase gpz1 and/or p16 to improve the signal suppression.
;use gradient files:
;gpnam1: SINE.100

;Ralph Adams 12MAY2009

;;stop
```

8.3.3. 1D refocused $^{13}\text{C}\{^1\text{H}\}$ NMR pulse sequence ($^{13}\text{C}\{^1\text{H}\}_{\text{JR}}$) – ph_zg_refocus

This is the standard 1D ^{13}C NMR pulse sequence from Bruker adapted to include a delay between the pulse and acquisition, and for use with the polariser.

```

;ph_zg_refocus
;zg for use with parahydrogen polariser

#include <Avance.incl>
#include <Polariser.incl>

"d3=1/(2*cnst2)"

1 ze
2 1u
  subr POLARISE( d20, d21, d24 ) ;wait for sample and polarise; transfer when done
3 d1 pl12:f2
  p0 ph1
  d3 do:f2
  go=3 ph31 cpd2:f2
  30m wr #0 do:f2
  TOPOL      ;transfer sample to polariser
  lo to 2 times l0
  POLPOS      ;wait for sample in polariser
exit

ph1=0 2 2 0 1 3 3 1
ph31=0 2 2 0 1 3 3 1

;d1 : relaxation delay; set to very short for hyperpolarisation experiments
;ns : number of scans: set to = 1 for hyperpolarisation experiments
;d20: bubble time for polarisation
;d21: stop bubbling, wait before transferring the sample
;d24: settling after transfer
;l0 : accumulate L0 scans; re-polarising between scans
;cpd2: decoupling according to sequence defined by cpdprg2
;pcpd2: f2 channel - 90 degree pulse for decoupling sequence

```

8.3.4. 1D $^{13}\text{C}\{^1\text{H}\}$ NMR pulse sequence refocused for both J coupling and chemical shift evolution ($^{13}\text{C}\{^1\text{H}\}$ _JCSR) – ph_zg_refocused_J+CS

This is the standard 1D $^{13}\text{C}\{^1\text{H}\}$ NMR pulse sequence from Bruker adapted to include a refocusing section allowing both J coupling and chemical shift evolution, and for use with the polarisor.

```

;ph_zg_refocus
;zg for use with parahydrogen polariser

#include <Avance.incl>
#include <Polariser3.incl>

"d3=1/(2*cnst2)"

1 ze
2 1u
  subr POLARISE( d20, d21, d24 ) ;wait for sample and polarise; transfer when done
3 d1 pl12:f2
  p0 ph1
  d3 do:f2
  (center (p4 ph2):f2 (p2 ph3) )
  d3
  go=3 ph31 cpd2:f2
  30m wr #0 do:f2
  TOPOL      ;transfer sample to polariser
  lo to 2 times l0
  POLPOS      ;wait for sample in polariser
exit

ph1=0 2 2 0 1 3 3 1
ph2=0 2
ph3=0 2
ph31=0 2 2 0 1 3 3 1

;pl12 : f2 channel - power level for pulse (default)
;p0 : f1 channel - 90 degree high power pulse
;p2 : f1 channel - 180 degree high power pulse
;p3 : f2 channel - 180 degree high power pulse
;d1 : relaxation delay; set to very short for hyperpolarisation experiments
;ns : number of scans: set to = 1 for hyperpolarisation experiments
;d20: bubble time for polarisation
;d21: stop bubbling, wait before transferring the sample
;d24: settling after transfer
;l0 : accumulate L0 scans; re-polarising between scans
;cpd2: decoupling according to sequence defined by cpdprg2
;pcpd2: f2 channel - 90 degree pulse for decoupling sequence

```

8.3.5. 1D ¹³C INEPT NMR pulse sequence – ph_ineptnd

This is the standard 1D ¹³C INEPTnd NMR pulse sequence from Bruker adapted for use with the polarisor.

```

;ph_ineptnd_mkIII
;avance-version (02/05/31)
;INEPT for non-selective polarization transfer
;no decoupling during acquisition
;modified for use with the polariser mkII by REM and LSL
;$CLASS=HighRes
;$DIM=1D
;$TYPE=
;$SUBTYPE=
;$COMMENT=

#include <Avance.incl>
#include <Polariser3.incl>

"p2=p1*2"
"p4=p3*2"
"d4=1s/(cnst2*4)"

1 ze
2 30m
  subr POLARISE( d20, d21, d24 ) ;wait for sample and polarise; transfer when done
3 d1
  (p5 ph1):f2
  d4
  (center (p4 ph2):f2 (p2 ph4) )
  d4
  (p3 ph3):f2 (p1 ph5)
  go=3 ph31
  30m mc #0 to 2 F0(zd)
  TOPOL      ;transfer sample to polariser
  lo to 2 times l0
  POLPOS      ;wait for sample in polariser and set to manuel mode
exit

ph1=0 0 0 0 0 0 0 0 2 2 2 2 2 2 2 2
ph2=0 2
ph3=1 1 3 3
ph4=0 2
ph5=0 0 0 0 1 1 1 1 2 2 2 2 3 3 3 3
ph31=0 0 2 2 1 1 3 3

```

```
;p1 : f1 channel - power level for pulse (default)
;p2 : f2 channel - power level for pulse (default)
;p1 : f1 channel - 90 degree high power pulse
;p2 : f1 channel - 180 degree high power pulse
;p3 : f2 channel - 90 degree high power pulse
;p4 : f2 channel - 180 degree high power pulse
;p5 : f2 channel - 90 or 45 degree pulse as desired
;d1 : relaxation delay; 1-5 * T1
;d4 : 1/(4J(XH))
;d20: bubble time for polarisation
;d21: stop bubbling, wait before transferring the sample
;d24: settling after transfer
;l0 : accumulate L0 scans; re-polarising between scans
;cnst2: = J(XH)
;NS: 4 * n, total number of scans: NS * TD0
;DS: 16
```

```
;$Id: ineptnd,v 1.9 2005/11/10 12:17:00 ber Exp $
```


8.3.6. 1D $^{13}\text{C}\{^1\text{H}\}$ INEPT NMR pulse sequence – ph_ineptrd

This is the standard 1D $^{13}\text{C}\{^1\text{H}\}$ INEPTrd NMR pulse sequence from Bruker adapted for use with the polarisor.

```

;ph_ineptrd_mkIII
;avance-version (02/05/31)
;INEPT for non-selective polarization transfer
;with decoupling during acquisition
;Modified for use with the polariser mkII
;$CLASS=HighRes
;$DIM=1D
;$TYPE=
;$SUBTYPE=
;$COMMENT=

#include <Avance.incl>
#include <Polariser3.incl>

"p2=p1*2"
"p4=p3*2"
"d3=1s/(cnst2*cnst11)"
"d4=1s/(cnst2*4)"
"d12=20u"

1 ze
2 30m
  subr POLARISE( d20, d21, d24 ) ;wait for sample and polarise; transfer when done
3 30m do:f2
  d1
  d12 pl2:f2
  (p5 ph1):f2
  d4
  (center (p4 ph2):f2 (p2 ph4) )
  d4
  (p3 ph3):f2 (p1 ph5)
  d3
  (center (p4 ph2):f2 (p2 ph6) )
  d3 pl12:f2
  go=3 ph31 cpd2:f2
  30m do:f2 mc #0 to 2 F0(zd)
  TOPOL      ;transfer sample to polariser
  lo to 2 times l0
  POLPOS      ;wait for sample in polariser and set to manuel mode
exit

```

```

ph1=0 0 0 0 0 0 0 2 2 2 2 2 2 2
ph2=0 2
ph3=1 1 3 3
ph4=0 2
ph5=0 0 0 0 1 1 1 1 2 2 2 2 3 3 3 3
ph6=0 2 0 2 1 3 1 3
ph31=0 0 2 2 1 1 3 3

```

```

;p1 : f1 channel - power level for pulse (default)
;p2 : f2 channel - power level for pulse (default)
;p12: f2 channel - power level for CPD/BB decoupling
;p1 : f1 channel - 90 degree high power pulse
;p2 : f1 channel - 180 degree high power pulse
;p3 : f2 channel - 90 degree high power pulse
;p4 : f2 channel - 180 degree high power pulse
;p5 : f2 channel - 90 or 45 degree high power pulse
;d1 : relaxation delay; 1-5 * T1
;d3 : 1/(6J(XH)) XH, XH2, XH3 positive
;   1/(4J(XH)) XH only
;   1/(3J(XH)) XH, XH3 positive, XH2 negative
;d4 : 1/(4J(XH))
;d12: delay for power switching           [20 usec]
;d20: bubble time for polarisation
;d21: stop bubbling, wait before transferring the sample
;d24: settling after transfer
;l0 : accumulate L0 scans; re-polarising between scans
;cnst2: = J(XH)
;cnst11: 6 XH, XH2, XH3 positive
;      4 XH only
;      3 XH, XH3 positive, XH2 negative
;NS: 4 * n, total number of scans: NS * TD0
;DS: 16
;cpd2: decoupling according to sequence defined by cpdprg2
;pcpd2: f2 channel - 90 degree pulse for decoupling sequence

```

```
;$Id: ineptrd,v 1.9 2005/11/10 12:17:00 ber Exp $
```

8.3.7. 2D ^1H - ^1H OPSYdq-COSY NMR pulse sequence – ph_OPYdq_2D

In this sequence, the first 90° pulse of the COSY sequence is replaced by an OPSYdq sequence such that only double quantum states are filtered for use in the COSY section of the sequence.

```

;;start

;ph_OPYdq_2D
;OPSY with double quantum filter modified for use with the parahydrogen polariser
;Modified to work like a COSYgpqf but by selecting only two spin order terms

#include <Avance.incl>
#include <Grad.incl>
#include <Polariser.incl>

"d0=3u"

"d13=4u"
"in0=inf1"

1 ze
2 d1
    subr POLARISE( d20, d21, d24 )
3 30m
  d1
  p1 ph1      ; pH MODIFIED
  50u UNBLKGRAD
  p16:gp1*-1
  d16
  20u BLKGRAD
  p1 ph2      ; pH MODIFIED
  50u UNBLKGRAD
  p16:gp1
  d16
  p16:gp1
  d16
  20u BLKGRAD
  d0
  50u UNBLKGRAD
  p19:gp2
  d16
  p0 ph2
  d13
  p19:gp2
  d16
  4u BLKGRAD
  go=3 ph31
  TOPOL ;transfer sample to polariser
  d1 mc #0 to 2 F1QF(id0)

```

```
POLPOS ;wait for sample in poariser  
exit
```

```
ph1=0 2  
ph2=0 0 2 2  
ph3=0 2  
ph31=0 2
```

```
;d1 : relaxation delay; set to very short for hyperpolarisation experiments  
;d13: short delay [4 usec]  
;d20: bubble time for polarisation  
;d21: stop bubbling, wait before transferring the sample  
;d24: settling after transfer  
;l0 : accumulate L0 scans  
;p11 : f1 channel - power level for pulse (default)  
;p1 : f1 channel - 90 degree high power pulse  
;p2 : f1 channel - 180 degree high power pulse  
;p16: homospoil/gradient pulse  
;p19: gradient pulse for single quantum filter  
;d16: delay for homospoil/gradient recovery  
;NS: 1 * n, total number of scans: NS * TD0  
;in0:  $1/(1 * SW) = 2 * DW$   
;use gradient ratio: gpz1= 70% gpz2=10%  
;p16= 1-3 ms  
;p19= 600 us  
; increase gpz1 and/or p16 to improve the signal suppression.  
;use gradient files:  
;gpnam1: SINE.100  
;gpz1 70% refers to the gradient filter used to select double quantum coherences  
;gpz2 10% refers to the single quantum filter (used in the last 90)  
  
;Ralph Adams 12MAY2009  
  
;;stop
```

9. Abbreviations

$\%V_{\text{bur}}$: per cent buried volume
Å	: angstrom
ALTADENA Alignment	: Adiabatic Longitudinal Transport After Dissociation Engenders Nuclear Alignment
av.	: average
BBI	: Broadband inverse probe
cat	: catalyst
CDCl_3	: deuterated chloroform
CIDNP	: Chemically Induced Dynamic Nuclear Polarisation
COD	: 1,5-cyclooctadiene
COE	: cyclooctene
conc.	: concentration
COSY	: Correlation Spectroscopy
Cy	: cyclohexyl
D	: deuterium
DCM	: Dichloromethane
DFT	: Density Functional Theory
DMSO	: Dimethylsulphoxide
DNP	: Dynamic Nuclear Polarisation
dq	: double quantum

E	: enhancement
eq.	: equivalent(s)
ESI	: electrospray ionisation
Et	: ethyl
EXSY	: Exchange spectroscopy
FID	: Free Induction Decay
G	: Gauss
GI ₅₀	: A quantitative measure of how much of a compound is required to cause a 50 % reduction in proliferation of cancer cells
H	: Proton (and Henry's Law constant in Experimental)
HMBC	: Heteronuclear multiple-bond correlation spectroscopy
HMQC	: Heteronuclear multiple-quantum correlation spectroscopy
HSQC	: Heteronuclear single-quantum correlation spectroscopy
IC ₅₀	: A quantitative measure of how much of a compound is required to inhibit a given biological process by half
ICy	: Bis-1,3-cyclohexyl imidazole hydrochloride
IMe	: Bis-1,3-methyl imidazole hydrochloride
IMes	: Bis-1,3-(2,4,6-trimethylphenyl) imidazole hydrochloride
INEPT	: Insensitive Nuclei Enhanced by Polarisation Transfer
ⁱ Pr	: isopropyl
IR	: infrared
K	: Kelvin
L	: ligand
M	: metal

Me	: methyl
MeO	: methoxy ligand
MeOD	: deuterated methanol
MIC	: minimum inhibitory concentration
MKI/II/III	: referring to the first (Mark1), second (Mark 2) and third (mark 3) generation mixing chamber
MRI	: Magnetic Resonance Imaging
MS	: Mass spectroscopy
NCMe	: Acetonitrile
nd	: Not decoupled, in reference to the INEPT pulse sequence
NH-PHIP	: Non-hydrogenative parahydrogen induced polarisation
NHC	: N-heterocyclic carbene
NMR	: Nuclear Magnetic Resonance
NOESY	: nuclear Overhauser effect spectroscopy
obs.	: observed
OPSY	: Only <i>parahydrogen</i> spectroscopy
OPSYdq	: Only <i>parahydrogen</i> spectroscopy optimised for double quantum states
ORTEP	: Oak Ridge Thermal Ellipsoid Plot
PASADENA	: Parahydrogen And Synthesis Allow Dramatically Enhanced Nuclear Alignment
PCy ₃	: tricyclohexyl phosphine
Ph	: Phenyl
<i>p</i> H ₂	: parahydrogen
PHIP	: Parahydrogen induced polarisation

PPh ₃	: triphenyl phosphine
ppm	: parts per million
PTF	: polarisation transfer field
py	: pyridine
q	: quinoline
r	: repulsivity factor
R	: any group
rd	: refocused and decoupled, in reference to the INEPT pulse sequence
rel.	: relative
RF	: radio frequency
S/N	: signal to noise ratio
SABRE	: Signal Amplification By Reversible Exchange
SIMes	: bis-1,3-(2,4,6-trimethylphenyl) imidazoline hydrochloride
Sub	: substrate
T	: tesla
^t Bu	: tert-butyl
TEP	: Tolman's Electronic Parameter
THF	: tetrahydrofuran
TOCSY	: Total correlation spectroscopy
TXI	: Triple Resonance Inverse Probe
TXO	: Triple Resonances Obverse Probe
ufCOSY	: ultrafast COSY
UV	: ultraviolet

10. References

1. Singh, S.; Handa, T.; Narayanam, M.; Sahu, A.; Junwal, M.; Shah, R. P., A critical review on the use of modern sophisticated hyphenated tools in the characterization of impurities and degradation products. *J. Pharm. Biomed. Anal.* **2012**, *69*, 148-173.
2. Sanchez, S.; Ziarelli, F.; Viel, S.; Delaurent, C.; Caldarelli, S., Improved solid-state NMR quantifications of active principles in pharmaceutical formulations. *J. Pharm. Biomed. Anal.* **2008**, *47*, 683-687.
3. Geppi, M.; Mollica, G.; Borsacchi, S.; Veracini, C. A., Solid-State NMR Studies of Pharmaceutical Systems. *Applied Spectroscopy Reviews* **2008**, *43*, 202-302.
4. Brettmann, B. K.; Myerson, A. S.; Trout, B. L., Solid-state nuclear magnetic resonance study of the physical stability of electrospun drug and polymer solid solutions. *J. Pharm. Sci.* **2012**, *101*, 2185-2193.
5. Holzgrabe, U., Quantitative NMR spectroscopy in pharmaceutical applications. *Progress in Nuclear Magnetic Resonance Spectroscopy* **2010**, *57*, 229-240.
6. Malet-Martino, M.; Holzgrabe, U., NMR techniques in biomedical and pharmaceutical analysis. *J. Pharm. Biomed. Anal.* **2011**, *55*, 1-15.
7. Rabi, I. I.; Zacharias, J. R.; Millman, S.; Kusch, P., A New Method of Measuring Nuclear Magnetic Moment. *Physical Review* **1938**, *53*, 318-318.
8. Purcell, E. M.; Torrey, H. C.; Pound, R. V., Resonance Absorption by Nuclear Magnetic Moments in a Solid. *Physical Review* **1946**, *69*, 37-38.
9. Bloch F.; Hansen W. W.; M.E., P., Nuclear Induction, Proceedings of the American Physical Society. *Physical Review* **1946**, *69*, 674.
10. Powers, R., NMR metabolomics and drug discovery. *Magnetic Resonance in Chemistry* **2009**, *47*, S2-S11.
11. Claridge, T. D. W., *High-Resolution NMR Techniques in Organic Chemistry*. Elsevier2008; Vol. 19.
12. Arnold, J. T.; Dharmatti, S. S.; Packard, M. E., Chemical Effects on Nuclear Induction Signals from Organic Compounds. *The Journal of Chemical Physics* **1951**, *19*, 507-507.
13. Knight, W. D., Nuclear Magnetic Resonance Shift in Metals. *Physical Review* **1949**, *76*, 1259-1260.
14. Nelson, F. A.; Weaver, H. E., Nuclear Magnetic Resonance Spectroscopy in Superconducting Magnetic Fields. *Science* **1964**, *146*, 223-232.
15. Ferguson, R. C.; Phillips, W. D., High-Resolution Nuclear Magnetic Resonance Spectroscopy. *Science* **1967**, *157*, 257-267.
16. Voehler, M. W.; Collier, G.; Young, J. K.; Stone, M. P.; Germann, M. W., Performance of cryogenic probes as a function of ionic strength and sample tube geometry. *Journal of Magnetic Resonance* **2006**, *183*, 102-109.
17. Molinski, T. F., NMR of natural products at the 'nanomole-scale'. *Natural Product Reports* **2010**, *27*, 321-329.
18. Ernst, R. R. Nobel Lecture: Nuclear Magnetic Resonance Fourier Transform Spectroscopy. http://www.nobelprize.org/nobel_prizes/chemistry/laureates/1991/ernst-lecture.html (11 July 2013),
19. Wuthrich, K., Protein Structure Determination in Solution by NMR Spectroscopy. *The Journal of Biological Chemistry* **1990**, *265*, 22059-22062.
20. Ishima, R.; Torchia, D. A., Protein dynamics from NMR. *Nature Structural Biology* **2000**, *7*, 740-743.

21. Krishnan, P.; Kruger, N. J.; Ratcliffe, R. G., Metabolite fingerprinting and profiling in plants using NMR. *J. Exp. Bot.* **2005**, *56*, 255-265.
22. Griesinger, C.; Sørensen, O. W.; Ernst, R. R., A practical approach to three-dimensional NMR spectroscopy. *Journal of Magnetic Resonance (1969)* **1987**, *73*, 574-579.
23. Ernst, R. R.; Anderson, W. A., Application of fourier transform spectroscopy to magnetic resonance. *Review of Scientific Instruments* **1966**, *37*, 93-102.
24. Aue, W. P.; Bartholdi, E.; Ernst, R. R., Two-dimensional spectroscopy. Application to nuclear magnetic resonance. *The Journal of Chemical Physics* **1976**, *64*, 2229-2246.
25. Levitt, M. H., *Spin Dynamics: Basics of Nuclear Magnetic Resonance*. 2nd ed.; Wiley: Chichester, , 2007.
26. Lauterbur P.C., Image formation by induced local interactions - Examples employing nuclear magnetic resonance. *Nature* **1973**, *242*, 190-191.
27. Garroway, A. N.; Grannell, P. K.; Mansfield, P., Image formation in NMR by a selective irradiative process. *Journal of Physics C: Solid State Physics* **1974**, *7*, 457-462.
28. Damadian, R., Tumor detection by nuclear magnetic resonance. *Science* **1971**, *171*, 1151-1153.
29. Mansfield, P.; Maudsley, A. A., Planar spin imaging by NMR. *Journal of Magnetic Resonance (1969)* **1977**, *27*, 101-119.
30. Weisman, I. D.; Woods, M. W.; Burk, D.; Bennett, L. H.; Maxwell, L. R., Recognition of cancer in-vivo by nuclear magnetic resonance. *Science* **1972**, *178*, 1288-1290.
31. Morris, P., *Nuclear magnetic resonance imaging in medicine and biology*. Clarendon Press 1986.
32. Ogawa, S.; Lee, T. M.; Kay, A. R.; Tank, D. W., Brain magnetic-resonance-imaging with contrast dependent on blood oxygenation. *Proceedings of the National Academy of Sciences of the United States of America* **1990**, *87*, 9868-9872.
33. Roe, D. C.; Kating, P. M.; Krusic, P. J.; Smart, B. E., High resolution NMR techniques in catalysis. *Topics in Catalysis* **1998**, *5*, 133-147.
34. Brown, M. A.; Semelka, R. C., *MRI: basic principles and applications*. Wiley-Blackwell 2010.
35. Hoa, D.; Micheau, A. E-MRI online course. <http://www.imaio.com/en> ([15th February 2011]),
36. Hill, H. D. W., Improved sensitivity of NMR spectroscopy probes by use of high-temperature superconductive detection coils. *IEEE Transactions on Applied Superconductivity* **1997**, *7*, 3750-3755.
37. Kemsley, J., Sensitizing NMR. *Chem. Eng. News* **2008**, *86*, 12-15.
38. Viale, A.; Aime, S., Current concepts on hyperpolarized molecules in MRI. *Curr. Opin. Chem. Biol.* **2010**, *14*, 90-96.
39. Duckett, S. B.; Sleight, C. J., Applications of the parahydrogen phenomenon: A chemical perspective. *Progress in Nuclear Magnetic Resonance Spectroscopy* **1999**, *34*, 71-92.
40. Abragam, A.; Proctor, W. G., Spin Temperature. *Physical Review* **1958**, *109*, 1441-1458.
41. Gadian, D. G.; Panesar, K. S.; Perez Linde, A. J.; Horsewill, A. J.; Kockenberger, W.; Owers-Bradley, J. R., Preparation of highly polarized nuclear spin systems using brute-force and low-field thermal mixing. *Physical Chemistry Chemical Physics* **2012**, *14*, 5397-5402.
42. Krjukov, E. V.; O'Neill, J. D.; Owers-Bradley, J. R., Brute force polarization of Xe-129. *J. Low Temp. Phys.* **2005**, *140*, 397-408.
43. Kuhns, P. L.; Hammel, P. C.; Gonen, O.; Waugh, J. S., Unexpectedly rapid ¹⁹F spin-lattice relaxation in CaF₂ below 1 K. *Phys. Rev. B* **1987**, *35*, 4591-4593.

44. Owers-Bradley, J. R.; Horsewill, A. J.; Peat, D. T.; Goha, K. S. K.; Gadian, D. G., High polarization of nuclear spins mediated by nanoparticles at millikelvin temperatures. *Physical Chemistry Chemical Physics* **2013**, *15*, 10413-10417.
45. Albert, M. S.; Balamore, D., Development of hyperpolarized noble gas MRI. *Nuclear Instruments and Methods in Physics Research Section A: Accelerators, Spectrometers, Detectors and Associated Equipment* **1998**, *402*, 441-453.
46. Bifone, A.; Song, Y.-Q.; Seydoux, R.; Taylor, R. E.; Goodson, B. M.; Pietrass, T.; Budinger, T. F.; Navon, G.; Pines, A., NMR of laser-polarized xenon in human blood. *Proceedings of the National Academy of Sciences* **1996**, *93*, 12932-12936.
47. Swanson, S. D.; Rosen, M. S.; Agranoff, B. W.; Coulter, K. P.; Welsh, R. C.; Chupp, T. E., Brain MRI with laser-polarized Xe-129. *Magnetic Resonance in Medicine* **1997**, *38*, 695-698.
48. Navon, G.; Song, Y. Q.; Rööm, T.; Appelt, S.; Taylor, R. E.; Pines, A., Enhancement of Solution NMR and MRI with Laser-Polarized Xenon. *Science* **1996**, *271*, 1848-1851.
49. Costella, S.; Kirby, M.; Maksym, G. N.; McCormack, D. G.; Paterson, N. A. M.; Parraga, G., Regional pulmonary response to a methacholine challenge using hyperpolarized He-3 magnetic resonance imaging. *Respirology* **2012**, *17*, 1237-1246.
50. Albert, M. S.; Balamore, D., Development of hyperpolarized noble gas MRI. *Nuclear Instruments & Methods in Physics Research Section a-Accelerators Spectrometers Detectors and Associated Equipment* **1998**, *402*, 441-453.
51. Albert, M. S.; Cates, G. D.; Driehuys, B.; Happer, W.; Saam, B.; Springer, C. S.; Wishnia, A., Biological Magnetic-Resonance-Imaging using Laser Polarized Xe-129. *Nature* **1994**, *370*, 199-201.
52. Shukla, Y.; Wheatley, A.; Kirby, M.; Svenningsen, S.; Farag, A.; Santyr, G. E.; Paterson, N. A. M.; McCormack, D. G.; Parraga, G., Hyperpolarized ^{129}Xe Magnetic Resonance Imaging: Tolerability in Healthy Volunteers and Subjects with Pulmonary Disease. *Academic Radiology* **2012**, *19*, 941-951.
53. Lilburn, D. M. L.; Pavlovskaya, G. E.; Meersmann, T., Perspectives of hyperpolarized noble gas MRI beyond ^3He . *Journal of Magnetic Resonance* **2013**, *229*, 173-186.
54. Martin, C. C.; Williams, R. F.; Gao, J.-H.; Nickerson, L. D. H.; Xiong, J.; Fox, P. T., The pharmacokinetics of hyperpolarized xenon: Implications for cerebral MRI. *Journal of Magnetic Resonance Imaging* **1997**, *7*, 848-854.
55. Qing, K.; Ruppert, K.; Jiang, Y.; Mata, J. F.; Miller, G. W.; Shim, Y. M.; Wang, C.; Ruset, I. C.; Hersman, F. W.; Altes, T. A.; Mugler, J. P., Regional mapping of gas uptake by blood and tissue in the human lung using hyperpolarized xenon-129 MRI. *Journal of Magnetic Resonance Imaging* **2013**, 1-14.
56. Bartik, K.; Luhmer, M.; Dutasta, J.-P.; Collet, A.; Reisse, J., ^{129}Xe and ^1H NMR Study of the Reversible Trapping of Xenon by Cryptophane-A in Organic Solution. *Journal of the American Chemical Society* **1998**, *120*, 784-791.
57. Spence, M. M.; Rubin, S. M.; Dimitrov, I. E.; Ruiz, E. J.; Wemmer, D. E.; Pines, A.; Yao, S. Q.; Tian, F.; Schultz, P. G., Functionalized xenon as a biosensor. *Proceedings of the National Academy of Sciences* **2001**, *98*, 10654-10657.
58. Bajaj, V. S.; Hornstein, M. K.; Kreischer, K. E.; Sirigiri, J. R.; Woskov, P. P.; Mak-Jurkauskas, M. L.; Herzfeld, J.; Temkin, R. J.; Griffin, R. G., 250 GHz CW gyrotron oscillator for dynamic nuclear polarization in biological solid state NMR. *Journal of Magnetic Resonance* **2007**, *189*, 251-279.
59. Mak-Jurkauskas, M. L.; Bajaj, V. S.; Hornstein, M. K.; Belenky, M.; Griffin, R. G.; Herzfeld, J., Energy transformations early in the bacteriorhodopsin photocycle revealed by DNP-enhanced solid-state NMR. *Proceedings of the National Academy of Sciences of the United States of America* **2008**, *105*, 883-888.

60. Takahashi, H.; Viverge, B.; Lee, D.; Rannou, P.; De Paëpe, G., Towards Structure Determination of Self-Assembled Peptides Using Dynamic Nuclear Polarization Enhanced Solid-State NMR Spectroscopy. *Angewandte Chemie International Edition* **2013**, *52*, 6979-6982.
61. Gelis, I.; Vitzthum, V.; Dhimole, N.; Caporini, M. A.; Schedlbauer, A.; Carnevale, D.; Connell, S. R.; Fucini, P.; Bodenhausen, G., Solid-state NMR enhanced by dynamic nuclear polarization as a novel tool for ribosome structural biology. *Journal of biomolecular NMR* **2013**, *56*, 85-93.
62. Takahashi, H.; Ayala, I.; Bardet, M.; De Paëpe, G.; Simorre, J.-P.; Hediger, S., Solid-State NMR on Bacterial Cells: Selective Cell Wall Signal Enhancement and Resolution Improvement using Dynamic Nuclear Polarization. *Journal of the American Chemical Society* **2013**, *135*, 5105-5110.
63. Harel, E.; Schroder, L.; Xu, S. J., Novel Detection Schemes of Nuclear Magnetic Resonance and Magnetic Resonance Imaging: Applications from Analytical Chemistry to Molecular Sensors. *Annu. Rev. Anal. Chem.* **2008**, *1*, 133-163.
64. Ardenkjær-Larsen, J. H.; Laustsen, C.; Pullinger, B.; Kadlecsek, S.; Emami, K.; Rizi, R. In *Hyperpolarized water for interventional angiography*, Proc. Intl. Soc. Mag. Reson. Med2011; p 3534.
65. Park, I.; Bok, R.; Ozawa, T.; Phillips, J. J.; James, C. D.; Vigneron, D. B.; Ronen, S. M.; Nelson, S. J., Detection of early response to temozolomide treatment in brain tumors using hyperpolarized ¹³C MR metabolic imaging. *Journal of Magnetic Resonance Imaging* **2011**, *33*, 1284-1290.
66. Maly, T.; Debelouchina, G. T.; Bajaj, V. S.; Hu, K. N.; Joo, C. G.; Mak-Jurkauskas, M. L.; Sirigiri, J. R.; van der Wel, P. C. A.; Herzfeld, J.; Temkin, R. J.; Griffin, R. G., Dynamic nuclear polarization at high magnetic fields. *Journal of Chemical Physics* **2008**, *128*.
67. Bhattacharya, P.; Ross, B. D.; Bunger, R., Cardiovascular Applications of Hyperpolarized Contrast Media and Metabolic Tracers. *Experimental Biology and Medicine* **2009**, *234*, 1395-1416.
68. Dodd, M. S.; Ball, V.; Bray, R.; Ashrafian, H.; Watkins, H.; Clarke, K.; Tyler, D. J., In vivo mouse cardiac hyperpolarized magnetic resonance spectroscopy. *J. Cardiovasc. Magn. Reson.* **2013**, *15*.
69. Nelson, S. J.; Kurhanewicz, J.; Vigneron, D. B.; Larson, P. E. Z.; Harzstark, A. L.; Ferrone, M.; van Criekinge, M.; Chang, J. W.; Bok, R.; Park, I.; Reed, G.; Carvajal, L.; Small, E. J.; Munster, P.; Weinberg, V. K.; Ardenkjaer-Larsen, J. H.; Chen, A. P.; Hurd, R. E.; Odegardstuen, L.-I.; Robb, F. J.; Tropp, J.; Murray, J. A., Metabolic Imaging of Patients with Prostate Cancer Using Hyperpolarized [1-¹³C]Pyruvate. *Science Translational Medicine* **2013**, *5*, 198ra108.
70. McCarney, E. R.; Armstrong, B. D.; Lingwood, M. D.; Han, S., Hyperpolarized water as an authentic magnetic resonance imaging contrast agent. *Proceedings of the National Academy of Sciences of the United States of America* **2007**, *104*, 1754-1759.
71. Lingwood, M. D.; Siaw, T. A.; Sailasuta, N.; Abulseoud, O. A.; Chan, H. R.; Ross, B. D.; Bhattacharya, P.; Han, S., Hyperpolarized water as an MR imaging contrast agent: feasibility of in vivo imaging in a rat model. *Radiology* **2012**, *265*, 418-425.
72. Kurhanewicz, J.; Vigneron, D. B.; Brindle, K.; Chekmenev, E. Y.; Comment, A.; Cunningham, C. H.; DeBerardinis, R. J.; Green, G. G.; Leach, M. O.; Rajan, S. S., Analysis of cancer metabolism by imaging hyperpolarized nuclei: prospects for translation to clinical research. *Neoplasia (New York, NY)* **2011**, *13*, 81-97.
73. McRobbie, D. W., *MRI from picture to proton*. Cambridge University Press: Cambridge, 2003.

74. Kohler, S. J.; Yen, Y.; Wolber, J.; Chen, A. P.; Albers, M. J.; Bok, R.; Zhang, V.; Tropp, J.; Nelson, S.; Vigneron, D. B.; Kurhanewicz, J.; Hurd, R. E., In vivo ^{13}C metabolic imaging at 3T with hyperpolarized ^{13}C -1-pyruvate. *Magnetic Resonance in Medicine* **2007**, *58*, 65-69.
75. Polzin, J. A., Hyperpolarization shows promise for realizing the early health model. In *A GE Healthcare MR Publication* 2008.
76. Duckett, S. B.; Mewis, R. E., Improving NMR and MRI Sensitivity with Parahydrogen. In *Hyperpolarization Methods in Nmr Spectroscopy*, Kuhn, L. T., Ed. 2013; Vol. 338, pp 75-103.
77. Rioux, F., The Covalent Bond in H_2 . *The Chemical Educator* **2001**, *6*, 288-290.
78. Blazina, D.; Duckett, S. B.; Halstead, T. K.; Kozak, C. M.; Taylor, R. J. K.; Anwar, M. S.; Jones, J. A.; Carteret, H. A., Generation and interrogation of a pure nuclear spin state by parahydrogen-enhanced NMR spectroscopy: a defined initial state for quantum computation. *Magnetic Resonance in Chemistry* **2005**, *43*, 200-208.
79. Atkinson, K. D.; Cowley, M. J.; Elliott, P. I. P.; Duckett, S. B.; Green, G. G. R.; Lopez-Serrano, J.; Whitwood, A. C., Spontaneous Transfer of Parahydrogen Derived Spin Order to Pyridine at Low Magnetic Field. *Journal of the American Chemical Society* **2009**, *131*, 13362-13368.
80. Bowers, C. R.; Weitekamp, D. P., TRANSFORMATION OF SYMMETRIZATION ORDER TO NUCLEAR-SPIN MAGNETIZATION BY CHEMICAL-REACTION AND NUCLEAR-MAGNETIC-RESONANCE. *Physical Review Letters* **1986**, *57*, 2645-2648.
81. Bowers, C. R.; Weitekamp, D. P., PARA-HYDROGEN AND SYNTHESIS ALLOW DRAMATICALLY ENHANCED NUCLEAR ALIGNMENT. *Journal of the American Chemical Society* **1987**, *109*, 5541-5542.
82. Pravica, M. G.; Weitekamp, D. P., NET NMR ALIGNMENT BY ADIABATIC TRANSPORT OF PARA-HYDROGEN ADDITION-PRODUCTS TO HIGH MAGNETIC-FIELD. *Chemical Physics Letters* **1988**, *145*, 255-258.
83. Eguillor, B.; Caldwell, P. J.; Cockett, M. C. R.; Duckett, S. B.; John, R. O.; Lynam, J. M.; Sleigh, C. J.; Wilson, I., Detection of Unusual Reaction Intermediates during the Conversion of $\text{W}(\text{N}_2)_2(\text{dppe})_2$ to $\text{W}(\text{H})_4(\text{dppe})_2$ and of H_2O into H_2 . *Journal of the American Chemical Society* **2012**, *134*, 18257-18265.
84. Eisenberg, R., PARAHYDROGEN-INDUCED POLARIZATION - A NEW SPIN ON REACTIONS WITH H_2 . *Accounts of Chemical Research* **1991**, *24*, 110-116.
85. Eisenschmid, T. C.; McDonald, J.; Eisenberg, R.; Lawler, R. G., INEPT in a Chemical Way - Polarization Transfer from Para-hydrogen to P-31 by Oxidative Addition and Dipolar Relaxation. *Journal of the American Chemical Society* **1989**, *111*, 7267-7269.
86. Anwar, M. S.; Blazina, D.; Carteret, H. A.; Duckett, S. B.; Halstead, T. K.; Jones, J. A.; Kozak, C. M.; Taylor, R. J. K., Preparing high purity initial states for nuclear magnetic resonance quantum computing. *Physical Review Letters* **2004**, *93*.
87. Golman, K.; Axelsson, O.; Johannesson, H.; Mansson, S.; Olofsson, C.; Petersson, J. S., Parahydrogen-induced polarization in imaging: Subsecond C-13 angiography. *Magnetic Resonance in Medicine* **2001**, *46*, 1-5.
88. Goldman, M.; Johannesson, H.; Axelsson, O.; Karlsson, M., Hyperpolarization of C-13 through order transfer from parahydrogen: A new contrast agent for MFI. *Magn. Reson. Imaging* **2005**, *23*, 153-157.
89. Goldman, M.; Johannesson, H.; Axelsson, O.; Karlsson, M., Design and implementation of C-13 hyperpolarization from para-hydrogen, for new MRI contrast agents. *C. R. Chim.* **2006**, *9*, 357-363.
90. Zacharias, N. M.; Chan, H. R.; Sailasuta, N.; Ross, B. D.; Bhattacharya, P., Real-Time Molecular Imaging of Tricarboxylic Acid Cycle Metabolism in Vivo by Hyperpolarized 1-C-13 Diethyl Succinate. *Journal of the American Chemical Society* **2012**, *134*, 934-943.

91. Atkinson, K. D.; Cowley, M. J.; Duckett, S. B.; Elliott, P. I. P.; Green, G. G. R.; Lopez-Serrano, J.; Khazal, I. G.; Whitwood, A. C., Para-Hydrogen Induced Polarization without Incorporation of Para-Hydrogen into the Analyte. *Inorganic Chemistry* **2009**, *48*, 663-670.
92. Adams, R. W.; Aguilar, J. A.; Atkinson, K. D.; Cowley, M. J.; Elliott, P. I. P.; Duckett, S. B.; Green, G. G. R.; Khazal, I. G.; Lopez-Serrano, J.; Williamson, D. C., Reversible Interactions with para-Hydrogen Enhance NMR Sensitivity by Polarization Transfer. *Science* **2009**, *323*, 1708-1711.
93. Cowley, M. J.; Adams, R. W.; Atkinson, K. D.; Cockett, M. C. R.; Duckett, S. B.; Green, G. G. R.; Lohman, J. A. B.; Kerssebaum, R.; Kilgour, D.; Mewis, R. E., Iridium N-Heterocyclic Carbene Complexes as Efficient Catalysts for Magnetization Transfer from para-Hydrogen. *Journal of the American Chemical Society* **2011**, *133*, 6134-6137.
94. Adams, R. W.; Duckett, S. B.; Green, R. A.; Williamson, D. C.; Green, G. G. R., A theoretical basis for spontaneous polarization transfer in non-hydrogenative parahydrogen-induced polarization. *Journal of Chemical Physics* **2009**, *131*.
95. Aguilar, J. A.; Elliott, P. I. P.; Lopez-Serrano, J.; Adams, R. W.; Duckett, S. B., Only para-hydrogen spectroscopy (OPSY), a technique for the selective observation of para-hydrogen enhanced NMR signals. *Chemical Communications* **2007**, 1183-1185.
96. Gong, Q.; Gordji-Nejad, A.; Blümich, B.; Appelt, S., Trace Analysis by Low-Field NMR: Breaking the Sensitivity Limit. *Analytical Chemistry* **2010**, *82*, 7078-7082.
97. Glöggl, S.; Müller, R.; Colell, J.; Emondts, M.; Dabrowski, M.; Blümich, B.; Appelt, S., Para-hydrogen induced polarization of amino acids, peptides and deuterium-hydrogen gas. *Physical Chemistry Chemical Physics* **2011**, *13*, 13759-13764.
98. Dücker, E. B.; Kuhn, L. T.; Münnemann, K.; Griesinger, C., Similarity of SABRE field dependence in chemically different substrates. *Journal of Magnetic Resonance* **2012**, *214*, 159-165.
99. Kuhl, O., The chemistry of functionalised N-heterocyclic carbenes. *Chemical Society Reviews* **2007**, *36*, 592-607.
100. van Weerdenburg, B. J. A.; Gloeggler, S.; Eshuis, N.; Engwerda, A. H. J.; Smits, J. M. M.; de Gelder, R.; Appelt, S.; Wymenga, S. S.; Tessari, M.; Feiters, M. C.; Blumich, B.; Rutjes, F. P. J. T., Ligand effects of NHC-iridium catalysts for signal amplification by reversible exchange (SABRE). *Chemical Communications* **2013**, *49*, 7388-7390.
101. Fischer, E. O.; Maasböl, A., On the Existence of a Tungsten Carbonyl Carbene Complex. *Angewandte Chemie International Edition in English* **1964**, *3*, 580-581.
102. Schrock, R. R., First isolable transition metal methylene complex and analogs. Characterization, mode of decomposition, and some simple reactions. *Journal of the American Chemical Society* **1975**, *97*, 6577-6578.
103. Despagnet-Ayoub, E.; Grubbs, R. H., A ruthenium olefin metathesis catalyst with a four-membered N-heterocyclic carbene ligand. *Organometallics* **2005**, *24*, 338-340.
104. Prasang, C.; Donnadieu, B.; Bertrand, G., Stable planar six-pi-electron six-membered N-heterocyclic carbenes with tunable electronic properties. *Journal of the American Chemical Society* **2005**, *127*, 10182-10183.
105. Bazinet, P.; Yap, G. P. A.; Richeson, D. S., Constructing a stable carbene with a novel topology and electronic framework. *Journal of the American Chemical Society* **2003**, *125*, 13314-13315.
106. Alder, R. W.; Blake, M. E.; Bortolotti, C.; Bufali, S.; Butts, C. P.; Linehan, E.; Oliva, J. M.; Orpen, A. G.; Quayle, M. J., Complexation of stable carbenes with alkali metals. *Chemical Communications* **1999**, 241-242.
107. Scarborough, C. C.; Grady, M. J. W.; Guzei, I. A.; Gandhi, B. A.; Bunel, E. E.; Stahl, S. S., Pd-II complexes possessing a seven-membered N-heterocyclic carbene ligand. *Angewandte Chemie-International Edition* **2005**, *44*, 5269-5272.

108. Jazzar, R.; Liang, H.; Donnadieu, B.; Bertrand, G., A new synthetic method for the preparation of protonated-NHCs and related compounds. *Journal of Organometallic Chemistry* **2006**, *691*, 3201-3205.
109. Wanzlick, H. W., Aspects of Nucleophilic Carbene Chemistry. *Angewandte Chemie International Edition in English* **1962**, *1*, 75-80.
110. Lemal, D. M.; Lovald, R. A.; Kawano, K. I., Tetraaminoethylenes. The Question of Dissociation. *Journal of the American Chemical Society* **1964**, *86*, 2518-2519.
111. Winberg, H. E.; Carnahan, J. E.; Coffman, D. D.; Brown, M., Tetraaminoethylenes. *Journal of the American Chemical Society* **1965**, *87*, 2055-2056.
112. Denk, M. K.; Hatano, K.; Ma, M., Nucleophilic carbenes and the wanzlick equilibrium: A reinvestigation. *Tetrahedron Letters* **1999**, *40*, 2057-2060.
113. Hahn, F. E.; Wittenbecher, L.; Le Van, D.; Fröhlich, R., Evidence for an Equilibrium between an N-heterocyclic Carbene and Its Dimer in Solution. *Angewandte Chemie International Edition* **2000**, *39*, 541-544.
114. Liu, Y.; Lindner, P. E.; Lemal, D. M., Thermodynamics of a Diaminocarbene–Tetraaminoethylene Equilibrium. *Journal of the American Chemical Society* **1999**, *121*, 10626-10627.
115. Sch önherr, H.-J.; Wanzlick, H.-W., Chemie nucleophiler Carbene, XX HX-Abspaltung aus 1.3-Diphenyl-imidazoliumsalzen. Quecksilbersalz-Carben-Komplexe. *Chemische Berichte* **1970**, *103*, 1037-1046.
116. Arduengo, A. J.; Harlow, R. L.; Kline, M., A stable crystalline carbene. *Journal of the American Chemical Society* **1991**, *113*, 361-363.
117. Arduengo Iii, A. J.; Krafczyk, R.; Schmutzler, R.; Craig, H. A.; Goerlich, J. R.; Marshall, W. J.; Unverzagt, M., Imidazolylidenes, imidazolinyliidenes and imidazolidines. *Tetrahedron* **1999**, *55*, 14523-14534.
118. Herrmann, W. A., N-Heterocyclic Carbenes: A New Concept in Organometallic Catalysis. *Angewandte Chemie International Edition* **2002**, *41*, 1290-1309.
119. M.R. G., Advances in Imidazole Chemistry. In *Advances in Heterocyclic Chemistry*, Katritzky, A. R.; Boulton, A. J., Eds. Academic Press 1970; Vol. Volume 12, pp 103-183.
120. Wallach, J., *Ber. Dtsch. Chem. Ges* **1925**, *15*, 645.
121. Gridnev, A. A.; Mihaltseva, I. M., Synthesis of 1-Alkylimidazoles. *Synthetic Communications* **1994**, *24*, 1547-1555.
122. Kuhn, N.; Kratz, T., Synthesis of Imidazol-2-ylidenes by Reduction of Imidazole-2(3H)-thiones. *Synthesis* **1993**, *1993*, 561-562.
123. Kuhn, N.; Kratz, T., SYNTHESIS OF IMIDAZOL-2-YLIDENES BY REDUCTION OF IMIDAZOLE-2(3H)-THIONES. *Synthesis-Stuttgart* **1993**, 561-562.
124. Enders, D.; Breuer, K.; Raabe, G.; Runsink, J.; Teles, J. H.; Melder, J.-P.; Ebel, K.; Brode, S., Preparation, Structure, and Reactivity of 1,3,4-Triphenyl-4,5-dihydro-1H-1,2,4-triazol-5-ylidene, a New Stable Carbene. *Angewandte Chemie International Edition in English* **1995**, *34*, 1021-1023.
125. Arduengo, A. J.; Dias, H. V. R.; Calabrese, J. C.; Davidson, F., Homoleptic carbene-silver(I) and carbene-copper(I) complexes. *Organometallics* **1993**, *12*, 3405-3409.
126. Wang, H. M. J.; Lin, I. J. B., Facile Synthesis of Silver(I)–Carbene Complexes. Useful Carbene Transfer Agents. *Organometallics* **1998**, *17*, 972-975.
127. Guerret, O.; Solé, S.; Gornitzka, H.; Teichert, M.; Trinquier, G.; Bertrand, G., 1,2,4-Triazole-3,5-diyliidene: A Building Block for Organometallic Polymer Synthesis. *Journal of the American Chemical Society* **1997**, *119*, 6668-6669.
128. Tulloch, A. A. D.; Danopoulos, A. A.; Winston, S.; Kleinhenz, S.; Eastham, G., N-Functionalised heterocyclic carbene complexes of silver. *Journal of the Chemical Society, Dalton Transactions* **2000**, 4499-4506.

129. Garrison, J. C.; Youngs, W. J., Ag(I) N-Heterocyclic Carbene Complexes: Synthesis, Structure, and Application. *Chemical Reviews* **2005**, *105*, 3978-4008.
130. Wanzlick, H. W.; Schönherr, H. J., Direct Synthesis of a Mercury Salt-Carbene Complex. *Angewandte Chemie International Edition in English* **1968**, *7*, 141-142.
131. Öfele, K., 1,3-Dimethyl-4-imidazolinylden-(2)-pentacarbonylchrom ein neuer Übergangsmetall-carben-komplex. *Journal of Organometallic Chemistry* **1968**, *12*, P42-P43.
132. Arduengo, A. J. I. G., F.P. Jr.; Taverkere, P.K.; Simmons, H.E., (E.I. Du Pont de Nemours & Co., USA). US Patent 6,177,575, 2001.
133. Occhipinti, G.; Jensen, V. R.; Törnroos, K. W.; Frøystein, N. Å.; Bjørsvik, H.-R., Synthesis of a new bidentate NHC–Ag(I) complex and its unanticipated reaction with the Hoveyda–Grubbs first generation catalyst. *Tetrahedron* **2009**, *65*, 7186-7194.
134. Chianese, A. R.; Li, X. W.; Janzen, M. C.; Faller, J. W.; Crabtree, R. H., Rhodium and iridium complexes of N-heterocyclic carbenes via transmetalation: Structure and dynamics. *Organometallics* **2003**, *22*, 1663-1667.
135. Maishal, T. K.; Basset, J.-M.; Boualleg, M.; Coperet, C.; Veyre, L.; Thieuleux, C., AgOC(CF₃)(3): an alternative and efficient reagent for preparing transition metal-NHC-carbene complexes. *Dalton Transactions* **2009**, 6956-6959.
136. Reisinger, A.; Himmel, D.; Krossing, I., AgOC(CF₃)(3) and AgOSiPr(3) - Synthesis and characterization of a donor-free silver(I) alkoxide and silyl oxide. *Angewandte Chemie-International Edition* **2006**, *45*, 6997-7000.
137. Maishal, T. K.; Boualleg, M.; Bouhrara, M.; Coperet, C.; Jeanneau, E.; Veyre, L.; Thieuleux, C., Domination of Local Environment Over Pore Confinement Effects on the Catalytic Performances of Single-Site Cp*Ir(III)-NHC Heterogeneous vs. Homogeneous H/D Exchange Catalysts. *European Journal of Inorganic Chemistry* **2010**, 5005-5010.
138. Conley, M. P.; Copéret, C.; Thieuleux, C., Mesostructured Hybrid Organic–Silica Materials: Ideal Supports for Well-Defined Heterogeneous Organometallic Catalysts. *ACS Catalysis* **2014**, *4*, 1458-1469.
139. Chianese, A. R.; Li, X.; Janzen, M. C.; Faller, J. W.; Crabtree, R. H., Rhodium and Iridium Complexes of N-Heterocyclic Carbenes via Transmetalation: Structure and Dynamics. *Organometallics* **2003**, *22*, 1663-1667.
140. Kelly III, R. A.; Clavier, H.; Giudice, S.; Scott, N. M.; Stevens, E. D.; Bordner, J.; Samardjiev, I.; Hoff, C. D.; Cavallo, L.; Nolan, S. P., Determination of N-Heterocyclic Carbene (NHC) Steric and Electronic Parameters using the [(NHC)Ir(CO)₂Cl] System. *Organometallics* **2007**, *27*, 202-210.
141. Tolman, C. A., Steric effects of phosphorus ligands in organometallic chemistry and homogeneous catalysis. *Chemical Reviews* **1977**, *77*, 313-348.
142. Clavier, H.; Nolan, S. P., Percent buried volume for phosphine and N-heterocyclic carbene ligands: steric properties in organometallic chemistry. *Chemical Communications* **2010**, *46*, 841-861.
143. Huang, J.; Schanz, H.-J.; Stevens, E. D.; Nolan, S. P., Stereoelectronic Effects Characterizing Nucleophilic Carbene Ligands Bound to the Cp*RuCl (Cp* = η⁵-C₅Me₅) Moiety: A Structural and Thermochemical Investigation. *Organometallics* **1999**, *18*, 2370-2375.
144. Hillier, A. C.; Sommer, W. J.; Yong, B. S.; Petersen, J. L.; Cavallo, L.; Nolan, S. P., A Combined Experimental and Theoretical Study Examining the Binding of N-Heterocyclic Carbenes (NHC) to the Cp*RuCl (Cp* = η⁵-C₅Me₅) Moiety: Insight into Stereoelectronic Differences between Unsaturated and Saturated NHC Ligands. *Organometallics* **2003**, *22*, 4322-4326.
145. Gusev, D. G., Electronic and Steric Parameters of 76 N-Heterocyclic Carbenes in Ni(CO)(3)(NHC). *Organometallics* **2009**, *28*, 6458-6461.

146. Droge, T.; Glorius, F., The Measure of All Rings-N-Heterocyclic Carbenes. *Angewandte Chemie-International Edition* **2010**, *49*, 6940-6952.
147. Jokic, N. B.; Straubinger, C. S.; Goh, S. L. M.; Herdtweck, E.; Herrmann, W. A.; Kuhn, F. E., Symmetrical bis-(NHC) palladium(II) complexes: Synthesis, structure, and application in catalysis. *Inorganica Chimica Acta* **2010**, *363*, 4181-4188.
148. Dobereiner, G. E.; Nova, A.; Schley, N. D.; Hazari, N.; Miller, S. J.; Eisenstein, O.; Crabtree, R. H., Iridium-Catalyzed Hydrogenation of N-Heterocyclic Compounds under Mild Conditions by an Outer-Sphere Pathway. *Journal of the American Chemical Society* **2011**, *133*, 7547-7562.
149. Cowley, M. J.; Adams, R. W.; Atkinson, K. D.; Cockett, M. C. R.; Duckett, S. B.; Green, G. G. R.; Lohman, J. A. B.; Kerssebaum, R.; Kilgour, D.; Mewis, R. E., Iridium N-Heterocyclic Carbene Complexes as Efficient Catalysts for Magnetization Transfer from para-Hydrogen. *Journal of the American Chemical Society* **2011**, *133*, 6134-6137.
150. Green, R. A.; Adams, R. W.; Duckett, S. B.; Mewis, R. E.; Williamson, D. C.; Green, G. G. R., The theory and practice of hyperpolarization in magnetic resonance using parahydrogen. *Progress in Nuclear Magnetic Resonance Spectroscopy* **2012**, *67*, 1-48.
151. Duckett, S. B.; Mewis, R. E., Application of Parahydrogen Induced Polarization Techniques in NMR Spectroscopy and Imaging. *Accounts of Chemical Research* **2012**, *45*, 1247-1257.
152. Lloyd, L. S.; Hooper, A. J. J.; Asghar, A.; Burns, M. J.; Charlton, A.; Coombes, S.; Cowley, M. J.; Dear, G. J.; Duckett, S. B.; Genov, G. R.; Green, G. G. R.; Highton, L. A. R.; Khan, M.; Khazal, I. G.; Lewis, R. J.; Mewis, R. E.; Roberts, A. D.; Ruddlesden, A. J., Hyperpolarisation through reversible interactions with parahydrogen. *Catalysis Science & Technology* **2014**, *4*, 3544-3554.
153. Adams, R. W.; Duckett, S. B.; Green, R. A.; Williamson, D. C.; Green, G. G. R., A theoretical basis for spontaneous polarization transfer in non-hydrogenative parahydrogen-induced polarization. *Journal of Chemical Physics* **2009**, *131*, -.
154. Horsman, M. R.; Siemann, D. W.; Chaplin, D. J.; Overgaard, J., Nicotinamide as a radiosensitizer in tumours and normal tissues: the importance of drug dose and timing. *Radiotherapy and Oncology* **1997**, *45*, 167-174.
155. Green, K. N.; Steffan, J. S.; Martinez-Coria, H.; Sun, X.; Schreiber, S. S.; Thompson, L. M.; LaFerla, F. M., Nicotinamide Restores Cognition in Alzheimer's Disease Transgenic Mice via a Mechanism Involving Sirtuin Inhibition and Selective Reduction of Thr231-Phosphotau. *Journal of Neuroscience* **2008**, *28*, 11500-11510.
156. Mewis, R. E.; Atkinson, K. D.; Cowley, M. J.; Duckett, S. B.; Green, G. G. R.; Green, R. A.; Highton, L. A. R.; Kilgour, D.; Lloyd, L. S.; Lohman, J. A. B.; Williamson, D. C., Probing signal amplification by reversible exchange using an NMR flow system. *Magnetic Resonance in Chemistry* **2014**, *52*, 358-369.
157. Bhattacharya, P.; Chekmenev, E. Y.; Reynolds, W. F.; Wagner, S.; Zacharias, N.; Chan, H. R.; Bünger, R.; Ross, B. D., Parahydrogen-induced polarization (PHIP) hyperpolarized MR receptor imaging in vivo: a pilot study of ¹³C imaging of atheroma in mice. *NMR in Biomedicine* **2011**, *24*, 1023-1028.
158. Theis, T.; Truong, M. L.; Coffey, A. M.; Shchepin, R. V.; Waddell, K. W.; Shi, F.; Goodson, B. M.; Warren, W. S.; Chekmenev, E. Y., Microtesla SABRE Enables 10% Nitrogen-15 Nuclear Spin Polarization. *Journal of the American Chemical Society* **2015**, *137*, 1404-1407.
159. Barskiy, D. A.; Kovtunov, K. V.; Koptuyug, I. V.; He, P.; Groome, K. A.; Best, Q. A.; Shi, F.; Goodson, B. M.; Shchepin, R. V.; Coffey, A. M.; Waddell, K. W.; Chekmenev, E. Y., The Feasibility of Formation and Kinetics of NMR Signal Amplification by Reversible Exchange (SABRE) at High Magnetic Field (9.4 T). *Journal of the American Chemical Society* **2014**, *136*, 3322-3325.

160. Essig, M.; Shiroishi, M. S.; Thanh Binh, N.; Saake, M.; Provenzale, J. M.; Enterline, D.; Anzalone, N.; Doerfler, A.; Rovira, A.; Wintermark, M.; Law, M., Perfusion MRI: The Five Most Frequently Asked Technical Questions. *American Journal of Roentgenology* **2013**, *200*, 24-34.
161. Fekete, M.; Bayfield, O. W.; Duckett, S. B.; Hart, S.; Mewis, R. E.; Pridmore, N.; Rayner, P. J.; Whitwood, A., Iridium(III) Hydrido N-Heterocyclic Carbene-Phosphine Complexes as Catalysts in Magnetization Transfer Reactions (vol 52, pg 13453, 2013). *Inorganic Chemistry* **2014**, *53*, 2749-2749.
162. Mewis, R. E.; Green, R. A.; Cockett, M. C. R.; Cowley, M. J.; Duckett, S. B.; Green, G. G. R.; John, R. O.; Rayner, P. J.; Williamson, D. C., Strategies for the Hyperpolarization of Acetonitrile and Related Ligands by SABRE. *The Journal of Physical Chemistry B* **2014**, *119*, 1416-1424.
163. Lloyd, L. S.; Adams, R. W.; Bernstein, M.; Coombes, S.; Duckett, S. B.; Green, G. G. R.; Lewis, R. J.; Mewis, R. E.; Sleigh, C. J., Utilization of SABRE-Derived Hyperpolarization To Detect Low-Concentration Analytes via 1D and 2D NMR Methods. *Journal of the American Chemical Society* **2012**, *134*, 12904-12907.
164. Magnusson, P.; Johansson, E.; Mansson, S.; Petersson, J. S.; Chai, C. M.; Hansson, G.; Axelsson, O.; Golman, K., Passive catheter tracking during interventional MRI using hyperpolarized C-13. *Magnetic Resonance in Medicine* **2007**, *57*, 1140-1147.
165. Golman, K.; Olsson, L. E.; Axelsson, O.; Mansson, S.; Karlsson, M.; Petersson, J. S., Silvanus Thompson Memorial Lecture Molecular imaging using hyperpolarized C-13. *Br. J. Radiol.* **2003**, *76*, S118-S127.
166. Adams, R. W. Applications of Hyperpolarisation in Magnetic Resonance Imaging. University of York September 2009.
167. Adams, R. W. Applications of Hyperpolarisation in Magnetic Resonance Imaging. Ph.D, University of York 2009.
168. Lloyd, L. S.; Asghar, A.; Burns, M. J.; Charlton, A.; Coombes, S.; Cowley, M. J.; Dear, G. J.; Duckett, S. B.; Genov, G. R.; Green, G. G. R.; Highton, L. A. R.; Hooper, A. J. J.; Khan, M.; Khazal, I. G.; Lewis, R. J.; Mewis, R. E.; Roberts, A. D.; Ruddlesden, A. J., Hyperpolarisation through reversible interactions with parahydrogen. *Catalysis Science & Technology* **2014**, *4*, 3544-3554.
169. Burdick, B. A.; Benkovic, P. A.; Benkovic, S. J., Studies on models for tetrahydrofolic acid .8. hydrolysis and methoxyaminolysis of amidines. *Journal of the American Chemical Society* **1977**, *99*, 5716-5725.
170. Lewis, J. C.; Wiedemann, S. H.; Bergman, R. G.; Ellman, J. A., Arylation of heterocycles via rhodium-catalyzed C-H bond functionalization. *Organic Letters* **2004**, *6*, 35-38.
171. Makhloufi, A.; Wahl, M.; Frank, W.; Ganter, C., A New Mixed Amino-Amido N-Heterocyclic Carbene Based on Anthranilic Acid. *Organometallics* **2013**, *32*, 854-861.
172. Bugle, R. C.; Osteryoung, R. A., Reduction of azanaphthalenes by sodium borohydride in trifluoroacetic acid. *The Journal of Organic Chemistry* **1979**, *44*, 1719-1720.
173. Drost, R. M.; Bouwens, T.; van Leest, N. P.; de Bruin, B.; Elsevier, C. J., Convenient Transfer Semihydrogenation Methodology for Alkynes Using a Pd-II-NHC Precatalyst. *ACS Catalysis* **2014**, *4*, 1349-1357.
174. Smith, D. D.; Gallagher, A. T.; Crowley, V. M.; Gergens, W. M.; Abel, P. W.; Hulce, M., An Efficient Synthesis of 4(5)-Benzyl-L-histidines Employing Catalytic Transfer Hydrogenolysis at Elevated Temperatures. *Synthesis-Stuttgart* **2014**, *46*, 515-521.
175. Talwar, D.; Salguero, N. P.; Robertson, C. M.; Xiao, J., Primary Amines by Transfer Hydrogenative Reductive Amination of Ketones by Using Cyclometalated Ir-III Catalysts. *Chemistry-a European Journal* **2014**, *20*, 245-252.

176. Hoevener, J.-B.; Schwaderlapp, N.; Borowiak, R.; Lickert, T.; Duckett, S. B.; Mewis, R. E.; Adams, R. W.; Burns, M. J.; Highton, L. A. R.; Green, G. G. R.; Olaru, A.; Hennig, J.; von Elverfeldt, D., Toward Biocompatible Nuclear Hyperpolarization Using Signal Amplification by Reversible Exchange: Quantitative in Situ Spectroscopy and High-Field Imaging. *Analytical Chemistry* **2014**, *86*, 1767-1774.
177. Bhat, H.; Yang, Q.; Zuehlsdorff, S.; Li, K.; Li, D., Contrast-enhanced whole-heart coronary magnetic resonance angiography at 3 T with radial EPI. *Magnetic Resonance in Medicine* **2011**, *66*, 82-91.
178. Vale, A., Methanol. *Medicine* **2007**, *35*, 633-634.
179. Skrzydlewska, E., Toxicological and Metabolic Consequences of Methanol Poisoning. *Toxicology Mechanisms and Methods* **2003**, *13*, 277-293.
180. Tyagi, P.; Chancellor, M. B.; Li, Z.; de Groat, W. C.; Yoshimura, N.; Fraser, M. O.; Huang, L., Urodynamic and Immunohistochemical Evaluation of Intravesical Capsaicin Delivery Using Thermosensitive Hydrogel and Liposomes. *The Journal of Urology* **2004**, *171*, 483-489.
181. Shi, F.; Coffey, A. M.; Waddell, K. W.; Chekmenev, E. Y.; Goodson, B. M., Heterogeneous Solution NMR Signal Amplification by Reversible Exchange. *Angewandte Chemie International Edition* **2014**, *53*, 7495-7498.
182. Sheldon, R. A., Green solvents for sustainable organic synthesis: state of the art. *Green Chemistry* **2005**, *7*, 267-278.
183. Purwanto; Deshpande, R. M.; Chaudhari, R. V.; Delmas, H., Solubility of Hydrogen, Carbon Monoxide, and 1-Octene in Various Solvents and Solvent Mixtures. *Journal of Chemical & Engineering Data* **1996**, *41*, 1414-1417.
184. Kumar, A.; Kanwar, S. S., Synthesis of ethyl ferulate in organic medium using celite-immobilized lipase. *Bioresource Technology* **2011**, *102*, 2162-2167.
185. Barros, J. C.; Yaunner, R. S.; de Souza, A. L. F.; da Silva, J. F. M.; Antunes, O. A. C., Sonogashira coupling using PdEnCat (TM): a copper-, phosphine-, amine- and microwave-free alternative to the preparation of arylalkynes. *Applied Organometallic Chemistry* **2011**, *25*, 820-823.
186. Bouhrara, M.; Jeanneau, E.; Veyre, L.; Coperet, C.; Thieuleux, C., Dissymmetric gold(I) N-heterocyclic carbene complexes: a key unexpected structural parameter for highly efficient catalysts in the addition of alcohols to internal alkynes. *Dalton Transactions* **2011**, *40*, 2995-2999.
187. Kim, Y.-S.; Guo, X.-F.; Kim, G.-J., Highly active new chiral Co(III) salen catalysts immobilized by electrostatic interaction with sulfonic acid linkages on ordered mesoporous SBA-16 silica. *Chemical Communications* **2009**, 4296-4298.
188. Jesionowski, T.; Zdarta, J.; Krajewska, B., Enzyme immobilization by adsorption: a review. *Adsorption* **2014**, *20*, 801-821.
189. Kuil, M.; Soltner, T.; van Leeuwen, P. W. N. M.; Reek, J. N. H., High-precision catalysts: Regioselective hydroformylation of internal alkenes by encapsulated rhodium complexes. *Journal of the American Chemical Society* **2006**, *128*, 11344-11345.
190. Seelan, S.; Sinha, A. K., Phenol hydroxylation activity of metal phthalocyanine complexes encapsulated in zeolite-Y. *Applied Catalysis A: General* **2003**, *238*, 201-209.
191. Maurya, M. R.; Kumar, A.; Pessoa, J. C., Vanadium complexes immobilized on solid supports and their use as catalysts for oxidation and functionalization of alkanes and alkenes. *Coordination Chemistry Reviews* **2011**, *255*, 2315-2344.
192. Tyrrell, E.; Whiteman, L.; Williams, N., The synthesis and characterisation of immobilised palladium carbene complexes and their application to heterogeneous catalysis. *Journal of Organometallic Chemistry* **2011**, *696*, 3465-3472.

193. Jafarpour, L.; Stevens, E. D.; Nolan, S. P., A sterically demanding nucleophilic carbene: 1,3-bis(2,6-diisopropylphenyl)imidazol-2-ylidene). Thermochemistry and catalytic application in olefin metathesis. *Journal of Organometallic Chemistry* **2000**, *606*, 49-54.
194. Schwarz, J.; Böhm, V. P. W.; Gardiner, M. G.; Grosche, M.; Herrmann, W. A.; Hieringer, W.; Raudaschl-Sieber, G., Polymer-Supported Carbene Complexes of Palladium: Well-Defined, Air-Stable, Recyclable Catalysts for the Heck Reaction. *Chemistry – A European Journal* **2000**, *6*, 1773-1780.
195. Zeng, X.; Zhang, T.; Qin, Y.; Wei, Z.; Luo, M., Synthesis of a carbene transfer organometallic polymer and application to forming a recyclable heterogeneous catalyst for the Suzuki reactions of aryl chlorides. *Dalton Transactions* **2009**, 8341-8348.
196. Boydston, A. J.; Rice, J. D.; Sanderson, M. D.; Dykhno, O. L.; Bielawski, C. W., Synthesis and study of bidentate benzimidazolylidene - Group 10 metal complexes and related main-chain organometallic polymers. *Organometallics* **2006**, *25*, 6087-6098.
197. Magill, A. M.; McGuinness, D. S.; Cavell, K. J.; Britovsek, G. J. P.; Gibson, V. C.; White, A. J. P.; Williams, D. J.; White, A. H.; Skelton, B. W., Palladium(II) complexes containing mono-, bi- and tridentate carbene ligands. Synthesis, characterisation and application as catalysts in C-C coupling reactions. *Journal of Organometallic Chemistry* **2001**, *617-618*, 546-560.
198. Lorenzini, F.; Patrick, B. O.; James, B. R., Serendipitous syntheses of Rh(H)(2)Cl(PRPh₂)(3) complexes, and their crystal structures, where R = Me, Cy (cyclohexyl). *Inorganica Chimica Acta* **2008**, *361*, 2123-2130.
199. Chu, T. W.; Hu, S. W.; Wei, B.; Wang, Y.; Liu, X. Q.; Wang, X. Y., Synthesis and biological results of the technetium-99m-labeled 4-nitroimidazole for imaging tumor hypoxia. *Bioorganic & Medicinal Chemistry Letters* **2004**, *14*, 747-749.
200. Thomas, J. M.; Raja, R.; Lewis, D. W., Single-site heterogeneous catalysts. *Angewandte Chemie-International Edition* **2005**, *44*, 6456-6482.
201. Copéret, C.; Chabanas, M.; Petroff Saint-Arroman, R.; Basset, J.-M., Homogeneous and Heterogeneous Catalysis: Bridging the Gap through Surface Organometallic Chemistry. *Angewandte Chemie International Edition* **2003**, *42*, 156-181.
202. Thomas, J. M.; Raja, R., The advantages and future potential of single-site heterogeneous catalysts. *Topics in Catalysis* **2006**, *40*, 3-17.
203. Thomas, J. M.; Hernandez-Garrido, J. C.; Raja, R.; Bell, R. G., Nanoporous oxidic solids: the confluence of heterogeneous and homogeneous catalysis. *Physical Chemistry Chemical Physics* **2009**, *11*, 2799-2825.
204. Thomas, J. M.; Raja, R., Designed open-structure heterogeneous catalysts for the synthesis of fine chemicals and pharmaceuticals. *From Zeolites to Porous Mof Materials: The 40th Anniversary of International Zeolite Conference, Proceedings of the 15th International Zeolite Conference* **2007**, *170*, 19-40.
205. Ramarao, C.; Ley, S. V.; Smith, S. C.; Shirley, I. M.; DeAlmeida, N., Encapsulation of palladium in polyurea microcapsules. *Chemical Communications* **2002**, 1132-1133.
206. Cavarzan, A.; Reek, J. N. H.; Trentin, F.; Scarso, A.; Strukul, G., Substrate selectivity in the alkyne hydration mediated by NHC-Au(i) controlled by encapsulation of the catalyst within a hydrogen bonded hexameric host. *Catalysis Science & Technology* **2013**, *3*, 2898-2901.
207. Barros, J. C., Microencapsulated Palladium Catalysts: Pd EnCat (TM). *Australian Journal of Chemistry* **2010**, *63*, 850-850.
208. Bolfa, C.; Zoleo, A.; Sassi, A. S.; Maniero, A. L.; Pears, D.; Jerabek, K.; Corain, B., Cross-linked poly-vinyl polymers versus polyureas as designed supports for catalytically active M-0 nanoclusters - Part I. Nanometer scale structure of the polyurea support EnCat (TM) 40. *Journal of Molecular Catalysis a-Chemical* **2007**, *275*, 233-239.

209. Carpita, A.; Ribecai, A., Convenient copper- and solvent-free Sonogashira-type alkylation of aryl iodides and bromides using Pd EnCat (TM). *Tetrahedron Letters* **2009**, *50*, 204-207.
210. Centomo, P.; Zecca, M.; Kralik, M.; Gasparovicova, D.; Jerabek, K.; Canton, P.; Corain, B., Cross-linked poly-vinyl polymers versus polyureas as designed supports for catalytically active M-0 nanoclusters Part II. Pd-0/cross-linked poly-vinyl polymers versus Pd-0/EnCat (TM) 30NP in mild hydrogenation reactions. *Journal of Molecular Catalysis a-Chemical* **2009**, *300*, 48-58.
211. Kimachi, T.; Nagata, H.; Kobayashi, Y.; Takahashi, K.; Torii, E.; Ju-ichi, M., Regioselective Ring-Opening Reaction of Unsymmetrical 2,3-Diaryl Epoxides via Catalytic Hydrogenolysis with Pd(0)EnCat (TM). *Synlett* **2011**, 365-368.
212. Kuang, Y.-Y.; Chen, F.-E., Copper- and Phosphine-Free Sonogashira Coupling Reaction Catalyzed by Polyurea-Encapsulated Palladium(II). *Helvetica Chimica Acta* **2009**, *92*, 897-902.
213. Ley, S. V.; Stewart-Liddon, A. J. P.; Pears, D.; Perni, R. H.; Treacher, K., Hydrogenation of aromatic ketones, aldehydes, and epoxides with hydrogen and Pd(0)EnCat (TM) 30NP. *Beilstein Journal of Organic Chemistry* **2006**, *2*.
214. Sedelmeier, J.; Ley, S. V.; Lange, H.; Baxendale, I. R., Pd-EnCat (TM) TPP30 as a Catalyst for the Generation of Highly Functionalized Aryl- and Alkenyl-Substituted Acetylenes via Microwave-Assisted Sonogashira Type Reactions. *European Journal of Organic Chemistry* **2009**, 4412-4420.
215. Kingsbury, J. S.; Garber, S. B.; Giftos, J. M.; Gray, B. L.; Okamoto, M. M.; Farrer, R. A.; Fourkas, J. T.; Hoveyda, A. H., Immobilization of olefin metathesis catalysts on monolithic sol-gel: Practical, efficient, and easily recyclable catalysts for organic and combinatorial synthesis. *Angewandte Chemie-International Edition* **2001**, *40*, 4251-4256.
216. Çetinkaya, B.; Gürbüz, N.; Seçkin, T.; Özdemir, I., Synthesis and immobilization of N-heterocyclic carbene complexes of Ru(II): catalytic activity and recyclability for the furan formation. *Journal of Molecular Catalysis A: Chemical* **2002**, *184*, 31-38.
217. Mayr, M.; Buchmeiser, M. R.; Wurst, K., Synthesis of a silica-based heterogeneous second generation Grubbs catalyst. *Advanced Synthesis & Catalysis* **2002**, *344*, 712-719.
218. Fischer, D.; Blechert, S., Highly active silica gel-supported metathesis (pre) catalysts. *Advanced Synthesis & Catalysis* **2005**, *347*, 1329-1332.
219. Li, L.; Shi, J. L., A highly active and reusable heterogeneous ruthenium catalyst for olefin metathesis. *Advanced Synthesis & Catalysis* **2005**, *347*, 1745-1749.
220. Krause, J. O.; Lubbad, S. H.; Nuyken, O.; Buchmeiser, M. R., Heterogenization of a modified Grubbs-Hoveyda catalyst on a ROMP-derived monolithic support. *Macromolecular Rapid Communications* **2003**, *24*, 875-878.
221. Macquarrie, D. J.; Jackson, D. B.; Mdoe, J. E. G.; Clark, J. H., Organomodified hexagonal mesoporous silicates. *New Journal of Chemistry* **1999**, *23*, 539-544.
222. Gonzalez-Arellano, C.; Corma, A.; Iglesias, M.; Sanchez, F., Pd(II)-Schiff base complexes heterogenised on MCM-41 and delaminated zeolites as efficient and recyclable catalysts for the Heck reaction. *Advanced Synthesis & Catalysis* **2004**, *346*, 1758-1764.
223. Cauvel, A.; Renard, G.; Brunel, D., Monoglyceride synthesis by heterogeneous catalysis using MCM-41 type silicas functionalized with amino groups. *Journal of Organic Chemistry* **1997**, *62*, 749-751.
224. Zhang, H. D.; Xiang, S.; Xiao, J. L.; Li, C., Heterogeneous enantioselective epoxidation catalyzed by Mn(salen) complexes grafted onto mesoporous materials by phenoxy group. *Journal of Molecular Catalysis a-Chemical* **2005**, *238*, 175-184.
225. Maishal, T. K.; Alauzun, J.; Basset, J.-M.; Coperet, C.; Corriu, R. J. P.; Jeanneau, E.; Mehdi, A.; Reye, C.; Veyre, L.; Thieuleux, C., A Tailored Organometallic-Inorganic Hybrid Mesostructured Material: A Route to a Well-Defined, Active, and Reusable Heterogeneous

Iridium-NHC Catalyst for H/D Exchange. *Angewandte Chemie-International Edition* **2008**, *47*, 8654-8656.

226. Skovpin, I. V.; Zhivonitko, V. V.; Koptuyug, I. V., Parahydrogen-Induced Polarization in Heterogeneous Hydrogenations over Silica-Immobilized Rh Complexes. *Applied Magnetic Resonance* **2011**, *41*, 393-410.

227. Shyu, S. G.; Cheng, S. W.; Tzou, D. L., Immobilization of Rh(PPh₃)₃Cl on phosphinated MCM-41 for catalytic hydrogenation of olefins. *Chemical Communications* **1999**, 2337-2338.

228. Thomas, J. M., The concept, reality and utility of single-site heterogeneous catalysts (SSHCs). *Physical Chemistry Chemical Physics* **2014**, *16*, 7647-7661.

229. Truong, M. L.; Shi, F.; He, P.; Yuan, B.; Plunkett, K. N.; Coffey, A. M.; Shchepin, R. V.; Barskiy, D. A.; Kovtunov, K. V.; Koptuyug, I. V.; Waddell, K. W.; Goodson, B. M.; Chekmenev, E. Y., Irreversible Catalyst Activation Enables Hyperpolarization and Water Solubility for NMR Signal Amplification by Reversible Exchange. *The Journal of Physical Chemistry B* **2014**, *118*, 13882-13889.

230. Skovpin, I. V.; Zhivonitko, V. V.; Kaptein, R.; Koptuyug, I. V., Generating Parahydrogen-Induced Polarization Using Immobilized Iridium Complexes in the Gas-Phase Hydrogenation of Carbon-Carbon Double and Triple Bonds. *Applied Magnetic Resonance* **2013**, *44*, 289-300.

231. Permin, A.; Eisenberg, R., Parahydrogen induced polarization and the oxidative addition of hydrogen to iridium tribromostannyl carbonylate anions. *Inorganic Chemistry* **2002**, *41*, 2451-2458.

232. Harthun, A.; Giernoth, R.; Elsevier, C. J.; Bargon, J., Rhodium- and palladium-catalysed proton exchange in styrene detected in situ by para-hydrogen induced polarization. *Chemical Communications* **1996**, 2483-2484.

233. Giernoth, R.; Huebler, P.; Bargon, J., Intermediate Product-Catalyst Complexes in the Homogeneous Hydrogenation of Styrene Derivatives with Parahydrogen and Cationic RhI Catalysts. *Angewandte Chemie International Edition* **1998**, *37*, 2473-2475.

234. Zeng, H.; Xu, J.; Gillen, J.; McMahon, M. T.; Artemov, D.; Tyburn, J.-M.; Lohman, J. A. B.; Mewis, R. E.; Atkinson, K. D.; Green, G. G. R.; Duckett, S. B.; van Zijl, P. C. M., Optimization of SABRE for polarization of the tuberculosis drugs pyrazinamide and isoniazid. *Journal of Magnetic Resonance* **2013**, *237*, 73-78.

235. Schaper, L.-A.; Hock, S. J.; Herrmann, W. A.; Kühn, F. E., Synthesis and Application of Water-Soluble NHC Transition-Metal Complexes. *Angewandte Chemie International Edition* **2013**, *52*, 270-289.

236. Moore, L. R.; Cooks, S. M.; Anderson, M. S.; Schanz, H.-J.; Griffin, S. T.; Rogers, R. D.; Kirk, M. C.; Shaughnessy, K. H., Synthesis and Characterization of Water-Soluble Silver and Palladium Imidazol-2-ylidene Complexes with Noncoordinating Anionic Substituents. *Organometallics* **2006**, *25*, 5151-5158.

237. Özdemir, İ.; Yiğit, B.; Çetinkaya, B.; Ülkü, D.; Tahir, M. N.; Arıcı, C., Synthesis of a water-soluble carbene complex and its use as catalyst for the synthesis of 2,3-dimethylfuran. *Journal of Organometallic Chemistry* **2001**, *633*, 27-32.

238. Gallivan, J. P.; Jordan, J. P.; Grubbs, R. H., A neutral, water-soluble olefin metathesis catalyst based on an N-heterocyclic carbene ligand. *Tetrahedron Letters* **2005**, *46*, 2577-2580.

239. Nishioka, T.; Shibata, T.; Kinoshita, I., Sugar-Incorporated N-Heterocyclic Carbene Complexes. *Organometallics* **2007**, *26*, 1126-1128.

240. Zeng, H.; Xu, J.; McMahon, M. T.; Lohman, J. A. B.; van Zijl, P. C. M., Achieving 1% NMR polarization in water in less than 180 min using SABRE. *Journal of Magnetic Resonance* **2014**, *246*, 119-121.

241. Gaulier, C.; Hospital, A.; Legeret, B.; Delmas, A. F.; Aucagne, V.; Cisnetti, F.; Gautier, A., A water soluble Cu-I-NHC for CuAAC ligation of unprotected peptides under open air conditions. *Chemical Communications* **2012**, *48*, 4005-4007.
242. Teyssot, M.-L.; Chevry, A.; Traïkia, M.; El-Ghozzi, M.; Avignant, D.; Gautier, A., Improved Copper(I)-NHC Catalytic Efficiency on Huisgen Reaction by Addition of Aromatic Nitrogen Donors. *Chemistry – A European Journal* **2009**, *15*, 6322-6326.
243. Teyssot, M.-L.; Nauton, L.; Canet, J.-L.; Cisnetti, F.; Chevry, A.; Gautier, A., Aromatic Nitrogen Donors for Efficient Copper(I)-NHC CuAAC under Reductant-Free Conditions. *European Journal of Organic Chemistry* **2010**, *2010*, 3507-03515.
244. Gaulier, C.; Hospital, A.; Legeret, B.; Delmas, A. F.; Aucagne, V.; Cisnetti, F.; Gautier, A., A water soluble CuI-NHC for CuAAC ligation of unprotected peptides under open air conditions. *Chemical Communications* **2012**, *48*, 4005-4007.
245. Díez-González, S., N-Heterocyclic Carbenes : From Laboratory Curiosities to Efficient Synthetic Tools. In *N-Heterocyclic Carbenes* 2011.